Morphological Classification and Dynamics of X-ray Galaxy Clusters

Viral Parekh

November 2013

In fulfilment of the requirements for the degree of Doctor of Philosophy
in the Department of Astronomy
UNIVERSITY OF CAPE TOWN

Supervisor: Dr. Kurt van der Heyden

Abstract

In recent years multiwavelength observations have shown the presence of substructures related to merging events in a high fraction of galaxy clusters. Clusters can be grouped roughly into two categories – relaxed and non-relaxed – and a proper characterization of the dynamical state of these systems is of crucial importance both for astrophysical and cosmological studies.

In this thesis we investigated the use of a number of morphological parameters (Gini, M_{20}, Concentration, Asymmetry, Smoothness, Ellipticity and Gini of the second order moment (G_M)) introduced to classify clusters automatically as relaxed or dynamically disturbed systems. Initially we tested these parameters on the simple beta model simulations. We then applied our method to a sample of clusters at different redshifts extracted from the *Chandra* archive, and we investigated possible correlations between morphological parameters and other X-ray gas properties. We conclude that a combination of the adopted parameters is a useful tool to properly characterise the X-ray cluster morphology. We also investigated substructure identification via thermodynamic maps of galaxy clusters, which include electron density, temperature, pseudo-entropy and pseudo-pressure. We investigate the radial profiles derived from these maps.

According to our results, three parameters – Gini, M_{20} and Concentration – are very promising for identifying cluster mergers. The Gini coefficient is a particularly powerful tool, especially at high redshift, being independent of the choice of the position of the cluster centre. We find that high Gini (> 0.65), high Concentration (> 1.55) and low M_{20} ($<$ -2.0) values are associated with relaxed clusters, while low Gini (< 0.4), low Concentration (< 1.0) and high M_{20} ($>$ -1.4) characterise dynamically perturbed systems. We find that, high fluctuation and discontinuity in thermodynamic radial profiles are two typical and most sensitive indicators of substructure. We also applied our morphology parameters to thermodynamic maps of X-ray clusters to investigate their morphology and dynamical states. We also estimate the X-ray cluster morphological parameters in the case of radio loud (or halo) clusters. In excellent agreement with previous analyses, we confirm that diffuse intra-cluster radio sources are associated with major mergers.

Acknowledgements

Foremost, I would like to express my sincere gratitude to my adviser Dr Kurt van der Heyden for his continuous support and excellent guidance during my PhD research and write-up; for his patience, motivation, and enthusiasm. I truly admire his friendly and helpful nature. My undergraduate and Masters background was in electronics, yet he continually encouraged me to learn astronomy throughout my PhD studies. I can not imagine having had a better adviser and mentor for this work.

I am grateful to the South African Square Kilometre Array project, who funded my bursary as well as travel and equipment for four years.

My sincere thanks also go to Dr John Peterson and his research team at Purdue University, USA, who assisted me in learning and using the XMC technique; and Dr Benne Holwerda (ESA) for providing me with the morphology parameter calculation script. This research has made use of data obtained from the Chandra Data Archive and the Chandra Source Catalog, and software provided by the Chandra X-ray Center (CXC) in the application packages CIAO, ChIPS, and Sherpa. The author would like to thank the Centre for High Performance Computing for providing access to supercomputing resources for this work.

I am very fortunate to have had a PhD position in such a beautiful university - the University of Cape Town - situated on the slopes of Table Mountain which is surrounded by oceans. I am most grateful to the Astronomy Department, University of Cape Town, for providing all the facilities necessary to complete my research. Special thanks to Dr. Garry Angus and Lesley Jennings for reading and helping me to improve my thesis.

My heartfelt thanks to my wife, Ishita, for her understanding and endless love throughout this research. Last, but certainly not least, I would like to thank my parents for their warm blessing, spiritual support and encouragement.

Plagiarism Declaration

I, Viral Parekh, know the meaning of plagiarism and declare that all of the work in the document, save for that which is properly acknowledged, is my own.

Abbreviation

ACIS - Advanced CCD Imaging Spectrometer
AGN - Active Galactic Nucleus
APEC - Astrophysical Plasma Emission Code
ASKAP - Australian Square Kilometer Array Pathfinder
BCG - Brightest Cluster Galaxy
CALDB - CALibration DataBase
CCD - Charge Couple Device
CCT - Central Cooling Time
CHPC - Centre for High Performance Computing
CIAO - Chandra Interactive Analysis of Observations
CTI - Charge Transfer Inefficiency
EMU - Evolutionary Map of the Universe
FITS - Flexible Image Transport System
FOV - Field of View
GTI - Good Time Interval
HETG - High Energy Transmission Grating
HRC- High Resolution Camera
HST - Hubble Space Telescope
ICM - Intra-cluster medium
LETG - Low Energy Transmission Grating
LOFAR - Low Frequency Array
LLS - Largest Linear Size
LWA - Long Wavelength Array
MCMC - Markov Chain Monte Carlo
MIGHTEE - The MeerKAT International Giga-Hertz Tiered Extragalactic Exploration
NED - NASA Extragalactic Database
PHA - Pulse Height Amplitude
PI - Pulse Invariant

PSPC - Position Sensitive Proportional Counters
QE - Quantum Efficiencies
RMF - Response Matrix Function
SDSS - Sloan Digital Sky Survey
SPI - Smooth Particle Inference
SKA - Square Kilometre Array
XMC - Xray Monte Carlo
WODAN - Westerbork Observatons of the Deep APERTIF Northern-Sky

Contents

List of Figures

List of Tables

1

Introduction

1.1 The nature of galaxy clusters

In recent years our knowledge has expanded from the early legendary work of Astronomers such as Abell, Zwicky and others, about the nature and behaviour of galaxy clusters. Galaxy clusters are the most massive bound and quasi-relaxed objects in the Universe with typical masses of about $10^{15}\ M_{\odot}$. The largest galaxy clusters are typically Mpc in size. It is believed that, in any cluster, the majority ($\sim 80\%$) of the gravitating material is in the form of dark matter which is mainly responsible for a cluster's total gravitational mass, and hence structure. Luminous or visible matter is minimal ($\sim 3\%$ to 5%) and pertains to galaxies only. The remaining matter ($\sim 15\%$ to 17%) is in the hot, diffuse gas. This gas is detected in X-ray wavelength through its thermal bremsstrahlung emission with energy of several keV. This thermal plasma in the cluster medium (in between galaxies) is commonly referred to as the Intra-cluster medium (ICM). ICM is a key property of galaxy clusters, and represents the many features of the parent cluster. Clusters are widespread in the sky, and it would seem that they represent the unit of matter, or building brick, from which the Universe is assembled. Based on this assumption, smaller blocks (galaxies, groups and minor clusters) would have formed first and subsequently united under gravitational attraction, making bigger and bigger blocks with the flow of time.

Detailed knowledge of galaxy clusters has been obtained in recent years as the result of advancement of observational instruments. It is of great interest to astronomers to observe galaxy clusters in various wavelengths, from radio to gamma ray, to address the key questions related to formation and evolution of galaxy clusters. Below we give a brief background of Multiwavelength observation of galaxy clusters.

1.2 Multiwavelength observation of galaxy clusters

1.2.1 Optical observations

The story begins in the years 1958 and 1961, when the first comprehensive galaxy cluster catalogues were compiled by George Abell and Fritz Zwicky (Abell, 1958; Zwicky et al., 1961, 1968), respectively, from which they noticed over-dense regions of galaxies in the sky. For the purpose of these catalogues, they used Northern sky *Palomar Observatory Sky Survey* (POSS) photo plates and visually detected galaxy clusters. In this work, Abell could observe only clusters away from the galactic disk region, because the observation of galaxies is more difficult there due to extinction and high stellar density.

In the past, galaxy clusters have been studied extensively to understand the distribution of dark matter and baryon material, evolution of large scale structure of the Universe, and fundamental cosmology associated with it. Galaxy clusters are very complex systems. They include hundreds of galaxies which make them collectively the largest structure in the Universe. These galaxies are coupled tightly to each other and make either groups or clusters. For instance, our own *Milky Way* is part of a galaxy group. This group is famously known as the *Local Group*. In contrast to the *Local Group*, the nearest ($\sim$ 20 Mpc away) galaxy cluster to us is the *Virgo cluster*. The distinction between group and cluster is made by the number of member galaxies in each. Generally groups have $\lesssim$ 50 member galaxies within a sphere of diameter D $\lesssim 1.5h^{-1}$ Mpc, while clusters have $\gtrsim$ 50 member galaxies within a diameter of $\gtrsim 1.5h^{-1}$ Mpc. Groups have a total mass of $\sim 10^{14}\ M_{\odot}$ while clusters have 10^{14} to above $10^{15}\ M_{\odot}$ (Bahcall, 1996). A cluster is said to be richer and more luminous when it contains $>$ 300 member galaxies.

Most of the rich and regular clusters show a concentrated distribution of galaxies at the core. The density of galaxies (mainly elliptical and S0 types of galaxies) increases strongly towards the centre because the gravitational potential well is strongest at the cluster centre. Many clusters contain one super-giant central dominated (cD) elliptical galaxy at the cluster centre, also known as the brightest cluster galaxy (BCG), having luminosity $\sim 10^{12}\ L_{\odot}$. This cD galaxy growing mass because of galaxy mergers as well as accretion of cooling gas flowing towards the cluster centre. In some cases, where galaxy clusters have recently undergone major merger events, there may be two or more such galaxies which have not yet had time to merge into a new large central galaxy.

Galaxies inside a given cluster move away from us at Hubble velocity (i.e. due to the expansion of the Universe). In addition to this, galaxies in a cluster are more compact and have greater velocity dispersion. Galaxies have peculiar motions which show up as a velocity dispersion of 100-1000 km/s (median line-of-sight velocity dispersion) around the average (expansion) velocity. Below we show different optical galaxy classification schemes that are widely used.

1.2.2 Galaxy classification method

To investigate the classification of clusters, one has to consider morphology of their galaxies. Bautz & Morgan (1970) provided a systematic classification of optical galaxy clusters based on the degree to which a cluster is dominated by its brightest galaxies. B-M (Bautz and Morgan) Type I galaxy clusters have a single, centrally located cD galaxy. Generally, these cD galaxies are the most luminous in a cluster, and have extensive optical emission. B-M Type II clusters are dominated by the intermediate brightest galaxies between cD and normal giant elliptical galaxies. Finally, B-M Type III clusters do not contain any dominating galaxies.

Later on Rood-Sastry classified optical galaxy clusters based on the nature and distribution of the ten brightest cluster galaxies (Rood & Sastry, 1971). The six various classes of Rood-Sastry are defined as, (1) **cD**: the cluster is dominated by a central cD galaxy, (2) **B**: binary galaxies – the cluster is dominated by a pair of luminous galaxies, (3) **L**: line galaxies – minimum of three

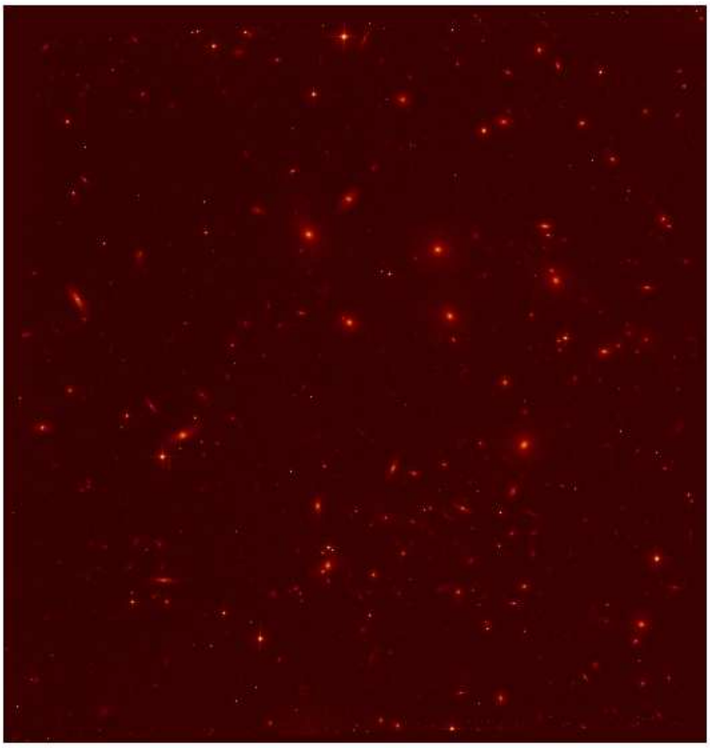

Figure 1.1: Hubble Space Telescope (HST) image of the A2163 cluster. Each individual object is a galaxy. Clearly, it is difficult to find member galaxies of A2163: one has to find redshift of each galaxy. Some galaxies appear to be in the background, while others appear to be in the foreground of this image.

brightest galaxies appear to be in a straight line, (4) **C**: core galaxies – core of the cluster formed by four or more of the ten brightest galaxies, (5) **F**: flat galaxies – the brightest cluster galaxies form a flattened distribution on the sky, and (6) **I**: irregular galaxies – irregular distribution of brightest galaxies in the cluster with no clear centre or core.

There is an advantage to examining the morphology of galaxies. Dressler (1980) systematically shown the relationship between galaxy morphology and local density of galaxies within a cluster, and gave it the term morphology-density relation. It is very useful in understanding the relationship between different morphological types of galaxies, which are based mainly on the Hubble types and the environments in which they are situated. This relationship also indicates that galaxy evolution is affected by the environments in which the galaxy itself is located. Different morphology of galaxies directly explains various galaxy transformation processes that occur within the cluster environment (Moore et al., 1998; Bravo-Alfaro et al., 2000; Bekki et al., 2002). These morphologies are possibly connected to the distance of the galaxy from the centre of the cluster. Also, the study of galaxy morphology is connected to the previous star formation and stellar distribution history of galaxies inside the cluster. For instance, observational evidence provides information that when galaxies enter high density environments such as clusters, their star formation activity is suppressed. Hence, investigating morphology of galaxies answers many questions related to its properties, formation history and overall morphology of clusters.

Based on various morphology classification strategies, galaxy clusters could be divided broadly into two categories, namely regular (relaxed) and irregular (distorted or merger) clusters. Ofcourse, passage between these two categories is continuous for intermediate clusters. Regular clusters are highly symmetric in shape and have a large number of member galaxies, causing dense central concentration (smoothly distributed galaxies). However, the latter category of clusters shows very little symmetry and no central concentration, and is sometimes also referred to as an open cluster (according to the Zwicky's classification criteria). Regular clusters may or may not have weak subclustering, in contrast to irregular clusters. Regular clusters often have giant cD-type galaxies at their centres. These galaxies are generally large and elliptical, and sometimes have strong radio sources (radio galaxies). These galaxies are very luminous and more concentrated in rich clusters. Generally, elliptical galaxies are visible in regular clusters, while irregular clusters contain galaxies of all types, although mainly spiral and irregular. Regular clusters are dynamically relaxed systems, while irregular clusters are dynamically less-evolved while their structure formation progresses with time.

1.2.3 Radio emission from galaxy clusters

Galaxy clusters are also visible in the radio wavelength. Generally a cluster's individual galaxies are a source of radio emission; and observational evidence also suggests that, in some cases, these optical galaxies have corresponding radio counterparts. Emission from these radio galaxies often extends quite beyond the galaxy's optical boundaries up to an order of 100 kpc. This suggests that the radio emitting regions interact with the ICM. Tailed radio galaxies and radio sources filling X-ray cavities at the centre of cool core clusters reveal this interaction (McNamara & Nulsen, 2007, and references therein). Furthermore, it is also equally important to investigate the role of non-thermal emission from galaxy clusters, to characterise the physical description of the ICM. Radio observations provide detailed evidence for these phenomena in terms of wide diffuse synchrotron sources (for example, *radio halos*, *relics* and *mini-halos*), which are closely associated with the ICM rather than individual galaxies within a cluster.

The radio emission from galaxy clusters is synchrotron emission due to the interaction between non-thermal population of relativistic electrons (power-law distribution) and a cluster's magnetic field. The synchrotron emission of such sources requires a population of $\approx$ GeV relativistic electrons and cluster magnetic fields on μG levels. The synchrotron emission is produced by the spiralling motion of relativistic electrons in a magnetic field, which results in emission of radio signals in the MHz band. The total synchrotron emission from a radio source gives an estimate of the strength of magnetic fields. The degree of polarisation is an important indicator of the field uniformity and structure. The intensity S_ν (erg/cm^2-Hz-s) of synchrotron emission is given as the power-law with a broad range of frequencies ν and radio spectral index α,

$$S_\nu \propto \nu^{-\alpha}.$$

The higher the magnetic field strength, the lower the electron energy needed to produce emission at a given frequency. In a magnetic field of $\sim$ 1 μG, synchrotron radiation can be detected, for example, at 100 MHz. The synchrotron radiation is essentially a continuum radiation with a fairly peaked spectrum concentrated near the critical frequency. Faint and low-surface brightness radio sources are more visible in low frequency observations ($\lesssim$ 1 GHz) due to their steep spectra. Hence low frequency observations with advanced radio telescopes which have higher sensitivity are required to detect these diffuse sources.

1.2.4 Diffuse radio sources

Extended radio sources, lying in galaxy clusters, are associated with diffuse, non-thermal and low surface brightness emission as well as being characterised by a steep spectrum (-0.7 $\gtrsim \alpha \gtrsim$ -1.4). This makes it difficult to detect them with current radio telescopes - single dish or interferometer. (1) Extended and low surface brightness diffuse radio sources are most easily detected with filled-aperture telescopes, but the low resolving power of single-dish radio telescopes could result in source confusion, and could create an image of an extended source from the combining of weak discrete radio sources. (2) Interferometer observations provide the necessary resolution to separate the individual radio galaxies, but generally lack information from short spacings to prevent the detection of wide faint structure. Lower sensitivity of current radio telescopes could be one of the reasons behind low detection rate of diffuse radio sources to date. It is important to study diffuse sources in the understanding of (i) the role of large scale magnetic fields and relativistic particles in the ICM, (ii) physical conditions in galaxy clusters and their dynamical activity using radio observations of diffuse sources such as *radio halos* and *relics*, and (iii) cluster history and evolution, as diffuse sources are large-scale features that are related to other cluster properties in the optical and X-ray domains.

The diffuse extended cluster-wide radio sources are currently grouped in three classes: *radio halos*, *relics* and *mini-halos* (Feretti et al., 2012, and references therein). The *radio halos* are found at the core of a cluster region, with typical size $\gtrsim$ 1 Mpc and steep spectra. The *relic* sources are similar to the halos in their low surface brightness, large size and steep spectra, but are found typically in peripheral regions of the cluster. Unlike halos, *relic* sources are highly polarised around 20%. The mini-halos are detected around a dominant powerful radio galaxy at the centre of cooling core clusters, up to a maximum of $\sim$ 500 kpc. In this our research, we are interested in studying properties of *radio halos* and *relics* only. Below we give a brief background of *radio halos* and *relics.*

Radio halos

Radio halos are cluster-wide extended diffuse sources with low surface brightness ($\sim$ 1-0.1 μJy arcsec^{-2} at 1.4 GHz), are unpolarised, and are centrally located. Current observation indicates that they are not linked with any single galaxy cluster member (i.e. one of the galaxies). They have regular morphologies and good spatial coincidence with their X-ray brightness distribution, as shown in Fig. 1.2. Because of the improvement in radio telescope observation, sensitivity and image processing, in the past decade a number of new halos have been discovered in rich galaxy clusters with GMRT, VLA and other radio telescopes (Giovannini et al., 1999; Kempner & Sarazin, 2001; Venturi et al., 2007, 2008; van Weeren et al., 2009a,b). So far, $\sim$ 45 *radio halos* have been detected (Feretti et al., 2012).

The radio properties of halos are coupled to the global properties of their host galaxy cluster. Clusters with the highest X-ray luminosity have a higher probability of hosting *radio halos.* Further, the monochromatic radio power of a halo at 1.4 GHz correlates with the X-ray luminosity, mass and temperature of a cluster (Giovannini & Feretti, 2002). It is expected that a large fraction of the most massive clusters, in the redshift range of $z \sim$ 0.2-0.4 and X-ray luminosity, $L_x > 5 \times 10^{44}$ erg/s, hosts a *radio halo.* Literature data for clusters at $z =$ 0-0.2 is in agreement with this statistical expectation (Giovannini et al., 1999). *Radio halos* are also linked with cluster dynamical activity. They are found typically in clusters with significant substructure and deviation from spherical symmetry in their X-ray morphology. This is confirmed by the high resolution X-ray data obtained with *Chandra* and *XMM* (Markevitch et al., 2000; Markevitch & Vikhlinin, 2001; Markevitch et al., 2002, 2003b,c). Therefore the available data suggest that *radio halos* are strictly related to the X-ray properties of the host clusters, as well as to the presence of cluster merger processes.

Halo morphology and sizes vary from giant ($\sim$ 1 Mpc) to small ($\sim$ 100 kpc), and could be detected, as indicated above, because of the advancement in sensitivity and angular resolution of radio telescopes. It seems that conditions at the time of origin could have played a role in the present appearance of halo morphology. There is a strong correlation between *radio halo* linear size and total radio output power (Giovannini et al., 2009). This correlation is continuous from small to giant size halos. It also confirms that both the larger and smaller *radio halos* belong to the same class of source. A smaller *radio halo* shows similar properties to those of larger *radio halos* (Feretti et al., 2010). Hence, there could be a common origin and physical mechanism for large and small *radio halos.*

Radio relics

Radio relics sources are low surface brightness, large size and steep spectrum sources located in peripheral regions of the cluster, as shown in Fig. 1.3. In most cases, the morphology of *relic sources* is elongated, and situated at either one side (single *relic*) or two sides (double *relics*) of

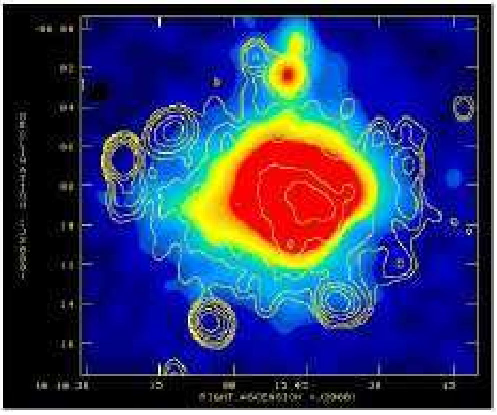

Figure 1.2: *Radio halo* of the A2163 cluster (Feretti et al., 2001). *Radio halo* emission is (white contours) spatially co-incidence with X-ray emission (in color).

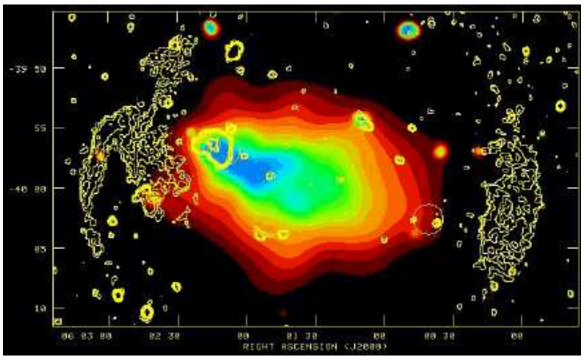

Figure 1.3: *Radio relic* of the A3376 cluster (Bagchi et al., 2006). *Radio relic* emission is in yellow contours and X-ray emission is in color.

the cluster (Bagchi et al., 2006; van Weeren et al., 2009a; Bonafede et al., 2009; Bagchi et al., 2011). *Relic* sources are highly polarised. Originally they were thought to be *relics* of presently non-active galaxies, but no evidence has yet been found in support of this supposition. Currently we know that $\sim$ 50 *relics* are hosted in 39 galaxy clusters (Feretti et al., 2012). Observation of *relics* gives the best indication of the presence of μG level magnetic fields and relativistic particles in the periphery of a cluster. Their observation also reveals the acceleration of relativistic particles at shock fronts at great distance (Mpc scale) from the cluster centre. Theoretical work proposes that they are tracers of shock waves in merger events (Ensslin et al., 1998; Hoeft et al., 2004). This prediction is in agreement with their elongated morphology and perpendicularity to the merger axis. This is confirmed by observational results.

Kempner et al. (2004) classified cluster *radio relics* in two classes: (1) radio Phoenix, which is associated with a past AGN outburst activity, and (2) radio Gischt, which is associated with cluster ICM. This classification is widely accepted in *radio relic* research. The radio properties of *relics* have been linked to the properties of their hosting clusters. Similar to *radio halos*, there is a correlation between the radio power of a *relic* at 1.4 GHz and the X-ray luminosity of clusters ($P_{1.4GHz} \propto L_x^{1.2}$) (Giovannini & Feretti, 2002; Cassano et al., 2011).

Origin of diffuse sources

Current observations show that these diffuse sources are found only in clusters which have undergone a recent merger event (Cassano & Brunetti, 2005; Brunetti et al., 2009; Cassano et al., 2011). Hence it is crucial to know the dynamical activity of a galaxy cluster. This merging activity gives rise to the thought that diffuse sources are energised by turbulence and shocks in mergers (Cassano & Brunetti, 2005). The formation and evolution of diffuse sources are still not clear. Several theories have been made for the mechanism of transferring energy into the relativistic electron population, and for the origin of relativistic electrons themselves. The relativistic particles could be injected in the cluster volume by AGN activity such as quasars, radio galaxies, etc. Most particle production has occurred in the past and is therefore connected to the dynamical history of the clusters. This primary electrons population needs to be re-accelerated (Brunetti et al., 2001; Petrosian, 2001) to compensate for radiative losses. A recent cluster merger is the most likely process to stimulate the re-acceleration of relativistic particles.

Another model for radiating particles in halos incorporates secondary electrons as the result of inelastic nuclear collisions which have occurred between the relativistic protons and thermal ions of the ambient ICM. The protons diffuse on a large scale because their energy losses are negligible. They can continuously produce in-situ electrons which are distributed throughout the cluster volume (Blasi & Colafrancesco, 1999; Miniati et al., 2001). It is possible that the high energy electrons, responsible for the synchrotron emission, arise from the decay of secondary products of the neutralino annihilation in the dark matter halos of galaxy clusters has also been proposed (Colafrancesco & Mele, 2001).

Different models have been suggested for the origin of the relativistic electrons radiating from *relics*. There is further evidence that *relics* can be tracers of shock-wave in merger events (Ensslin et al., 1998; Bagchi et al., 2006). These shocks, expanding with high velocity (Mach number $\sim$ 1-3), can accelerate electrons to high energies and compress magnetic fields, giving rise to synchrotron radiation being emitted from large regions. The accelerated particles will have a power-law energy distribution, as well as magnetic fields aligned parallel to the shock front. This is in agreement with their elongated structure almost perpendicular to the merger axis.

1.2.5 X-ray emission from cluster

We have noted empty volumes of space between galaxies in the optical observation of galaxy clusters, while X-ray observation reveals that this large space between a number of galaxies is filled with a diffuse, hot plasma. The extremely high concentration of matter within a cluster forms a deep gravitational ‘potential well’, which traps and heats a large amount of gas, causing most galaxy clusters to emit strongly in the X-ray wavelength of the electromagnetic spectrum. This hot gas has a typical temperature range of between $\sim$ 2 to 14 keV, the central gas density being $\sim 10^{-3}$ electron cm^{-3} and luminosity $L_x \sim 10^{43}$ to $\sim 10^{45}$ erg s^{-1} (Sarazin, 2003, 2009). The hot gas of a cluster extends up to $r \gtrsim$ Mpc from the cluster centre. The electron density is at its maximum at the cluster core, decreasing with radius r. The luminosity that we observe does not emanate from one single galaxy within a cluster, but instead from a spatially extended hot ICM. In addition, cluster X-ray emission does not vary with the time scale over which it has been detected. These make clusters very useful in the study of properties of the hot ICM.

From observation of spectral energy distribution of X-rays one can conclude that the X-ray emission process is (a) thermal bremsstrahlung (free-free radiation) and (b) line emission. Thermal bremsstrahlung is the optically thin radiation from the hot gas of a cluster. The cause of this radiation is the acceleration of electrons in the Coulomb field of protons and atomic nuclei. Accelerated electrically-charged particles emit radiation causing electron-proton scattering processes in an ionised gas to yield photon emission. The continuum emissivity due to thermal bremsstrahlung is given by

$$\epsilon_\nu^{ff} = \frac{32\pi e^6 n_e}{3m_e C^3}\left(\frac{2\pi}{3m_e k_B T}\right)^{1/2} e^{-h\nu/k_B T}\sum_i Z_i^2 n_i g_{ff}(Z_i, T, \nu), \tag{1.1}$$

where the emissivity ϵ_ν is determined as the emitted energy per unit time, frequency, and volume. n_e and n_i denote the number density of electrons and ions, respectively. Z and m_e are the charge of the ions and the electron mass, respectively. The sum (see Eq. 1.1) over the different ions in the plasma is mainly dominated by hydrogen and helium for Solar abundances. The Gaunt factor g_{ff} is a correction factor for quantum mechanical effects, as well as for the effect of distant collisions. The Gaunt factor is a slowly varying function of temperature and frequency. As a result, the dominant dependence of the free-free emissivity on frequency is the Boltzmann exponential factor, which, together with the square root factor $1/\sqrt{T}$, are the main dependants on temperature. Thermal bremsstrahlung produces a roughly exponential continuum component in the X-ray spectrum. At the high temperature of T $\gtrsim 3 \times 10^7$ K, thermal bremsstrahlung is the dominant emission mechanism. The temperature of a cluster's hot gas can be determined from the spectral properties of this radiation.

Further X-ray radiation from hot plasma at lower temperature (T $\lesssim$ 2 keV) is line emission. The discovery of line emission in the X-ray spectrum of clusters reveals that the X-ray emission originates from a hot, diffuse gas. The most important line, the Lyman-α line of 25-fold ionized iron, originates from massive clusters placed at energies just below 7 keV (Schneider, 2006). We can also see, at lower energies of 6.4 keV, that less ionised iron has a strong transition. Hence, the hotter the gas, the more highly ionised it is and the weaker the line emission.

One of the important aspects of studying X-ray galaxy clusters is to estimate its mass from X-ray observation (the total mass of hot gas is typically $M_{gas} \sim 10^{14}$-10^{15} $M_\odot$). Typically, the distribution of mass among galaxy clusters can be estimated using any of these methods: (i) weak gravitational lensing (Refregier, 2003; Massey et al., 2006; Clowe et al., 2006), which distort the background images of galaxies; (ii) strong gravitational lensing (Wu, 2000; Shapiro & Iliev, 2000), which can create multiple images of background galaxies near the cluster centre; (iii) X-ray observation, which reveals temperature and emissivity of surrounding hot gas of clusters; (iv) statistical analysis of the position and velocity of member galaxies; and (v) the Caustic technique (Diaferio, 1999; Diaferio et al., 2005) which, like weak lensing, disregards the cluster dynamical state to measure the mass using the projected positions and velocities of galaxies, both in the cluster and the infall regions surrounding the cluster. Of these, X-ray observation (iii above) is the most useful because galaxy clusters appear as well-resolved extended emissions. In the X-ray band, the gas luminosity and temperature are the direct observables used to infer total mass of the cluster. Furthermore, observations of galaxy clusters in the X-ray band provide an efficient way to identify clusters out to redshift > 1. Also, it allows accurate computation of the survey volume within which clusters are found. These are all important factors in estimating how cluster mass function varies with redshift, and what cosmological model is applicable (Vikhlinin et al., 2009b). For these reasons most cosmological studies are based on samples of X-ray selected galaxy clusters (Benson et al., 2013). Thus, the study of galaxy clusters in the X-ray band provides an opportunity to map the overall structure and evolution of the Universe, as well as an understanding of the overall history of cosmic baryons.

Galaxy clusters are good tools with which to study cosmology and test various cosmological models (Allen et al., 2011, and references therein). Galaxy clusters help to constrain cosmological parameters via measurement of their number density as a function of the mass scale and of the cosmic epoch (Rosati et al., 2002; Tozzi, 2007). Since they form the largest perturbation in the Universe, their contents could be representative of the Universe as a whole. Dynamical time scales of clusters are comparable to the age of the Universe, so it is assumed that they retain an imprint of how they were formed, thus providing strong constraints on all theories of large scale structure formation [and even modified gravity (e.g. Diaferio & Ostorero, 2009; Angus et al., 2013)]. Unlike galaxies, which are certainly open objects, large clusters probably retain all of the enriched material that was created in their pre-collapse and cluster-cluster merger. The significant link between cosmological parameters and galaxy clusters morphology has received much recent attention (Richstone et al., 1992; Evrard et al., 1993; Mohr et al., 1995). This link has generally been formulated in terms of the frequency of "substructure" in galaxy clusters. Mohr et al. (1995) have used eight various initial density fields in their N-body/3-D cluster simulation. Using the centroid shift and axial ratio technique, typically used to study dynamical state of galaxy clusters, they found morphological variations in three different cosmological models, suggesting relaxed and spherically symmetric systems evolved in low ω_0 models.

Properties of X-ray clusters

Images of X-ray clusters reveal the surface brightness or electron density distribution among them. Generally X-ray galaxy clusters are identified by the centrally-peaked surface brightness profiles in X-ray surveys. Surface brightness distribution also helps in the understanding of morphology of X-ray clusters, as depicted in Fig. 1.4. This could lead to further investigation of the cluster dynamical stage. Generally relaxed clusters are symmetric around the centre, where emission is at its peak. They have a highly flux-concentrated core. In contrast, non-relaxed clusters are asymmetric and disturbed; sometimes without a concentrated core or X-ray peak emission at the centre.

Another vital property of an X-ray cluster is its cooling flow. The central hot gas has high gas densities (as compared with the outer region of the cluster), which in the result of excessive X-ray emission and the peak of surface brightness in the core of the cluster. Because of this X-ray radiation, the gas loses energy, resulting in a drop in temperature towards the cluster centre. In this part of the cluster, the gas can cool quite rapidly, in which case its pressure decreases. This indicates that the hydrostatic equilibrium cannot be sustained for a long period of time close to the core of the cluster. In order to maintain this pressure equilibrium, the outer material needs to flow towards the cluster core. This is in result of superpositions of many gas phases, each one

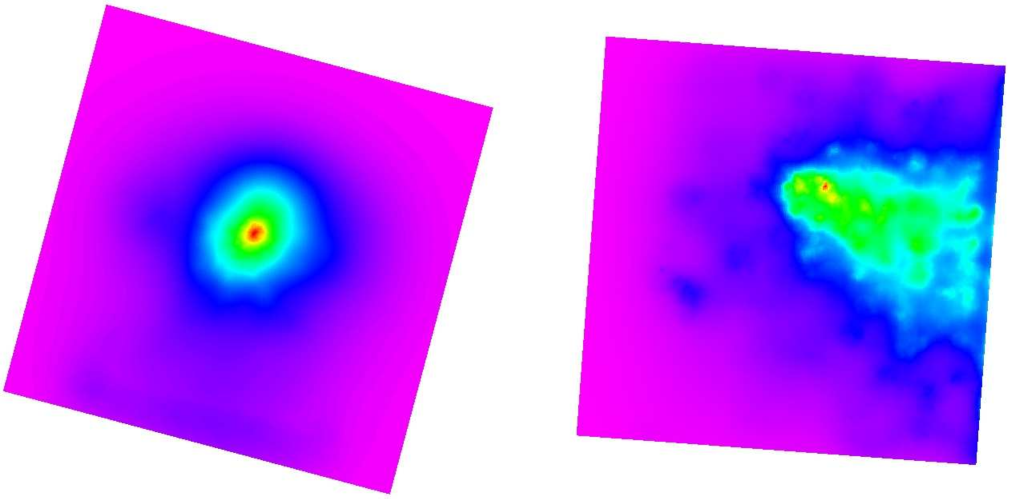

Figure 1.4: (Left) A2597; typical relaxed cluster. Morphology looks very symmetric and cluster peak emission (red) from the cluster centre. (Right) A3376; typical non-relaxed cluster. X-ray emission is completely disturbed and very asymmetric morphology.

characterised by a different temperature, in the cluster cores. This flow of gas is known typically as cooling flow (Sarazin, 1988; Fabian, 1994). Generally, this cooling flow is observed in massive and relaxed clusters around a bright (cD) galaxy. The theoretical model of cooling flow assumes the rate of flow to be of the order of $\sim 100\ M_{\odot}/\mathrm{yr}$. However, it is confirmed by spectroscopic observation of the *RGS-XMM-Newton* that these theoretical very high cooling rates have been significantly overestimated (Peterson & Fabian, 2006). This mismatch between the theoretical and observed spectrum of cooling flow leads to another theory of AGN (active galactic nuclei) feedback, which prevents the gas from cooling below a certain temperature. Many galaxy clusters host AGN in the form of radio galaxies, which emit a jet (visible in radio) in either one direction (very rare) or two (very common) from the centre of the cluster which, it is believed, affects the ICM. The high spectral resolution observations suggest that this jet may heat the surrounding ICM and disturb the cooling flow.

Different X-ray properties (such as luminosity, temperature and mass) of galaxy clusters play a vital role in establishing scaling relations among them (Arnaud & Evrard, 1999; Neumann & Arnaud, 1999; Maughan, 2007; Diaferio et al., 2008; Pratt et al., 2009; Mittal et al., 2011; Maughan et al., 2012). It is expected that the more massive clusters will be hotter, more luminous, and will have the greatest velocity dispersion of galaxies. Based on a theoretical framework, one can establish the relationships between these X-ray cluster properties. These inter-relations of cluster properties serve as an important tool in examining a structural regularity in galaxy clusters. We can measure luminosity (L_x) and temperature (T) directly from X-ray observations. Further, these inter-relations can often be approximated by simple power-laws, and can be used for rough estimates of cluster mass for a large number of objects. This study also provides very useful insight into the galaxy cluster formation, evolution and the underlying cosmological scenario. For example, X-ray luminosity is related to temperature as, $L_x \propto T^3$ for $T \gtrsim 2$ keV. With the use of the L_x-T relationship, one can probe fluctuations in cluster gas fractions and determine the ratio of the ICM gas to the total mass of the cluster. This relationship also plays an important role in examining the history of heating mechanisms in clusters. Another significant scaling relationship between cluster temperature and gas mass is $T \propto M^{2/3}$. This relationship suggests that X-ray temperature provides an accurate measurement of cluster mass. X-ray luminosity also correlates with cluster mass, $L_x \propto M^{1.8\pm0.1}$. However, the L_x-M correlation is not as tight as that between T–M, having a $\sim$ 50% scatter (Reiprich & Böhringer, 2002). This scatter arises because the determination of L_x and M are independent of each other, whereas in the mass determination the T is a readily observable parameter, resulting in a tight correlation between T–M. However, calculating L_x is relatively easier than measuring T, for which significantly longer observation (or exposure time) is required. The study of scaling relations of thermal cluster properties provides the means to differentiate the various mechanisms that provide heating to a cluster, and hence exceeding the entropy of the ICM. The importance of thermodynamic structure (entropy and pressure) of the ICM is to determine which of the processes, gravitational or non-gravitational, provide input energy in terms of heating to the ICM (Tozzi & Norman, 2001; Voit et al., 2002; Voit, 2005; Borgani et al., 2005; Boehringer & Werner, 2009).

Gravitational processes are related to shock heating, infalling gas, structure formation and the collapse of clusters, whereas non-gravitational processes are associated with supernovae, stellar winds, radiative cooling and AGN activity (Tozzi & Norman, 2001; Sarazin, 2009). An important (ICM) non-gravitational heating source is supernovae which themselves are associated with the deaths of massive stars. The supernovae could be driving galactic winds. They could also provide a more continuous source of heating. In the current epoch, galaxies in clusters have very few such massive stars. So this heating could have occurred during the epoch of star formation and galaxy formation. However, this mechanism could also require that a large amount of the supernovae explosion energy be converted into heat in the ICM, which is arguable. Another significant non-gravitational source worth considering is AGN. AGN might provide energy (in terms of heat) into the ICM via the ejection of jets of relativistic particles. However, it is difficult to determine what fraction of the energy produced by AGN goes into the surrounding ICM heating. It is only the kinetic energy ejected by AGN in jets or in relativistic particles which is likely to be useful. It may be useful that the early-type galaxies found in clusters generally host radio galaxies and radio quasars, which are more likely to deposit energy into the ICM. If the heating source is purely gravitational during formation of a cluster, then the excess in entropy is proportional to the cluster temperature, but if the heating originates from non-gravitational processes, then entropy is proportional to the total stellar mass in the cluster.

The current observational scenario reveals that X-ray data are not in agreement with scaling relations which are based on pure gravitational thermal heating (Sarazin, 1988; Ricker & Sarazin, 2001; Ponman et al., 2003). Kaiser (1986) suggested that the excess in entropy is linked only with the gravitational processes, such as adiabatic compression, during the collapse and shocks because of supersonic accretion of the surrounding gas (which is known as the *self-similar* model). Recent observations show, however, that non-gravitational processes are also very important in determining the distribution of entropy in the ICM (Tozzi & Norman, 2001; Voit, 2005). The deviations of the scaling relations are particularly noticeable for groups and cooler clusters. Entropy profiles of groups and clusters exhibit deviations from a self-similar model, with profiles tending to flatten in the core regions, suggesting the lack of the expected low-entropy gas in central regions of the cluster (Voit et al., 2005; Finoguenov et al., 2005a; Pratt et al., 2010). This implies a number of indications that non-gravitational heating processes could affect the heating of ICM. Also, in clusters, the gas is distributed in more widely, which is not in agreement with what would be expected from gravitational heating alone. This advocates that some non-gravitational heating mechanisms have triggered and amplified the gas distribution extensively. This would reduce the mean density of the gas and X-ray luminosity, mainly in poorer clusters, i.e. for those objects whose virial temperature is comparable with the extra heating temperature.

1.2.6 Evolution of galaxy clusters

The evolution of galaxy clusters is a very complex and multicomponent merger system in the Universe. It is now well proven that massive galaxy clusters form and evolve at the intersection of the cosmic web filaments through merging and accretion of smaller mass systems (e.g. Maurogordato et al., 2011, and references therein). Clusters evolve as a result of these mergers, and this is considered to be a highly energetic process. Huge gravitational energy is released during cluster collisions ($\approx 10^{64}$ ergs), and several billion years are required for the cluster to re-establish a situation of (quasi-)equilibrium after a major merger episode. Galaxy clusters have a long evolutionary history, from their origins to the present epoch. Multiple merger episodes are considered to be the most common physical process for disturbing both its cool core and relaxed nature. Hence, we believe that clusters are expanded by subcluster merger. Even in the present epoch, clusters are growing by matter accretion at the junction of large scale filaments of galaxies. It is therefore important to the study of clustering evolution to test cosmological models and physical processes which govern the formation of galaxies (Diaferio, 2000).

Substructure studies are very important in order to understand cluster mass estimates and other physical properties, such as temperature. Substructure is the presence of two or more clumps of galaxies and/or gas within a cluster. Both observations as well as numerical simulations have shown that merging events deeply affect the properties of the different cluster components (e.g. Ferrari et al., 2008, and references therein). Multiple merger episodes could, for instance, be responsible for disturbing the dynamically relaxed cores of the X-ray emitting hot ICM (Burns et al., 2008), as well as the ICM density, temperature and metallicity distribution (Kapferer et al., 2006). In addition, it is well known that a disturbed X-ray morphology is typical of dynamically perturbed galaxy clusters (Kapferer et al., 2006, and references therein). The merging activity of clusters also distorts the X-ray surface brightness profile that we observe in many cluster images.

Joint X-ray and optical studies can provide detailed information about the dynamical state of a cluster (e.g. Ferrari et al., 2006), but they are extremely time demanding from the observational and analysis point of view. For statistical studies of large cluster samples we need to identify robust indicators that can somehow quantify the dynamical state of a cluster. Since the morphology of clusters is deeply related to their evolutionary history, different morphological estimators have been proposed. Thanks to the *Einstein* X-ray telescope, which has allowed us to study accurately the distribution of the X-ray emitting plasma in a cluster, we have learned about different morphology, shape and structure of the X-ray cluster from small to extended scale (Forman & Jones, 1982; Jones & Forman, 1992, 1999). Generally the morphology and shape of galaxy clusters range from (1) a regular and smooth single component, (2) double components of equal size and luminosity, (3) double components with unequal size and luminosity (primary with small secondary), (4) non-relaxed and complex clusters deviated from their symmetry, (5) elliptical shape cluster, (6) cluster with offset centre, and (7) single galaxy-dominated clusters (Jones & Forman, 1992). The importance of this classification concerns the examination of degree or level of substructure among given X-ray cluster observations (Jones & Forman, 1999).

Jones & Forman (1991) showed that around 30% of clusters observed with the *Einstein* satellite contain substructure. More recently, Schuecker (2005) noticed in *ROSAT* observations that $\sim$ 50% of clusters have substructure. With higher resolution telescopes such as the *Chandra* and *XMM-Newton*, it has become easier to identify subclusters, bimodality and X-ray centroid shifts in clusters. However, some mergers are too complex to be identified from only X-ray morphological analysis and, particularly in the case of high redshift clusters, some special techniques and statistics are required, which can provide a more quantitative and robust measure of the degree of the cluster disturbance.

1.2.7 Chandra X-ray telescope

The high sensitivity and exquisite angular resolution in the *Chandra* images have lead to quantitative changes in our understanding of various X-ray objects, for example, how galaxy clusters grow and evolve. The *Chandra* telescope has discovered a lot of new astrophysical phenomena and sources. So it is also important to understand this telescope itself and become familiar with its instruments. In this section, we give a brief introduction of various instruments of the *Chandra* telescope. The *Chandra* X-ray Observatory has four science instruments in addition to the nested mirror assembly. It works similarly to other telescopes, in that the incoming X-ray photons are focused by the mirrors on the focal plane science instruments - ACIS (Advanced CCD Imaging Spectrometer) and HRC (High Resolution Camera). These instruments capture the sharp images formed by the mirrors and record the information (energy, position, time of arrival, etc.) about incoming photons which are called X-ray “events”. In addition to these instruments, there are two further science instruments which provide more information about the X-ray energy, the LETG (Low Energy Transmission Grating) and HETG (High Energy Transmission Grating) spectrometers. These grating arrays or spectrometers are located between the mirrors and imaging instruments (ACIS and HRC) and can be used on requirement. Since our study is confined to ACIS imaging alone, the following is a short introduction to ACIS instruments.

ACIS Instrument

Pennsylvania State University and MIT built the ACIS with charge-couple devices (CCDs) fabricated by MIT’s Lincoln Laboratory. The schematic diagram of ACIS detectors is shown in Fig. 1.5. This CCD imaging detector in the *Chandra* telescope contains two arrays: a square for imaging (ACIS-I) and a narrower strip (ACIS-S) which allows simultaneous acquisition of high-resolution images and moderate resolution of spectra. We can also obtain higher resolution spectra by combining the ACIS with transmission gratings. Both of these have total ten planar, and each CCD has 1024 × 1024 pixels. ACIS-I comprises a 2 × 2 array of CCDs, and provides high-resolution spectrometric imaging. It has a 17-arcmin-square field of view (FOV). ACIS-S is a 6 × 1 array mounted in the direction of the grating dispersion, and is the primary read-out detector for the HETG. ACIS-S has an 8.3 by 50.6-arcmin of field of view. In both the detectors, pixel size is

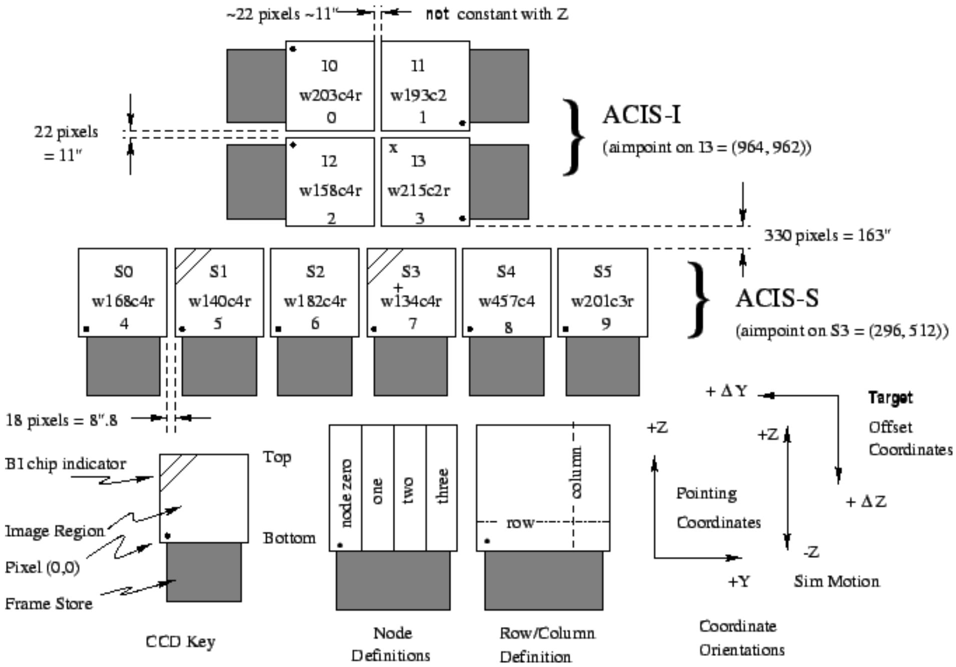

Figure 1.5: Layout of the ACIS *Chandra* detector. There are two aim-points denoted with '+' and 'x' on the ACIS-S3 and ACIS-I3 chips, respectively. We see that there are four CCDs (I0-I4) for the ACIS-I and six CCDs (S0-S5) for the ACIS-S detector. Various orientation positions of S and I detectors as well as coordinates system are shown in the bottom right.

23.985 microns, which corresponds to 0.4920 arcsec ($\sim 0.5''$). The ACIS uses two types of CCDs, eight front-illuminated (FI) and two back-illuminated (BI). At lower energies, the BI CCDs have higher efficiency than the FI CCDs. One BI CCD was placed at the on-axis focal position of the 6 × 1 array which provides high-resolution spectrometric imaging extending to lower energies, but with a smaller FOV than the 2 × 2 array. The other BI device is also in the 6 × 1 array. These detectors are operated at -90 to -120°C. ACIS has an operating energy range of 0-10 keV.

1.2.8 Distant X-ray clusters

High redshift or distant clusters are of interest because they contain younger galaxies than those in current epoch clusters and, as a class, they may be dynamically less evolved than nearby clusters. In the past, observations of distant clusters have been used in attempting to determine cosmological parameters such as H_0 and q_0. X-ray observations alone are able to measure accurately the distant cluster redshift, which is a complicated process to achieve with a large optical telescope. However, it is challenging to observe high redshift clusters using X-ray observation because of fewer photon counts and low S/N. Deep observations via *Chandra* and *XMM-Newton* telescopes allow investigation of the ICM of clusters at redshifts as high as $z \sim 1.3$ (corresponding to look-back time of $\sim$ 9 Gyr) (Rosati et al., 2002; Rosati, 2004; Tozzi, 2007). At this large look-back time, distribution of surface brightness of these systems is similar to that of low-redshift clusters. Furthermore, the spatial distribution of hot X-ray gas at high redshift is well correlated with the member galaxy distribution, which is also found in a low redshift cluster. In low redshift cluster observations, *Chandra* has revealed a complex thermodynamical structure of the ICM at the kpc scale. *Chandra* is capable of resolving high redshift cluster cores, and mapping cluster morphologies at scales below 100 kpc. These high redshift cluster observations suggest that there are already, at $z < 1$, galaxy clusters in an advanced dynamical stage of formation, in which all the baryons have had enough time to thermalise in the cluster potential well. In this high redshift cluster observation, astronomers have commenced by measuring temperatures (and mass) of major subclumps at redshift > 0.6, which is important in the understanding of scaling relations (e.g. $L_x - T$) in high redshift clusters.

A number of high redshift cluster observations have been carried out in order to understand cluster physics and morphology (Blanchard et al., 2005; Burenin et al., 2007; Muchovej et al., 2007). In a hierarchical cold dark matter formation scenario, one would expect the most massive clusters at high redshift to be accreting subclumps of comparable masses, and the level of substructure to increase at high redshifts. Another important aspect in this study is the distribution of heavy elements in the ICM. This could provide essential information as to how the ICM interacts with cluster galaxies. Accurate measurements of the heavy elements content of clusters over extensive look-back times provide a useful fossil record for the star formation history of cluster baryons. For example, the abundance of iron can be traced back to the highest redshifts where X-ray clusters are observed.

1.3 Motivation and methodology

Substructures, or a very complex cluster X-ray morphology, or X-ray centroid variations, are typical features that allow us to understand whether or not a cluster is virialized. This has important implications both in using clusters as tools for cosmology, and in studying the complex gravitational and non-gravitational processes acting during large-scale structure formation and evolution, since in both cases we need to know if observed clusters are relaxed or not. Hence it is of prime importance to characterise, systematically, structural properties of galaxy clusters when there are larger cluster samples available for statistical studies.

In this research, we investigate the seven morphology parameters, typically used for galaxy classification, to study X-ray galaxy cluster morphology, and we motivate which parameters are optimal in identifying substructure or in characterising dynamical states. The combination of morphology parameters has been used successfully to classify different galaxy morphologies (Zamojski et al. 2007; Scarlata et al. 2007; Holwerda et al. 2011a,b,c,d,e, 2012; Holwerda et al., submitted), and we propose to investigate their usefulness in galaxy cluster classification. We plotted the data in parameter-parameter planes and studied the position of each cluster in these plots. We found that the combination of some morphological parameters increases the potential to more completely characterise the cluster shape and dynamical state. Some of the parameters such as the Gini, Gini of the second order moment, and M_{20}, have never been explored to identify the dynamical state of X-ray clusters. Our focus is not limited to the separation of galaxy clusters into relaxed and non-relaxed categories, but to the study of correlations between X-ray gas properties and morphology parameters, as well as the evolution of morphological properties of galaxy clusters from the high redshift Universe to the present.

Various techniques have been suggested to provide a more quantitative and qualitative measure of the degree of the cluster disturbance. Power ratios (Buote & Tsai, 1995b; Jeltema et al., 2005; Böhringer et al., 2010) and the emission centroid shift (Mohr et al., 1993; Böhringer et al., 2010) are most commonly used to classify X-ray galaxy clusters from the morphological point of view. Recently, Andrade-Santos et al. (2012) have used a *residual flux method*. In order to calculate the substructure level in a given X-ray galaxy cluster, they take into account the ratio between number of counts on the residual (which they obtain by the subtraction of a surface brightness model from the original X-ray image) and the original cluster images. Weißmann et al. (2012) proposed using the maximum of the third order power ratios calculated in annuli of fixed thickness and constantly increasing radius to measure the degree of substructure. Rasia et al. (2012) used six different morphology parameters, namely: asymmetry, fluctuation of the X-ray brightness (smoothness), hardness ratios, concentration, centroid-shift method and third order power ratio, in order to characterise simulated clusters. They took hydrodynamical simulation of 60 clusters passed through with the added *Chandra* telescope simulator with uniform exposure time (100 ks) for all clusters. From of all of these parameters they found that only asymmetry and concentration parameters could directly and clearly separate relaxed and non-relaxed systems. The smoothness parameter is affected by choice of radii and smoothing kernel size. The centroid-shift parameter also works reasonably well, leaving only a few overlapping relaxed and non-relaxed clusters. The third order power ratio technique also depends on the choice of radius, and is limited to the detection of substructure near to the cluster centre.

Initially, we tested seven morphology parameters to distinguish between simple 2-D Beta model simulated relaxed and non-relaxed galaxy clusters. We also investigated the effects of noise and redshift on simulations. Then we passed these simulated clusters through the MARX software to mimic the *Chandra* telescope observations. From this initial simulation work, the morphology parameters proved to be a promising tool in separating relaxed and non-relaxed clusters. This encouraged us to extend the work to real data.

We explored the usefulness of the non-parametric morphology parameters on a subset of the $ROSAT$ 400 deg^2 cluster sample observed by the *Chandra* X-ray telescope (Vikhlinin et al. 2009a, hereafter V09). We choose this sample because it has good quality X-ray data and also a broad distribution of redshifts. There are a total of 85 (49 low-z (0.02-0.3) and 36 high-z (0.3-0.8)) galaxy clusters in our analysis. In addition, V09 has measured global properties of galaxy clusters (such as luminosity, temperature, mass, etc.) which we use for comparison with our measured morphology parameters.

As a test case, in this research we study the dynamical activity of clusters hosting diffuse radio sources. In particular, we focus our attention on clusters taken from Giovannini et al. (2009). Current results suggest a strong link between the presence of diffuse intra-cluster radio emission and cluster mergers (Ferrari et al., 2008; Feretti et al., 2012, and references therein). In line with what is done by Cassano et al. (2010b), but using our new X-ray morphological parameters, in this research we analyse the X-ray morphology of relaxed clusters and non-relaxed clusters (which includes both radio-quiet mergers and radio-loud mergers).

1.4 X-ray method of generation of thermodynamic maps

1.4.1 Current observations and data analysis techniques

Recently *Chandra* and *XMM-Newton* X-ray telescopes have given excellent opportunities to study the striking phenomena within galaxy clusters which were previously undetected (Forman et al., 2002). Many provocative features and physical processes of galaxy clusters have comes to light in the past few years. These have completely modified our perception of galaxy clusters, generating thought-provoking challenges in the analysis of all these cluster data. One of the overall astrophysical data analysis problems is the development of a model of a source which has the capability to deliver all of the complex characteristics of that source, including a spectrum that changes spatially in the sky. This problem is intensely felt in the case of X-ray observation of galaxy clusters, where we record the energy and position of individual incoming photons. At the same time, we intend to observe the 3-D structure of galaxy clusters projected on the sky, although limited spatial resolution of X-ray telescope mirrors makes this more challenging.

Much of the current work in X-ray analysis of galaxy clusters involves obtaining a complete description of the electron density and temperature structure of the hot ICM. In most cases one assumes spherical symmetry, and thus any quantity such as gas temperature or electron density is assumed to be a function of radius only. However, recent observation of X-ray clusters shows the irregular and very asymmetric nature of galaxy clusters, which display complex and unsmooth electron density and multiple temperature distribution. Clearly this distribution is more complex for clusters that are merging or forming, where one observes a lack of circular symmetry in the surface brightness. Clearly, then, we need to find a suitable technique which incorporates a complex ICM model, and which answers all these queries about the nature and behaviour of galaxy clusters. Before that, however, we need an understanding of various physical processes occurring over the lifetime of clusters. The following is a brief description of some of these processes.

One remarkable observation of the *Chandra* telescope reveals the very sharp surface brightness discontinuities in the A2142 galaxy cluster (Markevitch et al., 2000). Initially, it was considered that these were merger shocks. But careful analysis of this cluster did not reveal the variation in temperature, pressure and entropy distribution, ruling out the presence of merger shock in this cluster. Later on, Vikhlinin & Markevitch (2002) observed a cold cloud moving rapidly through the hotter gas, showing the contact discontinuities between a cold dense gas and a hot diffuse gas. This new kind of structure has subsequently been referred to as a "cold front". These cold fronts would seem to be contact discontinuities between the gas in the cool core of clusters and the surrounding intra-cluster gas. Vikhlinin & Markevitch (2002) observed similar phenomena in the A3667. These cold fronts and merger shocks offer unique insights into cluster physics; and provide the only means of measuring gas bulk velocities in the plane of the sky (Markevitch & Vikhlinin, 2007), acceleration of ICM, the growth of plasma instabilities, the strength and structure of magnetic fields, and the thermal conductivity.

Chandra observations uncover complex structures in cluster cores often in the form of X-ray cavities associated with radio lobes. One of the most famous examples of the effect of plasma bubbles on the hot ICM is in the Perseus cluster around the active central galaxy NGC1275. Based on the *ROSAT* observations, Boehringer et al. (1993) discovered clear evidence of the interaction between the X-ray emitting hot ICM and the relativistic particles in the radio lobes. Subsequent *Chandra* observations showed that the X-ray cavities that coincide with radio lobes have cool bright rims (Fabian et al., 2001). Furthermore, in addition to these inner bubbles, the Perseus cluster has outer "holes" in its surface brightness distribution. Radio observations of this cluster reveal that these outer holes, as well as the X-ray cavities seen in a few other groups and clusters, have no correlation with radio lobes. The fact that these "ghost cavities" exist suggests the possibility that they had been inflated during an earlier nuclear outburst, and that synchrotron losses had, as a result, depleted the high energy radio emitting electrons. Sanders et al. (2004) detected the low temperature swirl around the core in the temperature structure of the Perseus cluster. This might indicate that there is no bulk motion of the gas in the core of the Perseus cluster. Another example is the A2597 (McNamara et al., 2001; Clarke et al., 2005b) which showed the emergence of 'radio bubbles', displacing the hot cluster gas via radio emitting plasma. These nuclear outbursts have a major impact on the X-ray morphology of cluster cores. Fabian et al. (2003) have noted ripples or waves in cluster gas. In addition to these exciting X-ray objects, X-ray observation also gives significant information about temperature, metal distribution, electron density, and cluster dynamics, and is useful in terms of measuring the mass of galaxy clusters via hydrodynamic equations.

In the research of X-ray astronomy, a large variety of techniques is available for dealing with data analysis of galaxy clusters, producing quality results. Extracting various properties of the hot ICM in a cluster is a complicated process because the ICM is optically thin. While the structure of a cluster is seen as a 3-D projection on the sky, it collapses in a 2-D projection. Therefore, for the purpose of re-constructing the 3-D profile, it is necessary to hypothesise on the distribution of the X-ray emitting gas that resides in a cluster of spherical symmetry. The most conventional way is to extract the spectrum from the X-ray data obtained in the observation of a cluster, and fit it with a suitable plasma model, e.g. MEKAL or APEC. The ratio of various lines in spectra will give information about temperature and electron densities. From this temperature and electron density one can calculate entropy as well as pressure of the gas.

There are different methods of extracting the spectrum from a (counts) image of a galaxy cluster. The widely accepted option is the de-projection technique which was first introduced by Fabian et al. (1981). This technique is used to facilitate the 2-D annular X-ray spectra to recover 3-D source properties. The basic physical assumption of de-projection is that the extended source emissivity is constant (and optically thin) within spherical shells whose radii correspond to the annuli used to extract the source spectra (one should extract spectra in a series of annuli). Given this assumption, one can construct a model for each annular spectrum that is a linear volume-weighted combination of shell models. For typical thermal models, this would include the radial temperature and density profiles.

Another method of extracting the spectrum from a (counts) image was given by Ettori et al. (2002). They accumulated the spectrum of the cluster from concentric annuli centred on either the peak of surface brightness or centroid of the flux distribution, and analysed them to derive X-ray cluster quantities, e.g. temperature, density, etc., which are projected in each annulus. This is called an "onion peeling" process in which the outer rings subtend spatial regions progressively less affected by projection effects; and an inward recursive subtraction of their contribution to the inner rings yields the actual de-projected 3-D profiles. All of these methods are useful in studying the radial profiles of X-ray properties. For instance, how the temperature and electron density vary radially from the cluster core.

In recent years, a number of techniques have been developed to construct a temperature map or an electron density map of a cluster, in order to study the individual or interested regions in terms of thermal evolution and history. Sanders & Fabian (2001) have developed a technique called "adaptive binning", in which pixels of the image are adaptively binned depending on the number of photons in each region, and the spectrum from each individual bin or region is extracted and fitted with a plasma model. The fundamental idea behind the process of adaptive binning is to bin 2-D image pixels by a factor of two, until the fractional Poisson error of the count in each bin becomes less than or equal to a threshold value.

Adaptive binning of a 2-D image is known as a 'quad-tree' algorithm. The algorithm looks at the entire cluster image and computes S/N. If the S/N is greater than the input threshold, the image is divided equally in both the horizontal and vertical directions. For each sub-image, the process is repeated until either the S/N drops below the user-supplied value or a single pixel remains above the S/N limit. The output pixels are then a sum of the pixels in the sub-image divided by the area of the sub-image. This algorithm is applicable to a wide range of data obtained from observations or numerical simulations. However, this technique is limited to a restricted set of bin sizes. This restriction does not allow the technique to be fully adaptive and, because of constant S/N throughout the binning process, it causes poor resolution in the final binned image.

The adaptive binning technique has been improved by the "weighted Voronoi tessellations" technique (Diehl & Statler, 2006). This technique is applicable to many types of data, and creates geometrically unbiased binning structures (quasi-circle-like in shape) that are not obvious to the eye. It can be applied to simulated data or X-ray data to create adaptively binned intensity images, hardness ratio (given by the hard-band flux divided by the soft-band flux) maps, and temperature maps. Markevitch et al. (2000); Markevitch & Vikhlinin (2001); Govoni et al. (2004) have used the *Chandra* data to derive 2-D temperature maps of galaxy clusters. For each cluster, they simply convert an X-ray hardness ratio to temperature. The *Chandra* angular resolution is adequate enough to ignore any energy-dependent PSF effects. To derive a temperature map in this way, it is necessary to extract first a count image in various energy bands (soft and hard), smooth them, and, for each $2'' \times 2''$ pixel, fit a spectrum consisting of the flux values in each energy band, properly weighted by their statistical errors. Another similar technique, the wavelet-smoothed hardness ratio method, was developed by Henry et al. (2004); Finoguenov et al. (2005b); Sanderson et al. (2005) to create a temperature map and derive thermodynamic maps from it. It is also possible to observe statistically significant features in soft and hard surface brightness maps using a suitable smoothing. Combining this two smoothed intensity maps produces a hardness ratio map that could be translated as a projected temperature map.

The hardness ratio depends strongly on the ICM temperature and the line-of-sight-absorbing column density. It weakly depends on the metallicity of the ICM. If we assume that the variation of absorbing column density is small, then we can use the hardness ratio to estimate the cluster temperature directly. Before creating hardness ratio images, it is necessary to apply smoothing to remove the (Poisson) fluctuations and zero values of any image pixels. The smoothing process is accomplished by Wavelet decomposition (Vikhlinin et al., 1998), which is perfect for highlighting low surface brightness diffuse emission, even in the existence of bright point sources in the image. In this Wavelet smoothing, it is possible to identify the regions susceptible to temperature variation. Since the Wavelets do not smear the data, it is possible to achieve high spatial resolution while detecting the structure. If this temperature map is multiplied by the appropriate power of one of the intensity maps (which acts as an electron density map) then one can make pseudo entropy and pseudo pressure maps.

1.4.2 The XMC technique

In this research, we have investigated a novel approach, as an alternative to standard analysis techniques, known as the XMC (X-ray Monte Carlo) technique (Peterson et al. 2007; Andersson et al. 2007, 2009, hereafter KA09), to analyse the X-ray emitting ICM in galaxy clusters. There are two main advantages of the XMC compared with aforementioned techniques:

- In all previous techniques a common approach is to extract a spectrum from (various) portions of a detector plane where a source is lying, and approximate the presence of energy-dependent broad point spread functions of detectors. However, in fact this conventional extracted spectrum simply represents the accumulated number of photons as a proxy for the true source image and, at a given energy source emissivity, is spatially changing. The XMC, however, uses the spectrum and image of a cluster on an equal footing, and predicts detector positions and CCD energies simultaneously for each photon.
- Since the ICM has a multiple temperature distribution, there is a broad requirement to fit a complex model to the plasma. Fortunately, the XMC can use a model that is flexible enough to allow extremely complex gas temperature and density distributions in clusters, which is in contrast with previous methods which assume only a single temperature for a given set of photons and fit its values.

The XMC is well suited for detecting the effects of cooling cores and substructure from both the projected luminosity and temperature distributions of clusters. This innovative and promising method models the ICM in galaxy clusters as a set of X-ray emitting smoothed particles of plasma. Compared with traditional analysis, this approach reproduces many of the features observed in X-ray emission in a less assumption-dependent way, and allows for a much more detailed characterisation of the density, temperature and metal abundance structure of clusters.

For the purpose of comparison of the XMC-generated map with previous techniques, we show different maps in Fig. 1.6. It is seen that the XMC-generated temperature map looks much smoother; and the structure of the cluster is clearly visible as a multi-temperature ICM distribution in the colour map. However, the new method requires extreme computing power.

Our aim is to perform quantitative studies of substructure identification using an X-ray 2-D map of temperature, electron density, pseudo-entropy and pseudo-pressure. Since the era of the *ROSAT* telescope, it has been common practice to access the surface brightness map of galaxy clusters to investigate substructure. Recently, Jee & Tyson (2009); Andersson et al. (2009) noticed that the substructures are more sensitive to temperature distribution than to surface brightness. Govoni et al. (2004) used the temperature maps of nine galaxy clusters to study the geometry, stage and velocity of merger. Zhang et al. (2009) used 2-D thermodynamic maps of four clusters to study systematically the effect of substructure in the measurement of hydrostatic mass of galaxy clusters.

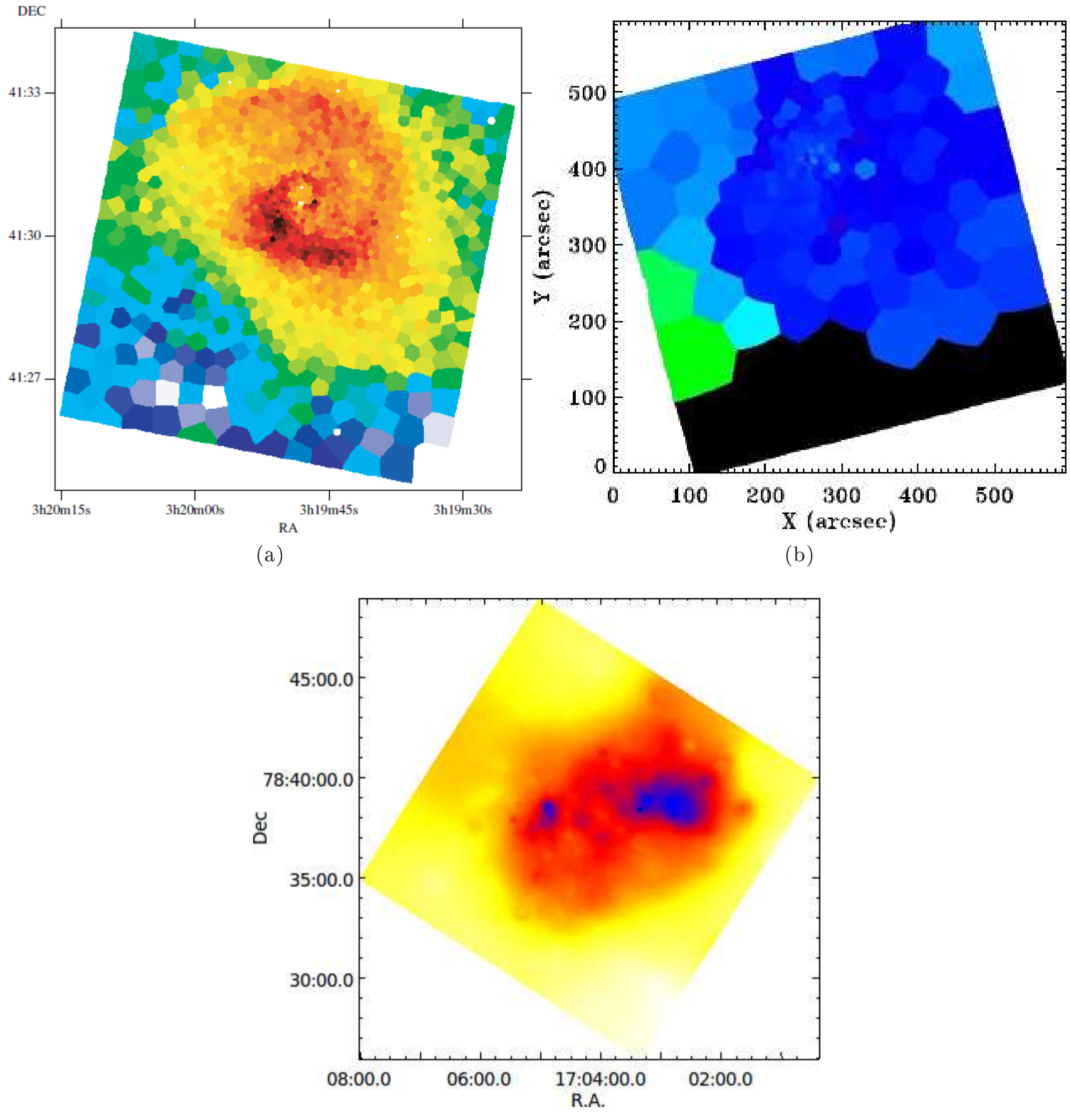

(a) (b)

(c)

Figure 1.6: Temperature maps generated by two techniques compared with that generated by the XMC: (a) generated by the adaptive binning technique, (b) generated with the Voronoi Tesla method; and (c) generated with the XMC technique. The XMC map appears much smoother, and the structure of the cluster is clearly visible.

Gu et al. (2009) used nine intermediate-redshift clusters to study the temperature substructure in the central region on $\sim 100\ h_{70}^{-1}$ kpc scales. It is believed that the distribution of temperature provides crucial information about the estimation of X-ray mass. Complex temperature distributions and substructure can both be used to pinpoint and describe the history of the merging process, and the fraction of substructure can be used to connect the cluster mass systematics with the history of mass assembly (Smith & Taylor, 2008).

We are at an advantage because we can access the superb spatial resolution of the *Chandra* and *XMM-Newton* telescopes in order to make 2-D maps to study the substructure in temperature and electron density distribution. The temperature distribution in the hot ICM is also important in the study of thermal structure and thermal history which are easily expressed by the "entropy" structure of the ICM. Entropy is the conserved parameter during any evolution of the ICM in which all processes are adiabatic. The entropy of the gas is a powerful probe of cluster physics and provides great insight into the state of the gas. The entropy S is defined as (Voit, 2005),

$$S = \frac{k_B T}{\mu m_p \rho^{0.66}}, \tag{1.2}$$

where k_B is the Boltzmann constant, T is the gas temperature, μ is the mean mass per particle in terms of the proton mass m_p, and ρ is the gas density. S is directly related to the general thermodynamic entropy per particle, s $= k_B\ ln\ S^{1.5} + s_0$, where s_0 is a constant that depends on the mixture of particle masses. In cluster literature, "entropy" is widely defined as K $= \frac{k_B T}{n_e^{0.33}}$ and Pressure as P $= k_B T \times n_e^{0.5}$, from which we can generate pseudo entropy and pseudo pressure maps, respectively. We used all these thermodynamic maps (electron density, temperature, entropy and pressure) and investigated its radial profiles and morphology using morphology parameters. We plotted each thermodynamic quantity as a function of R_{500} and evaluated the fluctuation and discontinuity in these radial profiles to be caused by substructure.

This thesis is structured as follows. Chapter 2 gives a brief introduction to the morphology parameters and tests the parameters on 2-D Beta model simulated clusters. Chapter 3 gives the parameter calculations on the *Chandra*-observed clusters and compares parameters with X-ray cluster properties. In Chapter 4, we present our XMC work and thermodynamics maps to study substructure using radial profiles. Chapter 5 shows the possible application of morphology parameters to study *radio halo* clusters; and finally, Chapter 6 gives the summary, as well as an outline for possible future work. We assume $H_0 = 73$ km $s^{-1} Mpc^{-1}$, $\Omega_M = 0.3$, and $\Omega_\Lambda = 0.7$ throughout the thesis unless otherwise stated.

2

Cluster morphology parametrisation

2.1 Background

In this Chapter, we give a brief introduction to morphology parameters, as well as calculations of these parameters on X-ray simulated clusters. We gave our motivation for doing this study in the previous Chapter. At the first place we want to simulate various categories of simple clusters and identify relaxed and non-relaxed clusters by means of morphology parameters. In this primary step, we use a 2-D Beta model to check the capability of a set of morphology parameters to separate the variety of X-ray cluster morphologies. We also test various systematics and instrumental effects which might affect the parameter calculation.

2.2 Introduction of morphology parameters

The non-parametric morphology parameters (Gini, M_{20}, Concentration, Asymmetry, Smoothness, Ellipticity and Gini of the second order moment) are widely used to automatically separate galaxies of different Hubble types. As an example, they are used for galaxy morphology classification in the analysis of the HST and SDSS galaxy surveys in an attempt to elucidate galaxy formation histories (Abraham et al., 2003; Conselice, 2003; Lotz et al., 2004; Zamojski et al., 2007; Holwerda et al., 2011a,b,c,d,e, 2012; Wang et al., 2012).

Abraham et al. (2003), Lotz et al. (2004) and Wang et al. (2012) also revealed the inter-relation between Gini, Concentration and M_{20}, as well as the possible inter-change between the Concentration and Gini parameter (which does not require precise knowledge of the cluster centre) for high-z galaxies. This encouraged us to investigate these parameters in more detail in order to study the dynamical activity of galaxy clusters, particularly high-z galaxy clusters. Another reason for our using this particular parameter set is that they have never before been used quantitatively in this way (combining all morphology parameters) to classify the dynamical state of X-ray galaxy clusters. Most of the other parameters are already extensively used in the literature (Mohr et al., 1995; Buote & Tsai, 1995a, 1996; Jeltema et al., 2005; Hashimoto et al., 2007; Maughan et al., 2008; Andersson et al., 2009; Böhringer et al., 2010; Weißmann et al., 2012; Rasia et al., 2012). We decided to include only morphology parameters (Gini, M_{20}, Concentration, Asymmetry, Smoothness, Ellipticity and Gini of the second order moment) in our study.

In this chapter, we compute these parameters for the Beta model simulated X-ray galaxy clusters. We adopt the definition of Concentration, Asymmetry and Smoothness from Conselice (2003), and of the Gini coefficient and M_{20} from Lotz et al. (2004). Gini of the second order moment was defined by Holwerda et al. (2011b). In this calculation, the required input parameters are the central position (x_c, y_c) of the galaxy clusters, as well as a fixed aperture size or area over which these morphology parameters are measured.

2.2.1 Gini coefficient and Gini of the second order moment (G_M)

The Gini parameter is widely used in the field of economics, where it originated as the Lorenz curve (Lorenz, 1905). It describes the inequality of wealth in a population. The Lorenz curve is plotted by the cumulative proportion of income as a function of population rank. As shown in Fig. 2.1, if 20% of the population has 20% of a country's total capital or in other word, if all individuals in a population, have exactly the same income, then the Lorenz curve is a straight diagonal line and it has unity slope. This line is known as the line of equality. Oppositely, if the Lorenz curve falls below the line of equality implies inequality in distribution of income among population. In the utmost case where all capital belongs to minuscule proportion of the population, the Lorenz curve is flat and near zero for most of its length until rising precipitously near its end.

The Gini coefficient (G) or Lorenz curve can be useful to parametrized the total amount of inequality in given distribution (of either income or flux). We illustrated the geometric meaning of G in Fig. 2.1. As we see, the Gini coefficient is simply the ratio between area A (the area enclosed between the line of equality and the Lorenz curve) and the total triangular area under the line of equality (A + B). The Gini coefficient spans from a minimum value of zero, when all individuals are equal, to a maximum of one in a population where all the capital is concentrated in a single individual.

Here we use Gini coefficient as a calculation of flux distribution in a cluster image. If the total flux is equally distributed among the pixels, then the Gini value is equal to zero (there is constant flux across the pixels regardless of whether those pixels are in the projected centre or not); but if the total flux is unevenly distributed and belongs to only a small number of pixels, then the Gini value is equal to one. We adopt the following definition from Lotz et al. (2004):

$$G = \frac{1}{\bar{K}n(n-1)} \sum_i (2i - n - 1)K_i, \tag{2.1}$$

where K_i is the pixel value in the i^{th} pixel of a given image, n is the total number of pixels in the image, and $\bar{K}$ is the mean pixel value of the image.

We also apply a Gini value to the second order moment of each pixel, defining Gini of the second order moment as:

$$G_M = \frac{1}{\bar{F}n(n-1)} \sum_i (2i - n - 1)F_i, \tag{2.2}$$

where F_i is the second order moment of each pixel:

$$F_i = K_i \times [(x - x_c)^2 + (y - y_c)^2], \tag{2.3}$$

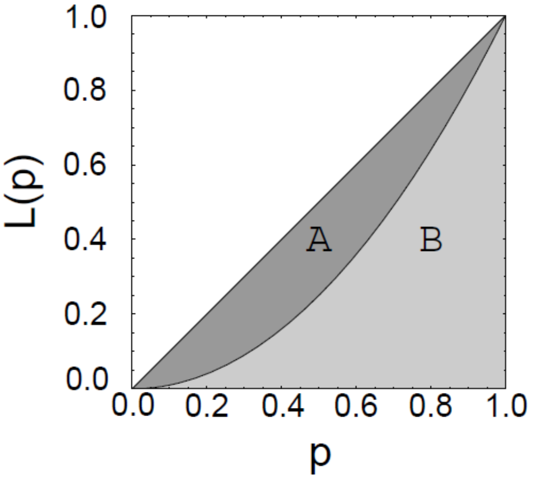

Figure 2.1: Geometric representation of the Gini parameter based on the Lorenz curve. In this plot, x-axis shows the quantile of the distribution, and y-axis shows the cumulative proportion. The Lorenz curve for a absolutely equal distribution corresponds to the diagonal line of equality. A schematic Lorenz curve, in the figure, divides the area beneath the line of equality into two areas, A and B. The greater the deviation of a measured Lorenz curve from the line of equality, the greater the inequality. The Gini coefficient corresponds to the ratio of area A to the total area under the diagonal A+B.

where $(x,\ y)$ is the pixel position with flux value K_i in the cluster image; and $(x_c,\ y_c)$ is the coordinate of the cluster centre.

2.2.2 Moment of light, M_{20}

Lotz et al. (2004) define the total second order moment F_{tot} as the flux in each pixel K_i multiplied by the squared distance to the centre of the source, summed over all the selected pixels:

$$F_{tot} = \sum_i F_i = \sum_i K_i[(x_i - x_c)^2 + (y_i - y_c)^2], \tag{2.4}$$

where $(x_c,\ y_c)$ is the centre of the cluster.

The second order moment can be used to trace various properties of galaxy clusters, such as the spatial distribution of multiple bright cores, sub-structure or mergers. M_{20} is defined as the normalised second order moment of the relative contribution of the brightest 20% of the pixels. To compute M_{20}, we rank-order the image pixels by flux, calculate F_i over the brightest pixels until their sum equals 20% of the total selected cluster flux, and then normalise by F_{tot}:

$$M_{20} = log\left(\frac{\sum_i F_i}{F_{tot}}\right), \text{while} \sum_i K_i \leq 0.2K_{tot}, \tag{2.5}$$

where K_{tot} is the total flux of the cluster image (image pixels are selected from the segmentation map*), and K_i is the flux value for each pixel i (where K_1 = the brightest pixel, K_2 = the second brightest pixel, etc).

---

*A map which defines the chosen circular aperture size with all pixels fixed to a value of 1.

2.2.3 Concentration, Asymmetry and Smoothness (CAS)

Concentration, Asymmetry and Smoothness parameters are commonly known as CAS.

Concentration is defined by Bershady et al. (2000) and Conselice (2003) as:

$$C = 5 \times log\left(\frac{r_{80}}{r_{20}}\right), \tag{2.6}$$

where r_{80} and r_{20} represent the radius within which 80% and 20% of the flux reside, respectively. Concentration is widely used in the classification of cool core or relaxed clusters, especially among distant clusters. Santos et al. (2008) define the surface brightness concentration parameter for finding cool core clusters at high redshift as,

$$c_{sb} = \frac{C_r(r < 40kpc)}{C_r(r < 400kpc)}, \tag{2.7}$$

where C_r ($r <$ 40 kpc) and C_r ($r <$ 400 kpc) are the integrated surface brightness within 40 kpc and 400 kpc, respectively. Instead of physical radii, we used the percentages of total flux within a given aperture size. This has an advantage in that the flux is independent of angular bin size and galaxy cluster redshift. Our sample includes a range of redshifts and, in the case of clusters closest to us, 250 kpc amounts to $\sim$ 225 pixels, whereas for those clusters furthest from us, 250 kpc corresponds to $\sim$ 16 pixels (if we bin the image by $\sim 2''$ pixel). In order to avoid this large deviation in pixel spread, it is best to use various percentages of the total flux of the galaxy clusters. For the inner radii we use 20%–50%, and for the outer radii we used 80%–90% of the total flux. For example, we use the C_{5080} Concentration parameter which means 50% of the flux within the inner radii and 80% within the outer radii.

The Asymmetry value will give rotational symmetry around the cluster centre, is calculated when a cluster image is rotated by 180° around its centre (x_c, y_c) and is then subtracted from its original image.

$$A = \frac{\sum_{i,j} \mid K(i,j) - K_{180}(i,j) \mid}{\sum_{i,j} \mid K(i,j) \mid}, \tag{2.8}$$

where $K(i,j)$ is the value of the pixel at the image position i, j, and $K_{180}(i,j)$ is the value of the pixel in the cluster's image rotated by 180° around its centre. The Asymmetry value is sensitive to any region of the cluster that is responsible for asymmetric flux distribution. Hence, if the sub-structure affects the flux distribution at any scale, we can pick it up from the Asymmetry value for that galaxy cluster.

We assume that, because non-relaxed galaxy clusters appear to have patchy flux distribution, they are made up of clumpy material. The Smoothness parameter can be used to identify patchy flux distribution. This is done by smoothing a cluster image with a filter of width σ, so that high frequency structure can be removed from the image. At this point the original image is subtracted from this newly smoothed, lower resolution image. The effect is to produce a residual map that has only high-frequency components of the galaxy cluster's flux distribution. The flux of this residual image is then summed and divided by the total flux of the original cluster image in order to find its smoothness value,

$$S = \frac{\sum_{i,j} \mid K(i,j) - K_s(i,j) \mid}{\sum_{i,j} \mid K(i,j) \mid}, \tag{2.9}$$

where $K_s(i,j)$ is the pixel in a smoothed image. Here we choose a Gaussian smoothing kernel of $\sigma = 12''$ as an arbitrary scale to smooth the cluster image.

2.2.4 Ellipticity

Ellipticity is commonly defined by the ratio between a semi-major axis (A) and a semi-minor axis (B) as

$$E = 1 - \frac{B}{A}, \tag{2.10}$$

where A and B can be computed directly from the second order moments of the flux in the cluster image as

$$A^2 = \frac{\overline{x^2} + \overline{y^2}}{2} + \sqrt{\left(\frac{\overline{x^2} - \overline{y^2}}{2}\right)^2 + \overline{xy}^2} \tag{2.11}$$

$$B^2 = \frac{\overline{x^2} + \overline{y^2}}{2} - \sqrt{\left(\frac{\overline{x^2} - \overline{y^2}}{2}\right)^2 + \overline{xy}^2}, \tag{2.12}$$

where

$$\overline{x} = \frac{\sum\limits_{i \in S} K_i x_i}{\sum\limits_{i \in S} K_i}, \qquad \overline{y} = \frac{\sum\limits_{i \in S} K_i y_i}{\sum\limits_{i \in S} K_i}, \tag{2.13}$$

$$\begin{aligned} \overline{x^2} &= \frac{\sum\limits_{i \in S} K_i x_i^2}{\sum\limits_{i \in S} K_i} - \overline{x}^2, \\ \overline{y^2} &= \frac{\sum\limits_{i \in S} K_i y_i^2}{\sum\limits_{i \in S} K_i} - \overline{y}^2, \\ \overline{xy} &= \frac{\sum\limits_{i \in S} K_i x_i y_i}{\sum\limits_{i \in S} K_i} - \overline{x}\,\overline{y}. \end{aligned} \tag{2.14}$$

Here $(x_i,\, y_i)$ is the $(x,\, y)$ coordinate of the image of a pixel i of value K_i inside an area S.

2.2.5 Uncertainty estimation

There are three sources of uncertainty in the calculation of the morphology parameters. These are: (1) shot noise in the image pixel values, (2) uncertainties in the centre of the cluster, and (3) variation in the area over which morphology parameters are calculated. The first two uncertainties can be approximated using a number of iterations of the Monte Carlo method. For estimating the third uncertainty, we used a jackknifing technique.

The shot noise effect can be approximated by replacing each pixel value with a Poisson random variable of the mean value of each pixel for the given image, and recalculating the parameters a number of times. After a set number of iterations (in our case ten), the rms of the spread in parameter values is an approximation of uncertainty in the parameters.

Resultant uncertainty from variation of the central position of a cluster is computed by deviating the input (x_c, y_c) coordinate within a fixed Gaussian width ($\sim 5''$ in our case). We then recalculate the parameters for several (x_c, y_c) value. After a number of iterations (ten), we compute the rms of the spread in parameter values as an approximate value of the uncertainty in the parameters.

As mentioned earlier, all parameters, except for the Gini coefficient, are sensitive to the cluster central position, being dependent on these central coordinates. The Gini coefficient is less sensitive to the shot noise than to changes in area, as the pixels are ordered first and do not depend on the central position of the cluster in any way. We estimated its uncertainty from a shot noise, and the rms in Gini values from a series of subsets of the pixels in the image (by allowing the pixels to be varied using Poisson statistics for a given area). This is known as jackknife error estimation. Yitzhaki (1991) suggested the use of the jackknife approach to estimate an uncertainty in the Gini coefficient. The jackknife and shot noise uncertainty estimates in the Gini coefficient are of similar order.

We used an error propagation formula to combined the shot noise and central position uncertainties for all parameters except the Gini coefficient. For the Gini coefficient, we combined the uncertainties from the shot noise and the jackknife estimation. Hence, in this work, all reported uncertainties (along with morphology parameter values in Table 2.2 and 2.4) are a combination of those mentioned above. We believe these three errors to be formal and not actual. For these parameters, an actual error could be large and mainly influenced by photon noise and X-ray counts.

2.2.6 Application of morphology parameters

As indicated earlier, we have a total of seven morphology parameters, each of which traces the different morphology of galaxy clusters, hence helping to quantify the shape and surface brightness distribution of the cluster. The Gini coefficient and Gini of the second order moments are useful to detect regular and smooth single components, where most of the flux comes from compact regions of the cluster (a few bright pixels, generally at the centre of the cluster, have the bulk of the flux). We expect high Gini value and low Gini of the second order moments to be associated with relaxed or cool core clusters (see definition of these parameters in § 2.2). The Concentration parameter traces how flux is concentrated in the centre of a cluster compared with that of the outer large region. Usually relaxed or cool core clusters have bright and compact cores as compared with those of non-relaxed or non-cool core clusters. So a high Concentration value indicates that a system is relaxed. The M_{20} parameter follows 20% of the brightest flux in a cluster image normalised by the total given aperture size (which is fixed). Therefore, if 20% of the flux resides in a small area (near to the cluster centre) then M_{20} gives a low value, which is indicative of relaxed or cool core systems. However, in the case of non-relaxed or non-cool core systems, 20% of the flux resides in a larger area compared with those of relaxed or cool core clusters, so a high M_{20} value suggests a non-relaxed or non-cool core system. Further, disturbed and distorted clusters have asymmetrical and patchy flux distribution, so we expect high Asymmetry and high Smoothness values to be associated with non-relaxed or non-cool core clusters. Hitherto, it has been believed that elliptical clusters show sub-structure, but, with the advent of various sub-structure detecting parameters, it is now believed that the Ellipticity parameter is not related to the cluster dynamical state, nor is it useful to detect non-relaxed clusters from relaxed clusters (Jeltema et al., 2005, and references therein). In following sections we will show the application of morphology parameters using simulated X-ray galaxy clusters.

2.3 2-D Beta model simulations

In order to test the fundamental ability of morphology parameters to separate relaxed clusters from non-relaxed, we attempted first to simulate simple images of galaxy clusters including various relaxed and non-relaxed morphologies. To start the process, our aim was to separate simulated double-components or multi-clusters from a gravitationally bounded virialized single-component system using a set of morphology parameters. For the purpose of simulation, we needed a simple surface brightness model which allowed us to represent these various cluster morphologies with the minimum of input parameters. Subsequently, we simulated this simple model using the instrument parameters (to add the various effects of real observation) of the ACIS *Chandra* CCDs to show the functionality of these morphology parameters.

We utilised the simple model to simulate the structure of X-ray clusters. The Beta model (Cavaliere & Fusco-Femiano, 1976; Arnaud, 2009; Sarazin, 2009) is commonly used to fit radial surface brightness profiles of X-ray clusters in order to calculate electron density and cluster mass (Vikhlinin et al., 2006). This simple Beta model is also widely used for an isothermal system (King, 1966), which assumes the total density profile of matter (luminous and dark) to be given by an isothermal distribution. The Beta model insufficiently describes the X-ray spatial emission from a cooling core cluster; but the Beta model often yields fair empirical fits to observed X-ray surface brightness radial profiles, and this surface brightness distribution has been used widely to describe X-ray galaxy clusters in a 2-D Lorentz model with a varying power-law. This is also known as a 2-D Beta model in the form of,

$$\eta_{gas}(r) = \eta_{gas}(0)\left[1 + \left(\frac{r}{r_c}\right)^2\right]^{-3\beta/2}, \tag{2.15}$$

where $x_{new} = (x - x_0)cos\theta + (y - y_0)sin\theta$,

$y_{new} = (y - y_0)cos\theta - (x - x_0)sin\theta$,

r_c is the core radius and β is the slope of surface brightness radial profile or power law index,

$r(x, y) = \left(\frac{\sqrt{x_{new}^2(1-\varepsilon)^2 + y_{new}^2}}{(1-\varepsilon)}\right)$, where ε = cluster ellipticity parameter and θ = angle of ellipticity.

Figs. 2.2 and 2.3 show simulations of relaxed and non-relaxed clusters using a 2-D Beta model. We list the simulation parameters in Table 2.1. Here we simulated six relaxed and six disturbed clusters with different morphologies to identify non-relaxed clusters from relaxed clusters using

Table 2.1: 2-D Beta model simulation input parameters.

z	0.1
pixel size	$2.5''$
core radius	~ 300 kpc
β	$0.8 \sim 1.2$

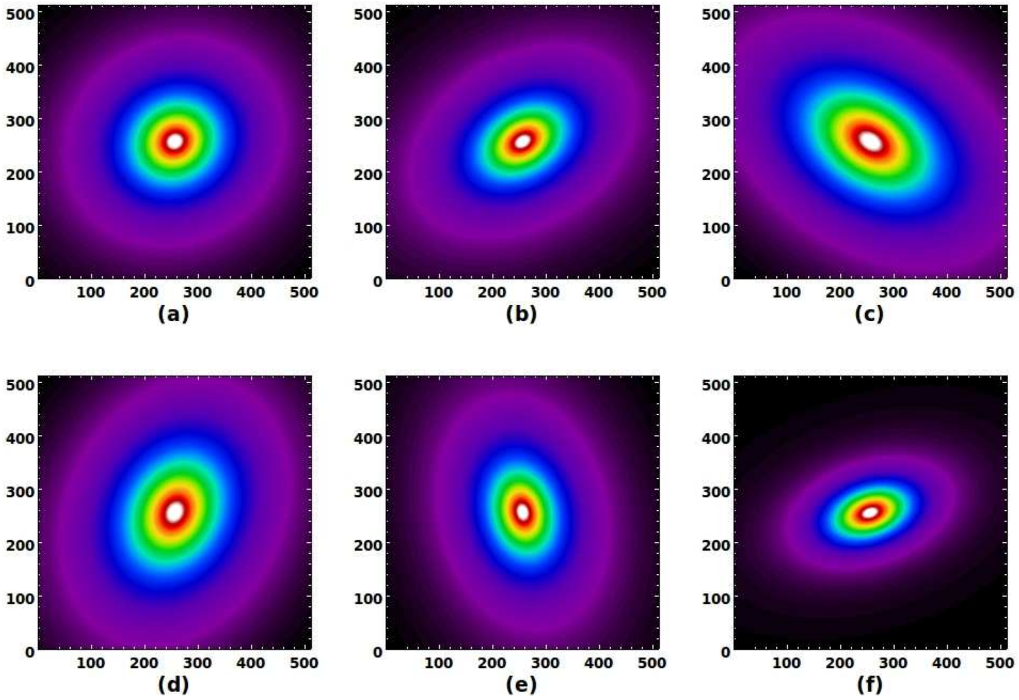

Figure 2.2: Various simulated morphologies of relaxed clusters with a 2-D Beta model.

seven morphology parameters. In Fig. 2.2, we simulated regular and smooth morphologies for relaxed clusters which have a high or peak flux value in the core region. This flux value decreases with increasing radius. Relaxed clusters have a compact and bright core. Conversely, non-relaxed clusters have quite irregular and asymmetrical morphology; and, in some cases, do not have a well defined cluster core. Non-relaxed clusters are spatially extended and have faint and diffuse flux distribution. In our non-relaxed cluster simulation, we included double component objects (Fig. 2.3 (a) to (d)), plus two objects with a small sub-structure (or another small cluster) close to the cluster core (Fig. 2.3 (e) and (f)). We approximated these disturbed clusters by using double Beta models.

2.4 Calculation of morphology parameters

Morphology parameters can be calculated in several ways, e.g. (1) by using a fixed aperture size centre on the cluster centroid, (2) by using the scaled radius of R_δ where δ = 200, 500, etc., which defines the overdensity with respect to the critical density of the Universe at the cluster redshift, (3) by applying a flux limit of 3σ or 5σ and calculating parameters for that region, (4) by calculating parameters for various aperture sizes in the range of 100 kpc, 200 kpc, etc. Our

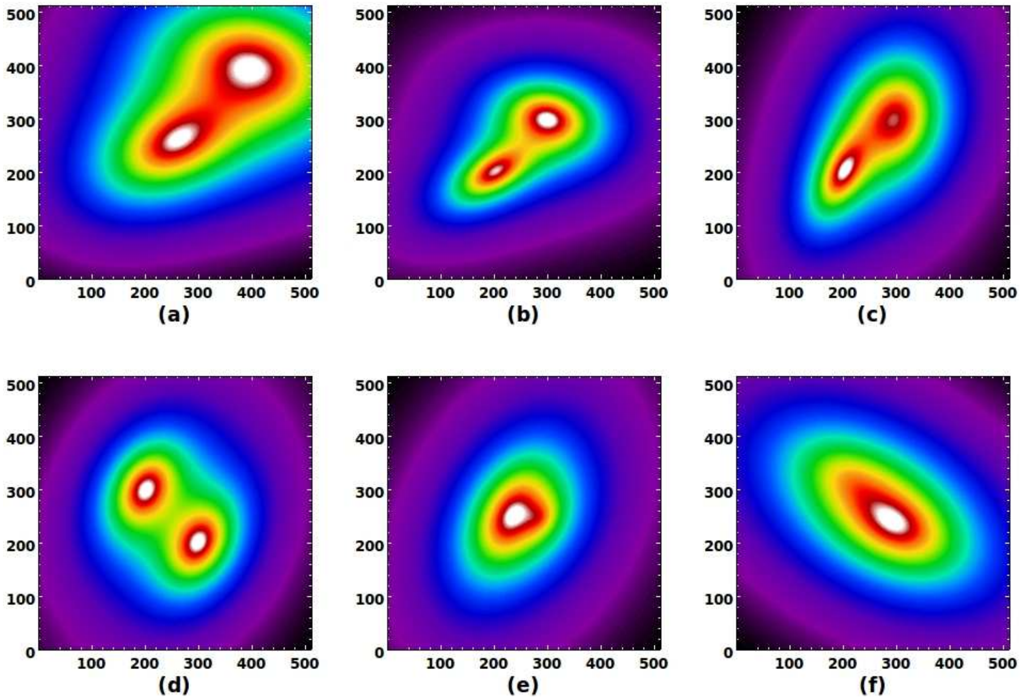

(a) (b) (c)

(d) (e) (f)

Figure 2.3: Various simulated morphologies of non-relaxed clusters with a 2-D Beta model.

choice is to calculate is using the segmentation map of the fixed physical size (§ 2.6). We also do tests based on segmentation maps that were produced by (1) determining the 3σ and 5σ flux value (where σ is noise level), in which case the difficulty is estimating background noise levels, particularly for low S/N cluster images or high redshift cluster observations; (2) setting a threshold limit by selecting pixels of 80% and 90% of maximum flux value of cluster image. This selection criterion requires prior removal of point sources from observation of actual X-ray galaxy clusters. In the experiment, both of these options failed to separate relaxed and non-relaxed clusters from our simulated images. We found it to be an optimal and suitable way to calculate the morphology parameters in a fixed physical (500 kpc) circular aperture size.

One of the most essential aspects is to find the centre of a cluster because all parameters (except the Gini, which does not require a precise centre for its calculation) are very sensitive to the chosen centre. We examined various options. One option was to find the centre coordinates corresponding to the peak flux value of a cluster. In this case it was not certain that we would detect any low surface brightness secondary component situated a distance from the main component (for example A85) which has peak flux at its centre. It is possible that the secondary component could interact with the primary component; but this is not included in parameter calculations because of its falling outside of the aperture size, and therefore we might not be able to interpret its correct dynamical state. Another option was visual inspection of a cluster centre; but this method is cumbersome when one needs to analyse large numbers of objects. We found that the flux weighted, or cluster centroid, method was most reliable and accurate in defining the central position of the cluster. We calculated this central position firstly by assigning initial coordinates based on visual observation of each cluster image, and then allowing the flux weighted coordinates to iterate in a fixed aperture size of, e.g., 500 kpc until they converged. The coordinates are therefore the unique point at the centre of the distribution of flux, essentially the light distribution equivalent to the “centre of mass".

2.5 Morphology parameter results

2.5.1 Distribution of morphology parameters

Fig. 2.4 shows the distribution of parameters for twelve simulated clusters (six clusters relaxed and six clusters non-relaxed). In this distribution, Gini, M_{20}, Concentration (all four ratios), Asymmetry, Smoothness and Gini of the second order moment parameters each show a different distribution for relaxed and non-relaxed clusters. The only exception is the Ellipticity parameter. For both the Gini and Concentration parameters, however, the non-relaxed clusters have distributions that peak at lower values, while the relaxed clusters have distributions that peak at higher values. A similar trend is visible for M_{20}, Asymmetry, Smoothness and Gini of the second order moment, although here the peak of relaxed clusters is on the lower side (low M_{20}, Asymmetry, Smoothness, and G_M) and the peak of non-relaxed clusters is on the higher side (high M_{20}, Asymmetry, Smoothness, and G_M). Table 2.2 gives each parameter value calculated for the Beta model simulated clusters, along with 1σ uncertainty.

2.5.2 Parameter vs Parameter planes

It is clear from the previous paragraph that Gini, M_{20}, Concentration, Asymmetry, Smoothness and Gini of the second order moments give a promising separation between relaxed and non-relaxed Beta model simulated clusters. Consequently, we investigated relaxed vs non-relaxed clusters in the parameter-parameter planes using combinations of morphology parameters to study the dynamical state of each galaxy cluster, as well as the relationship between each morphology parameter. It is important to note that the morphology parameter space is not an orthogonal, and that each parameter independently traces various structural characteristics of a galaxy cluster.

In Fig. 2.5 we compared each morphology parameter in relation to the others via a parameter vs parameter plane. It can be seen here that Concentration is tightly correlated with Gini while anti-correlated with M_{20}. Concentration (Santos et al., 2008; Hudson et al., 2010; Cassano et al., 2010b) is a very useful parameter for separating non-relaxed from relaxed clusters in combination with almost all morphology parameters. In Fig. 2.5, we plot the C_{5080} Concentration parameter. It is clear from Fig. 2.5 that relaxed clusters occupy the upper-left region, while non-relaxed clusters occupy the bottom-right region of the M_{20} vs Gini and Concentration planes. In the Gini vs Concentration plane, relaxed clusters fall in the upper-right region, while the bottom-left region is for non-relaxed clusters. In this work, we have found that the Gini coefficient is also important in separating non-relaxed from relaxed clusters when plotted against most other parameters.

The Gini, Concentration and M_{20} parameters are all inter-related as well, but they measure different properties of clusters. For example, (i) in Fig. 2.3d, the high M_{20} value indicates that 20% of the brightest pixels are far from the cluster centre (which increase the value of F_i in equation 2.5), while in Fig. 2.2f, the low M_{20} value suggests that 20% of the brightest pixels are very close to the cluster centre (which decrease the value of F_i in equation 2.5); (ii) the high Concentration value

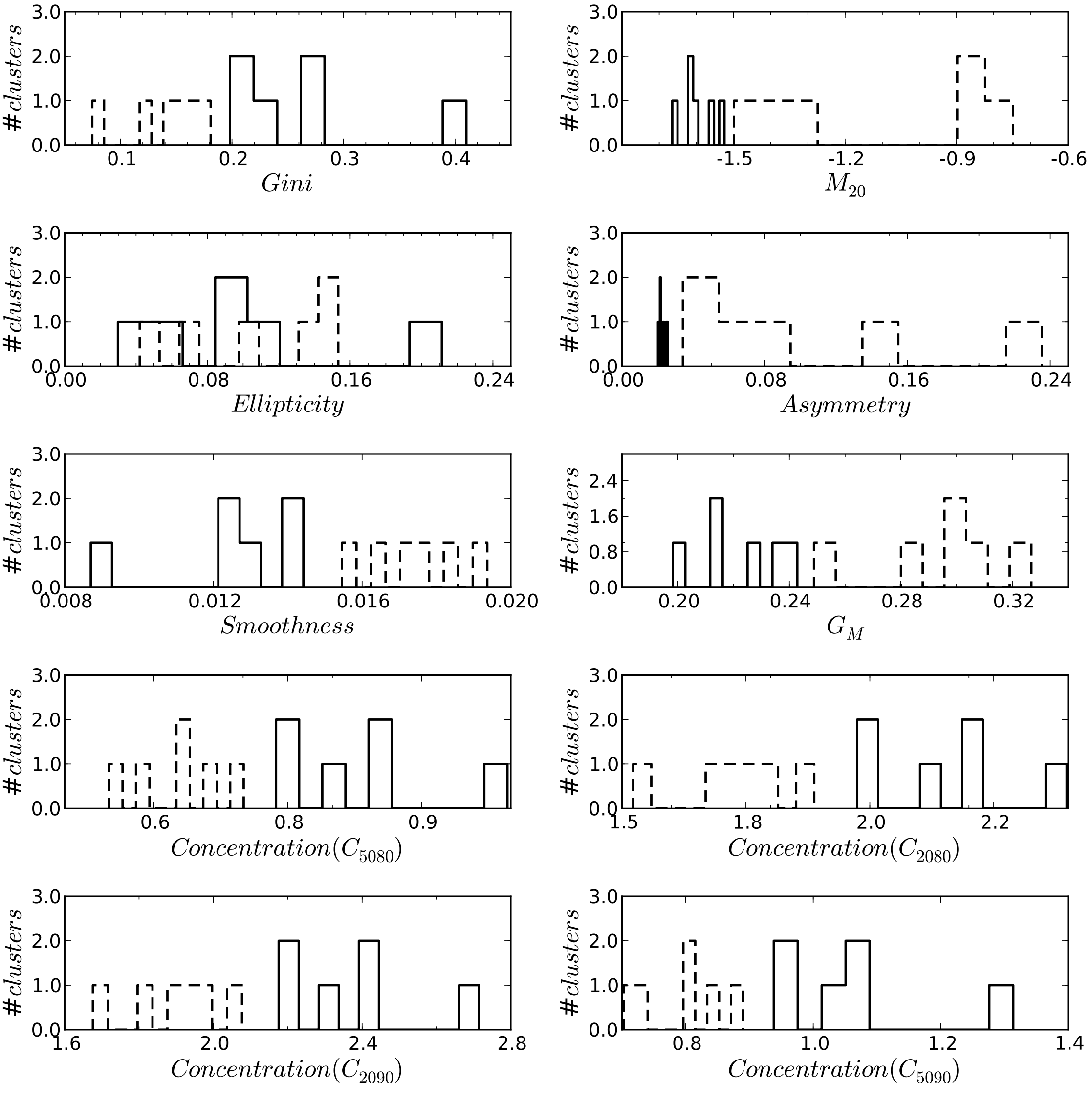

Figure 2.4: Distribution of seven morphology parameters: solid line = relaxed clusters; and dashed line = non-relaxed clusters. Here we used all four definitions of the Concentration parameter.

of Fig. 2.2f suggests that the flux residing in the inner radius (r_{50}) is very small compared with that of the outer radius (r_{80}) (very compact flux, see equation 2.6), while the low Concentration value of Fig. 2.3d suggests that the radius which contains the 50% of flux is large (but smaller than the r_{80} radius), and not compact; (iii) the high Gini coefficient of Fig. 2.2f suggests that, for the given aperture size of 500 kpc, a small number of pixels contains most of the flux, or that there are fewer number of bright pixels in the 500 kpc region, while the low Gini coefficient of Fig. 2.3a suggests that, for the given aperture size of 500 kpc, the flux is equally distributed among the pixels. Here we have successfully separated relaxed and regular clusters from double components and clusters with small sub-structure which are non-relaxed.

The Gini coefficient could be useful as a proxy of Concentration for detecting sub-structure in clusters. The advantage of using the Gini coefficient is that it is independent of the precise location of a galaxy cluster's centre. Furthermore, relaxed clusters are less smooth (with less patchy emission), and are noticeably symmetric around the centre of the cluster. We have not seen any correlation between the other six parameters, or cluster morphology, and the Ellipticity parameter. In general, these morphology parameters show more promise in the study of the dynamical state of galaxy clusters.

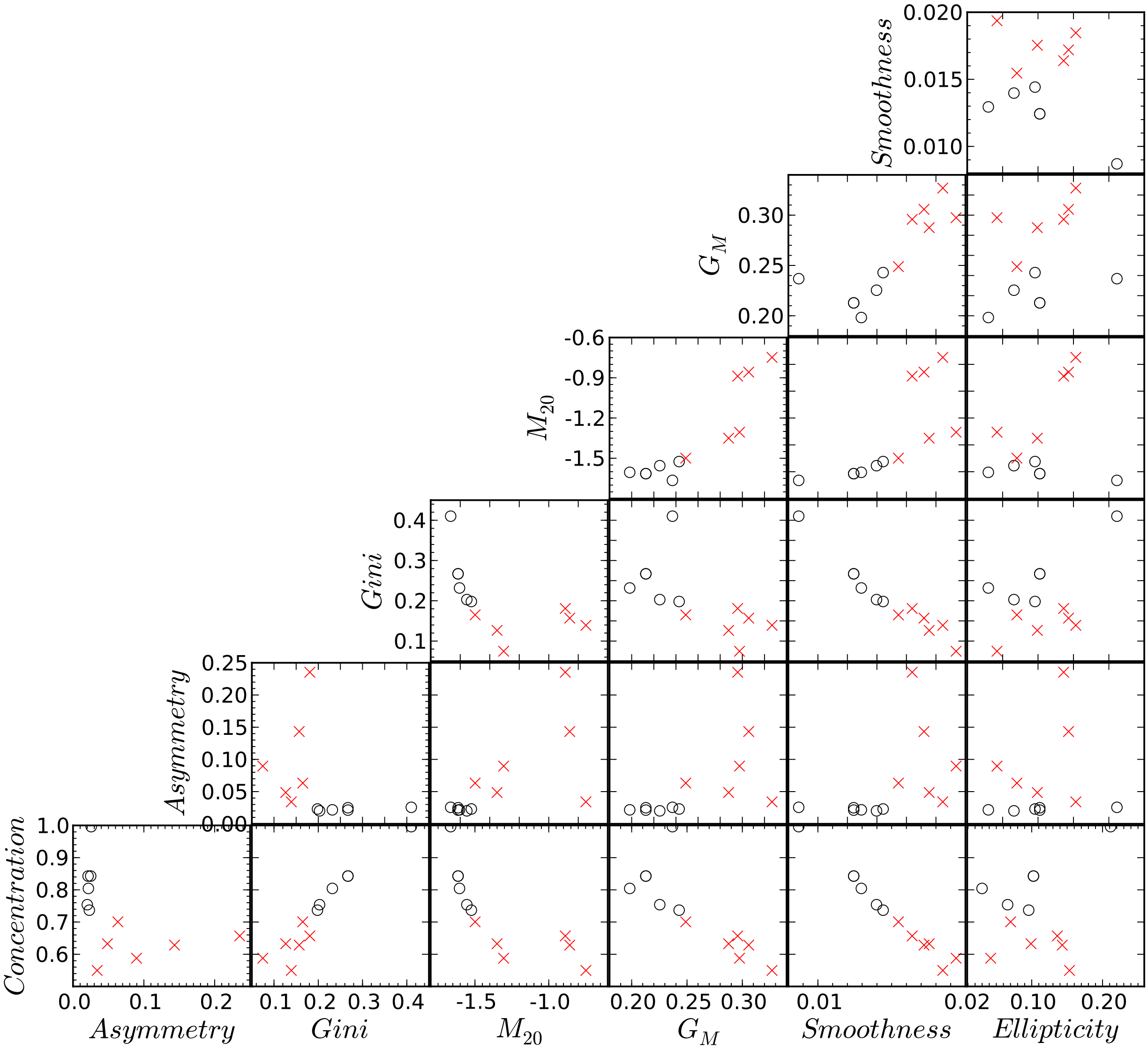

Figure 2.5: Seven morphology parameters plotted in the parameter-parameter planes. Here we plotted C_{5080} as the Concentration parameter. ○ = relaxed clusters; and × = non-relaxed clusters.

Table 2.2: Value of morphology parameters for six relaxed and six non-relaxed Beta model simulated clusters. Values are listed with appropriate uncertainties for each parameter.

Cluster	Gini	M_{20}	Concentration	Asymmetry	Smoothness	G_M	Ellipticity
relaxed cluster 1	0.232 ± 0.001	-1.605 ± 0.001	2.366 ± 0.000	0.022 ± 0.016	0.013 ± 0.000	0.198 ± 0.000	0.030 ± 0.000
relaxed cluster 2	0.267 ± 0.001	-1.615 ± 0.002	2.479 ± 0.001	0.021 ± 0.024	0.012 ± 0.000	0.213 ± 0.000	0.102 ± 0.000
relaxed cluster 3	0.198 ± 0.000	-1.524 ± 0.001	2.167 ± 0.000	0.023 ± 0.016	0.014 ± 0.000	0.243 ± 0.000	0.096 ± 0.000
relaxed cluster 4	0.203 ± 0.001	-1.555 ± 0.001	2.217 ± 0.000	0.020 ± 0.025	0.014 ± 0.000	0.225 ± 0.000	0.066 ± 0.000
relaxed cluster 5	0.267 ± 0.001	-1.614 ± 0.001	2.479 ± 0.000	0.025 ± 0.029	0.012 ± 0.000	0.213 ± 0.000	0.102 ± 0.000
relaxed cluster 6	0.410 ± 0.001	-1.665 ± 0.001	2.930 ± 0.001	0.026 ± 0.032	0.009 ± 0.000	0.237 ± 0.000	0.211 ± 0.000
non-relaxed cluster 1	0.075 ± 0.000	-1.306 ± 0.008	1.729 ± 0.002	0.090 ± 0.009	0.019 ± 0.000	0.297 ± 0.001	0.042 ± 0.000
non-relaxed cluster 2	0.181 ± 0.001	-0.888 ± 0.000	1.932 ± 0.008	0.235 ± 0.009	0.016 ± 0.000	0.296 ± 0.001	0.136 ± 0.000
non-relaxed cluster 3	0.157 ± 0.000	-0.858 ± 0.003	1.848 ± 0.004	0.143 ± 0.011	0.017 ± 0.000	0.306 ± 0.000	0.143 ± 0.000
non-relaxed cluster 4	0.139 ± 0.000	-0.748 ± 0.000	1.617 ± 0.000	0.034 ± 0.014	0.018 ± 0.000	0.327 ± 0.000	0.153 ± 0.000
non-relaxed cluster 5	0.165 ± 0.000	-1.499 ± 0.001	2.061 ± 0.000	0.063 ± 0.010	0.015 ± 0.000	0.249 ± 0.000	0.070 ± 0.000
non-relaxed cluster 6	0.126 ± 0.000	-1.350 ± 0.004	1.861 ± 0.001	0.049 ± 0.016	0.018 ± 0.000	0.288 ± 0.000	0.099 ± 0.000

2.6 Effect of aperture size

These parameters depend on the surface brightness distribution, hence their values are very much affected by the choice of aperture size. To study the effect of this on each parameter, we calculated the morphology parameters for a range of aperture sizes from small to large radii. We found that too small a radius ($<$ 500 kpc) is insufficient for calculating the 2-D Asymmetry and Smoothness parameters. This is obvious because galaxy clusters are extended objects and their morphology or shape cannot be characterised within small radii. Furthermore, the Gini coefficient strongly depends on the number of pixels included in the aperture. If one adds a large number of sky pixels to the aperture, the value of Gini increases with the number of pixels, making it difficult to estimate its true value. We found that the 1000 kpc radius is too large and includes too many 'sky' pixels. We therefore chose to use a fixed physical size radius rather than a fixed over-density (R_{500}*) radius because it is difficult to measure R_{500} accurately for these simulated (as well as non-relaxed) clusters. Hence, in this analysis (and for our simulated images at $z = 0.1$), we decided to use a fiducial 500 kpc aperture size for each simulated cluster, giving sufficient radius to study the cluster morphology and categorise its dynamical state.

2.7 Systematics

We investigated a number of possible systematic effects, discussed below, in order to study how robust these parameters are in various conditions.

2.7.1 Effects of noise in simulation image

To check robustness of these parameters, we added Poisson noise to each simulated cluster image. We defined the mean signal-to-noise per image pixel as,

$$< S/N >= \frac{1}{n}\sum_{i=1}^{n} \frac{S_i}{\sqrt{\sigma^2_{background} + S_i}}, \tag{2.16}$$

where S_i is i^{th} pixel flux, $\sigma_{background}$ is the (added) sky background noise, and n is the total number of pixels in the image. Fig. 2.6 illustrates the effect of adding Poisson noise to the cluster images. We simulated various (low to high) S/N ratios by adding the (sky) background noise.

Fig. 2.7 shows how the morphology parameters behave with different S/N. We added the noise to a few (original) cluster images with increasing S/N (from 0.1 to 11). We then re-calculated the morphology parameters for each simulated cluster of different S/N. Data points of each individual cluster were joined with a line to show the trend between morphology parameters and various S/N (see Fig. 2.7). Fig. 2.7 shows that all parameters are robust against different S/N, except for the Smoothness parameter. However, all parameters are weak when S/N is very low $\lesssim 1$.

---

*R_{500} is the radius defined as that enclosing a region with an over-density $\triangle = 500$ times the critical density at the cluster redshift.

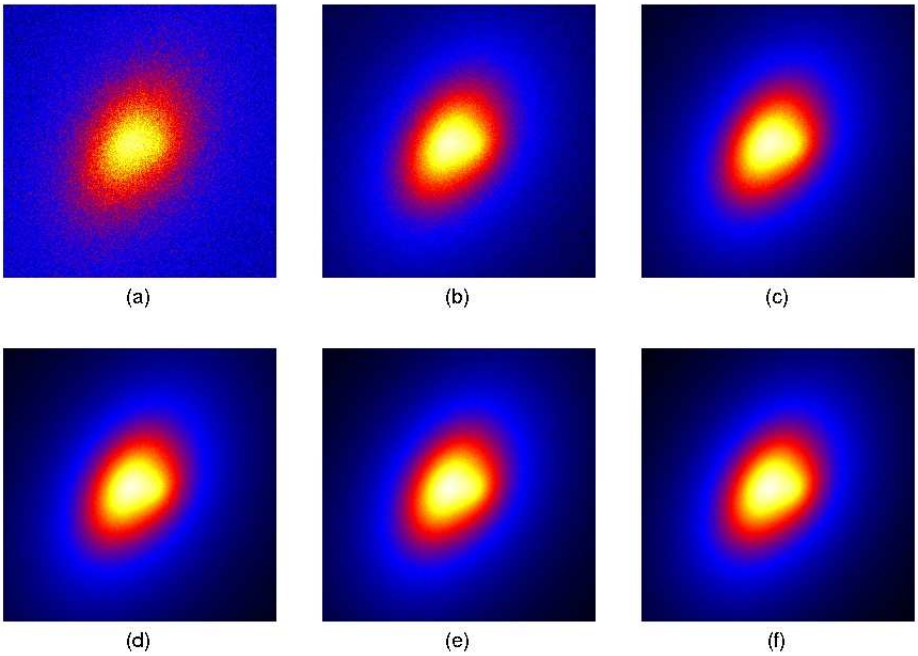

Figure 2.6: Beta model simulated clusters with added Poisson noise. From (a) to (f) shows the various S/N of 0.1 to 11 for the same (simulated) cluster.

2.7.2 Redshift effect

Our objective was to see how stable morphology parameters are in classifying objects over a range of redshifts. It is important to be able to classify high redshift clusters because most of the current survey (Semler et al., 2012) aims to observe high redshift objects and understand the dark matter distribution in the early Universe as well as cluster evolution. High redshift clusters have low S/N and it is therefore difficult to identify sub-structure among them. This could affect their mass estimation, so it is essential to identify sub-structure among high redshift clusters.

In the interests of separating the different dynamical states of distant galaxy clusters, we shifted our simulated clusters to higher redshift ($z = 0.5, 1, 2$) to understand the behaviour of morphology parameters. To do this, we simply re-binned cluster images according to the cluster's angular bin size at redshifts 0.5, 1 and 2, as well as dimming the flux at respective redshifts according to the luminosity distance of each. We then added Poisson noise, as described in the previous section. We show how the cluster appears at redshifts 0.1, 0.5, 1 and 2 in Fig. 2.8 with the (fix) S/N of 1.

Figs. 2.9 and 2.10 show how the morphology parameters behave with different redshifts at fixed S/N of 11 and 1, respectively. We simulated a few original clusters artificially at higher redshift with various S/N from 0.1 to 11, as mentioned above, and re-calculated the morphology parameters for each simulated cluster. The data points of each individual cluster were joined with a line to illustrate the trend between morphology parameters and redshift. As we observe in Figs. 2.9 and 2.10, with the exception of the Smoothness and Asymmetry parameters, all parameters are quite robust against different redshifts.

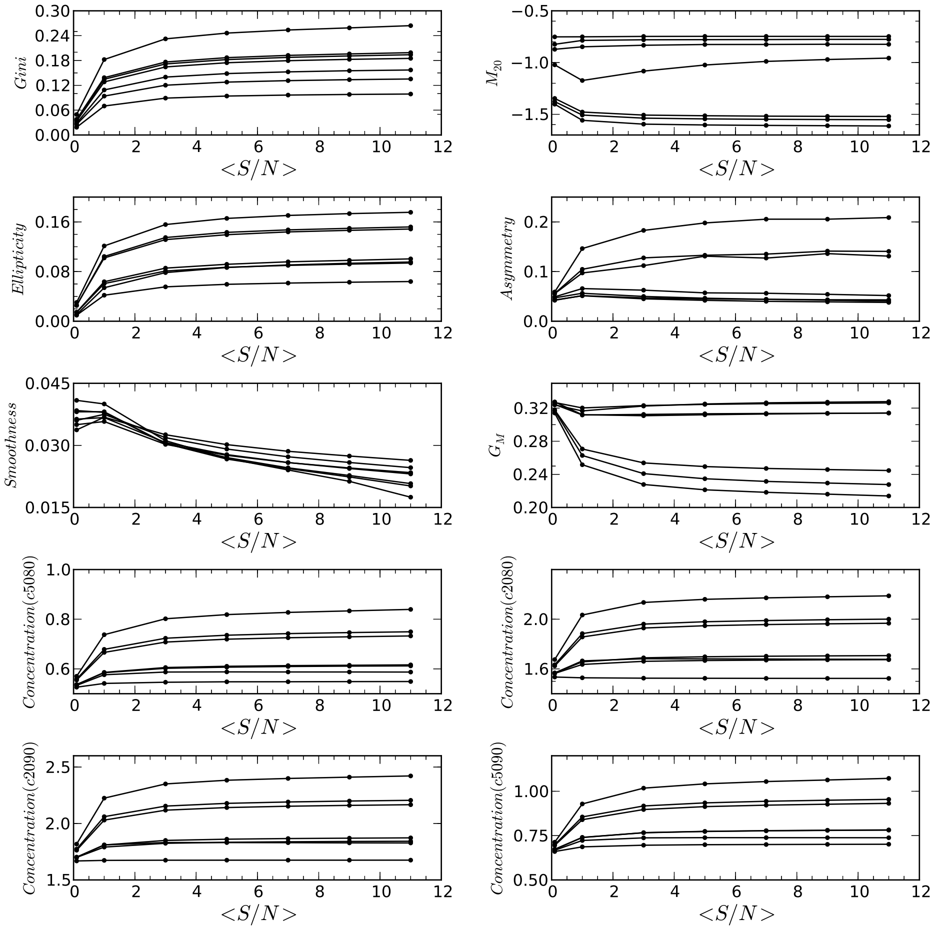

Figure 2.7: Robustness of morphology parameters which are calculated for several clusters against different S/N for the same cluster images. See text for details.

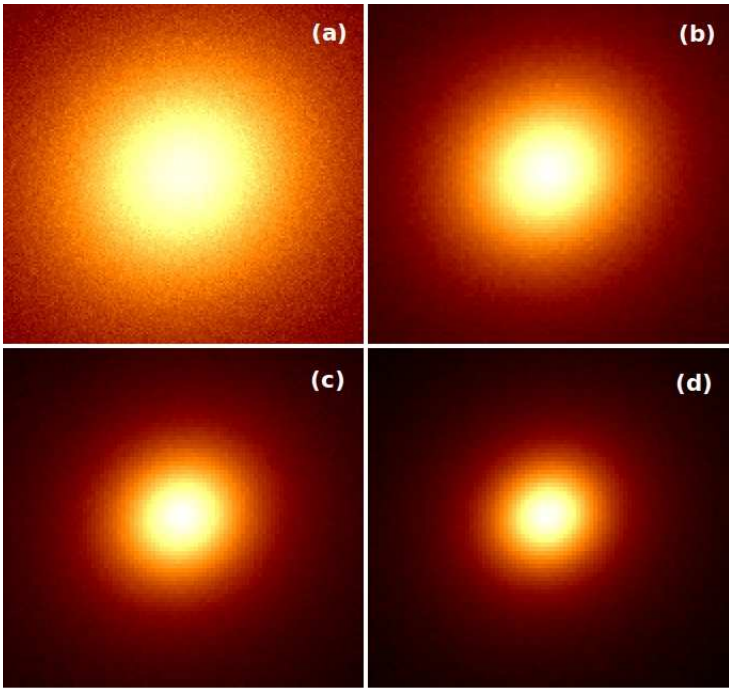

Figure 2.8: Beta model simulated clusters with added Poisson noise (S/N = 1). (a) to (d) illustrates the cluster at redshift of 0.1, 0.5, 1 and 2, respectively.

2.8 *Chandra* telescope simulations

In earlier sections we demonstrated the ability of the morphology parameters to quantitatively separate relaxed clusters from non-relaxed clusters which had been simulated with the simple Beta model. At this point it is equally important to check the ability of these parameters to work under real observational conditions and effects. In this section, we assess the practical feasibility of the morphology parameters by simulating X-ray observations of the cluster model with the various instruments and detectors of the *Chandra* telescope.

We used MARX[*] *Chandra* telescope simulator software (version of 4.5.0) to re-simulate the simple 2-D Beta model clusters, as described in § 2.3. We passed Beta model cluster images through MARX to mimic the *Chandra* observation. The simulated clusters, as shown in Fig. 2.11, are relaxed clusters, while those shown in Fig. 2.12 are non-relaxed clusters. MARX software facilitates simulation of the complete performance of the on-orbit *Chandra* X-ray Observatory (Wise et al., 1997; Gardini, 2002). In addition, it includes models of the different combinations of on-board scientific instruments such as the *Chandra* mirrors, the transmission grating assemblies (LETG and HETG), and the HRC and ACIS focal plane detectors. Further, it includes a built-in model of *Chandra's* aspect motion and implemented routines of post-processing which can be utilised to simulate either the effects of ACIS photon pile-up, or an existing detector response matrix file (RMF) for further spectral analysis purpose. It provides support in simulating various simple astrophysical source models (e.g. point like, Beta, or extended) as well as allowing users to incorporate their own models, rendering the MARX software particularly useful and user friendly.

---

[*] http://space.mit.edu/ACS/MARX

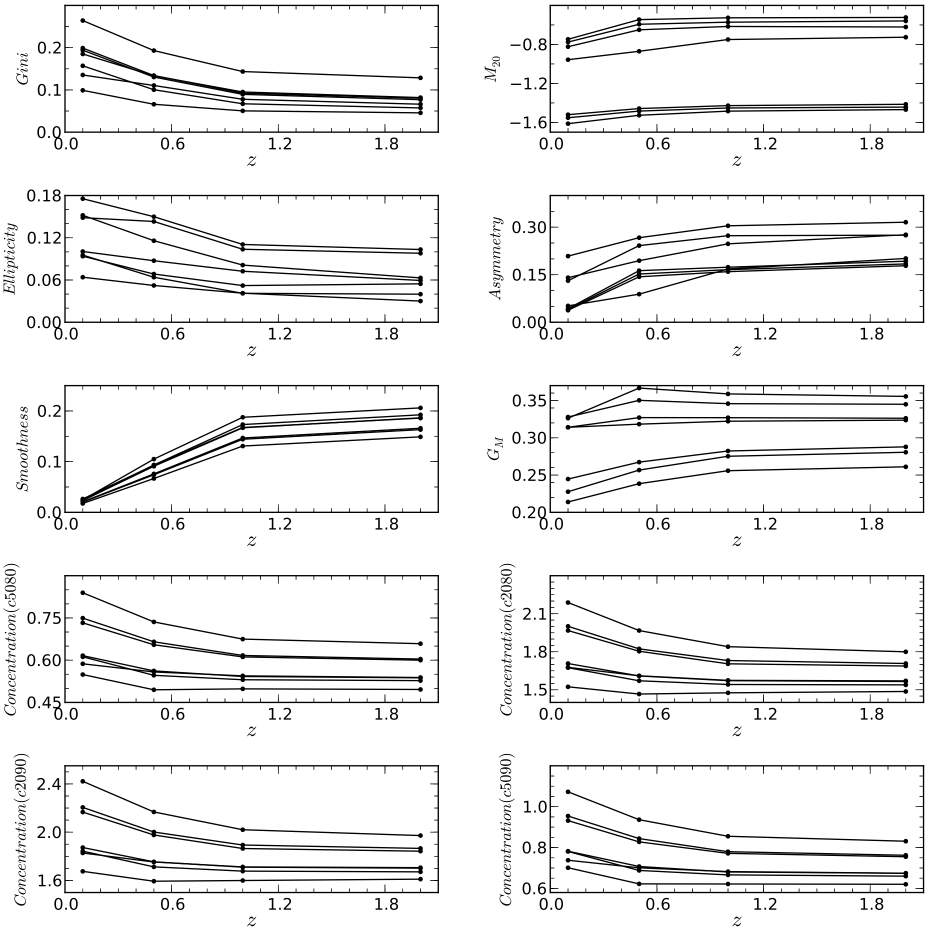

Figure 2.9: Robustness of morphology parameters which are calculated for several clusters against simulated clusters at different redshifts with S/N of 11.

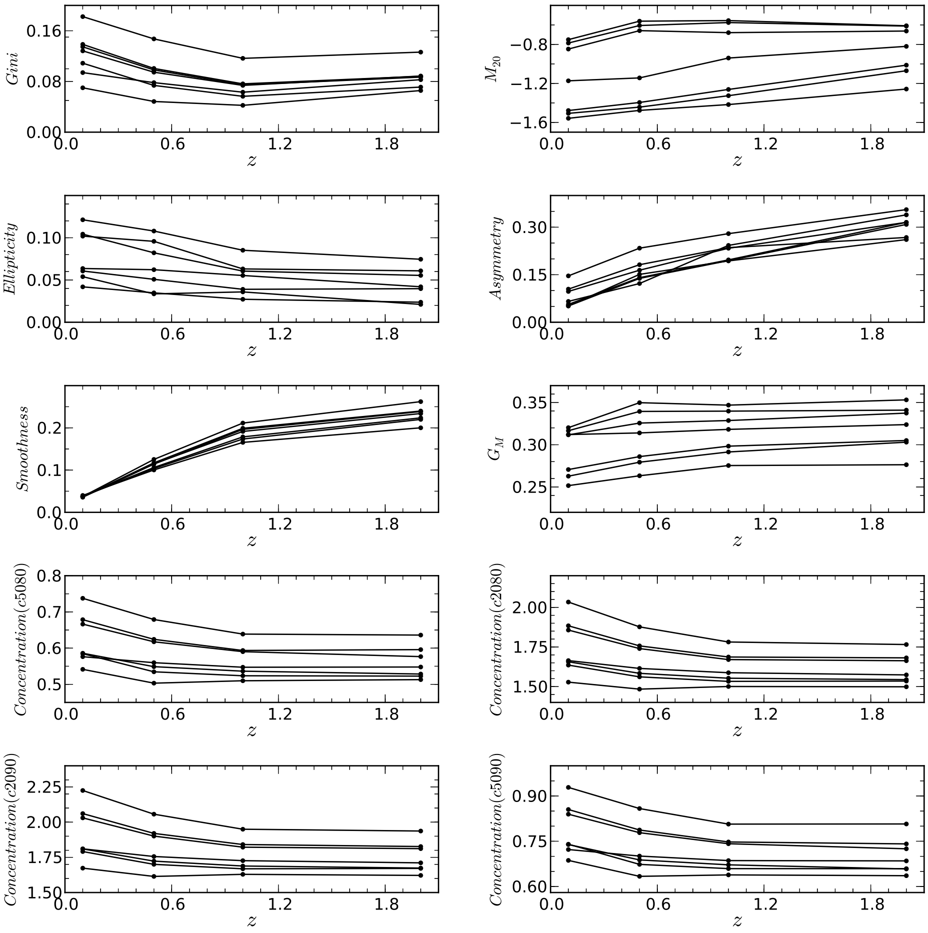

Figure 2.10: Same as Fig. 2.9 except for S/N of 1.

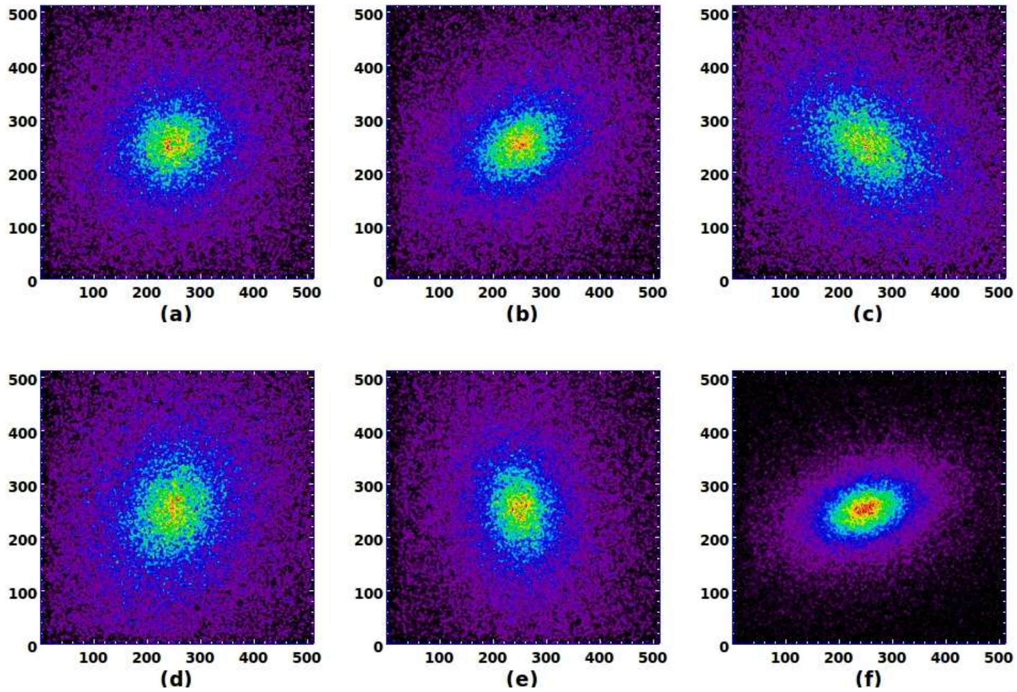

Figure 2.11: Relaxed clusters simulated with MARX *Chandra* simulator.

In simulation, users can supply arbitrary spectral energy distributions, which are defined through an input ASCII file generated by either Xspec or Sherpa.

MARX is written in the C language, and consists of a single executable file. It is necessary to give a list of input parameters to MARX, including exposure time, total flux from the input source model (photons s^{-1} cm^{-2}), detector coordinates and configuration, spectral model file, input source model (either from an external file or built-in), etc. The simulation takes around 5 seconds to generate the output. The user has then the option of working with either the original binary output format of MARX directly, or creating FITS events files and images. We used MARX's built-in tool `marx2fits` to generate FITS events files from the MARX output format files. All aspect solutions files are generated with the `marxasp` tool. The resulting FITS events files will contain a binary table. This table has properties of detected photons such as pulse height, position and arrival time. It also contains simulation variables such as the true photon energy and mirror shell off which the photon is reflected. These generated level 1 events files require further processing with the CIAO[*](Fruscione et al., 2006) task called `acis_process_events`, which updates time, coordinates, pulse-height, grade, and status information. It also applies the latest gain corrections and calibrations to ACIS level 1 events files, and generates the standard level 2 events files which are compatible with CIAO software (similar to standard *Chandra* output). Images and spectra may be generated from these simulated events files using CIAO tools such as `dmcopy` and `dmextract`, respectively. In this study, we processed all simulations events file with the CIAO-4.3 version. We used the CALDB version 4.4.6. In Table 2.3, we list all parameters used during the simulation.

---

[*] Chandra Interactive Analysis of Observations

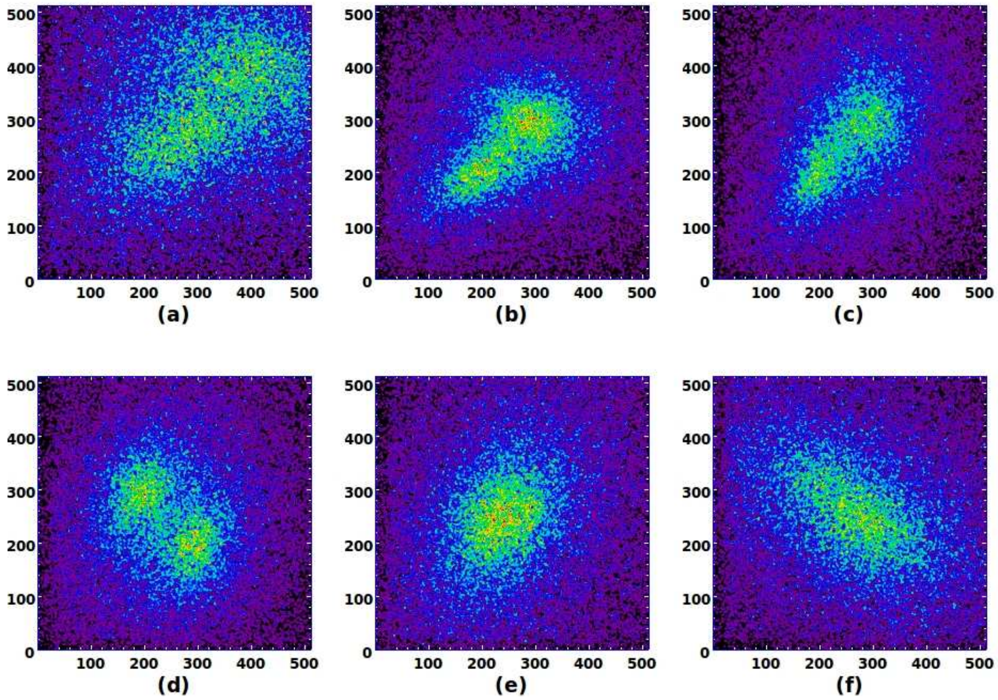

Figure 2.12: Non-relaxed clusters simulated with MARX *Chandra* simulator.

2.8.1 Calculation of morphology parameters

In this section we show calculations of morphology parameters for the Beta model clusters passed through the MARX simulator to comprise the effect of *Chandra's* instrument. We chose clusters at $z = 0.1$. For this simulation, we used a 50 ks exposure time for all clusters. We smoothed each simulated cluster image with $\sim 12''$ ($\sim$ 5 pix.) Gaussian width to suppress the artifacts of the CCDs, to make sure of no zero counts in the cluster image. In calculating the Smoothness parameter, we smoothed the input image by $1'$ ($\sim$ 105 kpc at $z = 0.1$) and then subtracted it from the (smooth) input cluster image. We then used the 500 kpc cluster region for each cluster in order to calculate morphology parameters. Fig. 2.13 shows the distribution of parameters. We calculated the cluster centre in the same way as that given in § 2.4. All parameters are distributed in the same order for relaxed and non-relaxed clusters as compared with the Beta model simulated clusters. As shown before, all morphology parameters, except Ellipticity, show a different distribution for relaxed and non-relaxed clusters. For the Gini and Concentration parameters, the peak of the distribution of relaxed clusters falls on the right side (high Gini and Concentration), while the peak for non-relaxed clusters falls on the left side (low Gini and Concentration). An equivalent distribution is visible for M_{20}, Asymmetry, Smoothness and Gini of the second order moment, but the peak of non-relaxed clusters is on the right side (high M_{20}, Asymmetry, Smoothness, and G_M) while the peak of relaxed clusters is on the left side (low M_{20}, Asymmetry, Smoothness, and G_M). In Table 2.4 we give each parameter value calculated for a MARX simulated cluster along with 1σ uncertainty. In the following paragraph, we show how each cluster occupies its position in every parameter-parameter plane.

Fig. 2.14 shows the parameter-parameter planes. Again, we see a separation between relaxed

Table 2.3: MARX *Chandra* simulation parameters

z	0.1
pixel size	$2.5''$
exposure time	50 ks
detector	ACIS-I
spectrum	thermal(wabs*mekal)(0.1-10 keV)
temp	4 keV
nH	3×10^{20}
abundance	$0.3\ Z_{\odot}$

and non-relaxed clusters in all parameter-parameter planes. In Fig. 2.14 Concentration is tightly correlated with Gini and anti-correlated with M_{20}. Concentration is a very useful parameter for separating non-relaxed from relaxed clusters with almost all morphology parameters. In Fig. 2.14, we plot the C_{5080} Concentration parameter. As can be seen from Fig. 2.14, relaxed clusters occupy the upper-left region while non-relaxed clusters occupy the bottom-right corner of the M_{20} vs Gini and Concentration planes. In the Gini vs Concentration plane, relaxed clusters fall in the upper-right region while the bottom-left region is for non-relaxed clusters. In this work we have found that the Gini coefficient is also important in separating non-relaxed from relaxed clusters when plotted against most other parameters. These clearly show that, using morphology parameters, both cluster types are separated in *Chandra* telescope-like observations. The value of parameters is not affected much by the use of instruments. Again, the Ellipticity parameter is the exception, in that it is not useful in separating relaxed and non-relaxed clusters.

It is important, however, to mention that we have uniform exposure time of 50 ks in this MARX simulation, but that in real analysis, cluster samples (which may include low- or high-z) do not have uniform exposure time. To study the effect of different exposure times on parameters, we simulated the same group of clusters (relaxed and non-relaxed) with different exposure times (using MARX), and re-calculated all parameters. For calculating parameters, we initially smoothed each input cluster image by $12''$, as mentioned above. In calculating the Smoothness parameter, we used the $\sigma = 1'$ kernel smoothing size. The result of our distribution of parameters is plotted in Fig. 2.15. We see that Gini, M_{20} and Concentration parameters still separate relaxed from non-relaxed clusters, notwithstanding heterogeneous exposure time. Smoothness and Asymmetry parameters are not useful in terms of separating relaxed and non-relaxed clusters. We see an overlap between relaxed and non-relaxed clusters for these two parameters. Only the Smoothness parameter gives separation between relaxed and non-relaxed clusters when combined with either Gini, M_{20} or Concentration. In investigating further the Smoothness parameter, we used a $\sigma = 2'$ ($\sim$ 212 kpc at 0.1 redshift) and $3'$ ($\sim$ 320 kpc at 0.1 redshift) kernel smoothing size (selection based on aperture size of 500 kpc) to study the effect of various smoothing sizes of σ on the Smoothness parameter. We also smoothed input cluster images by $12''$ and $0.5'$, in calculating the Smoothness parameter. We found this smoothing size to be reasonable in the initial stage of smoothing input cluster images, since a larger smoothing size might have washed out, for example, clumpy and patchy features from the original input image. Our results are shown in Fig. 2.16. These different settings of σ cannot improve the Smoothness parameter. Nevertheless, overlap between relaxed and non-relaxed clusters is still evident.

Table 2.4: Value of morphology parameters for six relaxed and six non-relaxed Marx simulated clusters. Values are listed with appropriate uncertainties for each parameter.

Cluster	Gini	M_{20}	Concentration	Asymmetry	Smoothness	G_M	Ellipticity
relaxed cluster 1	0.264 ± 0.001	-1.440 ± 0.008	2.374 ± 0.010	0.278 ± 0.017	0.163 ± 0.001	0.262 ± 0.001	0.023 ± 0.001
relaxed cluster 2	0.292 ± 0.002	-1.490 ± 0.008	2.468 ± 0.011	0.263 ± 0.029	0.152 ± 0.001	0.265 ± 0.001	0.104 ± 0.002
relaxed cluster 3	0.243 ± 0.001	-1.299 ± 0.010	2.164 ± 0.010	0.292 ± 0.022	0.172 ± 0.002	0.299 ± 0.001	0.112 ± 0.002
relaxed cluster 4	0.242 ± 0.002	-1.333 ± 0.007	2.197 ± 0.009	0.278 ± 0.017	0.167 ± 0.001	0.282 ± 0.001	0.069 ± 0.002
relaxed cluster 5	0.296 ± 0.001	-1.488 ± 0.009	2.466 ± 0.012	0.273 ± 0.022	0.155 ± 0.001	0.268 ± 0.001	0.104 ± 0.002
relaxed cluster 6	0.415 ± 0.001	-1.625 ± 0.009	2.881 ± 0.011	0.212 ± 0.029	0.117 ± 0.001	0.275 ± 0.001	0.212 ± 0.002
non-relaxed cluster 1	0.180 ± 0.001	-0.798 ± 0.008	1.675 ± 0.011	0.358 ± 0.016	0.210 ± 0.001	0.357 ± 0.001	0.061 ± 0.002
non-relaxed cluster 2	0.223 ± 0.001	-0.899 ± 0.003	1.945 ± 0.016	0.364 ± 0.013	0.173 ± 0.002	0.335 ± 0.001	0.127 ± 0.002
non-relaxed cluster 3	0.209 ± 0.001	-0.833 ± 0.008	1.782 ± 0.011	0.326 ± 0.022	0.180 ± 0.001	0.346 ± 0.001	0.142 ± 0.002
non-relaxed cluster 4	0.199 ± 0.001	-0.743 ± 0.003	1.617 ± 0.005	0.320 ± 0.014	0.189 ± 0.002	0.364 ± 0.001	0.150 ± 0.001
non-relaxed cluster 5	0.211 ± 0.001	-1.130 ± 0.010	2.023 ± 0.011	0.313 ± 0.009	0.177 ± 0.001	0.299 ± 0.001	0.064 ± 0.002
non-relaxed cluster 6	0.200 ± 0.001	-0.961 ± 0.006	1.856 ± 0.005	0.337 ± 0.027	0.196 ± 0.001	0.337 ± 0.001	0.095 ± 0.002

Beta model simulation itself gives a smooth cluster image which might introduce bias to the calculation of the Smoothness parameter. In systematically investigating further the Smoothness parameter, we simulated the one Beta model cluster which has patchy and sub-clumps features (see Fig. 2.17(a)), and subsequently added the instrumental effects as shown in Fig. 2.17(b). We used four cluster objects of different size and flux in this simulation, to check the response of the Smoothness parameter particularly for this irregular cluster. Simultaneously, we looked for the effect of exposure time. We re-simulated this (Beta model) cluster with the MARX using 6 different exposure times (10k, 20k, 40k, 60k, 80k and 100k); then calculated all morphology parameters for each. We used an aperture size of 500 kpc, and smoothed the input images by $12''$. In calculating the Smoothness parameter, we used a smoothing kernel size of $\sigma = 1', 1.5', 2', 2.5' and 3'$ and plotted it, together with other parameters (see Fig. 2.18), against exposure time. In this plot we see that Gini, M_{20}, Concentration, Ellipticity, G_M and Asymmetry are quite robust when subjected to different exposure times, the Smoothness parameter being the exception. For the sole purpose of comparison, we also included the original Beta model cluster at exposure time = 200 ks, in order to see the whole trend. In the Smoothness plot, we see different trends at different smoothing kernel sizes. The Red line indicates the $\sigma = 1'$ smoothing kernel size. It shows that simulated clusters of different exposure time are smoothed by $\sigma = 1'$ and then subtracted from the input image (the $12''$ smoothed original image). All these Smoothness values are plotted against exposure time. Similarly, the yellow line is for $\sigma = 1.5'$, the green line is for $\sigma = 2'$, the blue line is for $\sigma = 2.5'$ and the black line is for $\sigma = 3'$. This shows clearly that the Smoothness parameter is very sensitive to the smoothing kernel size and to exposure time. It changes systematically with different exposure times. This makes it difficult to use the Smoothness parameter when we have a large cluster sample of heterogeneous exposure time.

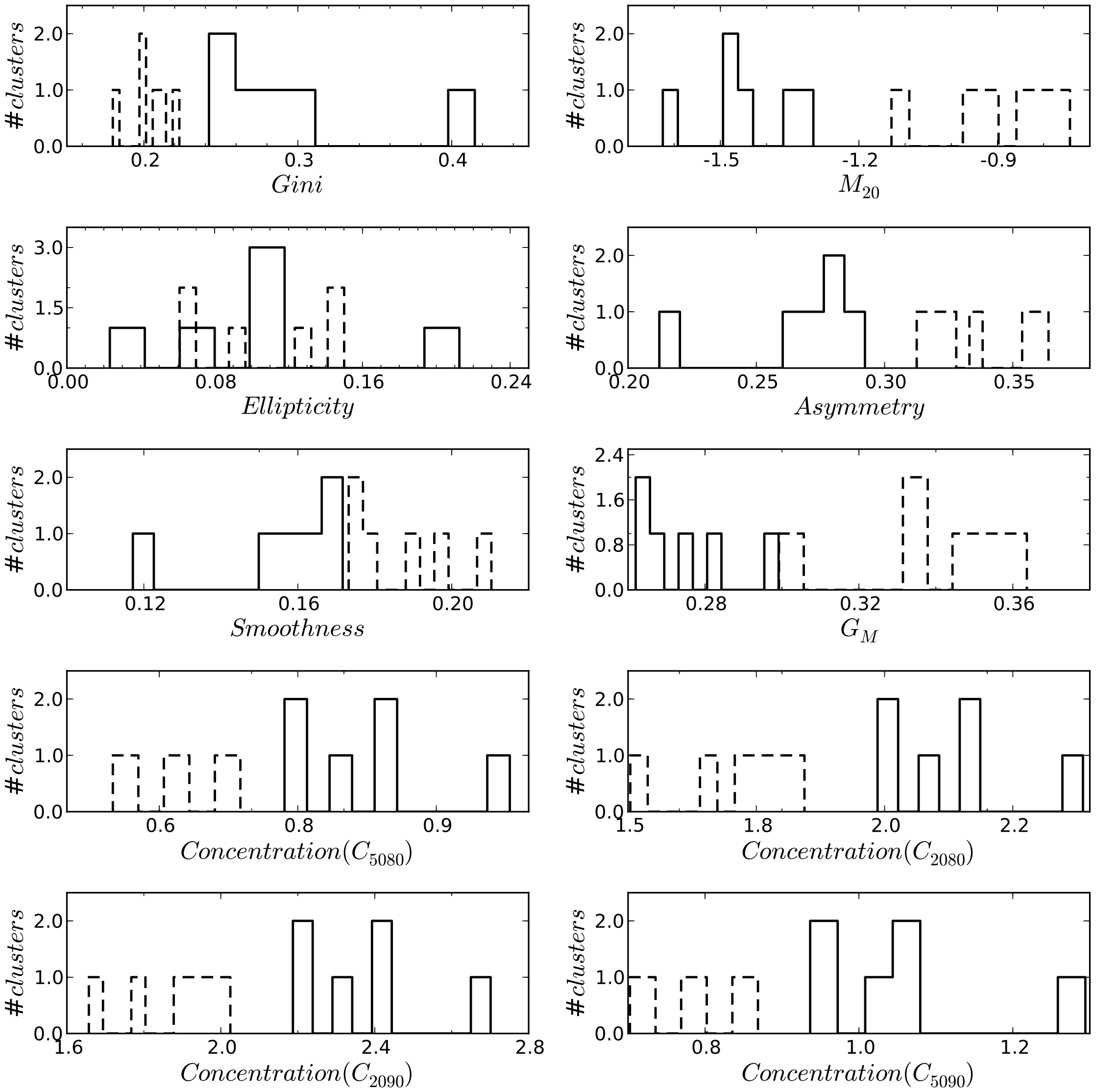

Figure 2.13: Distribution of seven morphology parameters calculated for the MARX simulated clusters. Solid line = relaxed clusters; and dashed line = non-relaxed clusters. Here we used all four definitions of the Concentration parameter.

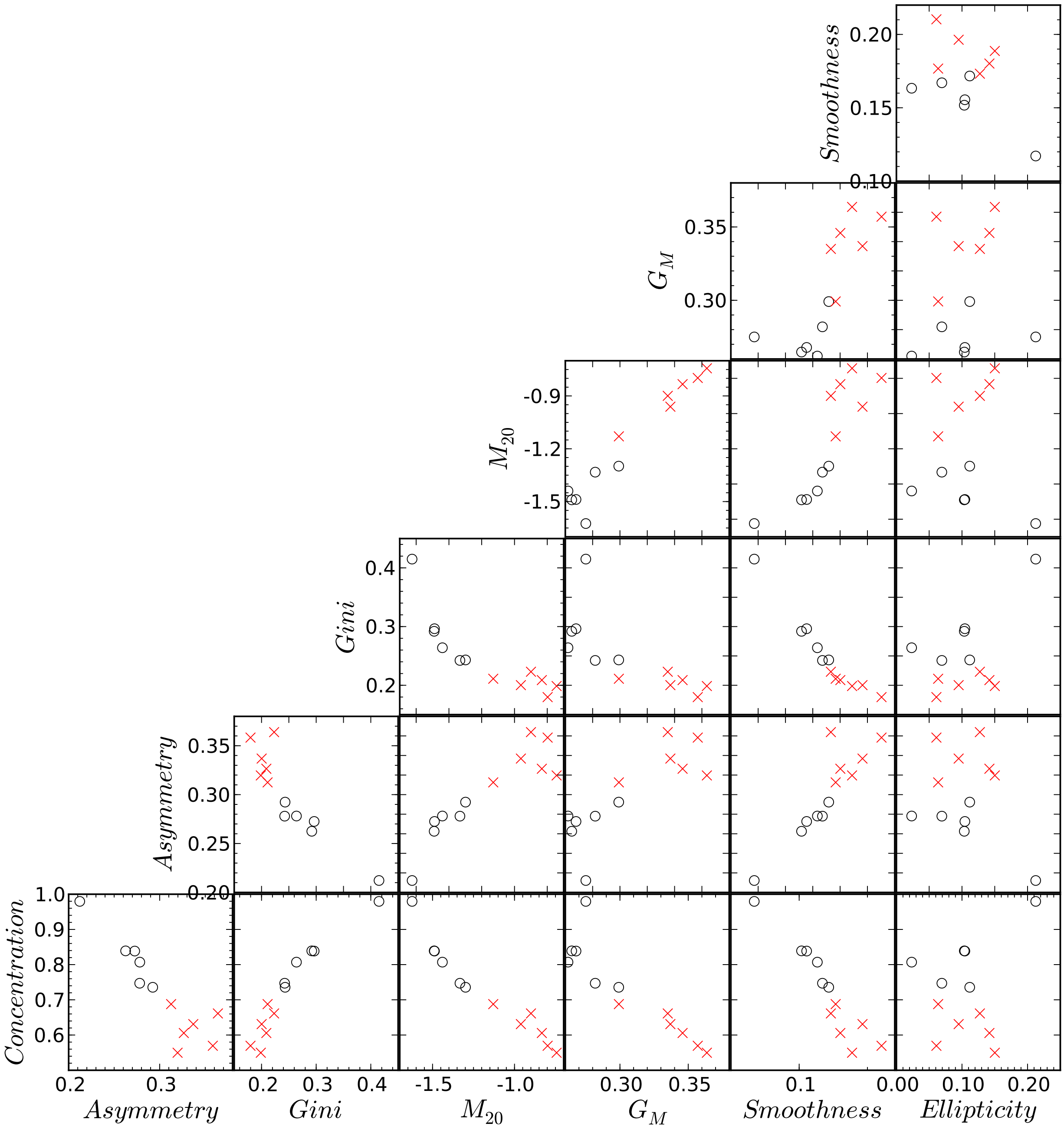

Figure 2.14: Seven morphology parameters plotted in parameter-parameter planes, calculated for the MARX simulated clusters. Here we plotted C_{5080} as the Concentration parameter. ○ = relaxed clusters; and × = non-relaxed clusters.

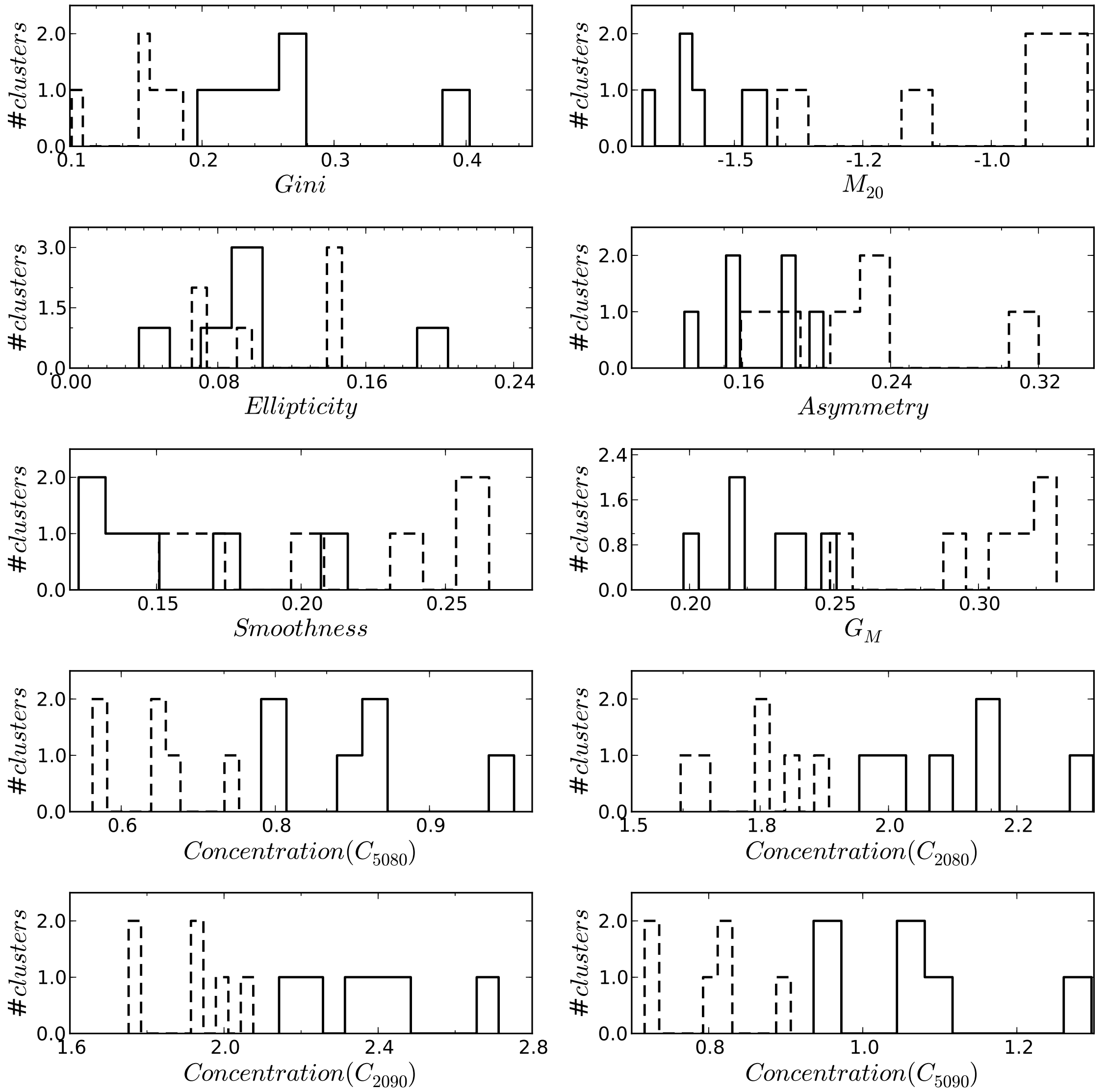

Figure 2.15: Distribution of morphology parameters calculated for the MARX simulated clusters at different exposure time. Symbols are the same as those in Fig. 2.13.

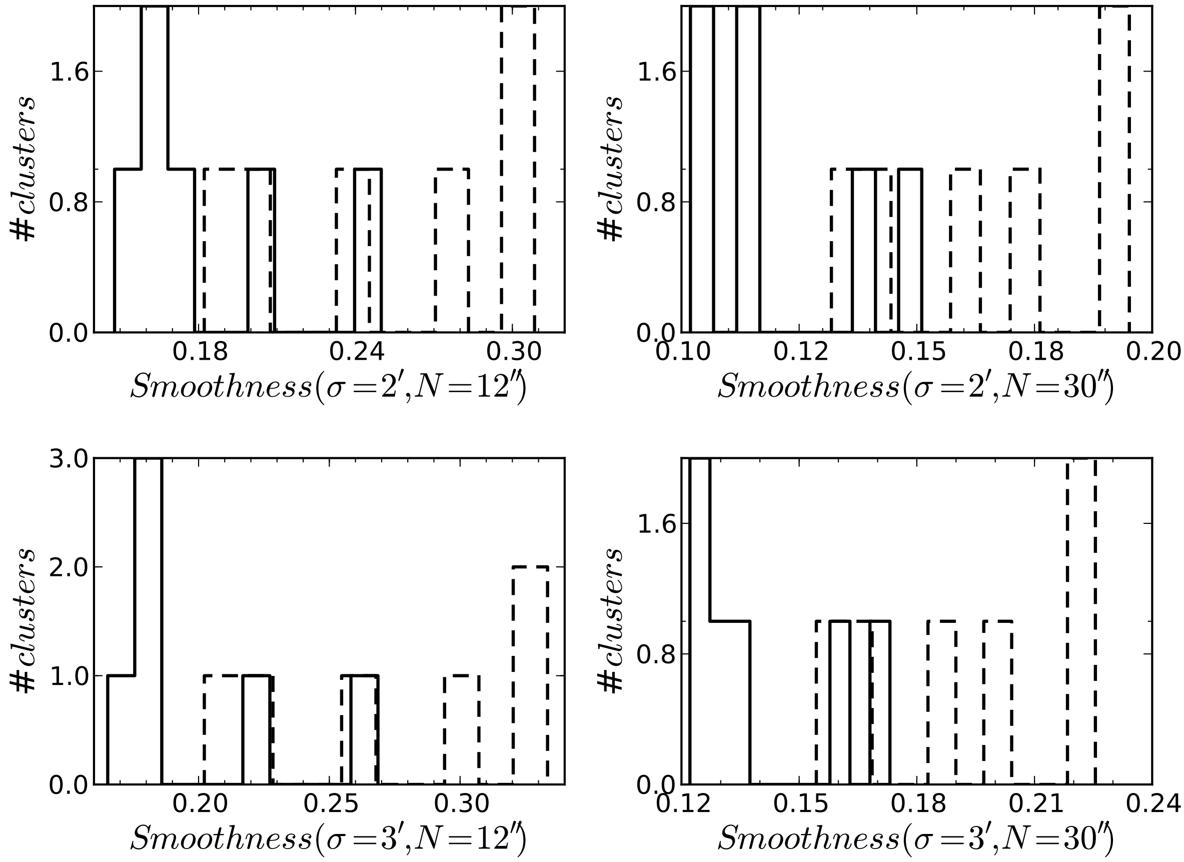

Figure 2.16: Distribution of the Smoothness parameter calculated for the MARX simulated clusters at different exposure times. We used two different Gaussian kernel sizes of σ to smooth the cluster image. N shows the initial smoothing size of the cluster input image.

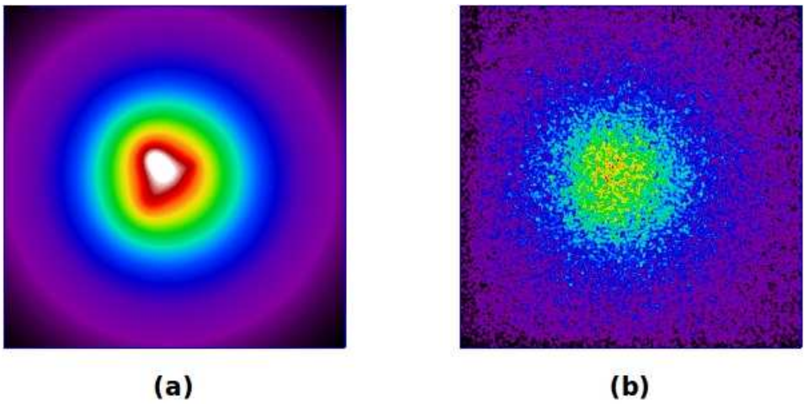
(a) **(b)**

Figure 2.17: (a) Beta model simulated sub-clumps cluster. (b) Fig. 2.17(a) re-simulated with the MARX.

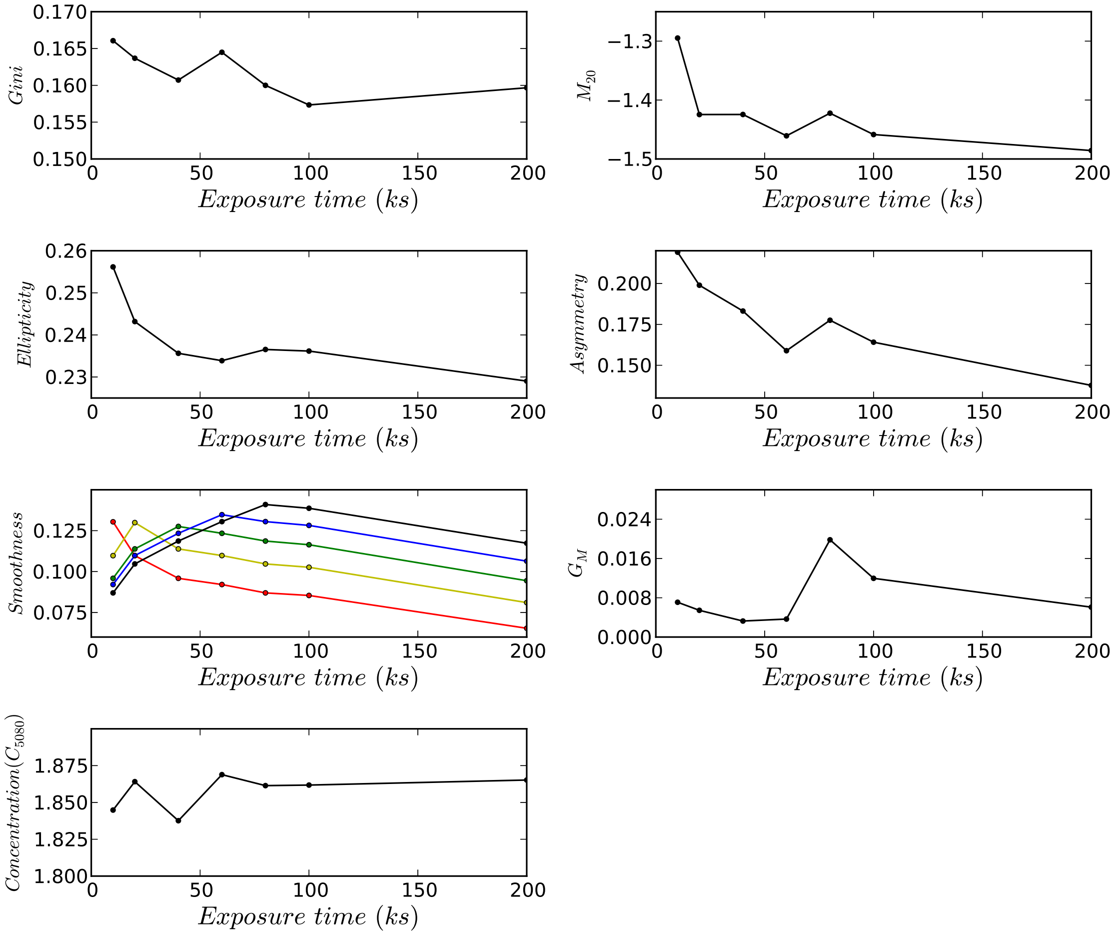

Figure 2.18: Morphology parameters calculated for the simulated sub-clumps cluster. Parameters are plotted against different exposure times (see text for details).

2.9 Discussion and Conclusion

We tested seven morphology parameters (Gini, M_{20}, Concentration, Asymmetry, Smoothness, Ellipticity and Gini of the second order moment) typically used for galaxy classification, to distinguish between simple 2-D Beta model simulated relaxed and non-relaxed galaxy clusters. The Beta model is quite useful in fitting the observed X-ray surface brightness radial profile, and this surface brightness distribution has been widely used to describe X-ray galaxy clusters (Arnaud, 2009). We found that Gini, M_{20}, Concentration, Smoothness and Asymmetry parameters can separate relaxed and non-relaxed simulated clusters. These parameters also trace the structural properties of galaxy clusters while identifying sub-structure into galaxy clusters.

We also investigated the effects of noise and redshift on the simulations. To test these effects, we simply added Poisson noise into the Beta model simulated clusters, and re-binned cluster images according to the angular bin size of corresponding redshift. These parameters, with the exception of Smoothness and Asymmetry, are very robust against low S/N cluster images and high redshift clusters. This suggests that morphology parameters can be used for the study of the dynamical state of distant clusters.

Finally, we subsequently passed these simulated clusters through the MARX software to mimic the *Chandra* telescope observations. From this simulation work, the morphology parameters proved to be a promising tool to separate relaxed and non-relaxed clusters (with added instruments effects). This encouraged us to extend the work to real data. However, not all the parameters are useful when clusters in a given sample have different exposure times. Specifically, Smoothness and Asymmetry are not capable of distinguishing different dynamical states of clusters when exposure time is different for each sample cluster. Both of these parameters systematically change with different exposure times. Only Gini, M_{20} and Concentration parameters are robust in this condition. In the next Chapter we will show this effect for real X-ray data.

3

Morphology parameters for *Chandra* observed clusters

3.1 Background

In Chapter 2 we showed that morphology parameters are useful in the study of dynamical state, substructure and morphology of (Beta model) simulated clusters. We showed further that these parameters could also be helpful when we added real observational effects to the simulations. This outcome gave us confidence in applying these parameters to real X-ray data and to putting forward applications of these parameter sets. This serves our two purposes: (1) to analyse the morphology of a large number of real clusters, study the dynamical state of each cluster, and classify relaxed (cool core) and non-relaxed (non-cool core) clusters; and (2) to investigate a possible correlation between X-ray cluster properties and morphology. To answer these two questions, in this Chapter we will evaluate the application of morphology parameters for real *Chandra* telescope observed X-ray galaxy clusters.

3.2 Sample selection and data reduction

3.2.1 *Chandra* sample

Our first goal was to determine the effectiveness of the parameters introduced in Chapter 2 for separating relaxed (cool core) and non-relaxed (non-cool core) clusters. Generally, cool core clusters are considered to be relaxed systems, while non-cool core clusters, in which the core of the cluster is erased or destroyed, are merger systems. In order to study the degree of dynamical activity in galaxy clusters, we then required high quality data, particularly for high-z clusters.

For our analysis, our initial aim was to simply separate known relaxed and non-relaxed clusters within our sample. Burenin et al. (2007) compiled a 400 deg^2 galaxy cluster catalogue based on the ROSAT PSPC survey. They detected a large number of extended X-ray sources with $f > 1.4\times10^{-13}$ erg s^{-1} cm^{-2} in the soft (0.5–2 keV) band. They compared all their detections with their optical counterparts, and confirmed 266 out of 283 as galaxy clusters. From this catalogue, a subsample of the low- and high-z galaxy clusters has been observed with the *Chandra* X-ray

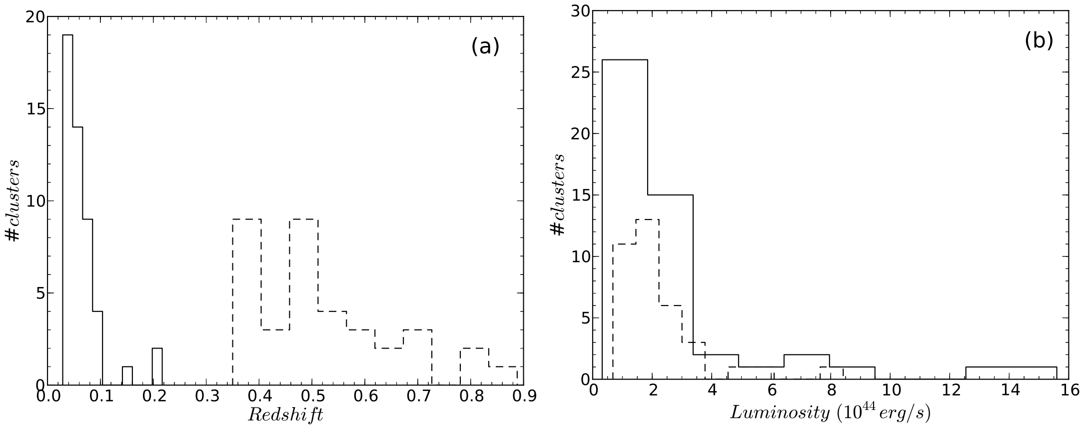

Figure 3.1: (a) Redshift and (b) luminosity distribution for low- and high-z clusters (from the V09). Solid line = low-z; and dashed line = high-z clusters.

telescope (V09). This sample includes a total of 49 low-z ($0.02 < z < 0.3$) and 36 high-z ($0.3 < z < 0.9$) galaxy clusters. Fig. 3.1a shows the distribution of redshift, while Fig. 3.1b shows the luminosity distribution. In this plot, median $z = 0.0853$ and median luminosity = 1.8 $\times 10^{44}$(erg/s) (0.5–2 keV). Tables 3.1 and 3.2 list the low- and high-z samples of galaxy clusters, respectively.

V09 study supplies essential information for each cluster, such as luminosity, temperature, mass and dynamical states. These properties of clusters are useful in comparison with their X-ray morphology. The total X-ray luminosity is calculated over the 0.5–2 keV band from accurate *Chandra* flux. The average temperature is measured from the spectrum integrated over a [0.15-1]R_{500} annulus.

Vikhlinin et al. (2007) classified cooling flow (relaxed) and non-cooling flow (non-relaxed) clusters using a surface brightness "cuspiness" parameter, by fitting a gas density model to the observed X-ray surface brightness. The cuspiness parameter is defined as

$$\alpha \equiv -\frac{d\,log(n)}{d\,log(r)}, \tag{3.1}$$

where n is the electron density, and r is the distance from the centre of galaxy cluster for which $r = 0.04\ R_{500}$, R_{500} being the radius defined as that enclosing a region with an over-density $\triangle$ = 500 times the critical density at the cluster redshift. This radius is chosen to be small enough to accommodate strong cooling effects, but it is also sufficient to avoid the gas density profile flattening due to central AGN feedback. Relaxed and non-relaxed clusters have different surface brightness profiles. In relaxed systems, the central peak density causes a 'cusp' in the surface brightness profile, which causes the high value of the profile's slope (high α value). In non-relaxed systems, the surface brightness profile is flattened, which gives a low α value. Therefore, based on this surface brightness profile, it is possible to separate relaxed and non-relaxed clusters. Furthermore, Vikhlinin et al. (2007) divided galaxy clusters based on the cuspiness parameter with $\alpha > 0.7$ for relaxed clusters, $0.5 < \alpha < 0.7$ for intermediate systems, and $\alpha < 0.5$ for non-relaxed clusters. The V09 used the cuspiness parameter to quantify the dynamical state of each cluster, and they chose a boundary value of $\alpha = 0.5$, which means that relaxed clusters have $\alpha > 0.5$. Based on

Table 3.1: Low-z (0.02–0.3) cluster sample from the V09. (1) cluster name; (2) redshift; (3) total X-ray flux (0.5–2 keV); (4) total X-ray luminosity (0.5–2 keV); (5) average temperature in $[0.15\text{-}1]R_{500}$ annulus; (6) dynamical state (a) (according to the V09); (7) dynamical state (b) (combination of morphology parameters) (SR = strong relaxed, R = relaxed, NR = non-relaxed, SNR = strong non-relaxed); (8) exposure time.

Name	z	flux (10^{-11}cgs)	Luminosity (erg s^{-1})	Temperature (keV)	Dynamical state (a)	Dynamical state (b)	Exposure time ks
A3571	0.0386	7.42	2.37×10^{44}	6.81 ± 0.10	R	NR	31.224
A2199	0.0304	6.43	1.27×10^{44}	3.99 ± 0.10	R	NR	17.787
2A-0335	0.0346	6.24	1.60×10^{44}	3.43 ± 0.10	R	SR	19.716
A496	0.0328	5.33	1.23×10^{44}	4.12 ± 0.07	R	NR	88.878
A3667	0.0557	4.64	3.14×10^{44}	6.33 ± 0.06	M	NR	60.403
A754	0.0542	4.35	2.78×10^{44}	8.73 ± 0.00	M	SNR	43.972
A85	0.0557	4.30	2.91×10^{44}	6.45 ± 0.10	R	NR	38.201
A2029	0.0779	4.23	5.72×10^{44}	8.22 ± 0.16	R	SR	10.739
A478	0.0881	4.16	7.24×10^{44}	7.96 ± 0.27	R	SR	42.393
A1795	0.0622	4.14	3.52×10^{44}	6.14 ± 0.10	R	SR	91.301
A3558	0.0469	4.11	1.96×10^{44}	4.88 ± 0.10	M	NR	14.024
A2142	0.0904	3.94	7.20×10^{44}	10.04 ± 0.26	R	NR	44.367
A2256	0.0581	3.61	2.66×10^{44}	8.37 ± 0.24	M	SNR	11.647
A4038	0.0288	3.48	6.18×10^{43}	2.61 ± 0.05	R	NR	33.523
A2147	0.0355	3.47	9.40×10^{43}	3.83 ± 0.12	M	SNR	17.879
A3266	0.0602	3.39	2.69×10^{44}	8.63 ± 0.18	M	SNR	29.289
A401	0.0743	3.19	3.90×10^{44}	7.72 ± 0.30	R	NR	18.005
A2052	0.0345	2.93	7.47×10^{43}	3.03 ± 0.07	R	NR	36.754
Hydra-A	0.0549	2.91	1.93×10^{44}	3.64 ± 0.06	R	R	89.809
A119	0.0445	2.47	1.06×10^{44}	5.72 ± 0.00	M	NR	11.537
A2063	0.0342	2.39	5.98×10^{43}	3.57 ± 0.19	R	NR	8.777
A1644	0.0475	2.33	1.14×10^{44}	4.61 ± 0.14	M	NR	18.712
A3158	0.0583	2.30	1.72×10^{44}	4.67 ± 0.07	R	NR	30.921
MKW3s	0.0453	2.08	9.28×10^{43}	3.03 ± 0.05	R	NR	57.123
A1736	0.0449	2.04	8.94×10^{43}	2.95 ± 0.09	M	SNR	14.918
EXO 0422	0.0382	2.01	6.35×10^{43}	2.84 ± 0.09	R	R	10.001
A4059	0.0491	2.00	1.05×10^{44}	4.25 ± 0.08	R	NR	13.236
A3395	0.0506	1.95	1.09×10^{44}	5.10 ± 0.17	M	SNR	21.094
A2589	0.0411	1.94	7.09×10^{43}	3.17 ± 0.27	R	NR	13.478
A3112	0.0759	1.89	2.43×10^{44}	5.19 ± 0.21	R	R	15.466
A3562	0.0489	1.84	9.58×10^{43}	4.31 ± 0.12	R	NR	19.283
A1651	0.0853	1.80	2.93×10^{44}	6.41 ± 0.25	R	NR	9.643
A399	0.0713	1.78	2.01×10^{44}	6.49 ± 0.17	M	NR	48.575
A2204	0.1511	1.74	9.35×10^{44}	8.55 ± 0.58	R	SR	9.609
A576	0.0401	1.72	5.99×10^{43}	3.68 ± 0.11	R	NR	29.078
A2657	0.0402	1.62	5.66×10^{43}	3.62 ± 0.15	R	NR	16.148
A2634	0.0305	1.61	3.20×10^{43}	2.96 ± 0.09	R	-	49.528
A3391	0.0551	1.58	1.05×10^{44}	5.39 ± 0.19	R	NR	17.461
A2065	0.0723	1.56	1.82×10^{44}	5.44 ± 0.09	M	NR	49.416
A1650	0.0823	1.53	2.33×10^{44}	5.29 ± 0.17	R	R	27.258
A3822	0.0760	1.48	1.91×10^{44}	5.23 ± 0.30	M	NR	8.067
S 1101	0.0564	1.46	1.03×10^{44}	2.44 ± 0.08	R	R	9.946
A2163	0.2030	1.38	1.37×10^{45}	14.72 ± 0.31	M	NR	71.039
ZwCl1215	0.0767	1.38	1.80×10^{44}	6.54 ± 0.21	R	NR	11.999
RX J1504	0.2169	1.35	1.56×10^{45}	9.89 ± 0.53	R	SR	13.290
A2597	0.0830	1.35	2.09×10^{44}	3.87 ± 0.11	R	SR	26.414
A133	0.0569	1.35	9.60×10^{43}	4.01 ± 0.11	R	R	34.471
A2244	0.0989	1.34	2.98×10^{44}	5.37 ± 0.12	R	NR	56.964
A3376	0.0455	1.31	5.89×10^{43}	4.37 ± 0.13	M	NR	44.267

Table 3.2: As in Table 3.1, but for high-z (0.3–0.9) clusters.

Name	z	flux (10^{-13}cgs)	Luminosity (erg s^{-1})	Temperature (keV)	Dynamical state (a)	Dynamical state (b)	Exposure time ks
0302-0423	0.3501	15.34	5.24×10^{44}	4.78 ± 0.75	R	SR	100.41
1212+2733	0.3533	10.53	3.61×10^{44}	6.62 ± 0.89	M	NR	14.581
0350-3801	0.3631	1.68	6.80×10^{43}	2.45 ± 0.50	M	NR	23.733
0318-0302	0.3700	4.63	1.82×10^{44}	4.04 ± 0.63	M	NR	14.578
0159+0030	0.3860	3.30	1.42×10^{44}	4.25 ± 0.96	R	R	19.880
0958+4702	0.3900	2.22	1.04×10^{44}	3.57 ± 0.73	R	R	25.231
0809+2811	0.3990	5.40	2.50×10^{44}	4.17 ± 0.73	M	SNR	19.338
1416+4446	0.4000	4.01	1.94×10^{44}	3.26 ± 0.46	R	NR	29.187
1312+3900	0.4037	2.71	1.37×10^{44}	3.72 ± 1.06	M	SNR	26.421
1003+3253	0.4161	3.04	1.53×10^{44}	5.44 ± 1.40	R	R	19.859
0141-3034	0.4423	2.06	1.32×10^{44}	2.13 ± 0.38	M	SNR	28.273
1701+6414	0.4530	3.91	2.39×10^{44}	4.36 ± 0.46	R	R	49.294
1641+4001	0.4640	1.43	9.46×10^{43}	3.31 ± 0.62	R	NR	45.345
0522-3624	0.4720	1.47	1.04×10^{44}	3.46 ± 0.48	M	NR	45.999
1222+2709	0.4720	1.39	9.88×10^{43}	3.74 ± 0.61	R	NR	49.117
0355-3741	0.4730	2.48	1.76×10^{44}	4.61 ± 0.82	R	R	27.190
0853+5759	0.4750	1.22	8.43×10^{43}	3.42 ± 0.67	M	NR	42.179
0333-2456	0.4751	1.33	9.79×10^{43}	3.16 ± 0.58	M	NR	34.160
0926+1242	0.4890	2.04	1.50×10^{44}	4.74 ± 0.71	M	NR	18.620
0030+2618	0.5000	2.09	1.57×10^{44}	5.63 ± 1.13	M	NR	57.362
1002+6858	0.5000	2.19	1.71×10^{44}	4.04 ± 0.83	M	NR	19.786
1524+0957	0.5160	2.45	2.07×10^{44}	4.23 ± 0.51	M	SNR	49.886
1357+6232	0.5250	1.90	1.63×10^{44}	4.60 ± 0.69	R	NR	43.862
1354-0221	0.5460	1.45	1.40×10^{44}	3.77 ± 0.53	M	NR	55.039
1120+2326	0.5620	1.68	1.79×10^{44}	3.58 ± 0.44	M	SNR	70.262
0956+4107	0.5870	1.64	1.85×10^{44}	4.40 ± 0.50	M	NR	40.165
0328-2140	0.5901	2.09	2.30×10^{44}	5.14 ± 1.47	R	NR	56.192
1120+4318	0.6000	3.24	3.75×10^{44}	4.99 ± 0.30	R	NR	19.837
1334+5031	0.6200	1.76	2.22×10^{44}	4.31 ± 0.28	M	NR	19.492
0542-4100	0.6420	2.21	2.91×10^{44}	5.45 ± 0.77	M	NR	50.008
1202+5751	0.6775	1.34	2.22×10^{44}	4.08 ± 0.72	M	SNR	57.210
0405-4100	0.6861	1.33	2.23×10^{44}	3.98 ± 0.48	M	NR	77.163
1221+4918	0.7000	2.06	3.35×10^{44}	6.63 ± 0.75	M	NR	78.887
0230+1836	0.7990	1.09	2.55×10^{44}	5.50 ± 1.02	M	SNR	67.178
0152-1358	0.8325	2.24	5.46×10^{44}	5.40 ± 0.97	M	NR	36.285
1226+3332	0.8880	3.27	8.42×10^{44}	11.08 ± 1.39	M	NR	64.21

this classification, we used 49 (34 relaxed + 15 non-relaxed) low-z clusters and 36 (12 relaxed + 24 non-relaxed) high-z clusters, a total of 46 relaxed and 39 non-relaxed clusters.

There are three high-z and two low-z clusters that have multiple components in their images.

- There are two subclumps visible in the high redshift 1701+6414 cluster. We used the North clump in our calculation. The other clump (in the S-W) is a foreground low-z X-ray cluster, confirmed by the NED database.

- In the case of the high redshift system 1641+4001, there is a small clump (foreground galaxy) in the S-W, which we excluded from our analysis.

- Double components are visible in the 0328-2140 system. One is in the East and the other in the West, the latter being a low redshift interloper. We used the high redshift East cluster.

- In A85, we focused on only the main North relaxed cluster, excluding the small southern clump (Kempner et al., 2002).

- In A1644 we excluded the small North component, and focused on the main larger southern cluster only (Johnson et al., 2010; Reiprich et al., 2004).

3.2.2 *Chandra* data reduction and image preparation

In our sample, each cluster had at least 1500–2000 photons (V09), which ensured good S/N. We visually checked all these clusters, and verified both that there was no cluster emission close to the CCD edges, and that the S/N was sufficient. In addition, we selected only those clusters whose emission was not too close to the CCD gaps. This inspection revealed that the relaxed cluster A2634 (Obs-Id 4816, ACIS-S) alone had low total counts. It was therefore excluded from our sample.

We processed all *Chandra* archival data with CIAO version 4.3 and CALDB version 4.4.6. We first used the `chandra_repro` task to reprocess all ACIS imaging data. This script creates a new second level event file as well as a bad pixel file by reading the data from the standard *Chandra* data distribution (which contains primary and secondary data files). This step applies the latest charge transfer inefficiency (CTI) correction, the latest time-dependent gain adjustment, the latest gain map, PHA and pixel randomisation, it cleans the VFAINT background (if any), and uses continuous clocking mode times of arrival. After reprocessing, we removed any high background flares (3σ clipping) with the task `lc_sigma_clip` routine and then attached the good time interval (GTI) file to the events. All of our event files included the 0.3–7 keV broad energy band. We binned each event file with $\sim 2''$ pixels. We detected point sources using the `wavdetect` task* with scale = 1, 2, 4, 8 and 16, which would be a reasonable default for *Chandra* data. This task uses the wavelets of various user defined scales to correlate it with a given cluster image and then explore the outcome for substantial correlation. The function of `wavdetect` is divided into two steps: first to determine probable source pixels within a given image by repeatedly correlating it with "Mexican Hat" wavelet functions with different user defined scale sizes; second to make a source list based on each wavelet scale. For each source, a cell is calculated that has most of the flux; and source

---

*http://cxc.harvard.edu/ciao4.3/threads/wavdetect/

properties are calculated within that cell. We then selected elliptical background annuli (twice the point source detected region) around each detected point source. Then we removed the point sources using the `dmfilth` task*, which replaces pixel values in selected source regions of an image with values interpolated from the surrounding background region. By setting randseed = 123, we used the POISSON interpolation method, which randomly samples values in the selected source regions from the Poisson distribution, whose mean is that of the pixel values in the background region. We took care not to remove point sources which were detected close to the cluster centre. We also aimed to study the effect of point sources on parameters, hence we calculated morphology parameters for both images, i.e. the one with point sources, the other without point sources. For creating the exposure map we used the `fluximage` task† with broad band energy (0.3–7 keV), then divided the counts image by the exposure map to remove the CCD gaps, CCD edge, vignetting, and telescope effects. This task generates the aspect histogram, instrument and exposure maps, automatically. We also used the `dmimgthresh` task to perform a 5% total counts cut to enable uniform exposure everywhere in the image. Two or more of the available multiple observations were combined to make a single image. In each image, 1 pix. is $\sim 2''$. Finally we smoothed the cluster images with a $\sigma = 10''$ Gaussian width (5 pix.). Smoothing is very important in calculating the Gini coefficient, because there will be zero count pixels in the unsmoothed image, which will not contribute to the flux distribution calculation and will change the Gini value greatly. For calculating the Smoothness parameter, we initially used unsmoothed cluster images.

Because of limited *FOV* of *Chandra*, in the study of nearby clusters, we decided to use a fixed circular aperture size over which morphology parameters are calculated for individual clusters (200 kpc for $z < 0.05$ and 500 kpc for $z > 0.05$) with sufficient area, and to retain consistency with our morphology parameter calculations on the same relative scale. The possible effects of aperture size are discussed in § 3.4.2.

3.3 Morphology parameter results

3.3.1 Distribution of morphology parameters

We calculated the morphology parameters (Gini, M_{20}, Concentration, Asymmetry, Smoothness, Ellipticity and Gini of the second order moment) for the *Chandra* sample. It is worth noting that, as a starting point, we adopted the classification of galaxy clusters based on the V09. We mentioned earlier, in § 3.2.1, that the V09 used the 'cuspiness' parameter to separate relaxed and non-relaxed clusters based on calculation of the X-ray gas density profiles of galaxy clusters.

Fig. 3.2 shows the distribution of parameters for our sample of 84 clusters. Except for three parameters, Gini, M_{20} and Concentration, most of the parameters show a similar distribution for relaxed and non-relaxed clusters. The Smoothness parameter separates the two peaks of relaxed and non-relaxed clusters towards low Smoothness and high Smoothness, respectively, but there are large numbers of clusters in the overlap region. Initially, we chose a Gaussian smoothing kernel of $\sigma = 10''$ as an arbitrary scale with which to smooth the cluster image. To further investigate the Smoothness parameter, we (1) varied the σ value between $0.5' to 1'$, and (2) varied the smoothing

---

[*] http://cxc.harvard.edu/ciao4.3/threads/diffuse emission/

[†] http://cxc.harvard.edu/ciao/ahelp/fluximage.html

size of input cluster images (initial smoothing) on the Smoothness parameter (see § 3.3.3). For the Gini and Concentration parameters, non-relaxed clusters are distributed towards low values of Gini and Concentration and, oppositely, relaxed clusters are characterised by high Gini and Concentration values. A similar trend is visible for the M_{20}, but the extreme of the relaxed clusters is on the left hand side (low M_{20} values) and the extreme of the non-relaxed clusters is on the right hand side (high M_{20} values). Table 3.3 and Table 3.4 list all parameter values together with 1σ uncertainty (Chapter 2, § 2.2.5) for relaxed and non-relaxed clusters, respectively.

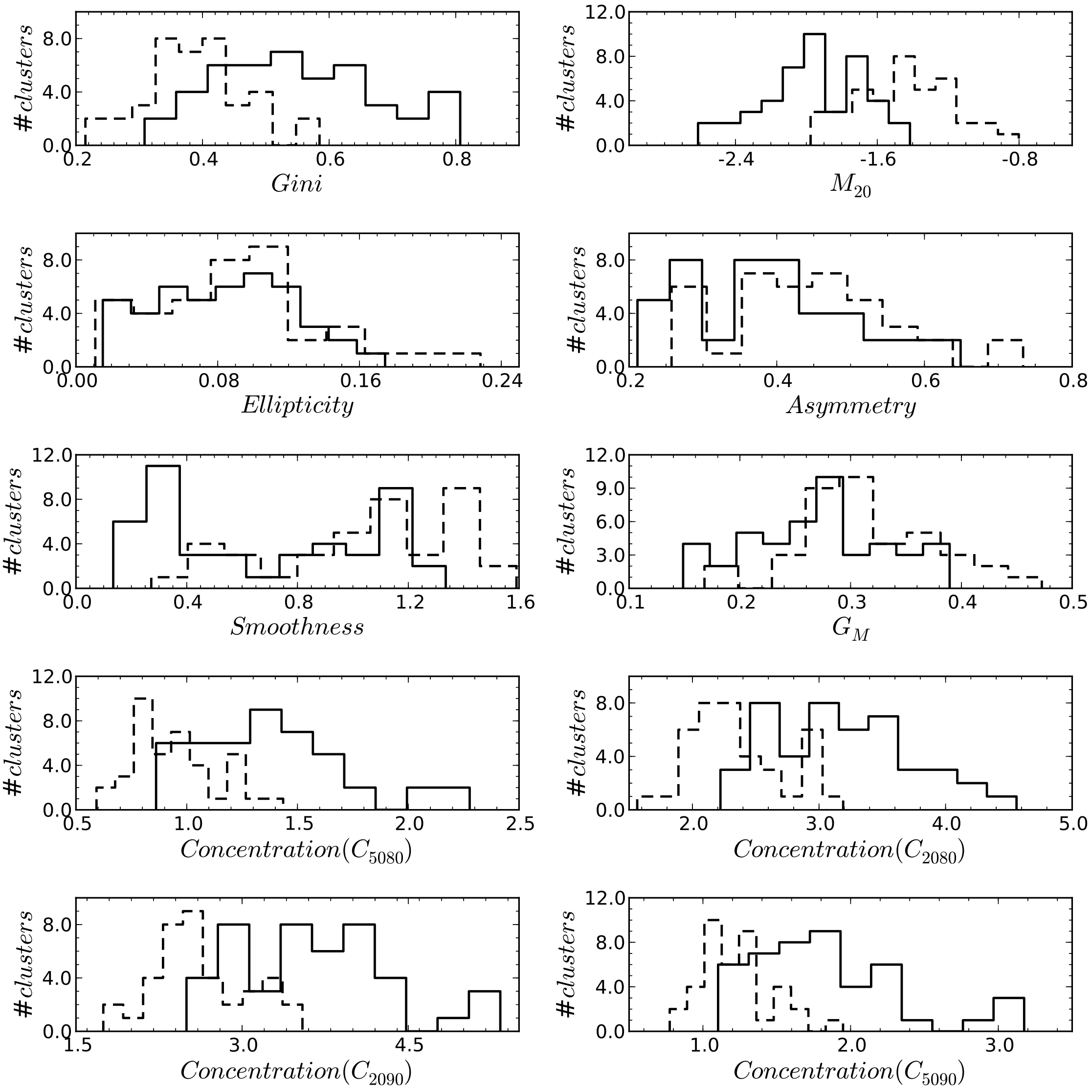

Figure 3.2: Seven morphology parameter distributions: solid line = relaxed cluster; dashed line = non-relaxed cluster. All four definitions of the Concentration parameter are displayed. Galaxy cluster separation (i.e. relaxed vs non-relaxed systems) is based on the V09.

Table 3.3: Morphology parameters value of relaxed clusters (V09). Values are listed with appropriate uncertainties of 1σ for each parameter.

Cluster name	Gini	M_{20}	Concentration	Asymmetry	Smoothness	G_M	Ellipticity
A3571	0.357 ± 0.001	-1.492 ± 0.014	2.558 ± 0.002	0.293 ± 0.007	0.284 ± 0.000	0.259 ± 0.001	0.084 ± 0.000
A2199	0.612 ± 0.002	-1.897 ± 0.009	3.427 ± 0.010	0.502 ± 0.022	0.329 ± 0.000	0.378 ± 0.002	0.083 ± 0.000
A0335	0.666 ± 0.002	-2.123 ± 0.053	5.343 ± 0.021	0.341 ± 0.013	0.321 ± 0.000	0.209 ± 0.002	0.082 ± 0.000
A496	0.564 ± 0.001	-1.667 ± 0.025	3.610 ± 0.024	0.577 ± 0.010	0.205 ± 0.000	0.284 ± 0.000	0.063 ± 0.000
A85	0.624 ± 0.002	-1.779 ± 0.035	4.256 ± 0.012	0.633 ± 0.008	0.464 ± 0.000	0.279 ± 0.001	0.026 ± 0.000
A478	0.703 ± 0.002	-2.145 ± 0.041	4.746 ± 0.011	0.286 ± 0.040	0.248 ± 0.000	0.279 ± 0.001	0.137 ± 0.000
A1795	0.779 ± 0.001	-2.148 ± 0.024	4.749 ± 0.016	0.351 ± 0.022	0.143 ± 0.000	0.389 ± 0.001	0.107 ± 0.000
A4038	0.503 ± 0.001	-1.929 ± 0.009	3.797 ± 0.008	0.297 ± 0.017	0.563 ± 0.000	0.206 ± 0.000	0.140 ± 0.000
A2052	0.622 ± 0.001	-1.934 ± 0.038	3.913 ± 0.031	0.649 ± 0.029	0.308 ± 0.000	0.332 ± 0.002	0.086 ± 0.000
Hydra-A	0.543 ± 0.003	-2.087 ± 0.034	4.780 ± 0.019	0.258 ± 0.032	0.152 ± 0.000	0.149 ± 0.004	0.060 ± 0.000
A2063	0.376 ± 0.001	-1.729 ± 0.008	2.940 ± 0.002	0.403 ± 0.010	1.156 ± 0.000	0.281 ± 0.000	0.046 ± 0.000
A3158	0.470 ± 0.001	-1.767 ± 0.005	3.210 ± 0.007	0.267 ± 0.004	0.788 ± 0.000	0.232 ± 0.000	0.118 ± 0.000
MKW3s	0.509 ± 0.002	-1.988 ± 0.018	3.785 ± 0.006	0.222 ± 0.028	0.317 ± 0.000	0.173 ± 0.001	0.134 ± 0.000
EXO0422	0.622 ± 0.003	-2.304 ± 0.019	4.795 ± 0.008	0.355 ± 0.030	0.911 ± 0.000	0.254 ± 0.000	0.071 ± 0.000
A4059	0.424 ± 0.001	-1.747 ± 0.014	3.264 ± 0.007	0.211 ± 0.013	0.135 ± 0.000	0.167 ± 0.001	0.093 ± 0.000
A2589	0.381 ± 0.001	-1.415 ± 0.014	2.534 ± 0.017	0.471 ± 0.004	0.669 ± 0.000	0.317 ± 0.001	0.045 ± 0.000
A3112	0.544 ± 0.004	-2.121 ± 0.040	4.175 ± 0.013	0.276 ± 0.063	0.309 ± 0.000	0.170 ± 0.003	0.143 ± 0.000
A1651	0.569 ± 0.001	-1.957 ± 0.008	3.885 ± 0.011	0.354 ± 0.009	1.001 ± 0.000	0.266 ± 0.000	0.075 ± 0.000
A576	0.308 ± 0.002	-1.651 ± 0.010	2.546 ± 0.004	0.267 ± 0.001	0.606 ± 0.000	0.251 ± 0.001	0.050 ± 0.000
A2657	0.380 ± 0.001	-1.607 ± 0.018	2.934 ± 0.012	0.402 ± 0.011	1.034 ± 0.000	0.250 ± 0.001	0.048 ± 0.000
A3391	0.408 ± 0.001	-1.549 ± 0.003	2.801 ± 0.003	0.431 ± 0.003	1.335 ± 0.000	0.332 ± 0.000	0.115 ± 0.000
A1650	0.673 ± 0.002	-1.869 ± 0.038	4.031 ± 0.006	0.429 ± 0.018	0.476 ± 0.000	0.379 ± 0.002	0.122 ± 0.000
S1101	0.645 ± 0.002	-2.111 ± 0.019	4.592 ± 0.017	0.238 ± 0.032	0.461 ± 0.000	0.172 ± 0.003	0.110 ± 0.000
zwcl1215	0.439 ± 0.001	-1.625 ± 0.004	3.059 ± 0.001	0.369 ± 0.002	1.204 ± 0.000	0.294 ± 0.000	0.120 ± 0.000
A2597	0.781 ± 0.002	-2.426 ± 0.076	6.698 ± 0.048	0.397 ± 0.077	0.295 ± 0.000	0.277 ± 0.001	0.152 ± 0.000
A133	0.508 ± 0.004	-2.201 ± 0.031	4.230 ± 0.006	0.254 ± 0.040	0.320 ± 0.000	0.179 ± 0.002	0.094 ± 0.000
A2244	0.638 ± 0.002	-1.983 ± 0.020	4.249 ± 0.005	0.266 ± 0.039	0.314 ± 0.000	0.219 ± 0.003	0.030 ± 0.000

Continued on next page

Table 3.3 – *Continued from previous page*

Cluster name	Gini	M_{20}	Concentration	Asymmetry	Smoothness	G_M	Ellipticity
RXJ1504	0.807 ± 0.005	-2.471 ± 0.084	6.260 ± 0.043	0.397 ± 0.141	0.370 ± 0.000	0.242 ± 0.005	0.124 ± 0.000
A2204	0.732 ± 0.006	-2.611 ± 0.110	6.041 ± 0.007	0.361 ± 0.089	0.545 ± 0.000	0.208 ± 0.002	0.051 ± 0.000
A2029	0.718 ± 0.002	-2.088 ± 0.046	4.714 ± 0.025	0.445 ± 0.033	0.163 ± 0.000	0.280 ± 0.001	0.113 ± 0.000
A2142	0.564 ± 0.001	-1.959 ± 0.011	3.887 ± 0.021	0.365 ± 0.020	0.329 ± 0.000	0.239 ± 0.000	0.174 ± 0.000
A3562	0.541 ± 0.001	-1.870 ± 0.005	3.542 ± 0.005	0.542 ± 0.004	1.211 ± 0.000	0.384 ± 0.001	0.107 ± 0.000
A401	0.439 ± 0.001	-1.734 ± 0.003	3.262 ± 0.002	0.222 ± 0.002	0.739 ± 0.000	0.205 ± 0.000	0.102 ± 0.000
0302-0423	0.796 ± 0.008	-2.511 ± 0.114	6.428 ± 0.183	0.322 ± 0.188	0.767 ± 0.000	0.345 ± 0.006	0.071 ± 0.000
0159+0030	0.559 ± 0.008	-2.288 ± 0.048	4.504 ± 0.065	0.597 ± 0.090	1.198 ± 0.000	0.334 ± 0.001	0.022 ± 0.000
0958+4702	0.550 ± 0.004	-2.165 ± 0.021	4.241 ± 0.015	0.416 ± 0.074	1.310 ± 0.000	0.354 ± 0.003	0.015 ± 0.000
1416+4446	0.528 ± 0.009	-1.972 ± 0.079	4.240 ± 0.031	0.553 ± 0.033	1.009 ± 0.000	0.274 ± 0.002	0.103 ± 0.000
1003+3253	0.595 ± 0.008	-2.369 ± 0.069	5.140 ± 0.039	0.451 ± 0.059	1.166 ± 0.000	0.353 ± 0.002	0.100 ± 0.000
1701+6414	0.479 ± 0.009	-2.017 ± 0.105	3.766 ± 0.020	0.513 ± 0.086	0.878 ± 0.000	0.240 ± 0.004	0.096 ± 0.000
1641+4001	0.481 ± 0.006	-1.913 ± 0.025	3.966 ± 0.042	0.349 ± 0.034	1.166 ± 0.000	0.282 ± 0.001	0.042 ± 0.000
1222+2709	0.444 ± 0.006	-1.983 ± 0.042	3.568 ± 0.035	0.412 ± 0.027	1.200 ± 0.000	0.301 ± 0.002	0.036 ± 0.000
0355-3741	0.497 ± 0.005	-2.031 ± 0.037	4.109 ± 0.031	0.429 ± 0.041	1.182 ± 0.000	0.303 ± 0.002	0.058 ± 0.000
1357+6232	0.419 ± 0.003	-1.696 ± 0.023	3.075 ± 0.005	0.385 ± 0.033	0.945 ± 0.000	0.262 ± 0.002	0.019 ± 0.000
0328-2140	0.430 ± 0.004	-1.767 ± 0.068	3.141 ± 0.015	0.480 ± 0.075	0.944 ± 0.000	0.281 ± 0.004	0.073 ± 0.000
1120+4318	0.506 ± 0.005	-1.665 ± 0.038	3.531 ± 0.040	0.506 ± 0.062	1.149 ± 0.000	0.287 ± 0.001	0.061 ± 0.000

Table 3.4: Morphology parameters value of (V09) non-relaxed clusters. Values are listed with appropriate uncertainties of 1σ for each parameter.

Cluster name	Gini	M_{20}	Concentration	Asymmetry	Smoothness	G_M	Ellipticity
A3558	0.327 ± 0.001	-1.448 ± 0.017	2.547 ± 0.012	0.358 ± 0.007	0.520 ± 0.000	0.276 ± 0.001	0.117 ± 0.000
A2147	0.268 ± 0.001	-1.243 ± 0.003	2.216 ± 0.006	0.359 ± 0.005	1.188 ± 0.000	0.305 ± 0.000	0.083 ± 0.000
A3266	0.220 ± 0.001	-1.196 ± 0.020	2.110 ± 0.014	0.276 ± 0.007	0.514 ± 0.000	0.279 ± 0.001	0.103 ± 0.000
A119	0.417 ± 0.001	-1.158 ± 0.001	2.275 ± 0.003	0.574 ± 0.002	1.542 ± 0.000	0.434 ± 0.000	0.063 ± 0.000
A1644	0.352 ± 0.001	-1.843 ± 0.014	2.823 ± 0.012	0.381 ± 0.014	0.843 ± 0.000	0.273 ± 0.001	0.043 ± 0.000
A1736	0.215 ± 0.001	-0.932 ± 0.001	1.803 ± 0.002	0.415 ± 0.005	1.379 ± 0.000	0.352 ± 0.001	0.011 ± 0.000
A3395	0.394 ± 0.001	-0.801 ± 0.001	1.743 ± 0.006	0.734 ± 0.006	1.411 ± 0.000	0.473 ± 0.001	0.228 ± 0.000
A2065	0.477 ± 0.001	-1.697 ± 0.017	3.581 ± 0.003	0.402 ± 0.002	0.549 ± 0.000	0.230 ± 0.001	0.149 ± 0.000
A3822	0.450 ± 0.001	-1.542 ± 0.008	3.073 ± 0.007	0.536 ± 0.009	1.450 ± 0.000	0.370 ± 0.000	0.119 ± 0.000
A3667	0.435 ± 0.000	-1.590 ± 0.004	2.701 ± 0.005	0.302 ± 0.005	0.536 ± 0.000	0.285 ± 0.001	0.079 ± 0.000
A754	0.341 ± 0.000	-1.053 ± 0.005	2.347 ± 0.008	0.406 ± 0.003	0.524 ± 0.000	0.308 ± 0.000	0.202 ± 0.000
A2256	0.373 ± 0.000	-1.273 ± 0.003	2.634 ± 0.001	0.333 ± 0.002	1.024 ± 0.000	0.277 ± 0.000	0.133 ± 0.000
A399	0.389 ± 0.001	-1.439 ± 0.013	2.980 ± 0.005	0.372 ± 0.004	0.698 ± 0.000	0.229 ± 0.000	0.080 ± 0.000
A2163	0.378 ± 0.001	-1.443 ± 0.018	2.772 ± 0.031	0.281 ± 0.010	0.272 ± 0.000	0.196 ± 0.003	0.082 ± 0.000
A3376	0.413 ± 0.000	-1.183 ± 0.002	2.362 ± 0.002	0.564 ± 0.002	1.159 ± 0.000	0.397 ± 0.001	0.072 ± 0.000
1212+2733	0.417 ± 0.002	-1.670 ± 0.036	2.919 ± 0.007	0.388 ± 0.030	1.206 ± 0.000	0.293 ± 0.003	0.102 ± 0.000
0350-3801	0.465 ± 0.005	-1.734 ± 0.019	3.286 ± 0.024	0.591 ± 0.044	1.453 ± 0.000	0.386 ± 0.001	0.082 ± 0.000
0318-0302	0.554 ± 0.002	-1.631 ± 0.042	3.520 ± 0.026	0.532 ± 0.043	1.306 ± 0.000	0.339 ± 0.002	0.073 ± 0.000
0809+2811	0.366 ± 0.002	-1.334 ± 0.031	2.689 ± 0.039	0.449 ± 0.022	1.291 ± 0.000	0.309 ± 0.002	0.115 ± 0.000
1312+3900	0.322 ± 0.004	-1.359 ± 0.009	2.461 ± 0.016	0.507 ± 0.024	1.443 ± 0.000	0.354 ± 0.001	0.030 ± 0.000
0141-3034	0.347 ± 0.004	-0.961 ± 0.003	2.232 ± 0.018	0.623 ± 0.020	1.591 ± 0.000	0.432 ± 0.002	0.048 ± 0.000
0522-3624	0.444 ± 0.006	-1.429 ± 0.051	3.634 ± 0.021	0.471 ± 0.017	1.013 ± 0.000	0.307 ± 0.002	0.087 ± 0.000
0853+5759	0.418 ± 0.010	-1.294 ± 0.049	3.043 ± 0.038	0.715 ± 0.009	1.075 ± 0.000	0.331 ± 0.003	0.030 ± 0.000
0333-2456	0.414 ± 0.004	-1.435 ± 0.016	2.785 ± 0.010	0.462 ± 0.030	1.363 ± 0.000	0.341 ± 0.001	0.117 ± 0.000
0926+1242	0.506 ± 0.007	-1.764 ± 0.046	3.563 ± 0.036	0.558 ± 0.039	1.420 ± 0.000	0.399 ± 0.001	0.158 ± 0.000
0030+2618	0.258 ± 0.004	-1.639 ± 0.013	2.450 ± 0.024	0.258 ± 0.013	0.578 ± 0.000	0.282 ± 0.001	0.045 ± 0.000
1002+6858	0.474 ± 0.006	-1.914 ± 0.029	3.657 ± 0.026	0.475 ± 0.050	1.388 ± 0.000	0.362 ± 0.002	0.065 ± 0.000

Continued on next page

Table 3.4 – *Continued from previous page*

Cluster name	Gini	M_{20}	Concentration	Asymmetry	Smoothness	G_M	Ellipticity
1524+0957	0.343 ± 0.003	-1.343 ± 0.030	2.701 ± 0.043	0.366 ± 0.025	1.065 ± 0.000	0.262 ± 0.003	0.102 ± 0.000
1354-0221	0.343 ± 0.005	-1.481 ± 0.030	2.477 ± 0.026	0.477 ± 0.049	0.977 ± 0.000	0.308 ± 0.003	0.028 ± 0.000
1120+2326	0.367 ± 0.003	-1.237 ± 0.005	2.477 ± 0.016	0.439 ± 0.030	0.964 ± 0.000	0.272 ± 0.003	0.087 ± 0.000
0956+4107	0.416 ± 0.005	-1.450 ± 0.041	2.969 ± 0.038	0.388 ± 0.021	1.156 ± 0.000	0.300 ± 0.001	0.147 ± 0.000
1334+5031	0.428 ± 0.006	-1.815 ± 0.081	3.075 ± 0.078	0.517 ± 0.055	1.350 ± 0.000	0.376 ± 0.002	0.068 ± 0.000
0542-4100	0.389 ± 0.003	-1.508 ± 0.076	3.040 ± 0.025	0.464 ± 0.031	0.935 ± 0.000	0.264 ± 0.005	0.099 ± 0.000
1202+5751	0.303 ± 0.003	-1.231 ± 0.012	2.372 ± 0.037	0.409 ± 0.043	1.191 ± 0.000	0.297 ± 0.003	0.106 ± 0.000
0405-4100	0.489 ± 0.006	-1.976 ± 0.045	3.959 ± 0.059	0.448 ± 0.086	0.903 ± 0.000	0.291 ± 0.004	0.014 ± 0.000
1221+4918	0.362 ± 0.003	-1.488 ± 0.026	2.855 ± 0.026	0.282 ± 0.028	0.811 ± 0.000	0.230 ± 0.003	0.091 ± 0.000
0230+1836	0.310 ± 0.003	-1.079 ± 0.045	2.271 ± 0.040	0.442 ± 0.032	1.093 ± 0.000	0.296 ± 0.002	0.130 ± 0.000
0152-1358	0.337 ± 0.003	-1.532 ± 0.064	2.405 ± 0.023	0.510 ± 0.011	1.183 ± 0.000	0.348 ± 0.005	0.169 ± 0.000
1226+3332	0.585 ± 0.006	-1.859 ± 0.057	4.222 ± 0.157	0.277 ± 0.059	0.411 ± 0.000	0.168 ± 0.014	0.035 ± 0.000

Table 3.5: Statistics for the subsample of relaxed (R) and non-relaxed (N-R) clusters, and the combined (C) cluster sample from the V09.

	mean	median	K-S probability	R-S probability
	R N-R C	R N-R C		
Gini	0.55 0.39 0.47	0.54 0.39 0.44	1.42×10^{-07}	8.73×10^{-09}
M_{20}	-1.96 -1.44 -1.72	-1.96 -1.44 -1.73	8.65×10^{-09}	8.63×10^{-11}
Concentration	1.38 0.95 1.18	1.33 0.92 1.11	8.87×10^{-08}	2.26×10^{-9}
Asymmetry	0.39 0.44 0.42	0.38 0.44 0.40	0.12	0.027
Smoothness	0.68 1.05 0.85	0.61 1.09 0.94	0.0020	6.7×10^{-5}
G_M	0.27 0.31 0.29	0.28 0.30 0.28	0.012	0.003
Ellipticity	0.08 0.09 0.09	0.08 0.09 0.08	0.95	0.66

The Kolmogorov-Smirnov (K-S) test computes the probability, with the null hypothesis, that two samples are drawn from the same parent distribution. We performed the K-S test to investigate whether or not the relaxed and non relaxed cluster distributions were significantly different in our parameter set. The results are given for each parameter in Table 3.5, where a threshold of 1% means that the probability is < 0.01, implying a possible rejection of the null hypothesis. In the table we include the Wilcoxon rank sum (R-S) test which establishes the probability of whether the two samples with the null hypothesis have the same mean. A threshold of 0.1% implies that we reject the null hypothesis (that they have the same mean) if the probability is < 0.001. In addition, the mean and median values for all morphology parameters are supplied. From the statistical tests, we observed a significant separation between the two distributions (relaxed and non-relaxed clusters) for the Gini, M_{20} and Concentration, which rejects the null hypotheses that the two samples (relaxed and non-relaxed clusters) are the same and they have the same mean values. The K-S and R-S probabilities are < 0.01 and 0.001, respectively, for the Smoothness parameter; but we observed a high incidence of overlapping between relaxed and non-relaxed clusters for the Smoothness distribution. We found that the right side peak of non-relaxed clusters (dotted line) in the Smoothness distribution corresponds mainly to the high-z clusters which have low S/N compared with nearby clusters (which fall mainly on the left side). Further details concerning the Smoothness parameter is given in § 3.3.3. For the remaining parameters, we cannot reject the above null hypotheses, which means that Asymmetry, Gini of the second order moment and Ellipticity are not useful in separating relaxed and non-relaxed clusters.

3.3.2 Parameter vs Parameter planes

In the previous section we indicated that the three parameters, Gini, M_{20} and Concentration, illustrated a promising separation between relaxed and non-relaxed clusters. Furthermore, we investigated relaxed vs non-relaxed clusters in the parameter-parameter plane using combinations of morphology parameters to study the dynamical states of galaxy clusters and the correlation between each morphology parameter. In Fig. 3.3 we plotted our results in parameter-parameter planes. Three parameters, Gini, Concentration and M_{20}, look particularly powerful after combining with other parameters to differentiate between non-relaxed and relaxed clusters. Clusters with different dynamical states (as classified by the V09) occupy distinct regions in the parameter-parameter planes; for e.g., in the Concentration vs Asymmetry plot, all relaxed clusters occupy the upper region, while the lower region is occupied by non-relaxed clusters. In our analysis we did not observe any correlation between cluster dynamical states and Ellipticity or Asymmetry. As seen in Fig. 3.3, galaxy clusters within our sample show a range of different morphologies and are not concentrated in particular positions of the parameter-parameter space. This is probably because of the hierarchical cluster formation process, indicating that clusters pass through multiple (merger) phases in their evolution. Each phase is dynamically important, and traces the cluster properties. This could help in the understanding of large and complex structure formations in the standard cosmological model.

We used the Spearman rank-order correlation coefficient, ρ, and corresponding probability, p to quantify any correlation between parameter pairs. This resulted in a correlation coefficient between ranks of a group of individuals for a given pair of attributes. In order to calculate the Spearman coefficient, ρ, it is necessary to assign ranks (low to high or high to low) to a given set of variables, individually. Then next step is to measure the deviation between the ranks of variable pairs, square this rank difference, and sum up. The value of the rank order correlation coefficient varies between -1 and 1. If the variables are negatively correlated (anti-correlation) then ρ falls between -1 and 0, but a value for ρ between 0 and 1 implies a positive correlation between given variables. $\rho = 0$ implies no correlation between variables. The p value suggests the Spearman correlation probability that two sets of data are uncorrelated. Low probability indicates two data sets are less uncorrelated and high probability indicates two data sets are more uncorrelated.

Fig. 3.3 indicates that the Concentration is tightly correlated with the Gini, while anti-correlated with the M_{20} (see also Table 3.6 and Table 3.7). The Concentration (Santos et al., 2008; Hudson et al., 2010; Cassano et al., 2010b) is a useful parameter in separating non-relaxed from relaxed clusters with almost all morphology parameters. Fig. 3.3 illustrates our plot of the C_{5080} Concentration parameter, which means 50% of the flux within the inner radius and 80% within the outer radius. As seen in Fig. 3.3, relaxed clusters occupy the upper left corner, while non-relaxed clusters occupy the bottom-right corner of the M_{20} vs Gini and Concentration planes. In the Gini vs Concentration plane, relaxed clusters fall in the upper-right corner, while the bottom-left corner is occupied by non-relaxed clusters. In this study we found that the Gini coefficient was also useful in separating non-relaxed clusters from relaxed clusters when plotted against most other parameters. The Gini, Concentration and M_{20} parameters are all inter-related as well (Table 3.6); and the Gini coefficient could be useful to use as a proxy of the Concentration for detecting substructure in high-z clusters. The advantage of using the Gini coefficient is that it is independent of the precise location of a galaxy cluster's centre. The Asymmetry parameter is correlated with Gini of the second order moment and Smoothness parameters (Okabe et al., 2010; Zhang et al., 2010; Rasia et al., 2012). We did not observe any correlation between the other six parameters and Ellipticity. In general, three parameters - Gini, M_{20} and Concentration - are very promising tools in the study of the dynamical state of clusters.

Table 3.6: Spearman coefficient, ρ, for the subsample of relaxed, non-relaxed, and combined clusters, between each morphology parameter.

	Gini	M_{20}	Concentration	Asymmetry	Smoothness	G_M	Ellipticity
	R N-R C	R N-R C	R N-R C	R N-R C	R N-R C	R N-R C	R N-R C
Gini	-	-0.75 -0.58 -0.83	0.87 0.81 0.93	0.05 0.34 -0.02	-0.40 0.14 -0.38	0.11 0.14 -0.12	0.25 -0.04 0.05
M_{20}	-0.75 -0.58 -0.83	-	-0.91 -0.80 -0.92	0.13 0.12 0.24	0.18 0.15 0.40	0.07 0.21 0.29	-0.15 0.18 0.04
Concentration	0.87 0.81 0.93	-0.91 -0.80 -0.92	-	-0.06 0.04 -0.16	-0.29 -0.10 -0.41	-0.05 -0.20 -0.28	0.13 -0.10 -0.01
Asymmetry	0.05 0.34 -0.02	0.13 0.12 0.24	-0.06 0.04 -0.16	-	0.38 0.76 0.56	0.68 0.83 0.72	-0.22 -0.05 -0.12
Smoothness	-0.40 0.14 -0.38	0.18 0.15 0.40	-0.29 -0.10 -0.41	0.38 0.76 0.56	-	0.42 0.85 0.65	-0.33 -0.01 -0.13
G_M	0.11 0.14 -0.12	0.07 0.21 0.29	-0.05 -0.20 -0.28	0.68 0.83 0.72	0.42 0.85 0.65	-	-0.20 -0.03 -0.06
Ellipticity	0.25 -0.04 0.05	-0.15 0.18 0.04	0.13 -0.10 -0.017	-0.22 -0.05 -0.12	-0.33 -0.019 -0.13	-0.20 -0.03 -0.06	-

Table 3.7: Spearman test probability value, p, for the subsample of relaxed, non-relaxed, and combined clusters, between each morphology parameter. This p value indicate the probability that two sets of data are uncorrelated.

	Gini			M_{20}			Concentration			Asymmetry			Smoothness			G_M			Ellipticity		
	R	N-R	C	R	N-R	C	R	N-R	C	R	N-R	C	R	N-R	C	R	N-R	C	R	N-R	C
Gini	-			0.0	0.0	0.0	0.0	0.0	0.0	0.70	0.03	0.83	0.01	0.37	0.0	0.46	0.37	0.26	0.09	0.77	0.61
M_{20}	0.0	0.0	0.0	-			0.0	0.0	0.0	0.38	0.46	0.02	0.23	0.36	0.0	0.62	0.19	0.01	0.32	0.26	0.67
Concentration	0.0	0.0	0.0	0.0	0.0	0.0	-			0.65	0.79	0.15	0.05	0.54	0.0	0.73	0.21	0.01	0.37	0.51	0.88
Asymmetry	0.70	0.03	0.83	0.38	0.46	0.02	0.65	0.79	0.15	-			0.01	0.0	0.0	0.0	0.0	0.0	0.14	0.74	0.26
Smoothness	0.01	0.37	0.0	0.23	0.36	0.0	0.05	0.54	0.0	0.01	0.0	0.0	-			0.01	0.0	0.0	0.03	0.91	0.21
G_M	0.46	0.37	0.26	0.62	0.19	0.01	0.73	0.21	0.01	0.0	0.0	0.0	0.01	0.0	0.0	-			0.19	0.85	0.57
Ellipticity	0.09	0.77	0.61	0.32	0.26	0.67	0.37	0.51	0.88	0.14	0.74	0.26	0.03	0.91	0.21	0.19	0.85	0.57	-		

Despite this reasonable division between relaxed and non-relaxed clusters, we observed an overlap between some clusters, such as A401, A3571, A1651, A3158, A3562, A576, A2063, ZWCL1215, A2657, A2589, A3391, 0355-374, 1641+4001, 1120+4318, 1222+2709, 0328-2140 and 1357+6232. These are identified as relaxed clusters in the V09, but in our parameter space they fall into the non-relaxed region. A401 (Murgia et al., 2010) and A3562 (Venturi et al., 2003) host *radio halos* (indicating merger clusters) which are clearly identified as non-relaxed clusters by our parameters (although they are classified as relaxed in the V09). Dupke et al. (2007) predicted a line of sight bullet-like cluster in A576, using a combination of *Chandra* and *XMM* observations. This gave us confidence that our parameter set provided a good indication of cluster dynamical states. The remaining clusters may be weak mergers (pre- or post-merger) or they may have a weak cool cores.

In cluster A85 (Kempner et al., 2002), in addition to the main cool core cluster, two subclusters are visible, in the far South and NW, respectively. We calculated parameters for the main relaxed cluster, and found that it falls into the relaxed category, although very close to the boundary of the non-relaxed side, which could indicate a weak interaction between the subcluster and the main cool core cluster. Further investigation of these clusters is required in order to study their dynamical states. Based on our measurements, we categorised most relaxed clusters by Concentration > 1.55 and $M_{20} <$ -2.0, while intermediate or weak cool core clusters were categorised by $1.0 <$ Concentration < 1.55 and $-2.0 < M_{20} < -1.4$, and distorted and non-relaxed clusters were categorised by Concentration < 1.0 and $M_{20} > -1.4$. According to the Gini coefficient, most relaxed clusters have a Gini value > 0.65 and non-relaxed have Gini value < 0.40, while all intermediate clusters fall between these two values. We chose these boundaries based on visual identification of each cluster morphology (Fig. 3.3). Mean and median values (Table 3.5) produce a significant overlap due to the presence of a large number of intermediate clusters in our sample.

3.3.3 Smoothness and Asymmetry parameters

In the previous section we showed that the Smoothness and Asymmetry parameters are not capable of separating relaxed and non-relaxed clusters. In this section we will test different possible smoothing and angular size issues relating to them. Okabe et al. (2010) used a $2'$ smoothing scale for calculating the fluctuation parameter. They, however, used it for R_{500} radius and the data of the *XMM-Newton* which has a large FOV compared with the *Chandra*. We used $0.5'$ (15 pix) and $1'$ (30 pix) smoothing scales, σ, with initial $4''$ (2 pix) and $10''$ (5 pix) smoothing of input cluster images (which is sufficient to not washed out any underlying substructure features). Results are shown in Fig. 3.4. We find that the different smoothing scales (σ) had little affect on the Smoothness parameter. In this analysis, we used a fixed angular size of $2''$/pix to bin each cluster image and the same angular smoothing scale (σ) for low- and high-z clusters. This angular scaling could affect the Smoothness parameter. To overcome this, and instead of using a fixed angular size, we scaled each cluster image (of low- and high-z) in terms of fixed physical size of 10 kpc/pix. We then used 50 and 150 kpc smoothing scales (σ) to smooth cluster images in order to calculate the Smoothness parameter. Both of these σ values were chosen based on the available aperture size (segmentation map) of cluster for which we calculated the Smoothness parameter. We also smoothed cluster input images with (1) 15 (1.5 pix) and (2) 30 (3 pix) kpc Gaussian kernel sizes (which is sufficient to not washed out any underlying substructure features). Fig. 3.5

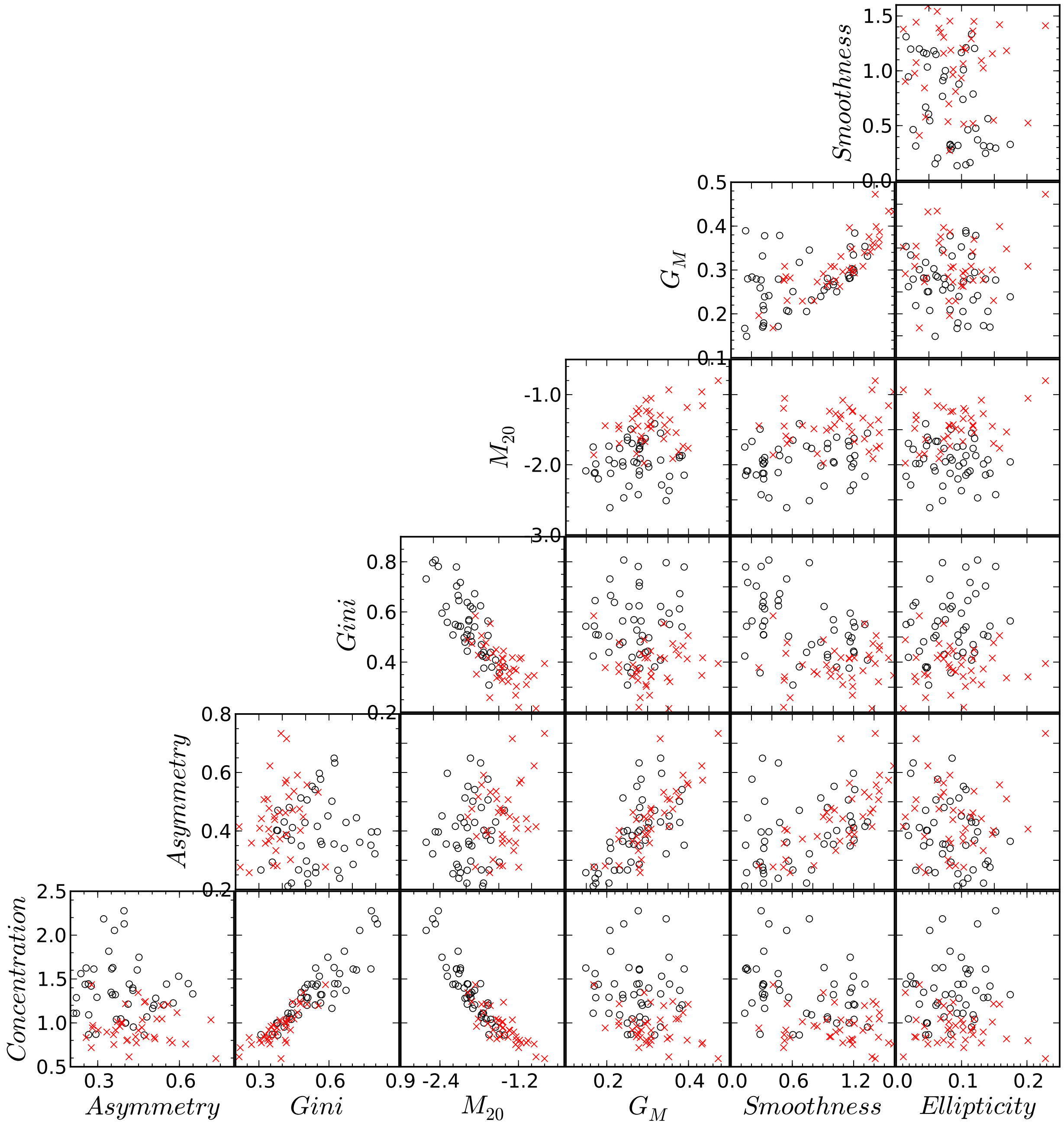

Figure 3.3: Seven morphology parameters plotted in the parameter-parameter planes. C_{5080} was plotted as the Concentration parameter. ○ = relaxed cluster; × = non-relaxed cluster. Galaxy cluster separation is based on the V09.

Table 3.8: Statistics for two redshift bins: low-z (0.02–0.3) and high-z (0.3–0.9).

Parameters	mean of low-z	mean of high-z	median of low-z	median of high-z	K-S probability	R-S probability
Gini	0.50	0.44	0.47	0.43	0.08	0.09
M_{20}	-1.75	-1.68	-1.76	-1.67	0.74	0.35
Concentration	1.21	1.14	1.14	1.06	0.57	0.47
Asymmetry	0.38	0.46	0.36	0.46	0.0002	0.0008
Smoothness	0.65	1.11	0.53	1.16	1.57×10^{-7}	2×10^{-6}
G_M	0.28	0.31	0.28	0.30	0.0016	0.004
Ellipticity	0.10	0.08	0.09	0.07	0.08	0.024

gives the calculated smoothness parameter for fixed physical smoothing kernel size. The Smoothness parameter had barely changed from the previous results, and had still not separated the two classes of cluster, i.e. relaxed and non-relaxed. Finally, we divided the subsample of low- and high-z clusters, and plotted separately for both the fixed angular size and physical size (Fig. 3.6). In this figure, we saw that there was no underlying redshift-dependent issue in the calculation of the Smoothness parameter. In the Smoothness distribution of Figs. 3.2, 3.4 and 3.5, we observed one peak (relaxed clusters) on the left side, and another peak (non-relaxed clusters) on the right side. We identified that the right side peak corresponds mainly to high-z (relaxed and non-relaxed) clusters which have low S/N compared with nearby clusters which fall on the left side. It is possible that the Smoothness parameter is strongly depends on S/N. In our sample, S/N is different for each cluster, and neither do these clusters have equal exposure time. Furthermore, most clusters (mainly high-z) do not have $\gg 1$ count in each (binned) pixel. So, in general, the Smoothness is not a good parameter for a large number of clusters in which each has a different exposure time. In § 3.4.3, further we show that the Smoothness parameter depends highly on S/N.

We also investigated the Asymmetry parameter using various smoothing Gaussian kernel sizes to smooth cluster input images. We rotated this smoothed image by 180°, subtracted it from the input image, and normalised it. Our results for the fixed angular and physical scale cluster images are given in Fig. 3.7. None of the results indicates the separation of relaxed and non-relaxed clusters. We also split the whole cluster sample into subsamples of low- and high-z to verify the Asymmetry parameter. But, as shown in Fig. 3.8, we concluded that calculation of the Asymmetry parameter is independent of cluster redshift. As for the Smoothness parameter, Asymmetry parameter is not useful because the S/N is inadequate in a given large sample of clusters (see § 3.4.3).

3.3.4 Redshift evolution

Based on current cosmological theories, massive galaxy clusters start to form around $z \sim 1$ and have continued to evolve upto the present epoch. To look into the evolutionary effect on the distribution of the parameters, we divided our entire sample into low-z (0.02–0.3) and high-z (0.3–0.9), and performed the K-S and R-S tests on each parameter distribution to observe the difference between the two redshift bins. Table 3.8 lists the mean, median and statistical test results for the two redshift bins.

As seen in Table 3.8, the K-S and R-S probabilities are $< 1\%$ and $< 0.1\%$, respectively, for the Asymmetry and Smoothness parameters implying that we can reject both null hypotheses

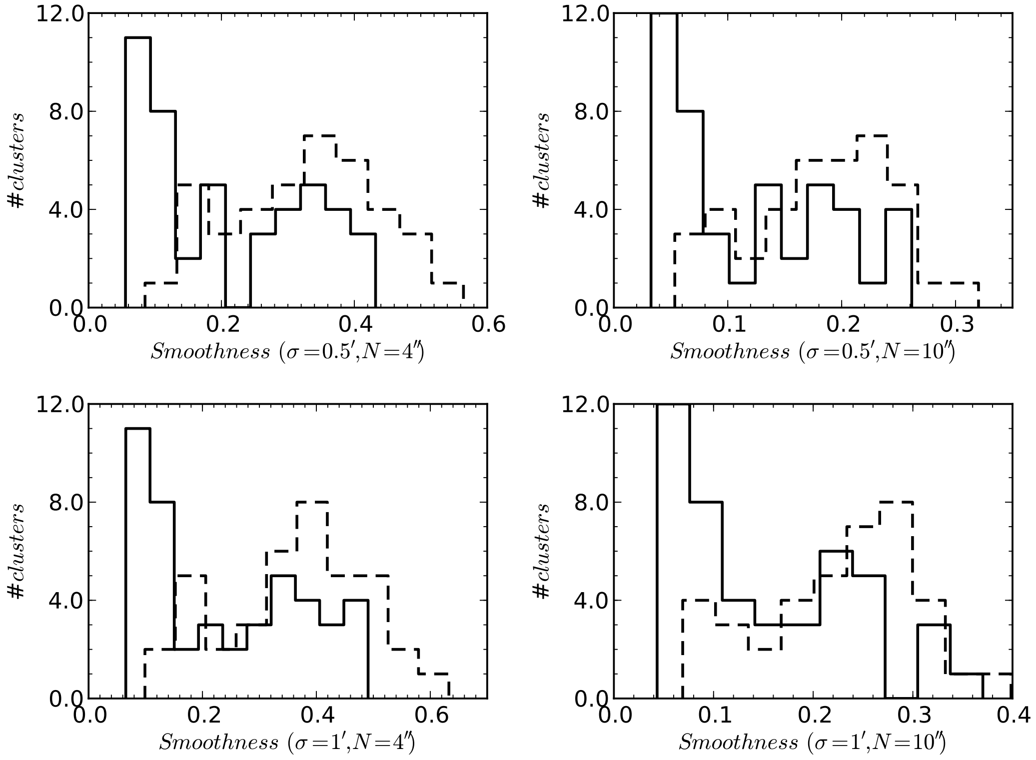

Figure 3.4: Calculation of the Smoothness parameter for two different Gaussian kernel sizes of fixed angular scale. N shows smoothing size for input cluster image. Galaxy cluster separation is based on the V09.

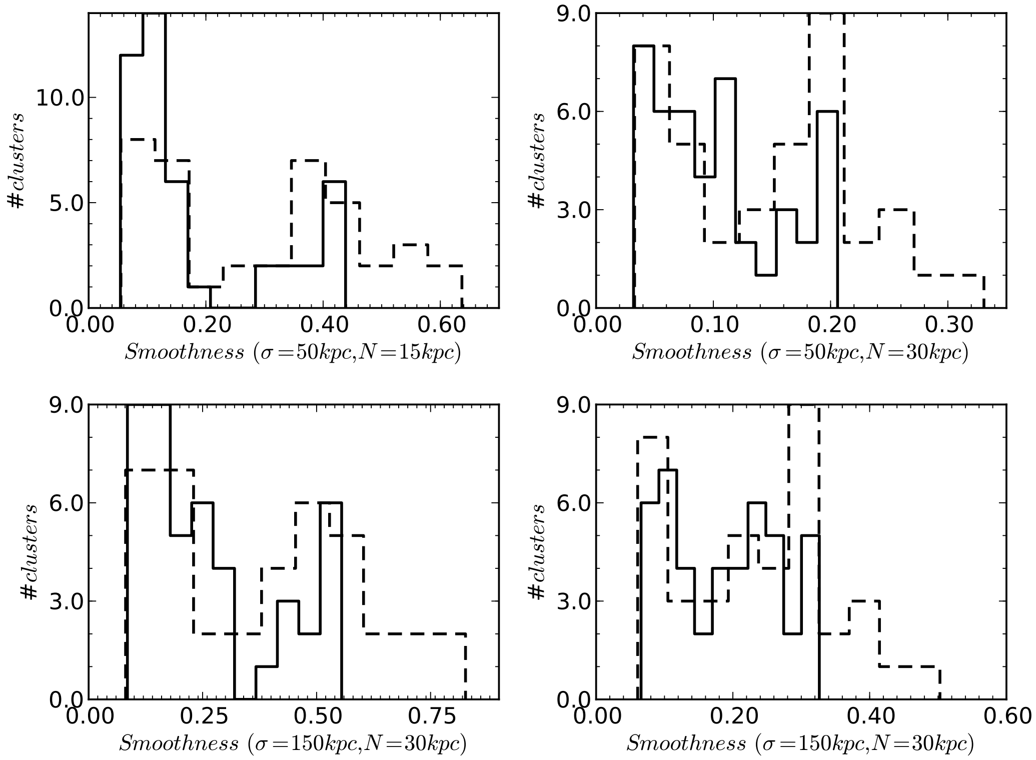

Figure 3.5: Calculation of the Smoothness parameter for two different Gaussian kernel sizes of fixed physical scale. N shows smoothing size for input cluster image. Galaxy cluster separation is based on the V09.

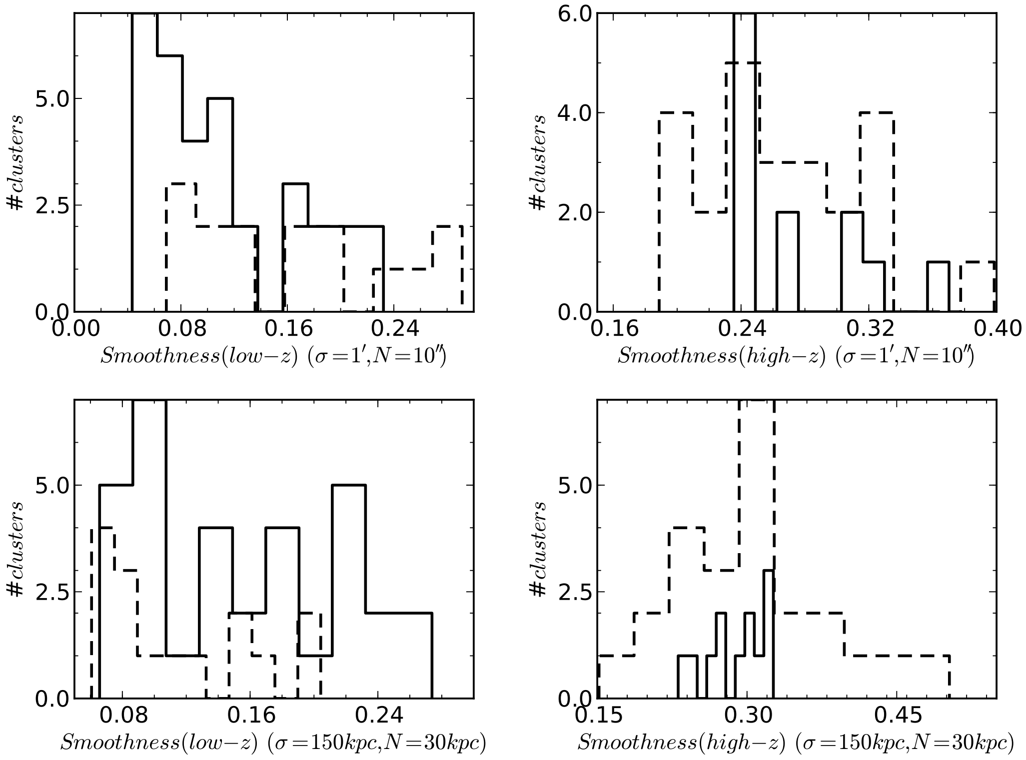

Figure 3.6: Smoothness parameter calculated for the subsample of low- and high-z clusters. We show both fixed angular and physical scale smoothing kernel sizes. N shows smoothing size for input cluster image. Galaxy cluster separation is based on the V09.

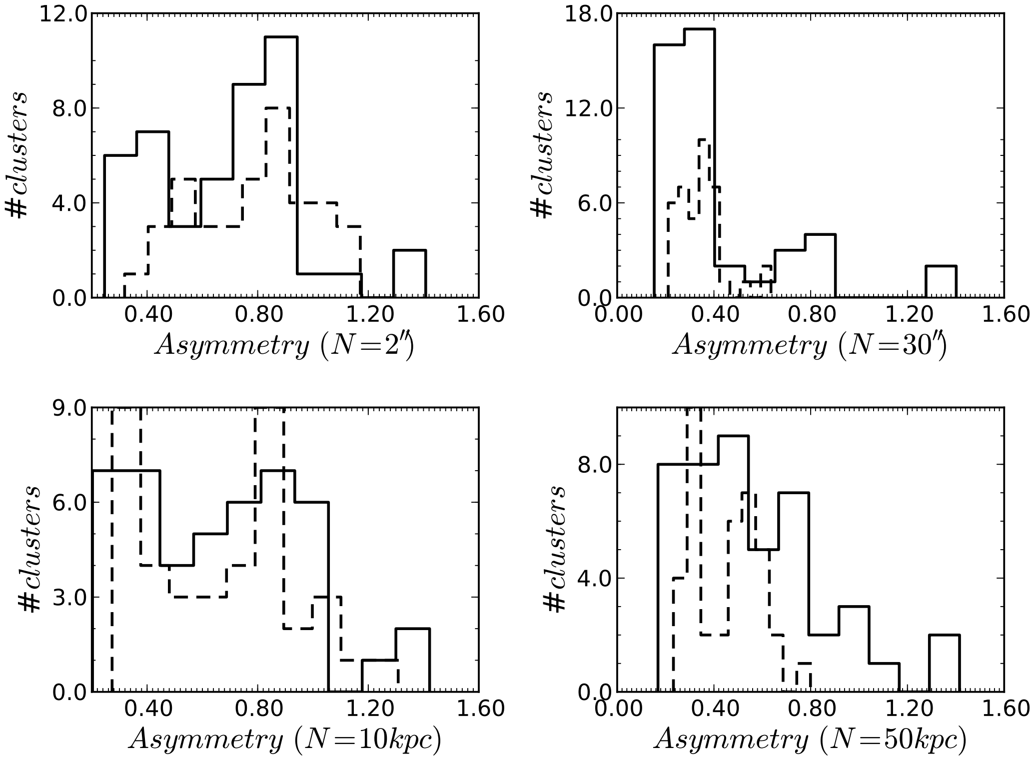

Figure 3.7: Calculation of the Asymmetry parameter for two different Gaussian kernel sizes of fixed angular and physical scale. N shows smoothing size for input cluster image. Galaxy cluster separation is based on the V09.

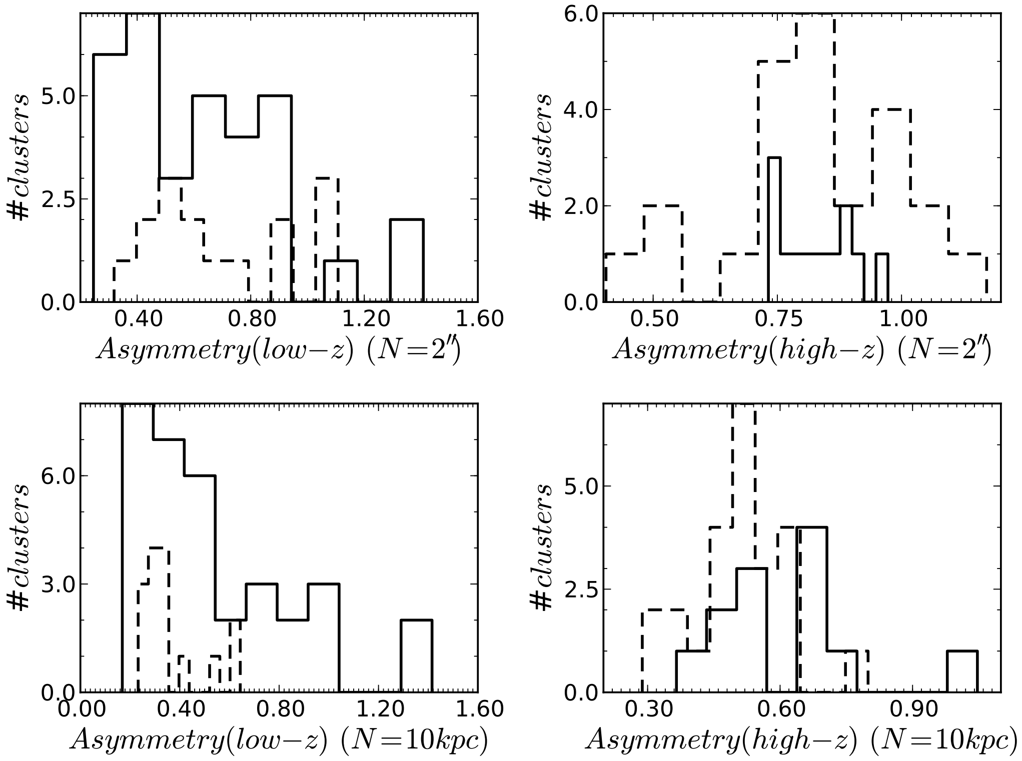

Figure 3.8: Asymmetry parameter calculated for the subsample of low- and high-z clusters. We show both fixed angular and physical scale smoothing kernel sizes in order to smooth cluster image. N shows smoothing size for input cluster image. Galaxy cluster separation is based on the V09.

mentioned in § 3.3.1. It is believed that early stage mergers (high-z) are more asymmetric and contain more patchy and clumpy material compared with low redshift clusters. As mentioned in § 3.3.3, however, high-z clusters have low S/N compared with low-z clusters, and hence have high Smoothness values. Weak evolution is visible in the Gini and Gini of the second order moment, which indicates the possibility that high redshift clusters are more extended (which could mean that they do not have a density peak at the cluster centre) compared with those of low redshift. The M_{20}, Concentration and Ellipticity do not show significant evolution. We plotted these two redshift samples (low and high) in Fig. 3.9. The combination of three promising parameters (Gini, M_{20} and Concentration) were plotted with boundaries between relaxed and non-relaxed clusters. For example, in the Gini vs M_{20} plot in Fig. 3.9, non-relaxed clusters appeared in the upper left quadrant, while relaxed clusters appeared in the bottom right quadrant.

According to the V09 classification, there are a total of 48 low-z and 36 high-z clusters, of which 33 are low-z relaxed, 12 are high-z relaxed, 15 are low-z non-relaxed and 24 are high-z non-relaxed clusters. We divided this classification further, using all three promising parameters:

1. Based on the Gini, we found that 9 clusters are relaxed, 48 are intermediate (weak cool core) and 27 are non-relaxed. We then divided this classification into two redshift bins: in the low-z subsample there are 8 ($\sim$ 17%) relaxed, 25 intermediate ($\sim$ 52%) and 15 ($\sim$ 31%) non-relaxed clusters; in the high-z subsample there are 1 ($\sim$ 3%) relaxed, 23 ($\sim$ 64%) intermediate and 12 ($\sim$ 33%) non-relaxed clusters.

2. Based on the M_{20}, we found that 18 clusters are relaxed, 50 are intermediate (weak cool core) and 16 are non-relaxed. We then divided this classification into two redshift bins: in the low-z subsample there are 12 ($\sim$ 25%) relaxed, 28 intermediate ($\sim$ 58%) and 8 ($\sim$ 17%) non-relaxed clusters; in the high-z subsample there are 6 ($\sim$ 17%) relaxed, 22 ($\sim$ 61%) intermediate and 8 ($\sim$ 22%) non-relaxed clusters.

3. Based on the Concentration, we found 12 clusters are relaxed, 41 clusters are intermediate (weak cool core) and 31 clusters are non-relaxed. We then divided this classification into two redshift bins: in the low-z subsample there are 10 ($\sim$ 21%) relaxed, 20 intermediate ($\sim$ 42%) and 18 ($\sim$ 37%) non-relaxed clusters; in the high-z subsample there are 2 ($\sim$ 6%) relaxed, 21 ($\sim$ 58%) intermediate and 13 ($\sim$ 36%) non-relaxed clusters.

This shows clearly that, in our sample, most of the clusters are in the intermediate stage ($\sim$ 57% based on the Gini coefficient, $\sim$ 60% based on the M_{20}, and $\sim$ 49% based on the Concentration parameter) and are evolving continuously via merger. From the above statistics, we observed that relaxed clusters are more dominant within the low-z sample, which could indicate that, in the current epoch, clusters show less substructure.

3.4 Systematics

We investigated a number of possible systematic effects, discussed below, to study how robust these parameters are in various conditions.

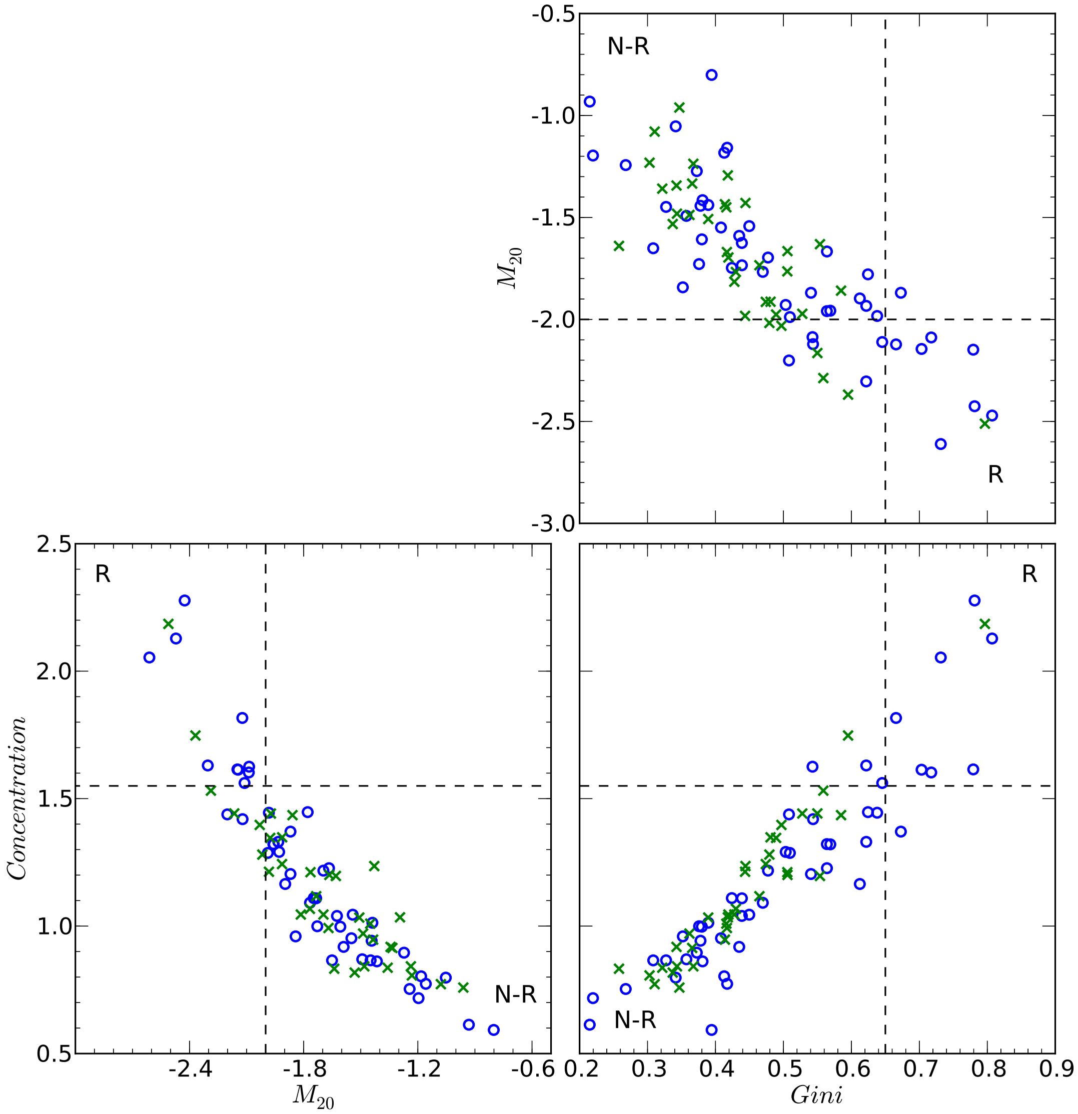

Figure 3.9: Three parameters plotted in the parameter-parameter planes to show cluster evolution with redshift. Here we plotted C_{5080} as the Concentration parameter. ○ = low-z cluster (0.02–0.3); × = high-z cluster (0.3–0.9). The dashed lines represent the boundaries between relaxed and non-relaxed clusters. Boundary values for Gini = 0.65, M_{20} = -2.0 and Concentration = 1.55. R indicates relaxed clusters and N-R indicates non-relaxed clusters.

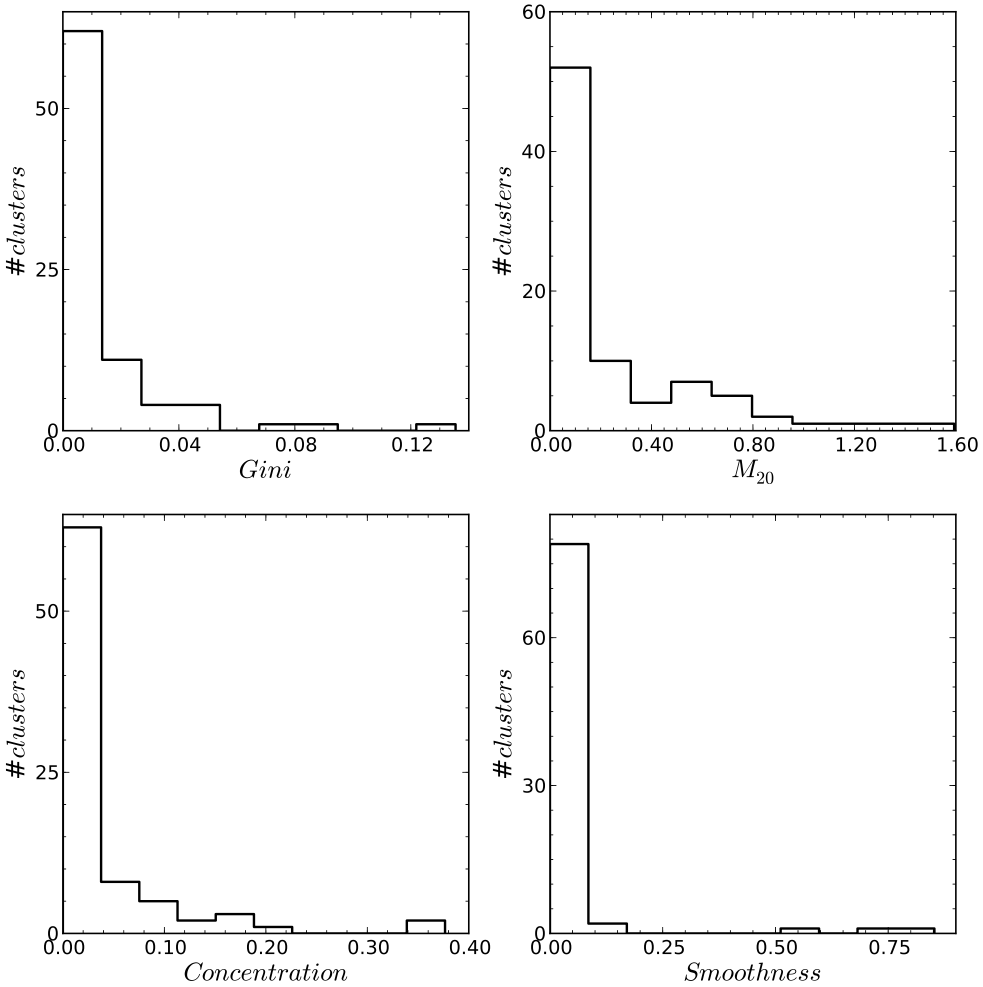

Figure 3.10: Four parameters calculated with and without point sources, with plotted offset between them. Here we plotted C_{5080} as the Concentration parameter. Less offset suggests that parameters are quite robust.

3.4.1 Effect of point sources

In order to test the effect of point sources on the calculation of parameters, we calculated morphology parameters on (exposure corrected and smoothed) cluster images without removing the point sources. We noticed that parameters are fairly robust against the inclusion (or exclusion) of point sources into the parameter calculation. Fig. 3.10 indicates how we plotted the offset for four parameters (Gini, M_{20}, Concentration and Smoothness) calculated with and without point sources. As we observed, less offset between parameters (with or without point sources) suggests that they are quite robust. The Gini and M_{20}, however, each show a small extended tail on the right hand side (Fig. 3.10). This result is obvious, because the Gini coefficient includes bright pixels from point sources in the calculation, and thus increases by a small value. In the case of the M_{20}, if the point sources are very close to the centre, its value will decrease by a small factor.

3.4.2 Aperture size effect

Aperture radii have an important effect when measuring morphology parameters. We chose to use a fixed physical size radius rather than a fixed overdensity (R_{500}) radius, because it is difficult to measure R_{500} accurately for non-relaxed clusters. The FOV of the *Chandra* telescope is limited for studies of nearby clusters (for $z < 0.05$, the cluster linear size is less than 2 kpc/pix.). Taking this into account, therefore, we used a 200 kpc fixed physical radius for nearby clusters ($z < 0.05$) and a 500 kpc fixed physical radius for distant clusters ($z > 0.05$) in our analysis. The large variation in aperture size does affect the parameters because they are related to surface brightness. Fig. 3.11 shows the effect of various aperture radii on the parameters. We chose a sample that included both distant and nearby clusters and calculated the morphology parameters in the radius sequence of 100 kpc to 1 Mpc. In Fig. 3.11, the nearby clusters are plotted with a dotted line, while the distant clusters are plotted with a continuous line. We also noted that we had used 100 kpc to 500 kpc aperture sizes for nearby clusters. As per Fig. 3.11, in the case of distant clusters, a few parameters (Asymmetry, Smoothness, G_M, and Ellipticity) remain constant in spite of aperture size, while the Gini, M_{20} and Concentration parameters are sensitive to the aperture radius within which they are calculated, while tending to be stable for aperture radii greater than 400 kpc. The three parameters, Gini, M_{20} and Concentration depend on selected aperture region. The Gini parameter systematically increases with aperture radius as more sky pixels (which are faint pixels situated near the cluster edges and blended with background) are included in the extraction aperture, conversely the exclusion of these low surface brightness pixels will systematically decrease Gini coefficient. In the case of M_{20}, F_{tot} (total second order moment within aperture size) will increase (faster than 20% of the total cluster flux within given aperture) with increasing aperture radius, hence M_{20} decrease (see Eq.2.5). On the other hand, in the case of Concentration parameter, the difference between outer radius (for example r_{80}) and inner radius (r_{50}) increase with increasing aperture size or in other word outer radius increase faster than inner radius which cause value of the Concentration parameter increase with increasing aperture size (see Eq.2.6). Other parameters largely depends on S/N of given cluster image than the selected aperture region of cluster. Parameter values for nearby clusters (in particular $z < 0.05$) are very sensitive to the chosen aperture size. For calculating morphology parameters of nearby clusters, we chose an intermediate radius of 200 kpc, which was enough to include sufficient cluster flux.

3.4.3 Exposure time effect

It is important to check the consistency of the parameters over different lengths of exposure time. Observations with a shorter exposure time are likely to have more noise in the data (lower S/N). Consequently, we were able to check the robustness of the parameters for cluster images with lower S/N. However, to rescale the real data by exposure time and then add Poisson noise gives an image which has an excessive amount of Poisson noise, in addition to the intrinsic noise present in the real observation. The simplest solution is to simulate a cluster image with no intrinsic noise, rather than using real data. To achieve this, we needed to estimate the different complex characteristics of a model to simulate galaxy clusters. This task is considered difficult in the cases of non-relaxed and disturbed clusters. To overcome this problem, Hashimoto et al. (2007) suggested a novel technique for galaxy cluster simulations called “adaptive scalings”, using real data and adding noise to the

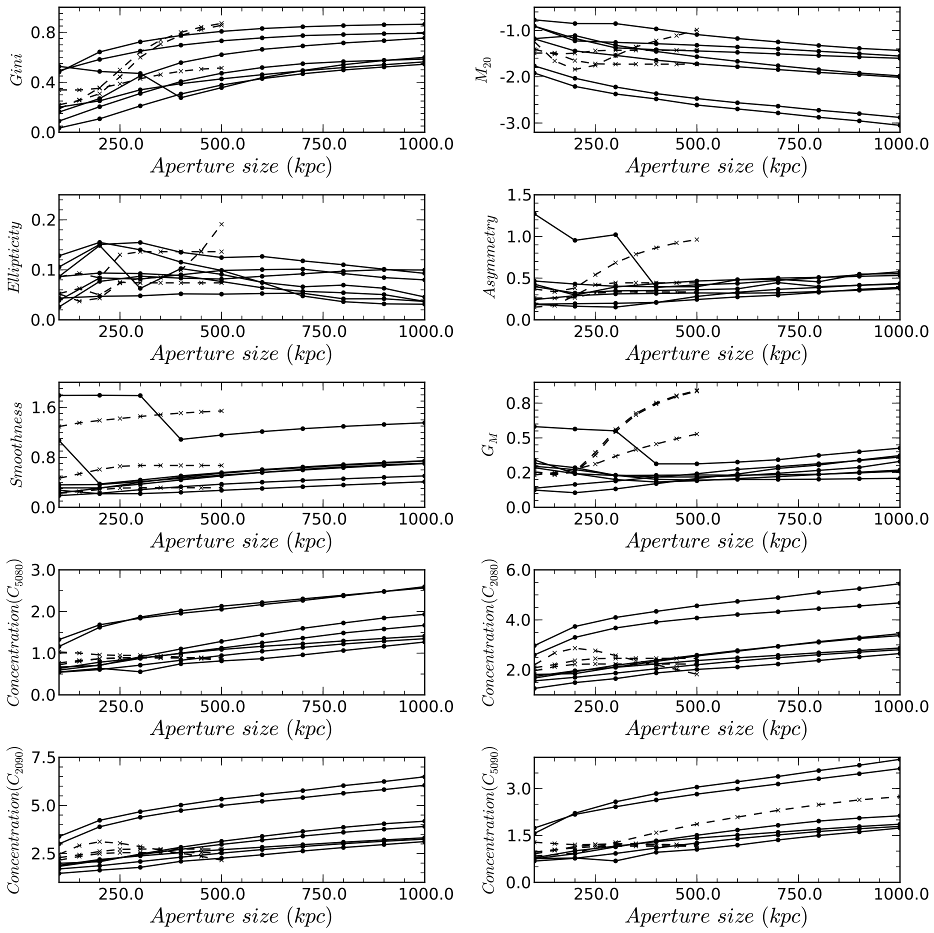

Figure 3.11: Morphology parameters calculated for a range of aperture sizes from 100 kpc to 1 Mpc for distant clusters. Nearby clusters are calculated in a range of radii from 100 kpc to 500 kpc only. Solid lines with • symbol are plotted for distant clusters, and dashed lines with × symbol are plotted for nearby clusters.

rescaled image. We describe below the various steps to simulate the exposure time effect on real data.

1. To simulate data with a desired integration time $t = t1$, first rescale an original unsmoothed (events) image (E_0) (including background) by a factor $K_0/(1\text{-}K_0)$, where $K_0 = t1/t0$, $t0$ is the original exposure time, and $t1$ is the desired exposure time ($t0 > t1$). This gives an intermediate scaled image E_1,

$$E_1 = E_0 \times \frac{K_0}{1 - K_0}. \tag{3.2}$$

2. After this rescaling, Poisson noise is added to the rescaled image E_1, by taking each pixel value as the mean for a Poisson distribution, and then randomly selecting a new pixel value from the Poisson distribution. To add Poisson noise to the image, we used the python *numpy module*, random.poisson.

3. This noise-added image is then further rescaled by a factor (1-K_0), giving a final image whose signal is properly scaled by K_0 relative to the original image, but its noise is scaled by $\sqrt{K_0}$, assuming that the intrinsic noise in the real data is Poissonian. The resulting final cluster image is smoothed by a Gaussian width, $\sigma = 10''$.

An example of this adaptive method is given in Fig. 3.12; an example of the low exposure time effect on a cluster. Subsequently we calculated our morphology parameters for each short to long exposure cluster image.

Fig. 3.13 shows how morphology parameters behave with different exposure lengths. We simulated a few original clusters with various exposure times, as described above, and re-calculated the morphology parameters for each simulated cluster. The data points of each cluster were joined with a line, to illustrate the trend between morphology parameters and the various exposure times. As depicted in Fig. 3.13, all parameters are robust against different exposure times, with the exception of the Smoothness parameter. We noted, however, that the Gini, Gini of the second order moment and Asymmetry were not reliable when exposure time was $\lesssim 5$ ks. In the cases of the Gini and Gini of the second order moment, low exposure means low S/N, indicating that the Gini and Gini of the second order moment values are high for low exposure observations, although fairly consistent for exposure times $\gtrsim 5$ ks. For the short exposure times, there are few bright pixels within the given aperture radius (the rest are scattered to very low ~ 0). In other words, low S/N causes broader flux distribution in the faintest pixels, resulting in strong variation in the flux distribution, for which we calculated the Gini coefficient; and hence the Gini coefficient gives a high value compared with the long exposure time. The value of the Smoothness decreases continuously with increasing exposure time. This is to be expected because, for high S/N and exposure time, the flux distribution in any given cluster image becomes smooth and less patchy. Care must therefore be taken when calculating the Smoothness parameter. We found that the Smoothness is weakly correlated with the Gini of the second order moment and Asymmetry parameters, yet it is not established whether we can use these latter parameters as a substitute for the Smoothness. The remainder of the parameters were relatively constant over different exposure lengths.

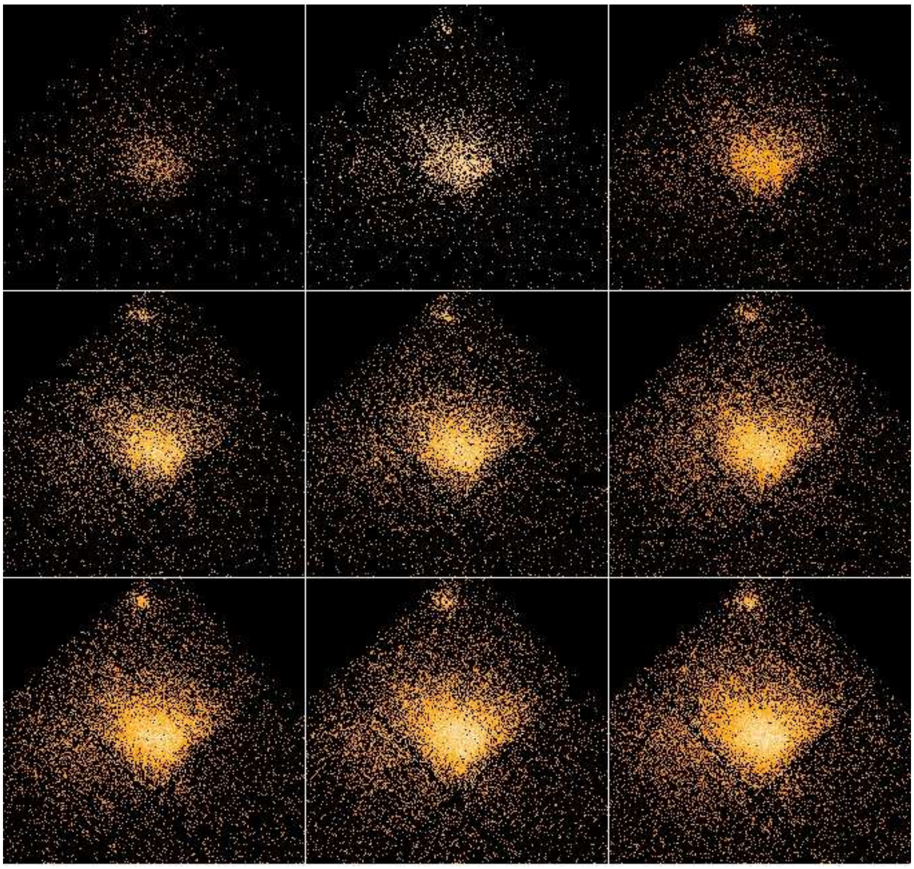

Figure 3.12: Simulated clusters for different exposure times. Horizontally, from top left to bottom right, the images were arranged from 2 ks to 18 ks, respectively, in order of 2 ks exposure time.

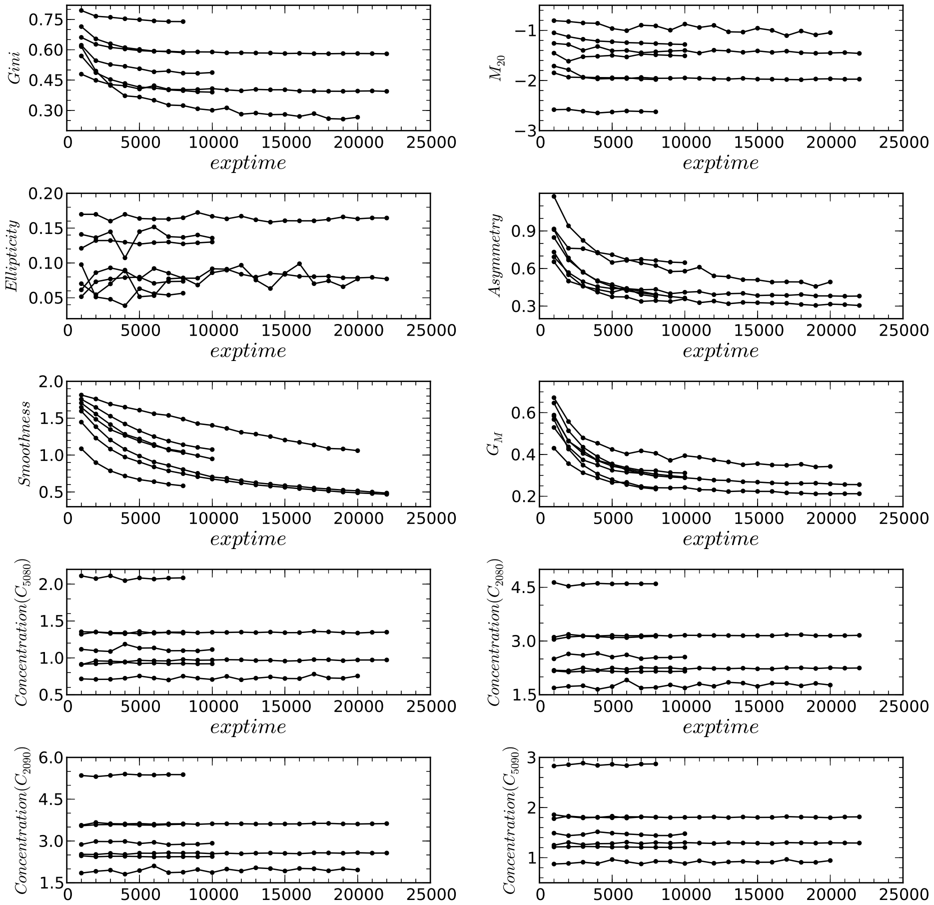

Figure 3.13: Robustness of morphology parameters calculated for several clusters against various simulated exposure lengths.

3.4.4 Redshift effect

It is hoped that these morphology parameters could be used to trace the evolution of galaxy clusters with redshifts. It is therefore important to understand the robustness as a function of redshift and, to this end, it is necessary to check the following criteria:

1. The effect of various angular bin sizes on morphology parameters.
2. The surface brightness dimming effect on morphology parameters.

We simulated several observations of galaxy clusters at a higher redshift ($z1$) than its real redshift ($z0$) using real data from our sample clusters. Again, we adopted the procedure describe by Hashimoto et al. (2007). Initially, we created an image (E_0) of the restframe 0.5-7 keV band at the actual redshift $z0$ of each cluster, and subtracted a mean background B (found at the edge of the CCD). Higher redshift causes surface brightness dimming, but only on the cluster flux. It does not affect the background which plays an important role in high redshift cluster observations. Furthermore, it is not enough to scale E_0 by $1/(1+z)^4$ because the background noise would not be correct. We therefore used an adaptive scaling technique similar to that of the exposure time case described in section § 3.4.3, to scale E_0 accurately with the appropriate amount of background noise. The adaptive scaling technique is not straightforward compared with that for the exposure time case. In the present case, it requires a pixel-to-pixel manipulation, because even though the background B is already subtracted from the cluster signal, the intrinsic noise remains proportional to E_0+B. The following steps describe the technique.

1. An intermediate scaled image E_1 was made from E_0 by a pixel-to-pixel manipulation, using

$$E_1(x, y) = \frac{E_0(x, y)^2 K_1^2}{[E_0(x, y)K_1 + B - K_1^2(E_0(x, y) + B)]}, \tag{3.3}$$

   where

$$K_1 = [(1 + z_0)/(1 + z_1)]^4. \tag{3.4}$$

2. Poisson noise was added to E_1 in the same way as described in § 3.4.3, generating an image $E_1^{'}$.

3. From this noise-added image, a new dimmed image, E_2, is generated, whose cluster flux is scaled by K_1 with respect to the original restframe image and the appropriate amount of Poisson noise. Here it is necessary to apply reverse pixel-to-pixel manipulation, as shown by

$$E_2(x, y) = E_1^{'}(x, y)\frac{E_0(x, y)K_1 + B - K_1^2[E_0(x, y) + B)]}{E_0(x, y)K_1}. \tag{3.5}$$

   Adding the subtracted constant background, B, to E_2 gives

$$E_2^{'}(x, y) = E_2(x, y) + B. \tag{3.6}$$

4. The resulting dimmed image, $E_2^{'}$, should be rebinned by a linear scale factor K_2, in order to account for the angular-size change due to the difference in redshift between two clusters

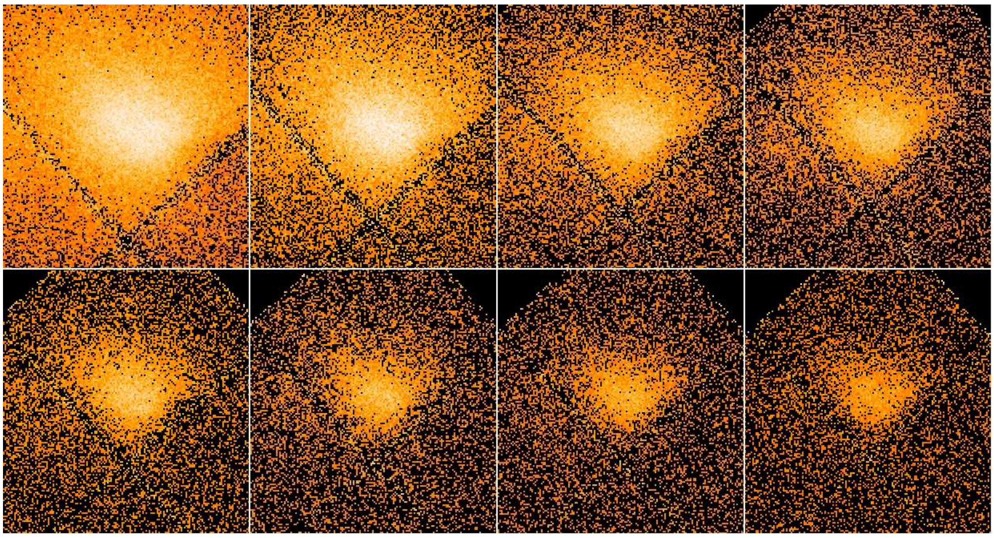

Figure 3.14: Simulated clusters for different redshifts. Figures are read from top left to bottom right in order of low- to high-z, respectively.

at $z0$ and $z1$. This simple rebinning, however, will again not generate the precise amount of noise caused by the angular-size change due to the different redshift effects. For the purposes of this study, this rebinned image was rescaled by a factor of $1/(K_2^2\text{-}1)$ to set accurately the underestimated noise caused by the simple rebinning. Poisson noise was again added to this rescaled image, by taking each pixel value as the mean of a Poisson distribution. The final image was created by scaling back this Poisson noise-added image by a factor of $(K_2^2\text{-}1)/\ K_2^2$. In order to conserve the surface brightness, it is necessary to use K_2^2 in the denominator.

In Fig. 3.14 we gave an example of clusters simulated via the method described above. This example illustrates how a cluster appears at high redshift. Subsequent to the simulation, we calculated morphology parameters for each cluster redshift and plotted them (Fig. 3.15).

Fig. 3.15 shows the morphology parameter measurements for simulated redshift clusters (Fig. 3.14). We simulated a few original clusters with various redshifts, using the method described above, and re-calculated morphology parameters for each simulated cluster. The data points of each cluster were joined with a line, to illustrate the trend between morphology parameters and the various redshifts. Fig. 3.15 illustrates that the Smoothness is systematically increased with redshift. The reason could be that high-z clusters are noisy and appear patchy. The Ellipticity parameter appears particularly noisy. Except for a few clusters, and after $z \gtrsim 0.5$, the Gini, M_{20}, Concentration, Asymmetry and Gini of the second order moment parameters are fairly constant, and the systematics caused by redshifts are small.

3.5 Combination of morphology parameters

We decided to further classify dynamical states of each cluster based on the combination of Gini, M_{20} and Concentration. In § 3.3.2, we defined three parameter boundaries, i.e. Gini (relaxed clusters have a Gini value > 0.65 and non-relaxed clusters have Gini value < 0.40, while all intermediate clusters fall between these two values), M_{20} (relaxed clusters have a M_{20} value $<$

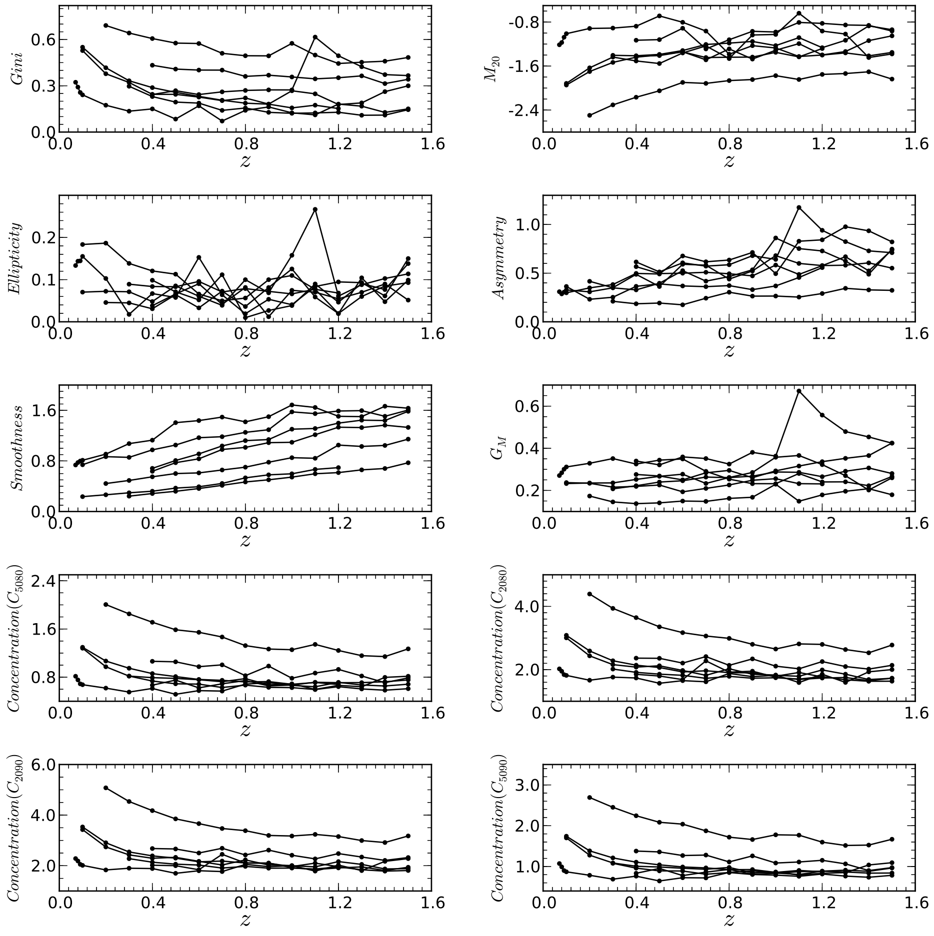

Figure 3.15: Robustness of morphology parameters which are calculated for several clusters against simulated clusters at different redshifts.

-2.0 and non-relaxed clusters have M_{20} value > -1.4, while all intermediate clusters fall between these two values) and Concentration (relaxed clusters have a Concentration value > 1.55 and non-relaxed clusters have Concentration value < 1.0, while all intermediate clusters fall between these two values). Based on the combination of these three parameters, we categorised the V09 sample of clusters into four stages - strong relaxed (strong cool core), relaxed (cool core), non-relaxed (weak cool core) and strong non-relaxed (non-cool core) clusters. We selected the following criteria for identifying the dynamical state of each cluster:

- If the Gini, M_{20} and Concentration all indicate relaxed state, then the cluster will be "strong relaxed or strong cool core".
- The intermediate state of clusters is further divided into two classes: if one or two parameters fall into the intermediate state and another is relaxed (non-relaxed), then the cluster will be "relaxed (non-relaxed) or cool core (weak cool core)".
- If all three parameters indicate a non-relaxed state, then the cluster will be "strong non-relaxed or non-cool core".

Based on these categories, in the entire V09 cluster sample, 8 (∼ 10%) clusters were strong relaxed, 11 (∼ 13%) were relaxed, 52 (∼ 62%) were non-relaxed, and 13 (∼ 15%) were strong non-relaxed. In the low-z sample, there were 7 (∼ 15%) strong relaxed, 6 (∼ 12.5%) relaxed, 29 (∼ 60%) non-relaxed, and 6 (∼ 12.5%) strong non-relaxed clusters. In the high-z sample, there were 1 (∼ 3%) strong relaxed, 5 (∼ 14%) relaxed, 23 (∼ 64%) non-relaxed, and 7 (∼ 19%) strong non-relaxed clusters. This could suggest that the highest fraction of clusters (in the V09 sample) are evolving or showing some substructure activity (particularly in the high-z sample) and that fewer clusters are fully evolved. Fig. 3.16 shows the 3-D plot of the Gini, M_{20} and Concentration parameters. A combination of these three parameters classified galaxy clusters as strong relaxed (•), relaxed (⋄), non-relaxed (+) and strong non-relaxed clusters (×). The following sections offer a comparison between the different dynamical states of clusters and their global properties.

3.6 Comparison of parameters with X-ray gas properties

3.6.1 X-ray luminosity, temperature and mass

Our study compared seven morphology parameters with three global cluster properties (luminosity, temperature and mass) taken from the V09 to search for any possible correlation of these global properties with cluster morphology. Fig. 3.17 shows a comparison, while Table 3.9 and Table 3.10 list the Spearman coefficient and probability values, respectively calculated for the clusters' global properties and galaxy cluster morphologies. Fig. 3.17 defines each clusters' dynamical state according to the combination of the Gini, M_{20} and Concentration morphology parameters (§ 3.5).

No obvious correlation between cluster morphology and X-ray global properties was found during our analysis. This may have been due to the fact that quantities such as X-ray luminosity and temperature are not solely related to the dynamical state of clusters (Hashimoto et al., 2007). These properties also depends strongly on cluster mass and on non-gravitational processes such as supernovae feedback, central AGN heating, etc. (Donnelly et al., 1999; Tozzi & Norman, 2001;

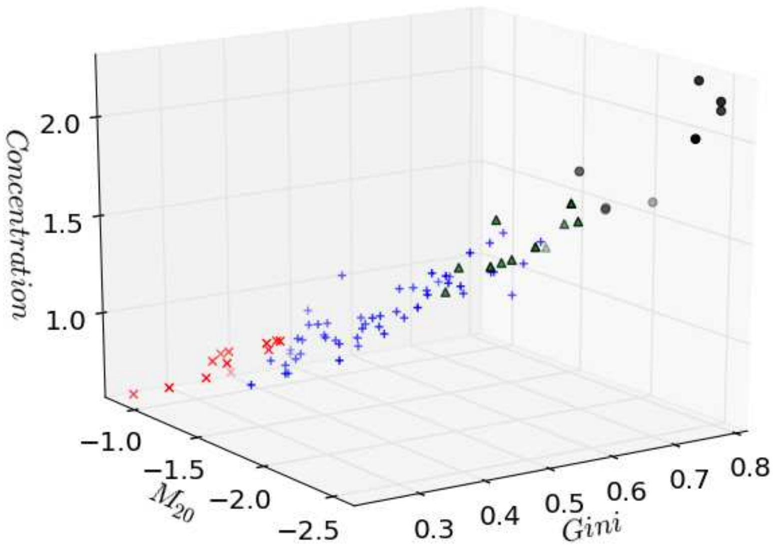

Figure 3.16: Gini, M_{20} and Concentration parameters plotted in the 3-D plot. We plotted C_{5080} as the Concentration parameter. ● = strong relaxed (strong cool core) clusters, △ = relaxed (cool core) clusters, + = non-relaxed (weak cool core) clusters, and × = strong non-relaxed (non-cool core) clusters.

Table 3.9: Spearman coefficient, ρ, for morphology parameters and X-ray global properties (luminosity, temperature and mass).

	Luminosity	Temperature	Mass
Gini	0.19	0.03	0.03
M_{20}	-0.13	0.03	0.07
Concentration	0.18	-0.03	-0.05
Asymmetry	-0.22	-0.23	-0.25
Smoothness	-0.33	-0.26	-0.30
G_M	-0.25	-0.17	-0.21
Ellipticity	0.26	0.30	0.35

Neumann et al., 2003). Buote & Tsai (1996) also compared their power-ratio measurements for X-ray clusters with the ICM temperature and luminosity, without finding any strong correlation between subclustering and global X-ray properties. In agreement with our conclusion, they pointed out that this lack of correlation is reasonable, since power ratios are a measure of cluster evolution that do not take into account the cluster mass, to which all the other X-ray quantities (e.g. luminosity and temperature) are sensitive. We observed that all relaxed clusters occupy high Gini, low M_{20} and high Concentration values in all three plots. We therefore concluded that, to identify the dynamical state of a galaxy cluster, X-ray global properties are not as useful as the surface brightness distribution or cluster morphology, quantifiable using morphology parameters.

3.6.2 X-ray cluster cooling time

X-ray emission is considered to be the primary cooling process for the ICM. Since X-ray bremsstrahlung emissivity is proportional to the square of the plasma density, the dense centres of a significant fraction of clusters have bright nuclei and low temperature, where cooling is at a maximum compared with that of other parts of the cluster. The cooling time is much shorter than the Hubble

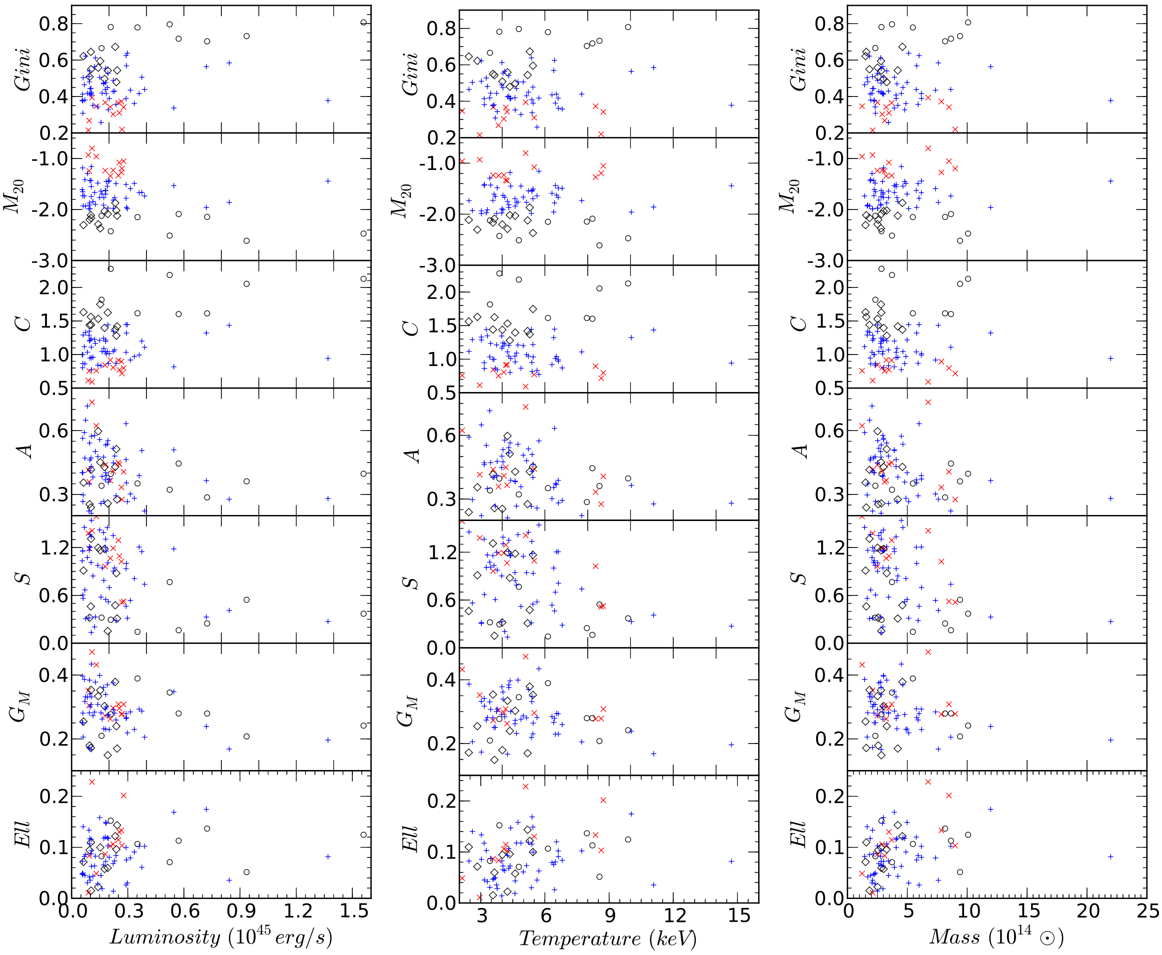

Figure 3.17: Comparison of **Left** Luminosity, **Middle** Temperature and **Right** Mass (estimated from the Y_X parameter) with morphology parameters. ○ = strong relaxed (strong cool core) clusters; ◊ = relaxed (cool core) clusters; + = non-relaxed (weak cool core) clusters; and × = strong non-relaxed (non-cool core) clusters. We plotted C_{5080} as the Concentration parameter. We take all these global properties (luminosity, temperature and mass) values from the V09.

Table 3.10: Spearman test probability, p, for morphology parameters and X-ray global properties (luminosity, temperature and mass).

	Luminosity	Temperature	Mass
Gini	0.08	0.77	0.77
M_{20}	0.23	0.81	0.56
Concentration	0.10	0.81	0.66
Asymmetry	0.05	0.03	0.02
Smoothness	0.0	0.02	0.01
G_M	0.02	0.13	0.05
Ellipticity	0.02	0.01	0.0

time at the centre of a cluster, allowing gas to cool from a high ICM temperature $\sim 10^8$ K down to $\sim 10^7$ K.

Numerical simulations suggest that cluster mergers may disturb the cooling flow, and it has been observed that in non-relaxed clusters the cooling flow is either absent or at a very low level (Ritchie & Thomas, 2002; Burns et al., 2008; Hudson et al., 2010). It is important to know how, and in what condition, this cooling flow is disrupted in non-relaxed clusters. We aimed to investigate the relationship between the degree of substructure and cooling times or rates of a cluster. We used the cooling time information supplied by Hudson et al. (2010). Table 3.11 lists the cooling time values for low-z clusters.

Hudson et al. (2010) calculated the average cooling time using the best-fit temperature as

$$t_{cool} = \frac{3}{2}\frac{(n_e + n_i)kT}{{n_e}^2\Lambda(T, Z)}, \tag{3.7}$$

where n_e and n_i are the electrons and number density of ions, respectively. They calculated the cooling function, $\Lambda(T, Z)$, by spline interpolation on a table of values for the APEC model, for an optically thin thermal plasma. They defined the central cooling time (CCT) as

$$t_{cool}(0) = \frac{3}{2}\zeta\frac{(n_{e0} + n_{i0})kT_{48}}{(n^2{}_{e0})\Lambda(T_{48})}, \tag{3.8}$$

where n_{e0} and n_{i0} are the central electron and ion densities, respectively, and T_{48} is the average temperature of the 0-0.048 R_{500} region.

Table 3.11 gives the cooling time values for the low-z clusters. Of the relaxed systems (as identified by the V09), A3158, A3391, Zwcl1215, A3562 and A401 have relatively high cooling time values. These systems were classified as non-relaxed clusters by our combination of morphology parameters. In the non-relaxed sample (again from the V09), only three clusters - A3558, A1644, and A2065 have relatively short cooling times. The short cooling times may suggest that the cores of these clusters might not yet be disturbed by cluster merger. Rossetti et al. (2007) analysed the *Chandra* and *XMM* observations of A3558 and found that its cool core had survived a merger. The *Chandra* observations show bright cluster nuclei, which also supports this idea. Chatzikos et al. (2006) showed that A2065 is an unequal mass merger, which could be a reason behind the survival of one of its cool cores. According to the classical definition of a cooling flow, $t_{cool} < t_{age}$, where t_{age} (age of galaxy cluster) $\sim$ 10 Gyr. We found the mean t_{cool} value for strong relaxed clusters to be 0.44 Gyr, for relaxed clusters 0.64 Gyr, for non-relaxed clusters 4.72 Gyr, and for strong non-relaxed clusters 12.5 Gyr. This implies that the cooling mechanism is completely disturbed in strong non-relaxed clusters, while only $\sim$ 17% are completely disturbed among non-relaxed clusters (five non-relaxed clusters have $t_{cool} > t_{age}$). Unfortunately, we did not have cooling time information for the high-z clusters in our sample.

The correlation of morphology parameters with cooling time is plotted in Fig. 3.18 for the Concentration, Gini and M_{20}, respectively, on a log-log scale. Figs. 3.18a, 3.18b and 3.18c show that two of our parameters, the Concentration and Gini, are anti-correlated, while the M_{20} is correlated with the cooling time of clusters. This indicates the possibility that surface brightness imaging data could be useful in deriving the cooling time information of the central intracluster gas using simple morphology parameters. Table 3.12 and Table 3.13 list the Spearman coefficient, ρ,

Table 3.11: Available cooling time, t_{cool}, values from Hudson et al. (2010) for the low-z clusters.

Cluster name	t_{cool} (Gyr)	Cluster name	t_{cool} (Gyr)
A3571	$2.13_{0.71}^{-0.43}$	A2597	$0.42_{0.04}^{-0.03}$
A2199	$0.6_{0.07}^{-0.06}$	A133	$0.47_{0.03}^{-0.03}$
A0335	$0.31_{0.01}^{-0.01}$	A2244	$1.53_{0.27}^{-0.2}$
A496	$0.47_{0.02}^{-0.02}$	RXJ1504	$0.59_{0.02}^{-0.02}$
A85	$0.51_{0.04}^{-0.04}$	A2204	$0.25_{0.01}^{-0.01}$
A478	$0.43_{0.1}^{-0.07}$	A2029	$0.53_{0.04}^{-0.04}$
A1795	$0.61_{0.02}^{-0.02}$	A2142	$1.94_{0.16}^{-0.14}$
A4038	$1.68_{0.12}^{-0.11}$	A3562	$5.15_{0.72}^{-0.57}$
A2052	$0.51_{0.02}^{-0.02}$	A401	$8.81_{1.41}^{-1.08}$
Hydra-A	$0.41_{0.02}^{-0.02}$	A3558	$1.69_{1.15}^{-0.5}$
A2063	$2.36_{0.14}^{-0.13}$	A2147	$17.04_{3.64}^{-2.72}$
A3158	$8.22_{0.54}^{-0.47}$	A3266	$7.62_{2.63}^{-1.6}$
MKW3s	$0.86_{0.18}^{-0.13}$	A119	$14.03_{5.95}^{-3.43}$
EXO0422	$0.47_{0.07}^{-0.05}$	A1644	$0.84_{0.32}^{-0.18}$
A4059	$0.7_{0.07}^{-0.06}$	A1736	$16.59_{13.17}^{-5.52}$
A2589	$1.18_{0.33}^{-0.22}$	A3395	$12.66_{3.04}^{-2.18}$
A3112	$0.37_{0.08}^{-0.05}$	A2065	$1.34_{0.37}^{-0.24}$
A1651	$3.63_{0.43}^{-0.37}$	A3667	$6.14_{0.52}^{-0.45}$
A576	$3.62_{0.84}^{-0.59}$	A754	$9.53_{2.37}^{-1.64}$
A2657	$2.68_{1.2}^{-0.66}$	A2256	$11.56_{2.43}^{-1.81}$
A3391	$12.46_{2.49}^{-1.89}$	A399	$12.13_{1.44}^{-1.22}$
A1650	$1.25_{0.29}^{-0.2}$	A2163	$9.65_{0.73}^{-0.78}$
S1101	$0.88_{0.2}^{-0.14}$	A3376	$16.47_{3.1}^{-2.35}$
zwcl1215	$10.99_{2.09}^{-1.61}$		

Table 3.12: Spearman coefficient, ρ, between morphology parameters and cluster cooling time.

Morphology parameters	Cooling time (Gyr)
Concentration	-0.82
Gini	-0.71
M_{20}	0.83

Table 3.13: Spearman test probability, p, between morphology parameters and cluster cooling time.

Morphology parameters	Cooling time (Gyr)
Concentration	0.0
Gini	0.0
M_{20}	0.0

and corresponding probability, p, respectively between the Concentration, Gini and M_{20} parameters and cluster cooling time.

In order to investigate linear fitting, we simply used the power-law model to establish a relationship between the morphology parameters and t_{cool} (Fig. 3.18). For all three parameters, compositely, we constituted $t_{cool} \propto \mathrm{Conc}^{-3.42\pm0.55}$, $t_{cool} \propto \mathrm{Gini}^{-3.0\pm0.35}$ and $t_{cool} \propto M_{20}^{4.23\pm0.32}$.

3.7 Scaling relation: Luminosity vs Temperature

Scaling relations between the X-ray observables are important in understanding the physical processes that give rise to these relations (Arnaud & Evrard, 1999; Neumann & Arnaud, 1999; Maughan, 2007; Pratt et al., 2009; Mittal et al., 2011; Maughan et al., 2012). Compared with temperature, X-ray luminosity can be a direct and easier measure from X-ray data, and it correlates with cluster mass. It allows for mass-function measurements using much larger cluster samples, understanding the selection functions of X-ray cluster surveys and examining the history of the heating mechanisms in clusters (e.g. Maughan et al., 2012, and references therein). Further, the observed $L_X - T$ relationship is important for calibrating the mass-luminosity relationship (Borgani et al., 1999). The total X-ray luminosity (or X-ray bolometric luminosity) of a cluster is related to the baryon number density through thermal bremsstrahlung, while the X-ray temperature is determined by the gravitating mass of the cluster. Hence, the $L_X - T$ relationship constitutes a direct and sensitive probe of the volume-averaged baryon fraction of the cluster.

We derived the $L_X - T$ scaling relation for our sample of clusters. We subdivided the clusters in our sample according to their different dynamical states, based on the combination of morphology parameters (§ 3.5). For low-z clusters, we used the bolometric luminosity (0.01–40 keV) of clusters as given by Reiprich & Böhringer (2002). For the high-z clusters, we derived bolometric luminosity (0.01–40 keV) using *webspec**. For calculating it, we used the Mekal spectra for a set of temperatures and compute fluxes in the 0.5-2 and 0.01-40 keV bands. Then we multiplied this ratio (between 0.5-2 and 0.01-40 keV bands) with the flux values as given by the V09 for each high-z cluster. For computing this, we fixed abundance to the solar value of 0.3. For both the low- and high-z samples we used temperature values from the V09 and derive the $L_X - T$ relationship. As described earlier

---

*http://heasarc.nasa.gov/webspec/webspec.html

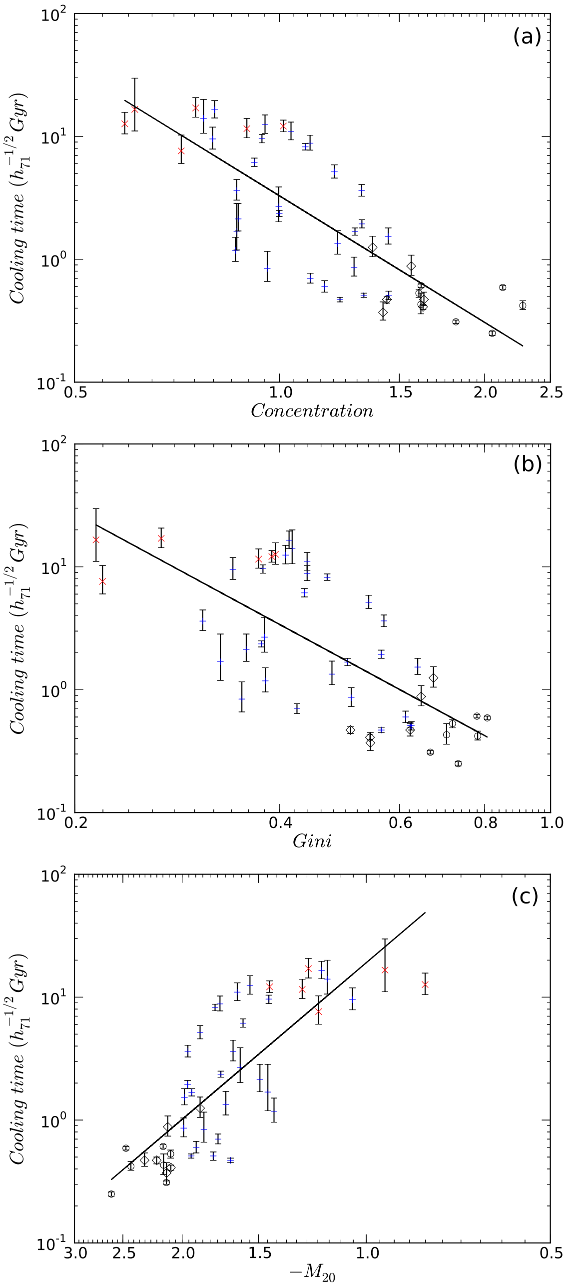

Figure 3.18: (a) Concentration (C_{5080}) parameter negatively correlated with cooling time for fixed radii. (b) Gini coefficient negatively correlated with cooling time. (c) M_{20} correlated with cooling time as calculated by equation 3.8. ○ = strong relaxed (strong cool core) clusters; ◊ = relaxed (cool core) clusters; + = non-relaxed (weak cool core) clusters; and × = strong non-relaxed (non-cool core) clusters. We used the power-law fitting to show the linear correlation.

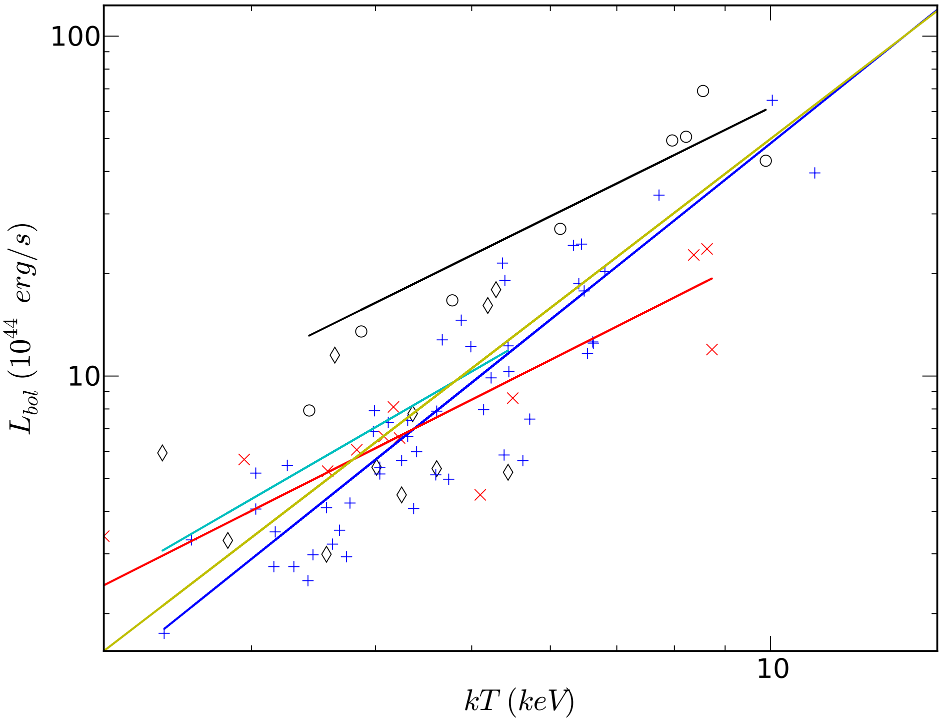

Figure 3.19: Relationship between luminosity and temperature for our sample clusters. ○ = strong relaxed (strong cool core) clusters; ◇ = relaxed (cool core) clusters; + = non-relaxed (weak cool core) clusters; and × = strong non-relaxed (non-cool core) clusters. We used the power-law model to determine best-fit line for the $L_X - T$ relationship. The solid black line = best-fit for strong relaxed; the solid cyan line = best-fit for relaxed; the solid blue line = best-fit for non-relaxed; the solid red line = best-fit for strong non-relaxed; and the solid yellow line = combined best-fit for the whole sample clusters.

(§ refcombpara), in our sample, we had a total of 8 strong relaxed, 11 relaxed, 52 non-relaxed and 13 strong non-relaxed clusters. The X-ray luminosity-temperature relationship for these 84 clusters is shown in Fig. 3.19. In this figure, ○ shows the strong relaxed (strong cool core), ◇ shows the relaxed (cool core), + shows the non-relaxed (weak cool core), and × shows the strong non-relaxed (non-cool core) clusters. In Fig. 3.19, we also showed a best-fitted line calculated using the power-law model

$$L_X = L_6 \left(\frac{T}{6\ keV} \right)^{\alpha_{LT}}, \tag{3.9}$$

where L_X is the bolometric luminosity, and T is the temperature normalised by 6 keV which is the common temperature for rich clusters (close to the mean temperature of 5.09 keV of our sample clusters). On cluster scales, the relationship between the total X-ray luminosity and temperature is approximately a power-law. Table 3.14 lists the best-fit slope (α_{LT}) and amplitude (L_6) values. We noticed that the combined slope of all clusters is $\gtrsim 2$. We also listed slope values for each category of dynamical states. Fig. 3.19 records our observation that the four dynamical states of all clusters (as well as their best-fitted lines) were separated in the $L_X - T$ plane, indicating a possibility of different evolution for each of the four different dynamical states of clusters. There is, however, scattering between different dynamical states of clusters.

Table 3.14: Best-fit values for $L_X - T$ relationship.

Cluster dynamical state	α_{LT}	L_6
strong relaxed	1.44 ± 0.47	29.51 ± 5.24
relaxed	1.69 ± 1.00	14.04 ± 4.24
non-relaxed	2.34 ± 0.09	14.65 ± 0.96
strong non-relaxed	1.47 ± 0.30	11.15 ± 1.20
combine	2.24 ± 0.10	15.85 ± 1.04

3.8 Discussion and Conclusion

In this work we showed how we used morphology parameters, to date applied only to quantifying galaxy morphologies, to obtain constraints on the dynamical state of clusters. These parameters do not depend on any model parameter fits, such as the Beta model or power-law, and can therefore be applied to both disturbed and regular clusters. In principle, the Gini, Concentration and M_{20} are very promising for the detection of disturbances in clusters at any scale. The Concentration had already been used by a number of authors to quantify substructure, particularly at high-z where most of the observations have lower exposure time and suffer from low S/N (Santos et al., 2008; Cassano et al., 2010b). In order to measure the Concentration, it was necessary to fix the cluster centre position (either optical position of the BCG or the simple image first order moment or barycentre) and then define the inner and outer regions around the chosen centre. This is not always possible in many of the high-z (~ 1) clusters due to low photon counts and distorted cluster morphology. In this work, we showed a tight correlation between the Concentration and the Gini coefficient for both the low- and high-z clusters. This suggested that the Gini coefficient could be used as a replacement for the Concentration mainly for high-z clusters. The chief benefit of using the Gini coefficient is that we do not need a well-defined cluster centre. It works well for low photon counts as well as accurately quantifying substructure. It is completely independent of cluster shape, it does not depend on any symmetry underlying the cluster, and is independent of the location of projected (bright) pixels (whether they be at the centre or the edge) in the given aperture.

The Gini coefficient was also correlated with the M_{20}, which could suggest that, in a relaxed system, 20% of the X-ray flux is centrally located where the electron density is high, while this is not possible for distorted and non-relaxed clusters where mergers may change the cluster density distribution. Most relaxed and cool-core clusters have Gini > 0.65, which means that most of the flux comes from only a small number of bright pixels, mainly found at the cluster centre. Weak cool-core clusters were found between $0.4 <$ Gini < 0.65, and most disturbed clusters had Gini < 0.4. This is obvious because, in non-relaxed clusters, the X-ray emission (or bright pixels) is not compact but equally distributed in the given aperture radius which gives a low Gini value.

We also found a tight correlation between the Concentration and the M_{20}. Although these parameters have similar definitions, they measure different things. The M_{20} is useful in locating 20% of the brightest pixels in a given cluster image, while the Concentration measures the ratio between the inner and outer radii containing specific percentages of flux, to quantify which region is brighter. In the case of relaxed clusters, the inner region is brighter than the outer, and 20% of the bright pixels are closer to the cluster centre. We computed the Concentration for four definitions: 20-80%, 50-80%, 20-90% and 50-90% inner to outer radii. We noticed similar results for all four definitions of the Concentration parameter for all clusters. Most relaxed clusters had Concentration $>$ 1.55, Gini $>$ 0.65 and M_{20} $<$ -2.0, while weak cool core (intermediate) clusters had 1.55 $>$ Concentration $>$ 1.0, 0.65 $>$ Gini $>$ 0.4 and -1.4 $>$ M_{20} $>$ -2.0. Distorted and non-relaxed clusters had Concentration $<$ 1.0 and M_{20} $>$ -1.4, while the Gini coefficient had $<$ 0.4.

The Smoothness and Asymmetry parameters trace the 2-D morphology of galaxy clusters. Unlike the Gini, M_{20} and Concentration parameters, however, these two parameters did not show any sign of being able to classify galaxy clusters based on their dynamical state. We showed similar results in Chapter 2, where we calculated morphology parameters for MARX simulated clusters which had heterogeneous exposure time. In this situation, the Asymmetry and Smoothness were not useful parameters. They largely depended on cluster exposure time. In our sample, we did not have uniform exposure time for all clusters, which affects S/N and photon counts between clusters. This could have caused difficulty for the Smoothness and Asymmetry parameters to separate relaxed and non-relaxed clusters. Both of these parameters, however, could still be useful to trace or study other physical properties of galaxy clusters. For example, Zhang et al. (2010) demonstrated a relationship between the Asymmetry parameter and mass ratio, for masses deduced from X-ray hydrostatic equilibrium and weak-lensing. They also showed a relationship between the their Fluctuation (Smoothness) parameter and gas mass to weak lensing mass ratio. In our study, it was observed that the Gini of the second order moment parameter was also sensitive to S/N of data, rendering this parameter also not useful.

We used a combination of the Gini, M_{20} and Concentration parameters to further categorise clusters into strong relaxed (strong cool core), relaxed (cool core), non-relaxed (weak cool core) and strong non-relaxed (non-cool core) clusters. From this separation we found that, in the entire V09 cluster sample (low and high-z), we had 8 ($\sim$ 10%) strong relaxed, 11 ($\sim$ 13%) relaxed, 52 ($\sim$ 62%) non-relaxed and 13 ($\sim$ 15%) strong non-relaxed clusters. In the low-z sample, there were 7 ($\sim$ 15%) strong relaxed, 6 ($\sim$ 12.5%) relaxed, 29 ($\sim$ 60%) non-relaxed and 6 ($\sim$ 12.5%) strong non-relaxed clusters. In the high-z sample, 1 ($\sim$ 3%) strong relaxed, 5 ($\sim$ 14%) relaxed, 23 ($\sim$ 64%) non-relaxed and 7 ($\sim$ 19%) strong non-relaxed clusters were present. This could suggest that majority of clusters in the V09 sample continue to evolve, showing some substructure activity, and that the minority are fully evolved. There are more non-relaxed and strong non-relaxed clusters in the high-z sample than there are in the low-z sample.

We did not found any relationship between the morphology parameters and X-ray global properties of galaxy clusters. This is most likely due to the fact that morphology parameters are estimated without regard for the mass of clusters, to which other quantities, such as X-ray luminosity and temperature, are instead related. The Gini, Concentration and M_{20} appear to be correlated with the cooling time of clusters. X-ray imaging and surface brightness maps are therefore useful in investigating the cooling time of relaxed clusters.

The morphology parameters studied in this thesis were robust in various physical or observational conditions (high redshift, low exposure, etc). They helped us to investigate, with sufficient accuracy, cluster morphology and dynamical state. We noticed, however, that the Gini, Gini of the second order moment and Asymmetry are fairly weak parameters at $<$ 5 ks exposure time. The Smoothness parameter systematically decreased with increasing exposure time. The Smoothness parameter is therefore not suitable when comparing objects with a range of redshifts and/or exposure times. We therefore recommend that this be taken into account in any estimation of the Smoothness parameter for X-ray galaxy clusters. The Concentration and M_{20} are reasonably robust at low exposure times. Systematics associated with redshift effects are low, but some caution is required in the interpretation of the results based on simulated clusters. We concluded that the Concentration and M_{20} are more robust than the other parameters.

We derived the $L_X - T$ scaling relation for sample clusters, and separated the different dynamical states of cluster according to the combination of morphology parameters. This classification is important in the study of the $L_X - T$ scaling relation, in terms of understanding different heating mechanisms and energy input to the system. For example, Maughan et al. (2012) studied this relationship for a sample of 114 *Chandra* observed galaxy clusters. They categorised clusters into subsamples according to their X-ray morphology or whether they host strong cool cores. From this work, they concluded that massive relaxed or cool core clusters ($T > 3.5$ keV) obey strong self-similarity outside the core ($r < 0.15 R_{500}$) regions in an $L_X - T$ relationship with a slope of $\approx$ 2. On the other hand, the $L_X - T$ slope of non-relaxed clusters is significantly steeper than that of the self-similar model. Their results are consistent with a model of non-gravitational energy input in clusters that combines central heating with entropy enhancements from merger shocks. A self-similar correlation such as theirs had not been observed before in the $L_X - T$ scaling relation, possibly due to the fact that most previous analyses had not separated cool core and non-cool core subsamples (Maughan et al., 2012). This suggests that it is important to classify cluster dynamical states when studying scaling relations. Clearly, the $L_X - T$ relationship has to be measured in greater detail with larger samples of well exposed clusters in order to reach a consensus of its evolution. Knowledge of this evolution is crucial in measuring the mass function of clusters in order to constrain cosmological parameters.

In our $L_X - T$ relationship plot we showed that various dynamical states of clusters occupy well-defined loci in the $L_X - T$ plane. There is, however, scattering visible among different dynamical states of clusters, which suggests that there could be a bias in calculating bolometric luminosity and global temperature. For instance, in the case of merger clusters, the flux from disturbed and extended outskirts regions is typically diffuse and faint, and therefore unlikely to be detected because of the limited aperture size of X-ray telescopes (e.g. *ROSAT*) in the measurement of total X-ray luminosity and temperature (Hashimoto et al., 2007). This results in a systematic underestimation of bolometric luminosity and an overestimation of temperature. Similarly, the presence of a cluster cool core could raise bias in the calculation of either luminosity (overestimated) or temperature (underestimated). Fig. 3.19 indicates that both of these effects might introduce scattering into our plot.

It would be interesting to apply these basic morphology parameters to hydrodynamical simulations in order to investigate whether simulations actually re-create the true shape, flux distribution and substructure based on real clusters.

4

XMC modelling

4.1 Background

In this Chapter, we will show the importance of 2-D thermodynamic maps of galaxy clusters to study substructure or dynamical activity among them. We used the XMC technique to generate thermodynamic maps of low-z (0.02–0.3) clusters of the V09. As a start, we plotted radial profiles of each thermodynamic map of every cluster to investigate fluctuations and discontinuities in corresponding radial profiles. Subsequently, we applied morphology parameters on these maps to study their morphology. Then we compared the power-law slope values of each profile with surface brightness morphology parameters. We also investigated radial profiles of individually strong relaxed and strong non-relaxed clusters.

4.2 XMC method

Firstly, we describe the basic method and steps required to run the XMC. It is assumed that the given intra-cluster hot gas is composed of a number of Gaussian “blobs” or smooth particles. Each blob has its own temperature, flux, abundance, electron density, phi and psi (sky location), Gaussian width (size), redshift, absorption column, etc. X-ray emission from these hypothetical “blobs” is then propagated through the (simulated) telescope’s instrument, generating dummy X-ray events in a similar way to that which would come from an actual X-ray observation. These simulated events are compared with the real data events being modelled. The input ICM parameters (temperature, flux, sky position, etc.) are iterated using the adaptive Markov Chain Monte Carlo (MCMC) method to explore the likelihood distribution of the parameter space. When all parameters are converged after a sufficient number of iterations, the resulting distribution of blobs describes the shape and characteristics of the galaxy cluster under investigation (Andersson et al., 2007). The advantage of the XMC technique is that it explores, with the MCMC method, the extremely high dimensionality of parameter space of the blobs for a given ICM model. The MCMC technique efficiently samples the probability distribution of a model’s parameters without being trapped in local likelihood maxima. The results is a well fitted list of sample cluster models, all of which are consistent with the data.

Fig. 4.1 shows the basic block diagram of the XMC technique*. As shown in this Figure, real X-ray Chandra telescope data is modelled using the SPI (Smooth Particle Inference) technique which basically accumulates a number of two-dimensional spatial Gaussian blobs with individual spectral and spatial models. In our analysis, we used the APEC model to describe the X-ray emission from the hot ICM. Model photons are simulated and propagated through the *Chandra*-ACIS detector model, and to that are added particle background Monte Carlo events which include internal fluorescent lines, electronic & CCD noise and soft proton signals. Real data and model photons are binned in three-dimensional adaptive bins, and compared via a two-sample likelihood function. All spatial and spectral parameters for each blob are iterated in a Markov chain with an adaptive step length. Finally, all model samples in the converged part of the chain are used to reconstruct the cluster. However, because the XMC method is extremely computing intensive, we conducted this analysis on the Centre for High Performance Computing (CHPC) cluster in Cape Town, South Africa.

4.3 Data sample

In this analysis, we used two galaxy cluster samples. Our first sample is derived from the V09. Due to uncertainty and not having adequate S/N in high redshift galaxy cluster observations, we were restricted to low redshift clusters for the XMC analysis; furthermore, we did not have adequate information about the XMC version for the *Chandra* telescope. From the V09 we took the low redshift galaxy cluster sample, a detailed description of which is given in Chapter 3.

Our second sample is derived from the KA09, and described in Table 4.1. The clusters were observed with the *XMM-Newton* telescope. The sample was taken from the *XMM-Newton* archive as of 2006 May 10, and analysed using the XMC technique developed for the *XMM-Newton* telescope (KA09). In deriving the cluster sample, KA09 used the selection criteria that:

- the cluster should be a known X-ray source (galaxy clusters or groups) from the NASA Extragalactic Database (NED) with the public *XMM-Newton* observation archive,
- the *XMM-Newton* pointing was required to be within $3\overset{\prime}{.}5$ of the source position in the NED,
- cluster observation should contain time-integrated energy flux above 10^{-8} erg/cm^2 as well as redshift above 0.065.

The final selection includes 101 sources. This sample describes a wide range of cluster properties over a large range of redshift (KA09). The sample includes clusters which have luminosities ranging from 9×10^{43} erg/s to 1.1×10^{46} erg/s, average temperatures from 2.2 to 11.6 keV and redshifts from $z = 0.069$ to 0.89. KA09 calculated the bolometric luminosities (and applied a bolometric correction) from the observed flux, using tabulated redshifts as mentioned in the NED (Table 4.1).

---

*XMC manual

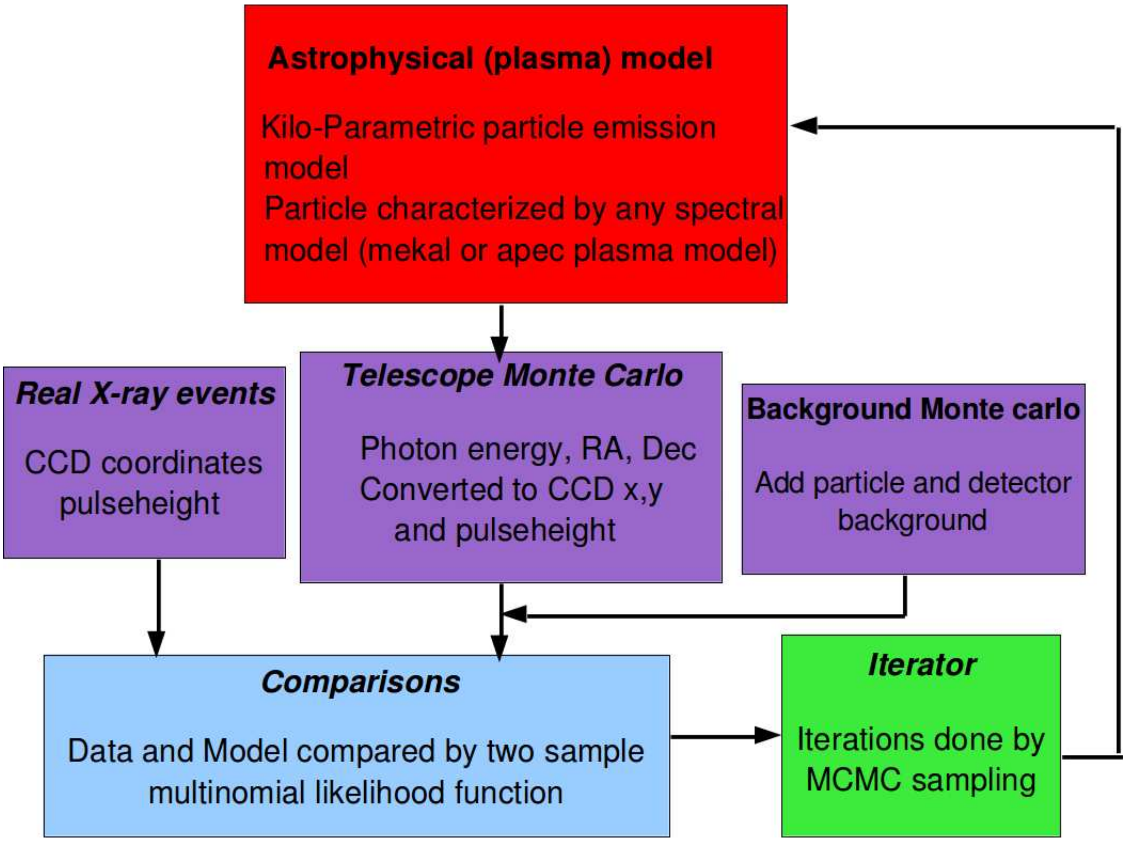

Figure 4.1: XMC flow chart showing the basic method for X-ray cluster modelling. (1) **Thousands of smooth particles represent the ICM. Each particle has its own sky position, size, temperature, metallicity, luminosity, etc. These parameters predict incoming photons from the precise sky co-ordinates with associated energies**. (2) **Position and energies of incoming photons are converted to detector co-ordinates and pulse height via the direct sampling Monte Carlo technique. These conversion methods utilise the telescope's response functions and create multiple photons per second. At this stage, the simulated background (sky + instrument) is also added to these simulated events**. (3) **These simulated data are compared with the actual X-ray events**. (4) **XMC used multi-dimensional likelihood statistics for comparison between simulated and real events**. (5) **In the successive steps, (free) parameters of the particles are iterated using the MCMC technique. The final results have a number of statistical samples of acceptable or converged fits which fall into the "confidence region" of the particle's input parameters. This well "fitted" number of particles describe the ICM.**

Table 4.1: Cluster sample from the KA09: (1) cluster name; (2) redshift; (3) temperature; (4) X-ray bolometric luminosity; (5) dynamical state (based on the combination of morphology parameters (Gini, M_{20} and Concentration); SR = Strong relaxed, R = Relaxed, NR = Non-relaxed, SNR = Strong non-relaxed)

Name	z	Temperature (keV)	L_{bol} (erg/s)	Dynamical state
CIZAJ1645.4-7334	0.069	$3.86^{0.24}_{-0.22}$	$3.9{\times}10^{44}$	R
A1837	0.07	$3.85^{0.08}_{-0.08}$	$1.7{\times}10^{44}$	NR
A3112	0.07	$4.32^{0.05}_{-0.04}$	$6.4{\times}10^{44}$	SR
A1775	0.072	$3.7^{0.1}_{-0.06}$	$2.9{\times}10^{44}$	NR
A399	0.072	$6.92^{0.23}_{-0.23}$	$7.4{\times}10^{44}$	NR
A1589	0.072	$4.81^{0.2}_{-0.18}$	$2.1{\times}10^{44}$	NR
A2065	0.073	$5.36^{0.11}_{-0.1}$	$6.4{\times}10^{44}$	NR
A401	0.075	$7.79^{0.22}_{-0.23}$	$1.4{\times}10^{45}$	NR
A2670	0.076	$4.02^{0.12}_{-0.11}$	$3.3{\times}10^{44}$	NR
A2029	0.077	$6.88^{0.11}_{-0.08}$	$2.2{\times}10^{45}$	SR
RXCJ1236.7-3354	0.08	$2.8^{0.11}_{-0.1}$	$1.6{\times}10^{44}$	R
RXCJ2129.8-5048	0.08	$4.55^{0.26}_{-0.19}$	$2.6{\times}10^{44}$	SNR
A2255	0.08	$6.98^{0.35}_{-0.28}$	$6.7{\times}10^{44}$	NR
RXCJ0821.8+0112	0.082	$3.69^{0.29}_{-0.24}$	$1.3{\times}10^{44}$	NR
RXCJ1302.8-0230	0.083	$3.52^{0.09}_{-0.09}$	$1.9{\times}10^{44}$	NR
A1650	0.084	$5.53^{0.07}_{-0.08}$	$7.8{\times}10^{44}$	R
A1651	0.084	$6.2^{0.18}_{-0.16}$	$1{\times}10^{45}$	NR
A2597	0.085	$3.46^{0.03}_{-0.03}$	$6{\times}10^{44}$	SR
A1750	0.086	$4.45^{0.13}_{-0.13}$	$3.1{\times}10^{44}$	NR
A478	0.088	$6.04^{0.04}_{-0.04}$	$2.7{\times}10^{45}$	SR
A278	0.089	$3.39^{0.13}_{-0.14}$	$1.5{\times}10^{44}$	NR
A2142	0.09	$8.15^{0.24}_{-0.28}$	$2.9{\times}10^{45}$	NR
A3921	0.094	$5.65^{0.15}_{-0.14}$	$6.3{\times}10^{44}$	NR
A13	0.094	$5.0^{0.17}_{-0.17}$	$2.8{\times}10^{44}$	NR
A3911	0.097	$5.94^{0.19}_{-0.14}$	$5.7{\times}10^{44}$	NR
RXCJ2319.6-7313	0.097	$2.27^{0.09}_{-0.07}$	$2.2{\times}10^{44}$	SR
CL0852+1618	0.098	$2.76^{0.25}_{-0.21}$	$9.63{\times}10^{43}$	NR
A3827	0.098	$6.93^{0.15}_{-0.13}$	$1.1{\times}10^{45}$	NR
RXCJ0211.4-4017	0.101	$2.22^{0.07}_{-0.07}$	$1.2{\times}10^{44}$	R
A2241	0.101	$3.66^{0.45}_{-0.28}$	$3{\times}10^{44}$	R
PKS0745-19	0.103	$6.44^{0.07}_{-0.07}$	$3.4{\times}10^{45}$	SR
RXCJ0645.4-5413	0.105	$7.39^{0.33}_{-0.26}$	$7.7{\times}10^{44}$	R
RXCJ0049.4-2931	0.11	$4.02^{0.19}_{-0.18}$	$3.4{\times}10^{44}$	R
A1302	0.116	$6.59^{0.46}_{-0.42}$	$5.6{\times}10^{44}$	NR
RXCJ0616.8-4748	0.116	$5.05^{0.45}_{-0.44}$	$3{\times}10^{44}$	NR
RXCJ2149.1-3041	0.118	$3.53^{0.07}_{-0.07}$	$3.8{\times}10^{44}$	SR
RXCJ1516.3+0005	0.118	$5.25^{0.16}_{-0.15}$	$4.7{\times}10^{44}$	NR
RXCJ1141.4-1216	0.119	$3.53^{0.06}_{-0.06}$	$4.1{\times}10^{44}$	SR
RXCJ0020.7-2542	0.131	$6.47^{0.27}_{-0.23}$	$5.8{\times}10^{44}$	NR
RXCJ1044.5-0704	0.134	$3.67^{0.04}_{-0.06}$	$7.3{\times}10^{44}$	SR

Continued on next page

Table 4.1 – *Continued from previous page*

Name	z	Temperature (keV)	L_{bol} (erg/s)	Dynamical state
RXCJ0145.0-5300	0.136	$6.8^{0.42}_{-0.44}$	8.3×10^{44}	NR
A1068	0.138	$3.81^{0.08}_{-0.07}$	8.4×10^{44}	SR
RXJ1416.4+2315	0.138	$3.58^{0.38}_{-0.33}$	2.2×10^{44}	NR
RXCJ0605.8-3518	0.141	$4.52^{0.08}_{-0.08}$	1×10^{45}	SR
A1413	0.143	$7.3^{0.19}_{-0.19}$	1.4×10^{45}	R
RXCJ2048.1-1750	0.147	$5.92^{0.28}_{-0.23}$	5.8×10^{44}	NR
A3888	0.151	$9.31^{0.69}_{-0.51}$	1.5×10^{45}	NR
A2034	0.151	$7.41^{0.27}_{-0.21}$	1.6×10^{45}	NR
RXCJ2234.5-3744	0.151	$7.88^{0.22}_{-0.22}$	1.5×10^{45}	NR
A2204	0.152	$6.44^{0.08}_{-0.09}$	3.5×10^{45}	SR
RXCJ0958.3-1103	0.153	$5.2^{0.19}_{-0.2}$	1×10^{45}	SR
A868	0.153	$5.86^{0.54}_{-0.39}$	6.8×10^{44}	NR
RXCJ2014.8-2430	0.154	$4.9^{0.08}_{-0.07}$	2×10^{45}	SR
A2104	0.155	$9.55^{1.43}_{-0.97}$	1.3×10^{45}	NR
RXCJ0547.6-3152	0.166	$6.92^{0.22}_{-0.2}$	1.1×10^{45}	NR
A2218	0.171	$7.17^{0.21}_{-0.17}$	1.1×10^{45}	NR
A1914	0.171	$9.49^{0.28}_{-0.18}$	2.7×10^{45}	NR
A665	0.182	$7.94^{0.23}_{-0.24}$	1.7×10^{45}	NR
A1689	0.183	$9.07^{0.17}_{-0.12}$	3.1×10^{45}	R
A383	0.187	$4.21^{0.09}_{-0.08}$	9.7×10^{44}	SR
A520	0.199	$8.45^{0.33}_{-0.26}$	1.7×10^{45}	SNR
A2163	0.203	$11.12^{0.3}_{-0.39}$	5.7×10^{45}	NR
A209	0.206	$7.21^{0.27}_{-0.26}$	1.5×10^{45}	NR
A963	0.206	$6.43^{0.22}_{-0.19}$	1.4×10^{45}	R
A773	0.217	$7.41^{0.33}_{-0.26}$	1.5×10^{45}	NR
A1763	0.223	$7.67^{0.34}_{-0.33}$	1.7×10^{45}	NR
A2261	0.224	$8.66^{0.71}_{-0.67}$	2.5×10^{45}	R
A267	0.231	$6.67^{0.38}_{-0.37}$	1.2×10^{45}	NR
A2390	0.231	$8.68^{0.29}_{-0.27}$	4×10^{45}	R
RXJ2129.6+0005	0.235	$5.74^{0.04}_{-0.1}$	2×10^{45}	SR
A1835	0.253	$7.14^{0.1}_{-0.11}$	4.9×10^{45}	SR
RXCJ0307.0-2840	0.253	$6.47^{0.38}_{-0.35}$	1.6×10^{45}	NR
E1455+2232	0.258	$4.59^{0.08}_{-0.09}$	1.9×10^{45}	SR
RXCJ2337.6+0016	0.273	$7.74^{0.66}_{-0.52}$	1.7×10^{45}	NR
RXCJ0303.8-7752	0.274	$8.21^{0.64}_{-0.62}$	1.8×10^{45}	NR
A1758	0.279	$9.16^{0.39}_{-0.43}$	1.9×10^{45}	SNR
RXCJ0232.2-4420	0.284	$7.13^{0.31}_{-0.29}$	2.6×10^{45}	NR
ZW3146	0.291	$6.21^{0.14}_{-0.1}$	4.1×10^{45}	SR
RXCJ0043.4-2037	0.292	$6.95^{0.46}_{-0.42}$	1.8×10^{45}	NR
RXCJ0516.7-5430	0.295	$8.33^{0.84}_{-0.74}$	1.7×10^{45}	SNR
RXJ0658-55	0.296	$11.58^{0.26}_{-0.35}$	5.7×10^{45}	SNR
RXCJ2308.3-0211	0.297	$7.22^{0.91}_{-0.67}$	1.3×10^{45}	NR
RXJ2237.0-1516	0.299	$3.46^{0.44}_{-0.42}$	3.1×10^{44}	SNR

Continued on next page

Table 4.1 – *Continued from previous page*

Name	z	Temperature (keV)	L_{bol} (erg/s)	Dynamical state
RXCJ1131.9-1955	0.307	$7.69^{0.55}_{-0.4}$	2.4×10^{45}	NR
RXCJ0014.3-3022	0.308	$8.36^{0.46}_{-0.45}$	3.1×10^{45}	NR
MS2137-23	0.313	$4.67^{0.17}_{-0.19}$	2.1×10^{45}	SR
MS1208.7+3928	0.34	$5.85^{1.04}_{-0.8}$	3.9×10^{44}	NR
RXJ0256.5+0006	0.36	$6.68^{1.02}_{-0.8}$	9.7×10^{44}	NR
RXJ0318.2-0301	0.37	$6.07^{1.07}_{-0.81}$	8.6×10^{44}	NR
RXJ0426.1+1655	0.38	$7.85^{2.64}_{-1.73}$	8×10^{44}	NR
RXJ1241.5+3250	0.39	$6.63^{0.74}_{-0.72}$	7.5×10^{44}	NR
A851	0.406	$6.25^{0.41}_{-0.45}$	9.9×10^{44}	SNR
RXCJ2228+2037	0.412	$9.03^{0.5}_{-0.49}$	2.6×10^{45}	NR
CL0016+16	0.541	$9.2^{0.5}_{-0.55}$	4×10^{45}	NR
MS0451.6-0305	0.55	$10.02^{0.8}_{-0.6}$	4.1×10^{45}	NR
RXJ1120.1+4318	0.6	$6.09^{0.89}_{-0.69}$	1.3×10^{45}	NR
MS1137.5+6625	0.782	$8.58^{2.33}_{-1.98}$	1.6×10^{45}	NR
MS1054.4-0321	0.823	$9.2^{1.26}_{-1.03}$	3×10^{45}	SNR
WARPJ0152.7-1357	0.837	$7.93^{0.73}_{-0.45}$	2×10^{45}	SNR
CLJ1226.9+333	0.89	$10.69^{0.82}_{-0.81}$	4.2×10^{45}	R

4.4 Data reduction and image preparation

XMC analysis for the *Chandra* telescope requires three input files: (1) the events file which includes information concerning cluster observation such as photon position, energy, photon arrival time, etc.; (2) the exposure map which is a combination of the amount of time the telescope spent on the source or on part of the sky, and instantaneous effective area across the field of view; and (3) the detector map which basically tells the XMC program which ACIS rmf (redistribution matrix file) to use from the given XMC-*Chandra* calibration files.

We processed all *Chandra* archival data with the CIAO version 4.3 and the CALDB version 4.4.6. First of all we used the `chandra_repro` task to reprocess all ACIS imaging data. This script creates a new second level event file as well as a bad pixel file by reading the data from the standard *Chandra* data distribution (which contains primary and secondary data files). This step applies the latest charge transfer inefficiency (CTI) correction, the latest time-dependent gain adjustment, the latest gain map, PHA and pixel randomisation. It also cleans the VFAINT background (if any) and uses continuous clocking mode times of arrival. After reprocessing, we removed any high background flares (3σ clipping) with the `lc_sigma_clip` routine task and then attached the good time interval (GTI) file to the events. All our event files include the 0.3–7 keV broad energy band. Without removing any point sources for the XMC analysis, we included them in the XMC modelling.

To generate an exposure map, we used the aspect solution, the bad pixel list, the detector mask and the parameter block files. All of these files are supplied with the *Chandra* archival data as ‘primary’ and ‘secondary’ products. To create an exposure map, we first copied the CCD

(ACIS-I or ACIS-S) region from the events file which contains the observation of cluster, using the task `dmcopy`. Then we computed the aspect histogram using the task `asphist`, and the aspect solution file which contains the telescope optical axis' ra, dec, and roll vs time information. The function of the aspect histogram is primarily to lessen the time needed in computing the response averaged during the observation. This aspect histogram can be used as an ingredient to generate the *Chandra* instrument map using the task `mkinstmap`. This task generates an instrument map which gives the effective area vs detector position for the analysis of imaging observation. This map is basically the product of the effective area of the X-ray mirror projected onto the detector surface with detector quantum efficiency (QE). It computes a 1024 × 1024 instrument map for mono-energy of 1.5 keV photons incident on the ACIS detector. Finally, we used this instrument map to create an exposure map using the task `mkexpmap`. An exposure map gives CCD effective area vs sky position, and used to convert a counts image of a cluster source to an image in flux units.

We used the automated script `mkdetmap` (supplied with the XMC) to create the detector map which basically tells the XMC program which ACIS rmf to use for the respective ACIS CCDs used in the observation. RMF describes the response of the detector as a function of energy (i.e. the physical properties of incoming photons in units of keV) and channel (i.e. detected properties as detector pulse height in units of PHA or PI). In principal, each element (gratings, focal plane detectors, etc.) of any telescope has a specific response to an incoming photon's individual physical characteristics, such as energy, time or position in the sky. Here we considered the RMF as a discrete representation of a given ACIS instrument's response to incoming photons. If $\hat{\mathrm{c}}$ represents the expected detector counts vs channel, $\hat{\mathrm{s}}$ is the physical spectrum (flux vs energy), and R is the response matrix, then the relationship between incoming photon and detected photon properties is described as $\hat{\mathrm{c}} = \mathrm{R} \times \hat{\mathrm{s}}$. This response is stored in the form of a 2-D matrix. The XMC program includes the calibration files (RMF, QE, etc.) for each CCD (ACIS-I (0, 1, 2, 3) and ACIS-S (7)).

Refer the KA09 for a description of how the *XMM-Newton* data were reduced and how Luminosity (and temperature) maps were created using the XMC technique for their sample clusters.

4.5 Smooth Particle Model Setup

Below we describe in detail the plasma and detector models used in the XMC modelling to characterise the ICM. These models include spectral and spatial model components, as well as soft galactic X-ray background, cosmic X-ray background (or hard extra galactic X-ray background) and instrument model (*Chandra*-ACIS).

Each smooth particle or blob in the XMC consists of these multiple components of plasma and detector models or, in other words, the multiple components model applies independently to each blob. In the XMC analysis, some model parameters are free to vary either locally (mainly ICM parameters) or globally (mainly X-ray background parameters). Local parameter refers to where the value of parameter changes for the individual blob in each iteration, and global parameter refers to where the value of parameter is fixed for each blob in every iteration. The number of free parameters depends on the quality of X-ray data and response of the XMC for various X-ray telescopes. For example, the XMC version for the *XMM-Newton* telescope is well tested (Andersson et al. 2007, KA09, Frank et al. 2013) and for that we keep the abundance as a free parameter. On the other hand, not much research has been done, using the XMC version for the *Chandra* telescope, about how the abundance parameter affect the fitting. However, we kept the abundance free for a few clusters, to check its effect on the final convergence, but found that the abundance parameter does not vary in the given range (0 to 2 $Z_{\odot}$), remained range bound between $\sim$ 0.8 to 1.2 for most clusters which we had kept abundance free. Fig. 4.2 shows the abundance map for each of two clusters. In these maps we note that the higher abundance value ($\gtrsim 1\ Z_{\odot}$) belongs to the outer cluster regions (closer to CCD edges), where X-ray observation is not reliable (due to the presence of noise), and the lower value ($0.8 \lesssim Z_{\odot} \lesssim 1$) belongs to the cluster region indicated by white contours (which remains a high abundance value for clusters). It is possible that the MCMC could not iterate efficiently for the abundance parameter and might be stuck between local maxima. Hence, for the remainder of our analysis, we kept a fixed abundance value of 0.3 $Z_{\odot}$ for all clusters, being the average value for most clusters. Ideally, this issue should be further investigational and fixed before future analysis is attempted. The following is a brief description of various model components.

4.5.1 Spectral and spatial model

This model is a combination of spectral and spatial models (wabs*lapec*sgau). For the purpose of modelling galaxy clusters, we used a set of spatial Gaussian blobs described by a two dimensional (x, y) position and a Gaussian σ width. In addition, each blob was assigned the WABS absorption model together with the spectral APEC model which includes hydrogen column density (n_H), temperature, abundance, redshift and flux. The latter model produced an ICM spectrum from each blob. Every blob has an individual single temperature (free local parameter) which may be different from the temperatures of other surrounding blobs. Since each blob is described by a Gaussian, there will always be overlapping among blobs which could results in (wide-spread) multi-temperature plasma. Table 4.2 shows values of each parameter from spectral and spatial models used to model emission from galaxy clusters.

As shown in Table 4.2, in the case of the spectral model (wabs*lapec), we used the NRAO H1 all sky survey data[*] for galactic absorption for each cluster (which was fixed for each individual cluster during the XMC analysis). It is advantageous to choose a parameter range that is wider than expected (Andersson et al., 2007). In our sample, the measured average temperature range was from 2–15 keV; and, based on that, we chose to vary the temperature in the 0.5 to 30 keV range. We fixed the abundance parameter at 0.3 $Z_{\odot}$ because based on our and our collaborators' experience, as mentioned above, this parameter does not converge well in the case of the XMC analysis of the *Chandra* data. We also fixed the corresponding redshift of each cluster (V09). In the case of the spatial model (sgau), the detector coordinates are similar to those of the *Chandra*-ACIS (chip I (0-1-2-3) and chip S (7)) detectors. Prior to starting the MCMC process, some photons in the input events were removed based on spatial position. Full coverage of ACIS-I images is 16.9 by 16.9 (x and y) arcmin and ACIS-S is 8.3 by 50.6 arcmin. The XMC set the centre at (-7.5, -162.5) for all blobs, and allowed these blobs to vary in the $503.5''(8.39')$ region in all four directions. ACIS photons outside of the $16.78' \times 16.78'$ squared, centred on the cluster, are removed. Each model

---

[*] http://cxc.harvard.edu/toolkit/colden.jsp

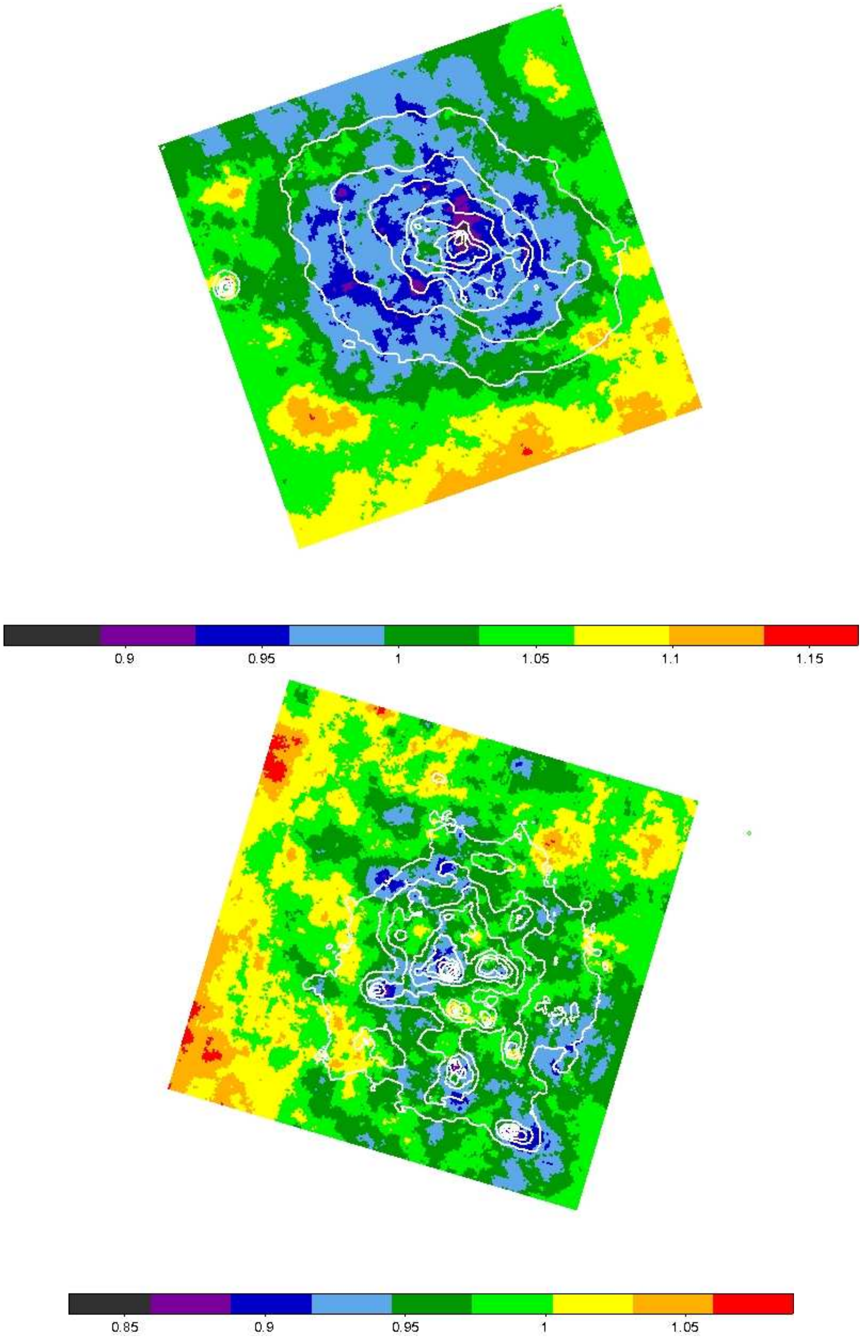

Figure 4.2: Abundance maps generated by the XMC technique for two clusters. The abundance parameter varies in the range of 0–2 $Z_{\odot}$. It is noted that the abundance does not vary in the cluster regions (white contour).

Table 4.2: Spectral and Spatial model parameters value for the XMC analysis.

Parameters	Fixed/Free	min and max values
Spectral model		
n_H	Fixed	NRAO H1 all sky survey
T (keV)	Free	0.5 - 30keV
$Z_\odot$	Fixed	0.3
z	Fixed	according to the V09
Spatial model		
x	Free	-8.4$'$ - 8.4$'$
y	Free	-8.4$'$ - 8.4$'$
ln σ ($''$)	Free	0 - 6$''$

component has its corresponding normalisation parameter, and the fraction of photons allocated to each are free parameters.

4.5.2 X-ray background

The X-ray background model has a total of four components. The first and second components (apec*uni+wabs*apec*uni) account for the soft galactic X-ray background (SXB) originating from our Galaxy. This uniform emission component consists of a thermal plasma spectral model APEC with WABS absorption. The soft X-ray photons have X-ray energies $\lesssim$ 1 keV. The SXB is adequately described as several thermal components in the 0.05–0.5 keV range. This emission consists of local (and thus weakly absorbed) thermal components plus an absorbed, more distant, contribution from the Galactic halo. Since the SXB originates from our Galaxy at $z = 0$ with the APEC model at temperature of 0.20 keV and solar metal abundance $Z_\odot = 1$, it describes the data well. Here we fixed all of these parameters for all smooth particles.

The third component (wabs*bknpower*uni) account for the cosmic X-ray background (CXB) originating from unresolved active galactic nuclei with X-ray energies of $\gtrsim$ 1 keV. This component is well modelled using a broken power-law with photon index $\Gamma_1 = 2$, $\Gamma_2 = 1.4$, and $E_{break} = 1.2$ keV. For each cluster, column absorption density is fixed according to that given by the NRAO H1 sky survey. Hence, the extra galactic background is represented by a model component with a spatially uniform, WABS absorbed, power-law spectrum.

The last component (acisback) is the instrument (ACIS) background model (Markevitch et al., 2003a). This model consists of various components relating to the detector. A soft proton background is modelled as a power-law with $\Gamma = 0.10$. Electronic noise from the detector is modelled as an exponential, with $F \propto e^{-E/Ei}$ where $E_i = 100$ eV. Different materials of the *Chandra* detectors are the cause of the fluorescent lines excited by high energy particles which can be modelled with the XMC. These internal lines include the Al ka, Si Ka, Si Kb, Au Ma,Au Mb, Au Mc, Ru La, Ru Lb, Ni Ka1, Cu Ka, Ni Kb, Au Ll and Au La1 complexes. The lines are approximated with delta functions at their respective energies. All of these parameters used in the instrument background component are kept fixed for all blobs, and they all retain individual values for all cluster data.

4.6 MCMC model and MCMC chain convergence

In the Monte Carlo analysis, the above model parameters provide the probability functions to simulate model photons which are propagated through the *Chandra* detector model. In the analysis, it is essential to supply two important factors to model the data according to the quality of input X-ray data and available computing power. These factors are: (1) the number of smooth particles or blobs which represent the ICM. This number varies between the minimum number of particles (100) and the maximum (1000). In our analysis we used 500 smooth particles for the modelling of each cluster. (2) the *oversimulation* factor (the ratio of simulated photons to actual data photons) which determines the number of model photons. Here we chose a model-to-data *oversimulation* factor of 10 for all cluster data sets (which means that the XMC generates ten times more model photons than data photons, having made the cuts as discussed previously, which are considered to be emitted from 500 blobs of ICM). At this stage, there is insufficient research output available to us for the appropriate *oversimulation* factor related to the XMC version for the *Chandra* compared with that of the XMC version for the *XMM-Newton* (Frank et al., 2013). In principle, however, it would be ideal to set the *oversimulation* factor as large as possible to reduce the model noise, but one is restricted by finite computing speed and internal memory (KA09).

The convergence criteria depends on the size of the input observation data and number of free parameters. In X-ray astronomy, a χ^2 statistic gives a well-known goodness of fit criterion for a given degree of freedom (dof) number, which is computed as the number of energy channels minus the number of model (free) parameters, and for a given confidence level. The most common fit statistic, χ^2, is used for finding the “best-fit” parameter value for a given model, i.e. the given model parameters are varied to find the parameter values which provide the most desirable fit statistic. It is defined as

$$\chi^2 = \frac{\sum_i (d(i) - d_m(i))^2}{\sigma(i)^2}, \tag{4.1}$$

where $d(i)$ represents actual data counts i^{th}, $d_m(i)$ represents the model or simulated counts i^{th}, and $\sigma(i)$ is the error associated with actual data counts. For our analysis, all the results derived from the model samples are from the iterations from 500 to 3000, as depicted in Fig. 4.3, where the value of χ^2 is reduced and stable, and is consider to be a converged chain where all corresponding parameters have the best-fit value for individual clusters. We are grateful to the CHPC facility for providing sufficient time for us to model all the V09 low-z clusters. Typically it takes approximate one week to reach sufficient number of iterations ($\sim$ 3000).

4.7 Parameters maps

From the XMC process, we have constructed spatial 2-D parameter maps of $norm_{APEC}$ (which is equivalent to emission measure (EM)) and temperature. Cluster luminosity is closely related to the X-ray emission measure of galaxy clusters. Consequently, instead of calculating luminosity, we opted to use the emission measure which is a closely related quantity of luminosity. We calculated the emission measure directly from the chain of converged iterations of MCMC samples. One of the parameters of blob, “blob-normalisation”, is actually APEC normalisation*, and is related to

---

*Xspec manual

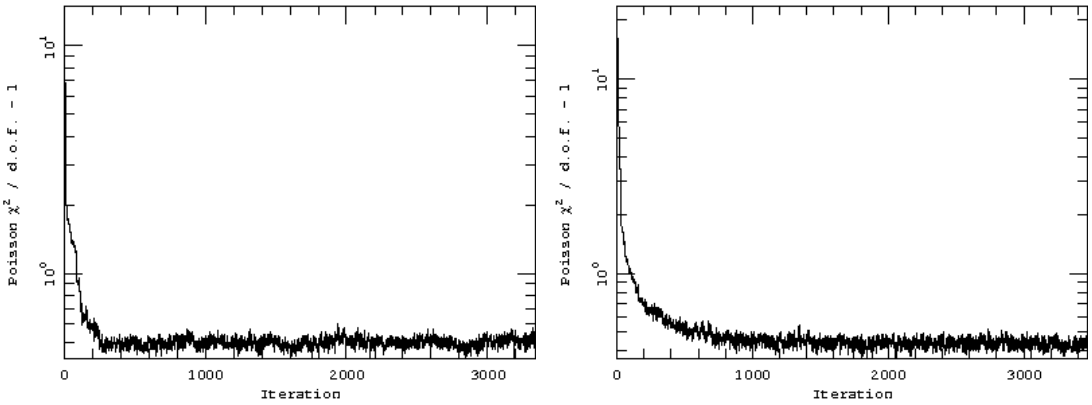

Figure 4.3: Poisson χ^2 per degree of freedom plot showing that model parameters converge after $\sim$ 500 MCMC iterations. We used iterations from 500 to 3000 for our analysis, and created parameter maps from then.

the emission measure of the ICM. In the MCMC analysis, this parameter was allowed to be free, varying (globally) the emission measure for all blobs as

$$norm_{APEC} = \frac{10^{-14}}{4\pi {D_A}^2(1+z)^2} \int n_e n_H dV, \tag{4.2}$$

where D_A is the angular diameter distance to the cluster (cm), n_e and n_H are the electron and Hydrogen atom densities (cm^{-3}). The last integral quantity is actually the emission measure, given as

$$EM = \int n_e n_H dV. \tag{4.3}$$

EM is directly connected to the X-ray luminosity via the cooling function $\wedge(T)$ ($Lum \propto EM \wedge(T)$). The cooling of a plasma by thermal radiation is usually expressed by the cooling function $\wedge(T)$. For most of the hotter clusters, where bremsstrahlung emission is significant, the cooling function, $\wedge \sim T^{1/2}$. On the other hand, at lower temperature clusters, the emission is depicted mainly by lines of different elements, which dramatically change the ICM cooling function. Therefore, in analysing the broad range of cluster temperatures, it is appropriate to use the emission measure rather than luminosity where the cooling function is inconstant. This emission measure map is also referred to as the "pseudo density" map and is also related to the cluster surface brightness. From this we are able to reconstruct the emission measure of the cluster by calculating

$$EM(x_i, y_i) = \sum_i EM_i \, \frac{e^{\frac{-(\rho-\rho_i)^2}{2\sigma_i^2}}}{2\pi\sigma_i^2}, \tag{4.4}$$

where EM_i is the normalisation for the i^{th} blob at each (x, y) position, ρ_i is the projected spatial position for the i^{th} blob, and σ_i is the spatial width for the i^{th} blob. Consequently, taking the average of the maps over the converged samples provides an image of the emission measure of the cluster which we consider as a density map. These maps conform with the precision given by the noise as well as the accuracy dictated by the SPI model, corrected for detector exposure and CCDs gap, vignetting, and PSF convolution, all of which distort the raw counts image. Furthermore, the position where the S/N is at its maximum is where blobs are best constrained, and the SPI average intensity maps are multi-resolution image reconstructions. Similarly, we are able to construct maps for other parameters, such as temperature or abundance, by using the following equation:

$$T(x_i, y_i) = \frac{\sum_i S_B i T_i \frac{e^{\frac{-(\rho-\rho_i)^2}{2\sigma_i^2}}}{2\pi\sigma_i^2}}{L(x_i, y_i)}, \tag{4.5}$$

where T_i is the value of the parameter (e.g. temperature or abundance) for the i^{th} blob at each (x, y) position, $S_B i$ is the APEC normalisation, σ_i is the spatial width for the i^{th} blob, and ρ_i is the projected spatial position for the i^{th} blob. Hence, these maps are emission weighted temperature maps. If only individual sample maps are created, then it may not be possible to reconstruct a visualization of the cluster satisfactorily, because the map consists of both the data and the noisy simulation. It is therefore necessary to find a means of averaging, preferably over a large set of samples. In the following section we will describe how to generate median maps.

4.7.1 Median maps

It is possible to calculate a median map by taking the median of the $EM_i(x, y)$ or $T_i(x, y)$ over all iterations i in the converged chain of MCMC samples. In Fig. 4.4, we show median maps for cluster EM for the ACIS-I runs. From the maps we see that, when the MCMC iteration starts, the given blobs are distributed completely randomly but, as the number of iterations increases, at $\sim$ 100 iterations the median map starts to reveal the structure of the cluster. This means that, at this stage, the MCMC chain is still evolving but is not fully converged with satisfactory solutions. As the chain evolves with time, we see that blobs are settling with a proper fit value (while the corresponding χ^2 value is reduced) and the structure of the cluster becomes visible at a higher number of iterations. The median surface brightness map of the last 1000 samples in the stationary part of the MCMC chain clearly matches the input model; and this converged part forms a reliable basis for further analysis. Similarly, we are able to construct a median map of emission weighted temperature.

As stated earlier, since we are using multiple blobs in the modelling, the average temperature from the SPI technique becomes higher than that of standard analysis. The reason is that we used hundreds of blobs, which are extended in the modelling of a single cluster so that multiple overlapping between blobs at any spatial position can take place. The XMC assigned temperature, position, abundance, etc., to each blob, changing the value in each MCMC iteration. This enabled us to construct a wide range of multiphase plasma temperatures at any given coordinate. Basically, this range depends on the prior range for the temperature given in the iteration. In generating EM or temperature maps, we took the median over all iterations (500-3000) in each $4'' \times 4''$ pixel. In some cases, it is possible to see artifacts (lumpy structures) in a median map. The reason may be that the blobs are constantly varying the given parameter space, and changing positions with each other. Taking a mean over a number of MCMC samples can reduce this effect. We have 3000 iterations, and have noticed this effect on a minimal number of clusters on a very small spatial scale.

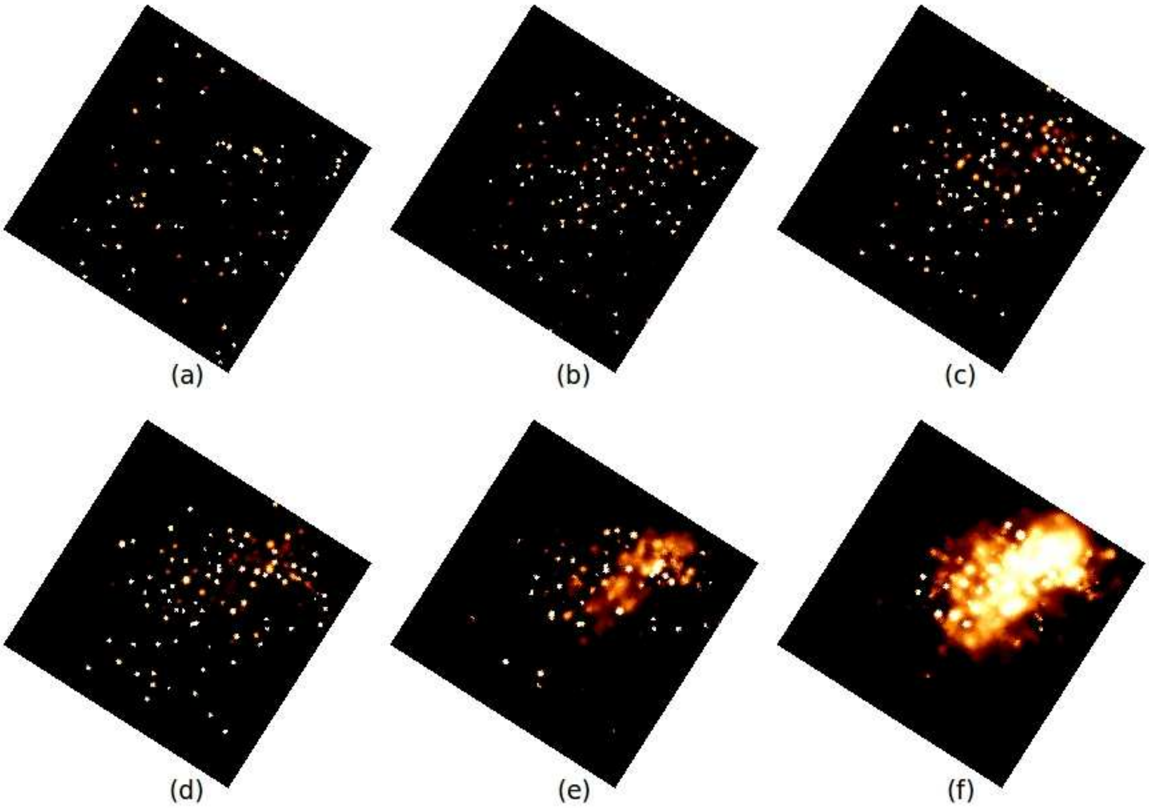

Figure 4.4: Median surface brightness maps of cluster for various iterations. $800'' \times 800''$ surface brightness maps of the ICM after 5, 10, 50, 100, 500 and 1000 MCMC iterations (top left (a) to bottom right (f)). Maps are centred on the aim point of the ACIS-I detector, i.e. (4096, 4096) in the CCD physical unit. These maps are calculated according to Eq. 4.4 and median over all iterations are taken in each $4'' \times 4''$ pixel.

4.7.2 Error estimation and systematic effects in the XMC maps

In the XMC generated maps, we estimated uncertainties by identifying ten independent sets of samples in the converged MCMC chain. We took, sequentially, 250 iterations in each sample, starting at iteration 500 (500, 750, 1000,..., 2750). The EM or temperature maps derived from these sets were then evaluated independently, and the uncertainty on these quantities is determined from the rms scatter within these ten sets. KA09 mentioned that the XMC technique has high dimensionality of overall parameter space. Further, that the lack of local likelihood maxima suggests that it is possible that the motions of blobs in the given parameter space are large and that, within certain iterations, there is no memory of previous states. In this estimation of error, each subset can be represented as an independent reconstruction of a cluster.

4.8 Combined thermodynamic profiles

In this section, we first show combined radial profiles of all low-z clusters of the V09 sample. We studied radial profiles of temperature, density, pseudo entropy ($\mathrm{T}/n_e^{1/3}$) and pressure maps ($\mathrm{T} \times n_e^{1/2}$) to understand the distribution of these quantities in relaxed and non-relaxed clusters.

Each of our 2-D maps are $16.6' \times 16.6'$ (250×250) centred on the (0, 0) physical unit of a modelled detector, which corresponds to ACIS-I or ACIS-S aim points. We used the centre of a cluster defined by the centroid of the density map for each cluster, and applied it to all corresponding thermodynamic maps. Then we used the scaled radius R_{500} to define the bin size over the distribution of the ICM, and divided the cluster into a number of annuli. We calculated R_{500} by the following equation:

$$R_{500} = \left(\frac{M_{500}}{1.33 \times \pi \times 500 \rho_c} \right)^{1/3}, \tag{4.6}$$

where M_{500} is the mass within the R_{500} radius taken from the V09 (M_T calculated by the M–T relation), and ρ_c is the critical density of the Universe at respective redshift of the cluster, defined by $\rho_c = 1.4 \times 10^{-7}$ $(\Omega_\wedge + (\Omega_m \times (1+z)^3))$. In order to calculate the radial profile, we defined each bin in the scaled radii of $[0.01–0.3]R_{500}$ which was normalised by the mean value within $[0.01–0.2]R_{500}$. For example, in the case of the temperature map, each radial bin of (0.01, 0.02, 0.03, 0.04, 0.05, 0.06, 0.07, 0.08, 0.09, 0.1, 0.15, 0.2, 0.25, 0.3)R_{500} was normalised by the mean of $\mathrm{T}_{[0.01-0.2]R_{500}}$. This procedure is the same as that for calculating radial profiles of other thermodynamic maps. Because fewer photons at higher distances from the cluster centre cause uncertainty in the maps, we restricted our measurements to within 0.3 R_{500} for low-z clusters, and took advantage of the XMC to measure thermodynamic quantities in small radii.

Fig. 4.5 shows temperature (keV), density (cm^{-5}), entropy ($\mathrm{keV*cm}^2$) and pressure ($\mathrm{dyne/cm}^2$) as a function of scaled radius for the sample of low-z clusters (strong relaxed, intermediate and strong non-relaxed). We differentiated clusters according to the combination of surface brightness morphology parameters (see Chapter 3). In Fig. 4.5, the solid black line shows strong relaxed clusters (strong cool core), while the blue and red dashed lines show intermediate and strong non-relaxed clusters (non-cool core), respectively. For simplicity, we combined the relaxed (cool core) and non-relaxed (weak cool core) clusters as intermediate clusters. We noticed, in all combined thermodynamic radial profiles, that there is a broad dispersion in the cluster core at $\sim 0.02\ R_{500}$. At radius $\sim 0.1\ R_{500}$, all profiles converged and again dispersed at $\sim 0.2\ R_{500}$, although the dispersion was not as large as that of the core.

In the temperature profiles given in Fig. 4.5, we observed two different trends of evolution between strong relaxed and strong non-relaxed clusters. In this temperature profile, we would have expected steep profiles for strong relaxed clusters, because of the cooling effect. However, it was only in the temperature profile that we observed overlap between strong relaxed (A478 and A2029) and strong non-relaxed clusters. This could suggest that a central (powerful) AGN of these two cooling flow clusters is responsible for increasing the temperature of the surrounding ICM, hence the flatter profile in the core. We also noticed that a few intermediate clusters (A3571, A3158, and A2163) had higher temperature in the core than that of strong non-relaxed clusters.

In the entropy profile (Fig. 4.5), we observed a dichotomy of strong relaxed and non-relaxed clusters, while intermediate clusters were spread between these two classes. Entropy declines in the core of strong relaxed clusters (although the temperature is high), while for strong non-relaxed clusters entropy is high in the core and the profile is flatter (Pratt & Arnaud, 2003; Voit, 2005; Donahue et al., 2006a; Sanderson et al., 2009b). This indicates the possibility that heat or energy input from the shock-heated region (mainly outskirts) of the cluster could be transported sufficiently to the core of the cluster to offset the energy lost from cooling. Entropy profiles of strong relaxed clusters are more tightly grouped than those of strong non-relaxed clusters. In strong relaxed clusters, there is therefore no obvious indication of the passage between the shock-heated (outskirts) region and the cooling dominated core. Generally, it is believed that, in strong relaxed clusters, the cooling process regulates the entropy in the cluster core in order to minimise the scatter between them. In contrast, the entropy profile of strong non-relaxed (and intermediate) clusters indicates larger diversity, a possible reason being different (gravitational) heating mechanisms at various locations affecting them. Entropy is a very important tool in classifying clusters, based on the clusters' central entropy distribution, and is a promising way of identifying mechanisms that prevent gas from condensing at their cores.

Fig. 4.5 also indicate that strong relaxed clusters have systematically denser and cuspy cores which are in equilibrium with surrounding pressure balance to sustain the regular cooling flow towards the centre. The Density profile of strong relaxed clusters is consistent with the drop in gas temperature in moving towards the core. In the core, strong relaxed clusters have higher electron density (and pressure) as compared with that of strong non-relaxed clusters. Some relaxed clusters (cool core) in the intermediate group have lower densities in their cores. This may indicate that either their periodic cooling mechanisms are out of phase, or that non-gravitational heating (powerful AGN) could be displacing material out of the core.

Fig. 4.6 shows the mean radial profiles of strong relaxed (mean values of whole solid black lines at each radial bin, as shown in Fig. 4.5), intermediate (mean values of whole blue dashed lines at each radial bin, as shown in Fig. 4.5), and strong non-relaxed clusters (mean values of whole red dashed lines at each radial bin, as shown in Fig. 4.5) along with fluctuations. Fluctuations are measured by taking the standard deviation of whole strong relaxed cluster profiles (standard deviations of whole solid black lines at each radial bin), intermediate cluster profiles (standard deviations of whole blue dashed lines at each radial bin), and strong non-relaxed cluster profiles (standard deviations of whole red dashed lines at each radial bin). In this case, fluctuations are actually measuring the diversity between each profile of strong relaxed, intermediate and strong non-relaxed clusters. The mean profile of each map shows the separation between different dynamical states of clusters. We see the separation between strong relaxed clusters (symbol 'o'), intermediate clusters (symbol '♢') and strong non-relaxed clusters (symbol 'x') in Fig. 4.6.

In the mean temperature profile, we notice fluctuations in the centre of the strong relaxed clusters, which could indicate the variation in the ICM temperature between strong relaxed clusters caused by non-gravitational (AGN) heating. It is acknowledge that there is large fluctuation between intermediate clusters due to the diverse nature of different merging phenomena and heating processes. In the case of strong non-relaxed clusters, there is a possibility that merger shock has increased the core temperature of all strong non-relaxed clusters in our sample, hence less fluctuation. In the mean entropy profile, strong relaxed clusters show less fluctuation, the possible cause being dissipation of heat in the dense core region of strong relaxed clusters. The mean density profile indicates the lowest fluctuation among all strong relaxed clusters, while the corresponding pressure profile gives some fluctuation. A possible reason is that the pressure gradient will vary for different cooling flow clusters, depending on outer density and temperature.

In these plots, we fitted (1) the power-law model with a constant base in the form of $F(r) = F_0 + F(R_{500})^{\alpha}$, and (2) the pure power-law model with a constant $F_0 = 0$, giving $F(r) = F(R_{500})^{\alpha}$. In the first power-law model, F_0 is a constant base, while α is the slope in both the power-law models. F = T (temperature), n_e (density), K (entropy) and P (pressure) for each profile of T, n_e, K and P, respectively; and $F_0 = T_0$, n_{e0}, K_0 and P_0 for each profile of T, n_e, K and P, respectively. Table 4.5 shows the values of F_0, F and α (power-law with a constant base), while Table 4.6 shows the values of F and α (pure power-law). We listed best-fit power-law model values for each profile and cluster dynamical group, as well as mean values for combined radial profiles (strong relaxed, intermediate and strong non-relaxed) of temperature, entropy, density and pressure, to establish the relationship with radius. For the purpose of clarity, Fig. 4.6 displays the best-fit line derived from the power-law model with a constant base.

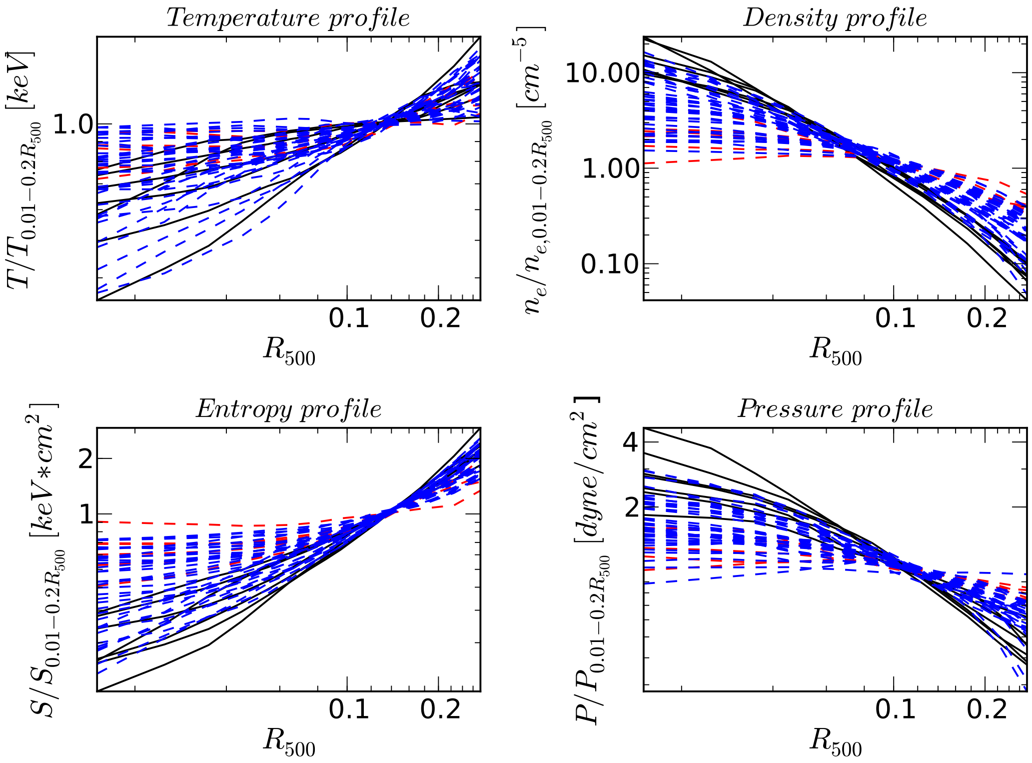

Figure 4.5: Thermodynamic radial profiles for all low-z clusters. We plotted profiles of strong relaxed, intermediate, and strong non-relaxed clusters. Solid black line = strong relaxed; blue dashed line = intermediate; and red dashed line = strong non-relaxed clusters.

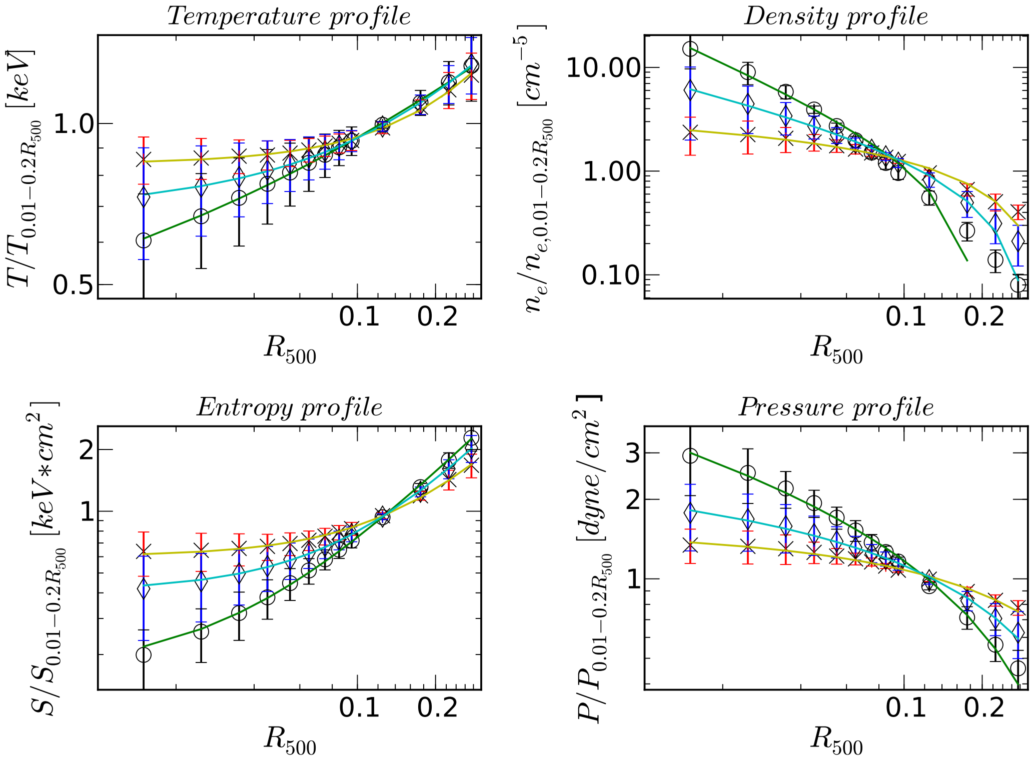

Figure 4.6: Mean thermodynamic radial profiles for all low-z clusters. We plotted profiles of strong relaxed, intermediate, and strong non-relaxed clusters. ‘o’ = strong relaxed clusters; ‘◇’ = intermediate clusters; and ‘x’ = strong non-relaxed clusters. We fitted the power-law model to evaluate the corresponding slope values. Green solid line = best-fit for strong relaxed clusters; cyan solid line = best-fit for intermediate clusters; and yellow solid line = best-fit for strong non-relaxed clusters.

Table 4.3: Best-fit (constant base) power-law slope values for the low-z clusters.

Cluster name	Best-fit values for temperature (keV)			Best-fit values for density (cm^{-5})			Best-fit values for entropy ($keV*cm^2$)			Best-fit values for pressure ($dyne/cm^2$)		
	α	T	T_0	α	n_e	$n_{e,0}$	α	K	K_0	α	P	P_0
2A-0335	0.33±0.08	2.57±0.15	-0.33±0.27	-1.00±0.12	0.26±0.13	-1.48±0.70	1.21±0.02	11.13±0.23	0.02±0.01	0.30±0.09	-3.66±0.31	2.97±0.50
A478	-0.60 ± 0.05	-0.03 ± 0.01	1.10 ± 0.01	-0.91±0.03	0.26±0.03	-0.90±0.13	0.98±0.02	5.71±0.15	0.22±0.01	0.02±0.05	-47.23±103.11	46.33±103.25
A1795	0.49±0.06	1.68±0.05	0.38±0.06	-0.67±0.10	0.74±0.33	-2.09±0.78	1.19±0.02	9.11±0.25	0.16±0.01	0.08±0.05	-10.11±4.83	9.53±4.95
A2597	1.09±0.04	4.86±0.24	0.47±0.02	-0.90±0.11	0.36±0.17	-1.63±0.68	1.70±0.05	24.48±1.56	0.17±0.02	-0.15±0.11	3.02±3.07	-3.14±3.27
RXJ1504	0.62±0.02	1.17±0.01	0.42±0.01	-1.36±0.09	0.43±0.17	-4.27±2.13	1.25±0.02	3.79±0.07	0.03±0.01	-0.57±0.05	1.21±0.31	-1.65±0.56
A2204	-0.14±0.10	-0.80±0.77	1.93±0.81	-1.67±0.02	0.11±0.01	-0.96±0.35	1.03±0.03	2.97±0.07	0.05±0.01	-0.35±0.04	2.70±0.65	-3.24±0.82
A2029	0.57±0.11	1.23±0.09	0.65±0.06	-0.80±0.06	0.41±0.11	-1.38±0.35	1.31±0.06	10.43±0.73	0.27±0.02	-0.04±0.05	18.52±27.43	-19.15±27.57
A2147	2.50±0.45	10.70±6.46	0.92±0.01	0.51±0.14	-5.29±0.42	2.94±0.41	1.81±0.15	12.16±2.31	0.65±0.02	0.33±0.16	-1.94±0.22	2.02±0.41
A3266	1.01±0.24	1.15±0.32	0.84±0.03	0.21±0.12	-7.39±1.98	5.84±2.40	1.06±0.12	4.05±0.55	0.51±0.04	0.35±0.06	-2.10±0.07	2.01±0.15
A1736	0.77±0.45	0.28±0.12	0.94±0.03	1.74±0.48	-7.68±4.82	1.30±0.05	2.12±0.33	6.81±2.94	0.87±0.01	2.16±0.57	-6.00±4.56	1.10±0.02
A3395	0.51±0.08	1.16±0.05	0.58±0.05	-0.29±0.10	2.19±1.34	-2.99±1.65	0.91±0.05	4.32±0.24	0.29±0.03	0.22±0.11	-2.75±0.62	2.78±0.76
A754	1.34±0.12	3.59±0.52	0.75±0.02	0.29±0.09	-5.78±0.55	4.26±0.84	1.47±0.08	9.47±0.94	0.49±0.02	0.39±0.10	-1.19±0.05	1.55±0.12
A2256	1.81±0.09	5.43±0.62	0.85±0.01	0.96±0.11	-5.42±0.69	1.83±0.07	2.11±0.04	19.60±1.04	0.68±0.00	1.31±0.23	-2.13±0.62	1.17±0.02
A3571	1.52±0.41	0.72±0.38	0.96±0.01	-0.08±0.09	15.82±20.45	-17.69±20.85	1.93±0.08	19.72±1.97	0.56±0.01	0.33±0.03	-4.81±0.11	3.46±0.21
A2199	0.05±0.11	3.26±5.78	-1.93±5.84	-0.65±0.05	0.72±0.18	-1.90±0.41	1.48±0.03	14.14±0.50	0.27±0.01	0.36±0.08	-5.31±0.22	3.55±0.45
A496	0.43±0.09	2.27±0.08	0.03±0.15	-1.04±0.03	0.17±0.02	-0.73±0.13	1.35±0.02	13.13±0.27	0.13±0.01	0.35±0.06	-3.21±0.11	2.51±0.22
A85	0.60±0.10	1.86±0.13	0.47±0.07	-1.06±0.02	0.12±0.01	-0.30±0.08	1.22±0.06	8.77±0.67	0.25±0.03	0.06±0.06	-9.78±8.80	9.68±8.91
A4038	1.53±0.21	4.87±1.34	0.79±0.03	-0.44±0.08	1.50±0.65	-2.73±0.99	1.61±0.09	15.66±1.76	0.38±0.03	0.11±0.11	-7.09±5.14	6.74±5.37
A2052	0.17±0.08	2.41±0.62	-0.68±0.70	-1.01±0.13	0.19±0.11	-0.93±0.59	1.10±0.07	8.11±0.71	0.15±0.05	0.12±0.13	-6.70±5.09	6.26±5.37
Hydra-A	1.44±0.13	5.35±0.85	0.70±0.02	-0.94±0.09	0.28±0.11	-1.26±0.51	1.59±0.05	17.88±1.18	0.26±0.02	-0.37±0.12	0.85±0.56	-0.83±0.76
A2063	1.04±0.03	3.53±0.14	0.57±0.01	-0.48±0.07	1.08±0.37	-2.01±0.61	1.53±0.07	14.50±1.28	0.32±0.02	0.03±0.05	-14.08±24.55	14.34±24.60
A3158	7.64±4.20	1864.36±10141.27	1.01±0.01	0.52±0.10	-5.23±0.30	2.87±0.27	1.59±0.07	6.19±0.59	0.74±0.01	0.80±0.16	-3.05±0.48	1.66±0.09
MKW3s	0.79±0.12	2.02±0.23	0.62±0.05	-0.67±0.07	0.60±0.19	-1.54±0.44	1.49±0.10	14.05±1.79	0.32±0.04	0.06±0.04	-11.38±6.72	10.99±6.82
EXO0422	1.05±0.13	3.42±0.53	0.61±0.04	-1.28±0.04	0.08±0.01	-0.51±0.15	1.42±0.05	13.90±0.86	0.20±0.02	-0.31±0.08	1.13±0.56	-1.16±0.71
A4059	0.37±0.13	2.54±0.16	-0.23±0.34	-0.23±0.10	3.88±2.64	-5.27±3.04	0.93±0.09	6.14±0.61	0.01±0.07	3.67±1.97	-40.30±104.91	1.03±0.03
A2589	0.26±0.18	1.79±0.44	-0.08±0.61	-0.19±0.12	4.58±4.64	-5.81±5.10	0.87±0.07	4.94±0.35	0.15±0.05	1.26±0.19	-3.40±0.79	1.25±0.03
A3112	0.83±0.07	2.77±0.21	0.50±0.04	-1.11±0.04	0.13±0.02	-0.68±0.17	1.49±0.04	15.74±0.90	0.21±0.02	-0.11±0.05	4.77±2.62	-4.96±2.71
A1651	1.52±0.20	1.89±0.49	0.90±0.01	-0.18±0.06	5.65±3.02	-7.13±3.29	1.43±0.05	8.84±0.53	0.48±0.01	0.25±0.06	-4.45±0.41	3.71±0.55
A576	0.36±0.20	0.85±0.09	0.57±0.19	-0.02±0.12	57.71±350.02	-59.17±350.49	0.93±0.07	3.97±0.30	0.37±0.03	0.53±0.09	-2.48±0.13	1.84±0.11
A2657	1.20±0.05	3.16±0.20	0.72±0.01	-0.08±0.10	15.03±22.12	-16.64±22.54	1.43±0.02	10.54±0.27	0.40±0.01	0.28±0.08	-2.61±0.24	2.50±0.36
A3391	0.32±0.17	0.74±0.10	0.64±0.18	0.16±0.05	-7.99±1.60	6.80±1.77	1.13±0.09	4.34±0.48	0.57±0.03	0.84±0.13	-2.46±0.34	1.48±0.06
A1650	0.51±0.13	0.77±0.06	0.75±0.06	-0.35±0.08	2.17±0.99	-3.47±1.32	1.14±0.02	6.24±0.13	0.37±0.01	0.25±0.09	-4.64±0.67	3.81±0.91
S1101	1.05±0.04	2.91±0.12	0.65±0.01	-0.67±0.12	0.81±0.45	-2.38±1.05	1.44±0.02	13.98±0.30	0.21±0.01	-0.06±0.09	11.13±19.14	-11.67±19.38
Zwcl1215	0.57±0.08	0.97±0.05	0.69±0.03	0.47±0.08	-5.30±0.21	3.07±0.29	1.29±0.04	5.90±0.26	0.54±0.01	1.33±0.14	-3.65±0.66	1.27±0.02
A133	0.52±0.03	2.76±0.05	0.05±0.05	-1.25±0.02	0.07±0.01	-0.24±0.07	1.14±0.04	9.32±0.45	0.08±0.02	0.08±0.06	-4.54±2.93	4.84±3.00
A2244	1.50±0.09	3.44±0.38	0.83±0.01	-0.28±0.05	2.95±1.04	-4.28±1.27	1.53±0.02	12.08±0.37	0.42±0.01	0.13±0.06	-6.07±1.88	5.70±2.00
A2142	1.17±0.06	2.98±0.22	0.71±0.01	-0.24±0.13	4.11±3.68	-5.80±4.29	1.39±0.04	11.11±0.62	0.31±0.02	0.13±0.08	-5.52±2.12	5.21±2.28
A3562	1.55±0.06	3.83±0.28	0.83±0.00	0.13±0.12	-12.63±7.12	10.67±7.65	1.53±0.03	10.32±0.36	0.50±0.01	0.37±0.12	-2.39±0.14	2.15±0.29
A401	1.96±0.14	4.15±0.78	0.91±0.01	0.47±0.12	-5.91±0.34	3.35±0.49	1.75±0.04	11.58±0.57	0.63±0.01	0.62±0.09	-2.41±0.17	1.69±0.08
A3558	0.45±0.40	0.48±0.09	0.78±0.14	-0.13±0.10	20.50±20.74	-23.39±21.54	1.01±0.10	4.04±0.46	0.46±0.04	0.32±0.04	-3.03±0.10	2.54±0.18
A119	0.52±0.05	0.87±0.03	0.71±0.02	0.48±0.06	-3.85±0.12	2.46±0.16	1.36±0.11	5.54±0.76	0.66±0.02	1.58±0.19	-3.30±0.79	1.15±0.01
A1644	-0.10±0.11	-1.97±2.67	3.47±2.75	-0.94±0.03	0.16±0.02	-0.34±0.09	0.73±0.06	4.62±0.24	0.01±0.06	0.76±0.21	-2.36±0.48	1.53±0.11
A2065	0.94±0.07	2.67±0.20	0.61±0.02	-0.22±0.13	3.61±3.53	-4.74±4.02	1.31±0.04	9.01±0.42	0.36±0.01	0.27±0.08	-1.88±0.21	2.10±0.29
A3822	1.59±0.29	3.60±1.34	0.82±0.02	0.09±0.06	-13.79±6.83	12.49±7.03	1.58±0.06	10.26±0.86	0.55±0.01	0.09±0.06	-4.26±2.31	4.53±2.37
A3667	3.10±0.16	28.98±5.96	0.93±0.00	0.74±0.14	-6.62±0.89	2.59±0.22	2.20±0.10	28.34±3.83	0.63±0.02	0.80±0.21	-2.82±0.59	1.62±0.11
A399	2.93±0.44	11.52±6.71	0.97±0.01	0.76±0.14	-5.47±0.74	2.24±0.17	2.16±0.06	18.15±1.48	0.75±0.01	0.96±0.19	-2.87±0.61	1.46±0.06
A2163	1.38±0.12	0.80±0.09	0.82±0.01	-0.41±0.15	-15.06±1.26	10.25±2.15	1.50±0.06	3.40±0.19	0.32±0.01	0.63±0.13	-4.25±0.28	3.06±0.23
A3376	2.07±0.12	11.46±1.84	0.80±0.01	1.08±0.08	-5.08±0.49	1.60±0.03	2.23±0.07	26.87±2.62	0.65±0.01	0.23±0.29	-0.25±0.14	1.16±0.18

Table 4.4: Best-fit (pure) power-law slope values for the low-z clusters.

Cluster name	Best-fit values for temperature (keV)		Best-fit values for density (cm^{-5})		Best-fit values for entropy ($keV{*}cm^2$)		Best-fit values for pressure ($dyne/cm^2$)	
	α	T	α	n_e	α	S	α	P
2A-0335	0.47 ± 0.02	2.50 ± 0.10	-1.27 ± 0.09	0.08 ± 0.03	1.18 ± 0.01	10.77 ± 0.15	-0.36 ± 0.04	0.46 ± 0.06
A478	0.09 ± 0.01	1.21 ± 0.03	-1.12 ± 0.04	0.10 ± 0.01	0.72 ± 0.02	4.51 ± 0.20	-0.52 ± 0.05	0.36 ± 0.06
A1795	0.28 ± 0.01	1.79 ± 0.04	-1.01 ± 0.08	0.15 ± 0.04	0.96 ± 0.03	7.21 ± 0.35	-0.43 ± 0.04	0.42 ± 0.05
A2597	0.50 ± 0.03	2.96 ± 0.21	-1.18 ± 0.08	0.10 ± 0.03	1.38 ± 0.05	16.77 ± 1.41	-0.46 ± 0.03	0.39 ± 0.04
RXJ1504	0.26 ± 0.01	1.33 ± 0.03	-1.51 ± 0.08	0.22 ± 0.07	1.18 ± 0.02	3.61 ± 0.07	-0.76 ± 0.03	0.49 ± 0.06
A2204	0.19 ± 0.01	1.26 ± 0.04	-1.72 ± 0.02	0.09 ± 0.01	0.93 ± 0.02	2.81 ± 0.06	-0.63 ± 0.04	0.62 ± 0.08
A2029	0.18 ± 0.01	1.51 ± 0.04	-1.07 ± 0.06	0.12 ± 0.03	0.90 ± 0.04	6.69 ± 0.53	-0.51 ± 0.04	0.37 ± 0.05
A2147	0.12 ± 0.03	1.34 ± 0.12	-0.41 ± 0.07	0.48 ± 0.11	0.48 ± 0.07	2.94 ± 0.42	-0.21 ± 0.02	0.66 ± 0.05
A3266	0.11 ± 0.02	1.25 ± 0.05	-0.49 ± 0.07	0.39 ± 0.09	0.43 ± 0.04	2.52 ± 0.20	-0.24 ± 0.02	0.60 ± 0.04
A1736	0.03 ± 0.01	1.07 ± 0.02	-0.17 ± 0.06	0.71 ± 0.13	0.14 ± 0.03	1.39 ± 0.11	-0.08 ± 0.03	0.83 ± 0.07
A3395	0.18 ± 0.01	1.46 ± 0.04	-0.68 ± 0.05	0.27 ± 0.05	0.59 ± 0.03	3.35 ± 0.18	-0.26 ± 0.02	0.59 ± 0.04
A754	0.24 ± 0.03	1.69 ± 0.13	-0.45 ± 0.06	0.43 ± 0.08	0.63 ± 0.06	3.92 ± 0.46	-0.15 ± 0.01	0.74 ± 0.03
A2256	0.18 ± 0.03	1.53 ± 0.12	-0.32 ± 0.07	0.52 ± 0.11	0.51 ± 0.07	3.24 ± 0.50	-0.11 ± 0.02	0.79 ± 0.05
A3571	0.03 ± 0.01	1.07 ± 0.02	-0.68 ± 0.08	0.29 ± 0.08	0.71 ± 0.08	4.84 ± 0.73	-0.43 ± 0.05	0.41 ± 0.07
A2199	0.17 ± 0.01	1.40 ± 0.03	-0.98 ± 0.06	0.15 ± 0.03	1.02 ± 0.05	8.39 ± 0.77	-0.45 ± 0.06	0.41 ± 0.08
A496	0.41 ± 0.01	2.27 ± 0.08	-1.22 ± 0.04	0.08 ± 0.01	1.15 ± 0.03	10.52 ± 0.50	-0.34 ± 0.04	0.47 ± 0.05
A85	0.29 ± 0.01	1.86 ± 0.07	-1.15 ± 0.02	0.08 ± 0.01	0.86 ± 0.04	6.04 ± 0.42	-0.35 ± 0.02	0.48 ± 0.04
A4038	0.25 ± 0.03	1.80 ± 0.14	-0.83 ± 0.07	0.21 ± 0.05	0.91 ± 0.07	7.01 ± 0.84	-0.38 ± 0.03	0.49 ± 0.05
A2052	0.30 ± 0.01	1.87 ± 0.05	-1.22 ± 0.08	0.08 ± 0.02	0.90 ± 0.03	6.64 ± 0.37	-0.39 ± 0.04	0.44 ± 0.06
Hydra-A	0.32 ± 0.04	2.07 ± 0.19	-1.19 ± 0.07	0.09 ± 0.03	1.12 ± 0.06	10.34 ± 1.03	-0.55 ± 0.03	0.32 ± 0.04
A2063	0.37 ± 0.03	2.22 ± 0.15	-0.83 ± 0.06	0.20 ± 0.04	0.97 ± 0.06	7.74 ± 0.81	-0.27 ± 0.01	0.56 ± 0.02
A3158	0.02 ± 0.01	1.08 ± 0.03	-0.41 ± 0.07	0.46 ± 0.10	0.30 ± 0.04	2.00 ± 0.18	-0.24 ± 0.04	0.63 ± 0.08
MKW3s	0.26 ± 0.02	1.79 ± 0.08	-0.97 ± 0.06	0.15 ± 0.03	0.96 ± 0.06	7.66 ± 0.80	-0.41 ± 0.03	0.43 ± 0.04
EXO0422	0.34 ± 0.03	2.14 ± 0.14	-1.41 ± 0.04	0.05 ± 0.01	1.09 ± 0.04	9.54 ± 0.71	-0.53 ± 0.03	0.34 ± 0.03
A4059	0.48 ± 0.03	2.52 ± 0.15	-0.71 ± 0.07	0.27 ± 0.07	0.92 ± 0.03	6.09 ± 0.35	-0.04 ± 0.04	0.89 ± 0.11
A2589	0.29 ± 0.02	1.74 ± 0.09	-0.68 ± 0.07	0.27 ± 0.07	0.72 ± 0.02	4.33 ± 0.19	-0.18 ± 0.03	0.64 ± 0.07
A3112	0.36 ± 0.02	2.20 ± 0.11	-1.28 ± 0.04	0.07 ± 0.01	1.14 ± 0.05	10.56 ± 0.83	-0.46 ± 0.03	0.39 ± 0.03
A1651	0.09 ± 0.01	1.23 ± 0.05	-0.69 ± 0.07	0.28 ± 0.06	0.63 ± 0.05	3.85 ± 0.41	-0.38 ± 0.04	0.46 ± 0.06
A576	0.13 ± 0.01	1.29 ± 0.04	-0.60 ± 0.07	0.33 ± 0.08	0.52 ± 0.03	2.91 ± 0.18	-0.27 ± 0.03	0.56 ± 0.06
A2657	0.25 ± 0.03	1.76 ± 0.12	-0.64 ± 0.07	0.31 ± 0.08	0.77 ± 0.05	5.17 ± 0.54	-0.27 ± 0.02	0.59 ± 0.04
A3391	0.11 ± 0.01	1.28 ± 0.03	-0.48 ± 0.05	0.38 ± 0.07	0.41 ± 0.03	2.47 ± 0.18	-0.20 ± 0.03	0.67 ± 0.07
A1650	0.11 ± 0.01	1.30 ± 0.03	-0.78 ± 0.07	0.23 ± 0.06	0.64 ± 0.04	3.90 ± 0.28	-0.39 ± 0.04	0.47 ± 0.07

Continued on next page

Table 4.4 – *Continued from previous page*

Cluster name	Best-fit values for temperature (keV)		Best-fit values for density (cm^{-5})		Best-fit values for entropy (keV*cm^2)		Best-fit values for pressure (dyne/cm^2)	
	α	T	α	n_e	α	S	α	P
S1101	0.29 ± 0.03	1.88 ± 0.11	-1.02 ± 0.09	0.15 ± 0.05	1.10 ± 0.04	9.46 ± 0.71	-0.50 ± 0.04	0.38 ± 0.05
Zwcl1215	0.14 ± 0.01	1.35 ± 0.03	-0.43 ± 0.07	0.44 ± 0.10	0.48 ± 0.04	2.81 ± 0.26	-0.17 ± 0.04	0.69 ± 0.08
A133	0.48 ± 0.01	2.74 ± 0.04	-1.32 ± 0.02	0.05 ± 0.00	1.04 ± 0.02	8.35 ± 0.29	-0.24 ± 0.01	0.60 ± 0.02
A2244	0.18 ± 0.03	1.51 ± 0.10	-0.74 ± 0.06	0.25 ± 0.06	0.78 ± 0.06	5.33 ± 0.61	-0.38 ± 0.03	0.47 ± 0.05
A2142	0.25 ± 0.03	1.73 ± 0.11	-0.75 ± 0.08	0.26 ± 0.08	0.89 ± 0.05	6.45 ± 0.61	-0.36 ± 0.03	0.48 ± 0.05
A3562	0.18 ± 0.03	1.53 ± 0.10	-0.56 ± 0.08	0.37 ± 0.10	0.64 ± 0.06	4.03 ± 0.47	-0.26 ± 0.03	0.60 ± 0.05
A401	0.10 ± 0.02	1.28 ± 0.07	-0.45 ± 0.08	0.44 ± 0.11	0.50 ± 0.06	3.05 ± 0.40	-0.24 ± 0.03	0.61 ± 0.06
A3558	0.07 ± 0.01	1.13 ± 0.04	-0.59 ± 0.07	0.33 ± 0.08	0.46 ± 0.03	2.65 ± 0.20	-0.32 ± 0.03	0.50 ± 0.05
A119	0.13 ± 0.01	1.33 ± 0.02	-0.37 ± 0.05	0.47 ± 0.07	0.38 ± 0.04	2.36 ± 0.21	-0.12 ± 0.03	0.77 ± 0.06
A1644	0.29 ± 0.02	1.84 ± 0.10	-1.05 ± 0.02	0.10 ± 0.01	0.72 ± 0.02	4.58 ± 0.14	-0.21 ± 0.04	0.65 ± 0.07
A2065	0.30 ± 0.02	1.94 ± 0.11	-0.68 ± 0.07	0.27 ± 0.07	0.77 ± 0.05	5.09 ± 0.45	-0.21 ± 0.02	0.66 ± 0.03
A3822	0.16 ± 0.03	1.42 ± 0.11	-0.53 ± 0.06	0.35 ± 0.07	0.58 ± 0.06	3.57 ± 0.45	-0.25 ± 0.01	0.57 ± 0.02
A3667	0.15 ± 0.04	1.48 ± 0.14	-0.41 ± 0.09	0.47 ± 0.13	0.67 ± 0.09	4.68 ± 0.87	-0.23 ± 0.04	0.65 ± 0.08
A399	0.07 ± 0.02	1.22 ± 0.06	-0.36 ± 0.07	0.50 ± 0.12	0.41 ± 0.06	2.65 ± 0.38	-0.20 ± 0.04	0.67 ± 0.08
A2163	0.08 ± 0.01	1.06 ± 0.03	-0.44 ± 0.09	1.35 ± 0.38	0.60 ± 0.06	1.92 ± 0.19	-0.29 ± 0.05	0.95 ± 0.14
A3376	0.28 ± 0.05	1.92 ± 0.23	-0.28 ± 0.06	0.55 ± 0.10	0.61 ± 0.09	4.03 ± 0.72	-0.03 ± 0.00	0.94 ± 0.01

Table 4.5: Power-law model with a constant base used to evaluate the slope of mean radial profiles. SR = strong relaxed clusters; SNR = strong non-relaxed clusters. We also listed best-fit values for the mean of combined SR, SNR and intermediate profiles.

Thermodynamic profiles	α	F	F_0
Mean T SR	0.45±0.02	1.62±0.02	0.36±0.03
Mean T SNR	1.34±0.07	2.27±0.21	0.84±0.01
Mean T Intermediate	0.85±0.03	1.79±0.05	0.69±0.01
Mean n_e SR	-1.10±0.07	0.16±0.05	-0.97±0.31
Mean n_e SNR	0.27±0.08	-5.67±0.59	4.31±0.85
Mean n_e Intermediate	-0.56±0.04	0.71±0.13	-1.38±0.25
Mean K SR	1.27±0.03	10.76±0.38	0.17±0.01
Mean K SNR	1.46±0.05	7.22±0.46	0.60±0.01
Mean K Intermediate	1.40±0.03	9.87±0.32	0.41±0.01
Mean P SR	-0.16±0.05	3.63±1.60	-4.05±1.72
Mean P SNR	0.54±0.08	-1.58±0.08	1.54±0.07
Mean P Intermediate	0.25±0.05	-3.26±0.23	2.95±0.31
combine mean of T	0.82±0.02	1.72±0.04	0.68±0.01
combine mean of n_e	-0.69±0.04	0.44±0.08	-0.99±0.19
combine mean of K	1.38±0.02	9.64±0.25	0.40±0.01
combine mean of P	0.15±0.04	-4.57±0.79	4.34±0.87

4.9 Calculation of morphology parameters for XMC Chandra maps

In Chapter 2 we gave a brief introduction to morphology parameters, and successfully demonstrated the usefulness of these parameter sets by calculating them on surface brightness images of *Chandra* observed clusters and separated relaxed and non-relaxed clusters. In particular, Gini, M_{20} and Concentration parameters proved to be very promising. In this section, we will apply morphology parameters to thermodynamic maps in order to study their morphology.

The thermodynamic properties of the ICM reflect the history of the cosmic evolution of baryons. In investigating the dynamical history of clusters, it is important to study the thermodynamic structure of a cluster; and it is equally important to measure the morphology of cluster thermodynamic maps. In the previous section, we observed a different distribution of temperature, entropy, density and pressure for strong relaxed and strong non-relaxed clusters. The study of morphology or shape of thermodynamic structure is hitherto unexplored in literature, particularly for entropy and pressure maps. We therefore take this opportunity to see whether morphology parameters contribute to the understanding of how temperature or entropy is distributed in a given cluster; and whether the observed thermodynamic structure of clusters can be used to obtain information on the nature of the feedback that affects the thermodynamical history of cosmic baryons. These parameters might also help to locate hot spots in the temperature map which could be due to strong AGN activity (Henry et al., 2004; Sanderson et al., 2005). We also aim to check whether the cluster temperature (or entropy) morphology is different for relaxed and non-relaxed clusters. This could help in understanding the relationship between cluster morphology and different feedback mechanisms responsible for generating heat or entropy in the ICM. However, surface brightness morphology is not related to any average value of either luminosity or temperature (cluster global properties, see

Table 4.6: Pure power-law model used to evaluate the slope of mean radial profiles. SR = strong relaxed clusters; SNR = strong non-relaxed clusters. We also listed best-fit values for the mean of combined SR, SNR and intermediate profiles.

Thermodynamic profiles	α	F
Mean T SR	0.27±0.01	1.76±0.03
Mean T SNR	0.14±0.02	1.37±0.07
Mean T Intermediate	0.21±0.02	1.60±0.06
Mean n_e SR	-1.30±0.06	0.07±0.01
Mean n_e SNR	-0.44±0.06	0.42±0.08
Mean n_e Intermediate	-0.85±0.04	0.18±0.03
Mean K SR	1.02±0.03	8.24±0.44
Mean K SNR	0.45±0.05	2.72±0.30
Mean K Intermediate	0.74±0.05	4.88±0.49
Mean P SR	-0.54±0.03	0.34±0.04
Mean P SNR	-0.18±0.02	0.69±0.04
Mean P Intermediate	-0.31±0.03	0.52±0.05
combine mean of T	0.21±0.02	1.59±0.06
combine mean of n_e	-0.92±0.04	0.15±0.02
combine mean of K	0.74±0.05	4.91±0.48
combine mean of P	-0.34±0.03	0.50±0.04

Chapter 3 § 3.6.1), but in the calculation of cluster thermodynamic morphology, it is, with the exception of density maps, independent of surface brightness morphology.

We found the cluster centre (centroid) (see Chapter 2, § 2.4) and applied a fixed aperture of physical size (see Chapter 3, § 3.4.2). In calculating the Smoothness parameter, we used a $1'$ Gaussian kernel size to smooth each low-z cluster image. We did not apply any additional smoothing to the input cluster image when calculating the parameters, since XMC generated maps are already smooth and free of CCD gaps and zero pixel counts. These morphology parameters were originally derived to calculate morphology of galaxies and clusters in their surface brightness image, where source peak emission (or maximum flux) lying at the cluster centre decreases radially, moving to the outer regions of the cluster. In the case of temperature and entropy maps, particularly for relaxed clusters, the situation is reversed. This means that the cluster core has a low temperature (and hence pixel value is low) compared with that of the outer region. Therefore, to maintain the 'definition' of (Gini, M_{20} and Concentration) morphology parameters, we inverted the pixel value of both the temperature and entropy maps of each of cluster. In this way, we obtained high pixel values in the core of the cluster, similar to those of the surface brightness distribution. We used the definition of the cluster dynamical states according to their surface brightness (combination of Gini, M_{20} and Concentration) (see Chapter 3, § 3.5).

As mentioned previously, high redshift clusters have low S/N, so in this analysis we included the low-z sample of the V09 exclusively. It is difficult to study the morphology of thermodynamic maps for high-z clusters because of the high uncertainty in photon counts. The following sections show morphology parameter calculations for density, temperature, entropy and pressure maps of low-z clusters.

4.9.1 Density map

Density maps, as previously discussed, are derived from the APEC normalisation (see Eq. 4.2). The structure of cluster visible in a density map is similar to that of the corresponding surface brightness image of the cluster (peak emission of the cluster is at the centre, and decreases radially). Hence we expect similar morphology and shape of clusters in the corresponding density maps, as well as surface brightness maps. Fig. 4.7 shows the distribution of morphology parameters calculated for density maps. In this plot, we showed the distribution of strong relaxed or strong cool core clusters (solid black line), relaxed or cool core clusters (dotted black line), non-relaxed or weak cool core clusters (dotted red line), and strong non-relaxed or non-cool core clusters (solid red line). We also showed the overall distribution of each parameter in each individual plot (dotted blue line). This overall distribution was plotted without showing any bias in cluster morphology but rather as a combined cluster morphology.

Since the morphology of each cluster in the density map is similar to the corresponding cluster morphology in the surface brightness map, the values of morphology parameters derived from density maps are also similar to those of surface brightness maps. We see that the Gini, M_{20} and Concentration parameters are able to distinguish strong relaxed and strong non-relaxed clusters, while there is an overlap between intermediate (relaxed and non-relaxed) clusters.

In the Gini plot, strong relaxed clusters are distributed on the right side (high Gini value) and strong non-relaxed clusters are distributed on the left side (low Gini value). Similarly, in the four Concentration plots, strong relaxed clusters are distributed on the right side (high Concentration) and strong non-relaxed clusters are distributed on the left side (low Concentration). The M_{20} parameter shows, as indicated previously, a reverse distribution, i.e. strong relaxed clusters appear on the left side (low M_{20}), strong non-relaxed clusters on the right side (high M_{20}) of the plot. None of the remaining parameters are able to separate the different cluster dynamical states. As noted in Chapter 2 (§ 3.3.3), the Smoothness and Asymmetry parameters are particularly sensitive to different lengths of exposure time of clusters. There is a large variation in exposure time (multiform exposure time) for low-z clusters, and hence these two parameters are not sufficiently robust for cluster morphology studies. Table 4.7 lists all parameter values calculated for density maps, together with the 1σ uncertainty (see Chapter 2, § 2.2.5).

Fig. 4.8 shows parameter vs parameter plots, i.e. the combination of all morphology parameters, indicating the morphology of clusters in density plots lying across the different morphology parameter-parameter planes. In each case, we plotted four distinct dynamical states of cluster, i.e. strong relaxed ($\circ$), relaxed ($\Diamond$), non-relaxed ($+$) and strong non-relaxed ($\times$). Different trends between parameters such as Gini vs Concentration and M_{20} vs Concentration are similar to those of cluster morphology in surface brightness maps. This means that, in the Concentration vs M_{20} plot, strong non-relaxed clusters fall in the bottom right region while strong relaxed clusters fall in the upper left region. In the Gini vs M_{20} plot, the upper left region is for strong non-relaxed clusters, while the bottom-right region is for strong relaxed clusters. These could indicate that the distribution of electron density in the core of a cluster is different for relaxed and non-relaxed clusters. Strong relaxed clusters have concentrated electron density in a small region of the core, compared with strong non-relaxed clusters which do not have a compact or concentrated electron density distribution in the core. It could be that both of these plots show cluster evolution in the trend of strong non-relaxed or non-cool core cluster → mild merger or weak-cool core cluster → relaxed or cool core cluster → strong relaxed, strong cool core or evolved cluster.

It is possible that (some) parameter values could be slightly different for the same cluster in the surface brightness and density plots. This would depend on different image quality and various artifacts in input event files, different sizes of blob and its smoothing sizes in density maps for different clusters, binning factor used for density maps, S/N of input cluster event files, noise in the XMC models (sky + instrument), etc. Overall trends between parameters are, however, similar except for the Gini of the second order moment and Smoothness parameters. A possible reason is that 2-D Gaussian blobs are already smoothed, making the density maps different from those of smoothed counts images. The Smoothness and G_M parameters are severely affected by S/N, rendering it unhelpful in analysis where a cluster sample is large and where each cluster has a different exposure time.

Table 4.8 lists the mean, median, K-S and R-S tests values for the subsample of only strong relaxed and strong non-relaxed clusters. The resultant probabilities from the K-S and R-S tests are the same for the Gini, M_{20} and Concentration parameters, since we separated the dynamical states of clusters in density maps based on these three parameters according to the surface brightness map of clusters. These probabilities for the G_M parameter is significant (< 0.01 and 0.001, respectively) to separate strong relaxed and strong non-relaxed clusters. The G_M parameter was not useful for real cluster data, but it turns out that the this parameter could be useful for highly smooth cluster images of the XMC modelling and for nearby clusters to separate relaxed and non-relaxed clusters. Further testing, however, require for this parameter. The K-S and R-S probabilities are not significant for the Asymmetry, Smoothness and Ellipticity parameters which means these parameters are not useful to separate different dynamical states of clusters.

Table 4.7: Value of morphology parameters for the low-z clusters (density maps). Values are listed with appropriate uncertainties of 1σ for each parameter.

Cluster name	Gini	M_{20}	Concentration	Asymmetry	Smoothness	G_M	Ellipticity
A3571	0.318 ± 0.001	-1.627 ± 0.018	2.627 ± 0.002	0.152 ± 0.029	0.023 ± 0.000	0.200 ± 0.002	0.116 ± 0.000
A2199	0.558 ± 0.003	-1.889 ± 0.045	3.686 ± 0.018	0.285 ± 0.012	0.022 ± 0.000	0.189 ± 0.002	0.122 ± 0.000
A0335	0.649 ± 0.003	-2.079 ± 0.085	5.394 ± 0.061	0.392 ± 0.029	0.034 ± 0.000	0.113 ± 0.006	0.080 ± 0.000
A496	0.551 ± 0.004	-2.115 ± 0.043	4.315 ± 0.033	0.294 ± 0.025	0.029 ± 0.000	0.116 ± 0.003	0.057 ± 0.000
A85	0.646 ± 0.003	-1.849 ± 0.038	4.311 ± 0.038	0.587 ± 0.026	0.021 ± 0.000	0.263 ± 0.003	0.022 ± 0.000
A478	0.690 ± 0.004	-2.219 ± 0.081	4.927 ± 0.014	0.214 ± 0.057	0.033 ± 0.000	0.178 ± 0.004	0.154 ± 0.000
A1795	0.720 ± 0.004	-2.216 ± 0.066	5.326 ± 0.012	0.285 ± 0.049	0.021 ± 0.000	0.186 ± 0.002	0.133 ± 0.000
A4038	0.504 ± 0.002	-1.913 ± 0.030	3.801 ± 0.031	0.230 ± 0.021	0.016 ± 0.000	0.177 ± 0.001	0.147 ± 0.000
A2052	0.536 ± 0.006	-2.209 ± 0.037	4.360 ± 0.013	0.208 ± 0.025	0.045 ± 0.000	0.136 ± 0.003	0.099 ± 0.000
Hydra-A	0.578 ± 0.010	-2.086 ± 0.111	4.910 ± 0.039	0.238 ± 0.083	0.052 ± 0.000	0.117 ± 0.007	0.068 ± 0.000
A2063	0.407 ± 0.003	-1.845 ± 0.033	3.369 ± 0.011	0.237 ± 0.026	0.034 ± 0.000	0.159 ± 0.003	0.060 ± 0.000
A3158	0.484 ± 0.001	-1.782 ± 0.011	3.195 ± 0.010	0.190 ± 0.016	0.010 ± 0.000	0.186 ± 0.000	0.136 ± 0.000
MKW3s	0.523 ± 0.003	-1.997 ± 0.054	3.834 ± 0.017	0.188 ± 0.062	0.027 ± 0.000	0.162 ± 0.004	0.140 ± 0.000
EXO0422	0.636 ± 0.005	-2.361 ± 0.070	5.099 ± 0.011	0.176 ± 0.044	0.049 ± 0.000	0.087 ± 0.006	0.071 ± 0.000
A4059	0.395 ± 0.003	-1.730 ± 0.033	3.266 ± 0.017	0.193 ± 0.025	0.045 ± 0.000	0.163 ± 0.006	0.078 ± 0.000
A2589	0.381 ± 0.003	-1.769 ± 0.035	2.870 ± 0.013	0.259 ± 0.024	0.039 ± 0.000	0.244 ± 0.002	0.166 ± 0.000
A3112	0.569 ± 0.019	-2.153 ± 0.143	4.279 ± 0.011	0.414 ± 0.130	0.082 ± 0.000	0.163 ± 0.006	0.147 ± 0.000
A1651	0.579 ± 0.004	-1.988 ± 0.020	4.104 ± 0.027	0.228 ± 0.061	0.031 ± 0.000	0.117 ± 0.002	0.076 ± 0.000
A576	0.329 ± 0.003	-1.613 ± 0.054	2.826 ± 0.008	0.308 ± 0.023	0.041 ± 0.000	0.217 ± 0.004	0.095 ± 0.000
A2657	0.387 ± 0.002	-1.676 ± 0.038	3.054 ± 0.019	0.295 ± 0.040	0.035 ± 0.000	0.154 ± 0.005	0.046 ± 0.000
A3391	0.462 ± 0.001	-1.727 ± 0.011	3.042 ± 0.005	0.268 ± 0.019	0.024 ± 0.000	0.231 ± 0.000	0.154 ± 0.000
A1650	0.602 ± 0.004	-2.150 ± 0.015	4.448 ± 0.029	0.281 ± 0.056	0.029 ± 0.000	0.183 ± 0.002	0.124 ± 0.000
S1101	0.654 ± 0.007	-2.110 ± 0.047	4.765 ± 0.017	0.332 ± 0.149	0.055 ± 0.000	0.158 ± 0.007	0.142 ± 0.000
zwcl1215	0.439 ± 0.002	-1.755 ± 0.008	3.193 ± 0.003	0.162 ± 0.017	0.027 ± 0.000	0.175 ± 0.000	0.126 ± 0.000
A2597	0.803 ± 0.004	-2.495 ± 0.096	6.196 ± 0.030	0.183 ± 0.092	0.052 ± 0.000	0.197 ± 0.004	0.069 ± 0.000
A133	0.507 ± 0.010	-2.187 ± 0.046	4.246 ± 0.018	0.352 ± 0.097	0.064 ± 0.000	0.144 ± 0.003	0.077 ± 0.000

Continued on next page

Table 4.7 – *Continued from previous page*

Cluster name	Gini	M_{20}	Concentration	Asymmetry	Smoothness	G_M	Ellipticity
A2244	0.608 ± 0.003	-2.082 ± 0.019	4.570 ± 0.020	0.193 ± 0.058	0.028 ± 0.000	0.101 ± 0.003	0.062 ± 0.000
RXJ1504	0.834 ± 0.013	-2.475 ± 0.177	6.211 ± 0.199	0.573 ± 0.154	0.184 ± 0.000	0.229 ± 0.021	0.128 ± 0.000
A2204	0.763 ± 0.011	-2.638 ± 0.198	6.458 ± 0.111	0.357 ± 0.155	0.142 ± 0.000	0.115 ± 0.009	0.052 ± 0.000
A2029	0.691 ± 0.003	-2.232 ± 0.049	4.943 ± 0.017	0.239 ± 0.040	0.024 ± 0.000	0.139 ± 0.003	0.088 ± 0.000
A2142	0.566 ± 0.003	-1.922 ± 0.046	3.842 ± 0.051	0.363 ± 0.029	0.018 ± 0.000	0.233 ± 0.002	0.176 ± 0.000
A3562	0.599 ± 0.002	-1.869 ± 0.027	3.730 ± 0.010	0.402 ± 0.021	0.023 ± 0.000	0.300 ± 0.003	0.072 ± 0.000
A401	0.445 ± 0.001	-1.752 ± 0.006	3.254 ± 0.005	0.127 ± 0.017	0.016 ± 0.000	0.158 ± 0.000	0.118 ± 0.000
A3558	0.316 ± 0.002	-1.438 ± 0.038	2.796 ± 0.036	0.416 ± 0.023	0.049 ± 0.000	0.253 ± 0.003	0.104 ± 0.000
A2147	0.264 ± 0.001	-1.500 ± 0.020	2.375 ± 0.008	0.214 ± 0.014	0.035 ± 0.000	0.235 ± 0.001	0.097 ± 0.000
A3266	0.220 ± 0.002	-1.276 ± 0.034	2.203 ± 0.020	0.241 ± 0.031	0.046 ± 0.000	0.246 ± 0.003	0.073 ± 0.000
A119	0.415 ± 0.001	-1.524 ± 0.015	2.484 ± 0.017	0.350 ± 0.004	0.022 ± 0.000	0.344 ± 0.001	0.109 ± 0.000
A1644	0.420 ± 0.006	-1.824 ± 0.026	3.147 ± 0.049	0.495 ± 0.014	0.059 ± 0.000	0.252 ± 0.002	0.055 ± 0.000
A1736	0.134 ± 0.001	-1.227 ± 0.024	1.945 ± 0.013	0.198 ± 0.012	0.049 ± 0.000	0.273 ± 0.001	0.022 ± 0.000
A3395	0.458 ± 0.001	-0.757 ± 0.003	1.729 ± 0.006	0.672 ± 0.015	0.036 ± 0.000	0.524 ± 0.001	0.324 ± 0.000
A2065	0.476 ± 0.002	-1.707 ± 0.041	3.512 ± 0.011	0.352 ± 0.012	0.026 ± 0.000	0.197 ± 0.002	0.162 ± 0.000
A3822	0.452 ± 0.002	-1.664 ± 0.022	3.292 ± 0.023	0.314 ± 0.006	0.027 ± 0.000	0.199 ± 0.001	0.136 ± 0.000
A3667	0.566 ± 0.001	-1.317 ± 0.041	3.515 ± 0.028	0.533 ± 0.013	0.012 ± 0.000	0.325 ± 0.004	0.122 ± 0.000
A754	0.372 ± 0.001	-1.110 ± 0.012	2.435 ± 0.014	0.397 ± 0.013	0.018 ± 0.000	0.244 ± 0.001	0.118 ± 0.000
A2256	0.377 ± 0.001	-1.353 ± 0.013	2.604 ± 0.003	0.207 ± 0.018	0.015 ± 0.000	0.233 ± 0.001	0.162 ± 0.000
A399	0.402 ± 0.002	-1.458 ± 0.025	2.962 ± 0.018	0.307 ± 0.015	0.016 ± 0.000	0.196 ± 0.001	0.104 ± 0.000
A2163	0.377 ± 0.003	-1.431 ± 0.063	2.742 ± 0.046	0.307 ± 0.052	0.039 ± 0.000	0.193 ± 0.009	0.083 ± 0.000
A3376	0.549 ± 0.001	-1.355 ± 0.008	2.780 ± 0.024	0.685 ± 0.012	0.024 ± 0.000	0.426 ± 0.004	0.072 ± 0.000

Table 4.8: Statistics for the subsample of strong relaxed (SR), and strong non-relaxed (SNR) clusters (density maps). K-S and R-S statistics were performed between strong relaxed and strong non-relaxed clusters to test whether they have the same distribution or not.

Parameters	mean SR SNR	median SR SNR	K-S prob. SR SNR	R-S prob. SR SNR
Gini	0.74 0.30	0.72 0.32	7.95×10^{-04}	2.70×10^{-03}
M_{20}	-2.34 -1.20	-2.23 -1.25	7.95×10^{-04}	2.70×10^{-03}
Concentration	1.92 0.75	1.83 0.78	7.95×10^{-04}	2.70×10^{-03}
Asymmetry	0.32 0.32	0.29 0.23	7.00×10^{-01}	7.75×10^{-01}
Smoothness	0.07 0.03	0.03 0.04	4.68×10^{-01}	1.99×10^{-01}
G_M	0.17 0.29	0.18 0.25	7.95×10^{-04}	2.70×10^{-03}
Ellipticity	0.10 0.13	0.09 0.11	7.77×10^{-01}	6.68×10^{-01}

4.9.2 Temperature map

We calculated morphology parameters for temperature maps of low-z clusters in order to understand the temperature distribution and cluster temperature morphology.

Fig. 4.9 illustrates the distribution of morphology parameters for temperature maps. In this plot, we showed the distribution of strong relaxed (solid black line), relaxed (dotted black dotted), non-relaxed (red dotted line) and strong non-relaxed (solid red line) clusters. We also showed the overall distribution of every parameter in each parameter distribution plot (dotted blue line). We noticed an overlap between strong relaxed and strong non-relaxed clusters in the Gini, M_{20} and Concentration distributions. The distribution of different dynamical states of clusters among these plots is indistinguishable. Table 4.9 lists all parameter values calculated for temperature maps, together with the 1σ uncertainty (see Chapter 2, § 2.2.5).

Fig. 4.10 shows the parameter vs parameter planes for temperature maps. In each case, we plotted four distinct dynamical states of cluster, i.e. strong relaxed ($\circ$), relaxed ($\Diamond$), non-relaxed ($+$) and strong non-relaxed ($\times$). On the various parameter planes we observed overlap between relaxed and non-relaxed clusters. We observed that the range of morphology parameters calculated for temperature maps was not similar to the range of parameters calculated for density or surface brightness maps.

In the M_{20} vs Concentration plot (Fig. 4.10) we noticed several peculiar objects, such as A3376, A3562, A3667, A85, A4059, A754, A2256, A478, A2029, A2204, A1795 and RXJ1504. A478 is a strong relaxed cluster, but its temperature plot has the highest M_{20} and lowest Concentration parameters of all strong relaxed clusters. A2029, A2204, A1795 and RXJ1504 are also strong relaxed clusters which, however, overlap with non-relaxed clusters. A754 and A2256 are strong non-relaxed clusters, but they have the lowest M_{20} and highest Concentration parameters compared with other strong non-relaxed clusters. The remaining clusters are non-relaxed, but they all fall in the upper-left corner of the M_{20} vs Concentration plot and overlap with (two) strong relaxed clusters.

These peculiar objects may provide a hint about their internal properties through their temperature morphology. In the case of peculiar strong relaxed clusters, if there is any powerful AGN activity or small scale substructure (which could be detected in cluster thermodynamic maps only) at the core of the cluster, it could disturb the temperature distribution of the relaxed core. It is possible that the punch delivered to the surrounding ICM via jet emission could be the result of

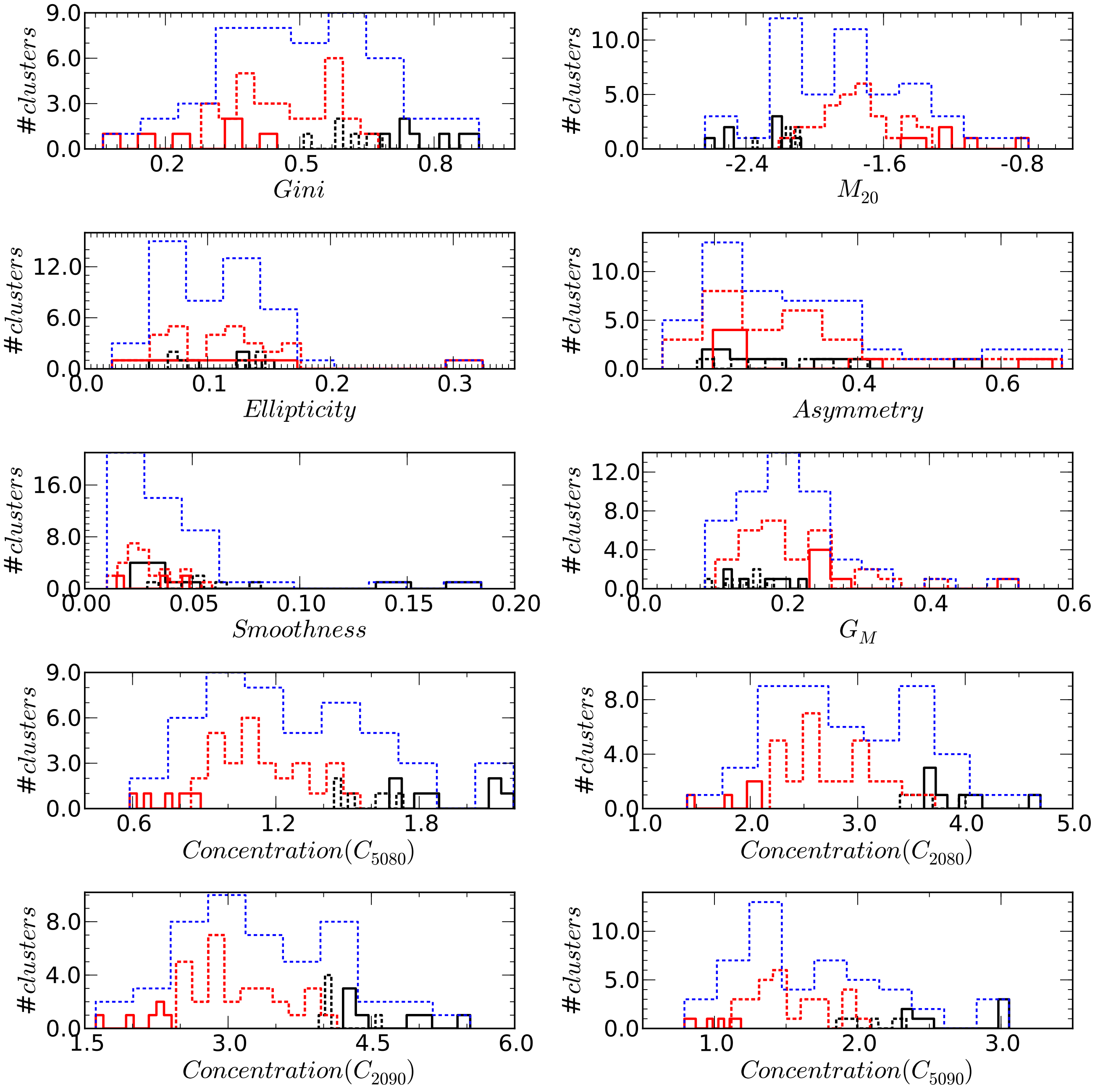

Figure 4.7: Distribution of seven morphology parameters based on the cluster density maps. Solid black line = strong relaxed (strong cool core) clusters; dotted black line = relaxed (cool core) clusters; dotted red line = non-relaxed (weak cool core) clusters; solid red line = strong non-relaxed (non-cool core) clusters; and dotted blue line = overall cluster morphology distribution for each parameter. All four definitions of the Concentration parameter were used. Cluster separation is based on the combination of Gini, M_{20} and Concentration parameters.

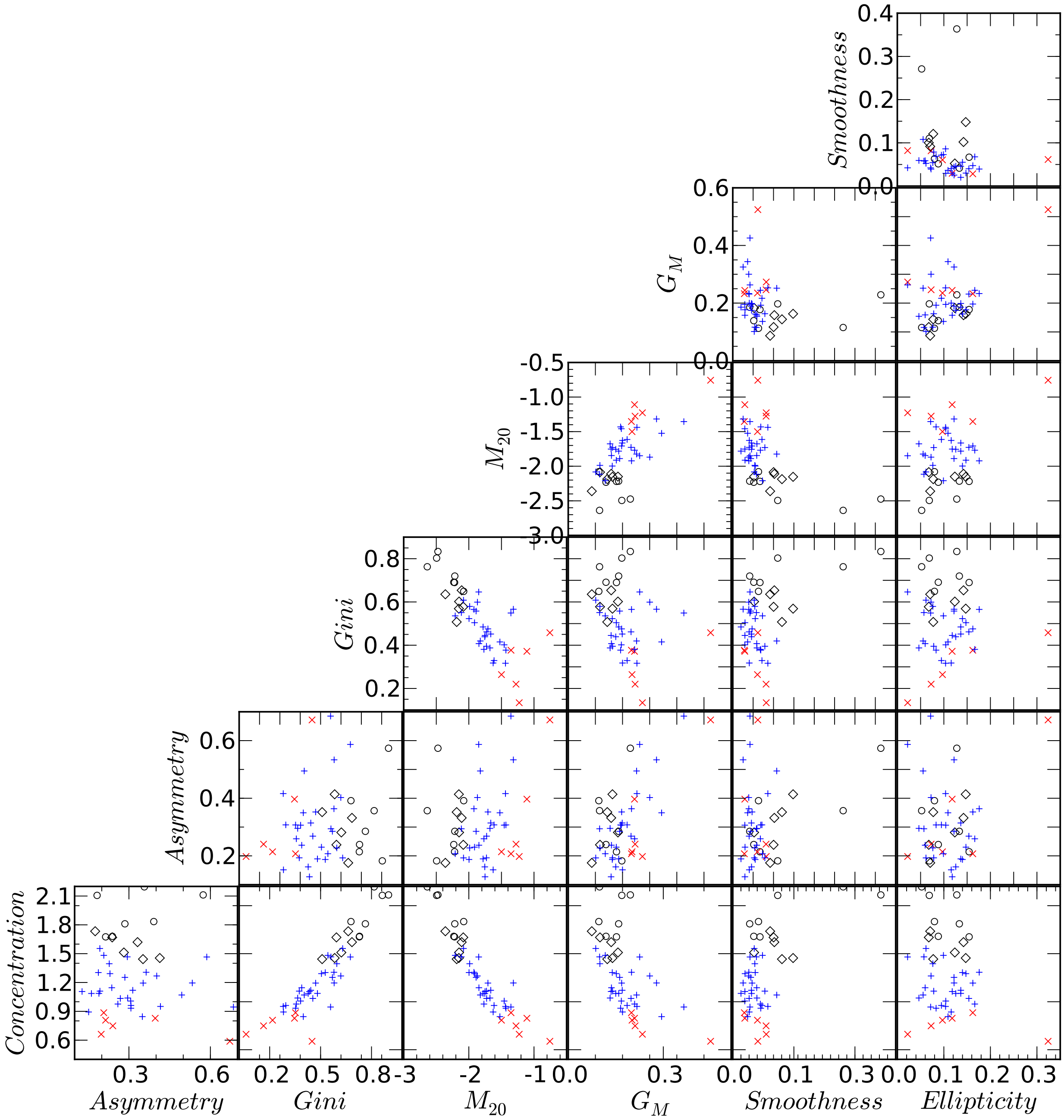

Figure 4.8: Seven morphology parameters plotted in the parameter-parameter planes (density maps). We plotted C_{5080} as the Concentration parameter. ○ = strong relaxed (strong cool core) clusters; ◇ = relaxed (cool core) clusters; + = non-relaxed (weak cool core) clusters; and × = strong non-relaxed (non-cool core) clusters.

AGN activity; and this could be the cause of asymmetry in the temperature distribution and the increase in temperature. These relaxed clusters therefore fall into the non-relaxed cluster category (low Concentration and high M_{20} values). This could suggest that morphology parameters might be helpful in investigating AGN activity and its effect on the surrounding medium, particularly in relaxed clusters using their temperature maps. In § 4.10, we describe each of these strong relaxed clusters in detail, with their radial profiles.

In the case of non-relaxed and strong non-relaxed peculiar objects, the temperature gradient is steep compared with other non-relaxed and strong non-relaxed clusters, respectively. It is possible that these peculiar clusters are evolving via infalling subgroups or minor clusters within the main cluster body; or it may be that the cluster outskirts are interacting with other groups or clusters. If these were the case, then there would be high temperature at the cluster outskirts; but the core of the cluster meanwhile, appeared unaffected by merger shocks in all peculiar disturbed (non-relaxed and strong non-relaxed) clusters. Cluster cores have been survived in these peculiar disturbed clusters only among other disturbed clusters within our sample. Due to the inversion of these cluster temperature maps, the cluster core region will become the brightest region (or have high pixel values and hence small r_{50} inner radius compared with large r_{80} outer radius). This will result in high Concentration values and low M_{20} values (20% of the bright pixels are close to the cluster centre) for these peculiar disturbed clusters.

In the plot of Gini vs Concentration or Gini vs M_{20}, there are five (A119, A3667, A85, A3562, and A3376) non-relaxed clusters and one strong non-relaxed (A3395) cluster with a relatively high Gini value (and high G_M value). As mentioned in the previous paragraph, A3667, A85, A3562 and A3376 have high Concentration values in their temperature plots so they have bright pixels located at the core of cluster. In the case of A119 and A3395, however, bright pixels (or low temperature plasma) are not located near the cluster centroid because they have low Concentration values. We found that 85% of clusters have low Gini value (< 0.15). This may indicate that, unlike surface brightness or density distribution, temperature distribution does not have compact bright pixels (or bright temperature spots) located at any one position in the given aperture. These temperature (bright) spots are distributed throughout the ICM in both the relaxed and non-relaxed clusters.

Table 4.10 lists the mean, median, K-S and R-S tests values for the subsamples of strong relaxed and strong non-relaxed clusters. The K-S and R-S probabilities are not significant (> 0.01 and 0.001, respectively) for any of the parameters to separate the strong relaxed and strong non-relaxed clusters in the temperature maps.

Table 4.9: Value of morphology parameters for the low-z clusters (temperature maps). Values are listed with appropriate uncertainties of 1σ for each parameter.

Cluster name	Gini	M_{20}	Concentration	Asymmetry	Smoothness	G_M	Ellipticity
A3571	0.061 ± 0.002	-0.625 ± 0.019	1.553 ± 0.019	0.214 ± 0.021	0.040 ± 0.007	0.336 ± 0.004	0.016 ± 0.008
A2199	0.124 ± 0.001	-0.887 ± 0.013	1.701 ± 0.018	0.371 ± 0.012	0.031 ± 0.003	0.339 ± 0.003	0.014 ± 0.004
A0335	0.173 ± 0.003	-1.553 ± 0.019	2.064 ± 0.034	0.269 ± 0.013	0.030 ± 0.003	0.293 ± 0.005	0.049 ± 0.004
A496	0.160 ± 0.003	-1.370 ± 0.011	1.984 ± 0.020	0.285 ± 0.014	0.029 ± 0.004	0.294 ± 0.007	0.004 ± 0.005
A85	0.264 ± 0.002	-1.263 ± 0.023	2.098 ± 0.022	0.441 ± 0.014	0.022 ± 0.005	0.404 ± 0.002	0.125 ± 0.003
A478	0.024 ± 0.002	-0.881 ± 0.018	1.570 ± 0.043	0.072 ± 0.021	0.034 ± 0.007	0.329 ± 0.003	0.010 ± 0.004
A1795	0.111 ± 0.002	-1.293 ± 0.021	1.744 ± 0.015	0.268 ± 0.018	0.024 ± 0.004	0.328 ± 0.004	0.029 ± 0.004
A4038	0.092 ± 0.002	-1.273 ± 0.008	1.752 ± 0.013	0.129 ± 0.018	0.025 ± 0.001	0.294 ± 0.003	0.055 ± 0.005
A2052	0.133 ± 0.003	-0.943 ± 0.014	1.754 ± 0.019	0.369 ± 0.019	0.034 ± 0.002	0.336 ± 0.004	0.045 ± 0.004
Hydra-A	0.119 ± 0.006	-1.085 ± 0.022	1.820 ± 0.032	0.228 ± 0.021	0.047 ± 0.004	0.287 ± 0.007	0.026 ± 0.006
A2063	0.117 ± 0.002	-1.290 ± 0.024	1.857 ± 0.026	0.181 ± 0.022	0.035 ± 0.004	0.290 ± 0.003	0.036 ± 0.006
A3158	0.111 ± 0.002	-1.074 ± 0.017	1.815 ± 0.019	0.150 ± 0.019	0.019 ± 0.005	0.271 ± 0.003	0.039 ± 0.003
MKW3s	0.080 ± 0.004	-1.251 ± 0.017	1.729 ± 0.019	0.156 ± 0.016	0.040 ± 0.003	0.300 ± 0.003	0.028 ± 0.004
EXO0422	0.117 ± 0.004	-1.309 ± 0.024	1.846 ± 0.035	0.122 ± 0.020	0.036 ± 0.005	0.286 ± 0.003	0.061 ± 0.006
A4059	0.175 ± 0.006	-1.637 ± 0.019	2.158 ± 0.043	0.188 ± 0.033	0.046 ± 0.012	0.279 ± 0.007	0.037 ± 0.011
A2589	0.154 ± 0.002	-0.795 ± 0.021	1.744 ± 0.024	0.310 ± 0.017	0.044 ± 0.007	0.351 ± 0.006	0.077 ± 0.008
A3112	0.094 ± 0.007	-1.381 ± 0.030	1.784 ± 0.043	0.192 ± 0.078	0.068 ± 0.008	0.297 ± 0.007	0.025 ± 0.013
A1651	0.084 ± 0.003	-1.212 ± 0.018	1.787 ± 0.022	0.116 ± 0.020	0.032 ± 0.005	0.287 ± 0.003	0.015 ± 0.005
A576	0.108 ± 0.004	-0.864 ± 0.016	1.683 ± 0.023	0.334 ± 0.021	0.044 ± 0.004	0.337 ± 0.006	0.027 ± 0.006
A2657	0.089 ± 0.003	-1.258 ± 0.011	1.756 ± 0.018	0.164 ± 0.015	0.041 ± 0.005	0.296 ± 0.003	0.016 ± 0.006
A3391	0.102 ± 0.002	-1.058 ± 0.015	1.760 ± 0.012	0.223 ± 0.014	0.024 ± 0.004	0.316 ± 0.002	0.039 ± 0.003
A1650	0.126 ± 0.002	-0.837 ± 0.011	1.740 ± 0.019	0.317 ± 0.023	0.031 ± 0.004	0.328 ± 0.004	0.039 ± 0.007
S1101	0.108 ± 0.004	-1.358 ± 0.026	1.823 ± 0.025	0.169 ± 0.038	0.050 ± 0.006	0.294 ± 0.005	0.050 ± 0.008
zwcl1215	0.084 ± 0.001	-1.020 ± 0.017	1.719 ± 0.030	0.147 ± 0.017	0.031 ± 0.004	0.309 ± 0.002	0.048 ± 0.004
A2597	0.223 ± 0.003	-1.563 ± 0.021	2.222 ± 0.034	0.358 ± 0.021	0.026 ± 0.004	0.295 ± 0.007	0.023 ± 0.004
A133	0.151 ± 0.006	-1.402 ± 0.024	1.952 ± 0.045	0.228 ± 0.037	0.051 ± 0.007	0.306 ± 0.009	0.039 ± 0.006

Continued on next page

Table 4.9 – *Continued from previous page*

Cluster name	Gini	M_{20}	Concentration	Asymmetry	Smoothness	G_M	Ellipticity
A2244	0.138 ± 0.003	-1.360 ± 0.014	1.940 ± 0.031	0.252 ± 0.023	0.032 ± 0.005	0.291 ± 0.006	0.014 ± 0.005
RXJ1504	0.085 ± 0.007	-1.393 ± 0.033	1.799 ± 0.067	0.124 ± 0.043	0.065 ± 0.012	0.294 ± 0.006	0.023 ± 0.012
A2204	0.063 ± 0.004	-1.291 ± 0.024	1.710 ± 0.042	0.143 ± 0.033	0.053 ± 0.010	0.308 ± 0.004	0.008 ± 0.008
A2029	0.108 ± 0.003	-1.152 ± 0.015	1.788 ± 0.024	0.280 ± 0.013	0.027 ± 0.005	0.311 ± 0.003	0.012 ± 0.009
A2142	0.124 ± 0.003	-1.352 ± 0.012	1.841 ± 0.036	0.187 ± 0.014	0.030 ± 0.006	0.302 ± 0.004	0.013 ± 0.008
A3562	0.255 ± 0.002	-1.421 ± 0.017	2.120 ± 0.021	0.467 ± 0.015	0.022 ± 0.002	0.411 ± 0.002	0.133 ± 0.004
A401	0.102 ± 0.003	-1.120 ± 0.009	1.774 ± 0.027	0.139 ± 0.016	0.025 ± 0.004	0.287 ± 0.002	0.048 ± 0.005
A3558	0.084 ± 0.004	-0.789 ± 0.025	1.647 ± 0.016	0.246 ± 0.022	0.052 ± 0.004	0.339 ± 0.005	0.042 ± 0.008
A2147	0.098 ± 0.002	-0.720 ± 0.014	1.635 ± 0.020	0.184 ± 0.019	0.038 ± 0.003	0.322 ± 0.003	0.083 ± 0.005
A3266	0.048 ± 0.005	-0.968 ± 0.025	1.620 ± 0.042	0.137 ± 0.029	0.057 ± 0.009	0.316 ± 0.005	0.028 ± 0.007
A119	0.177 ± 0.001	-0.899 ± 0.009	1.675 ± 0.018	0.190 ± 0.012	0.023 ± 0.004	0.402 ± 0.001	0.052 ± 0.004
A1644	0.121 ± 0.004	-1.279 ± 0.033	1.752 ± 0.024	0.245 ± 0.025	0.051 ± 0.006	0.335 ± 0.004	0.035 ± 0.005
A1736	0.072 ± 0.003	-0.572 ± 0.018	1.535 ± 0.017	0.225 ± 0.026	0.053 ± 0.005	0.353 ± 0.006	0.002 ± 0.002
A3395	0.191 ± 0.002	-0.685 ± 0.005	1.744 ± 0.021	0.360 ± 0.012	0.026 ± 0.003	0.415 ± 0.001	0.160 ± 0.003
A2065	0.156 ± 0.003	-1.264 ± 0.011	2.001 ± 0.024	0.219 ± 0.019	0.024 ± 0.004	0.282 ± 0.004	0.057 ± 0.006
A3822	0.108 ± 0.003	-1.226 ± 0.017	1.797 ± 0.014	0.225 ± 0.015	0.031 ± 0.004	0.313 ± 0.003	0.034 ± 0.005
A3667	0.253 ± 0.002	-1.420 ± 0.013	2.088 ± 0.024	0.385 ± 0.008	0.021 ± 0.005	0.377 ± 0.002	0.102 ± 0.003
A754	0.125 ± 0.002	-1.191 ± 0.013	1.861 ± 0.017	0.175 ± 0.010	0.019 ± 0.004	0.291 ± 0.002	0.064 ± 0.003
A2256	0.127 ± 0.003	-1.118 ± 0.019	1.855 ± 0.017	0.133 ± 0.021	0.020 ± 0.006	0.283 ± 0.003	0.060 ± 0.003
A399	0.075 ± 0.003	-1.268 ± 0.013	1.734 ± 0.012	0.129 ± 0.015	0.025 ± 0.004	0.304 ± 0.002	0.041 ± 0.007
A2163	0.041 ± 0.005	-1.021 ± 0.038	1.617 ± 0.053	0.162 ± 0.035	0.065 ± 0.014	0.314 ± 0.005	0.003 ± 0.009
A3376	0.366 ± 0.002	-1.305 ± 0.011	2.458 ± 0.033	0.615 ± 0.009	0.022 ± 0.003	0.449 ± 0.002	0.105 ± 0.005

Table 4.10: Statistics for the subsample of strong relaxed (SR), and strong non-relaxed (SNR) clusters (temperature maps). K-S and R-S statistics were performed between strong relaxed and strong non-relaxed clusters to test whether they have the same distribution or not.

Parameters	mean SR SNR	median SR SNR	K-S prob. SR SNR	R-S prob. SR SNR
Gini	0.11 0.11	0.11 0.11	9.94×10^{-01}	8.86×10^{-01}
M_{20}	-1.30 -0.88	-1.29 -0.84	3.68×10^{-02}	1.52×10^{-02}
Concentration	0.63 0.58	0.61 0.57	7.00×10^{-01}	3.91×10^{-01}
Asymmetry	0.22 0.20	0.27 0.18	5.43×10^{-01}	8.86×10^{-01}
Smoothness	0.06 0.06	0.05 0.05	7.00×10^{-01}	5.68×10^{-01}
G_M	0.31 0.33	0.31 0.32	6.21×10^{-01}	6.68×10^{-01}
Ellipticity	0.02 0.07	0.02 0.06	6.16×10^{-02}	8.65×10^{-02}

4.9.3 Entropy map

2-D entropy maps of clusters allow us to investigate the excess of heat input/generation in the ICM at different locations within a cluster, from the outskirts to the core. We investigated entropy structure or morphology of clusters, using morphology parameters in order to understand the entropy distribution.

Fig. 4.11 shows the distribution of morphology parameters for the pseudo entropy maps generated by the XMC technique. In this plot, we showed the distribution of strong relaxed (solid black line), relaxed (dotted black line), non-relaxed (dotted red line) and strong non-relaxed (solid red line) clusters. The dotted blue line indicates the overall distribution of each parameter. We observed that Gini, M_{20} and Concentration parameters separate the strong relaxed and strong non-relaxed clusters. This could indicate that the entropy map might be useful for separating strong relaxed and strong non-relaxed clusters, or that distribution of entropy might indicate the dynamical state of the cluster. Morphology parameter distribution for the entropy map is similar to distribution for surface brightness or density maps. This means high Concentration and high Gini values for strong relaxed clusters and low Concentration and low Gini values for strong non-relaxed clusters; and low M_{20} values for strong relaxed clusters and high M_{20} values for strong non-relaxed clusters. Table 4.11 lists all parameter values calculated for entropy maps, together with 1σ uncertainty (see Chapter 2, § 2.2.5).

In relaxed clusters, radiative cooling regulates the minimum entropy level of the ICM through a selective removal of gas with short cooling time, while non-gravitational heating such as AGN restricts the amount of gas which can cool down to form stars and prevent excessive cooling. Non-relaxed clusters are equally heated depending on the kinetic energy of the incoming shocks (Balogh et al., 2007). Further, in non-relaxed clusters, entropy is enhanced by adiabatic compression, and by merger shocks or infalling material (gravitational heating) that generate the strong accretion shocks which pass through the cluster. It is a common belief that the ICM entropy is much affected in the central region of clusters (Voit, 2005; Sanderson et al., 2005; Donahue et al., 2006b; Sanderson et al., 2009b). If this is the case then the Gini, M_{20} and Concentration should be useful parameters for tracing the central entropy region of a cluster.

We plotted parameter vs parameter in Fig. 4.12. In this plot, Concentration vs M_{20} shows the tight anti-correlation between different dynamical states of clusters. Strong relaxed clusters fall on the upper-left corner of the Concentration vs M_{20} plane, and have high Concentration values. This

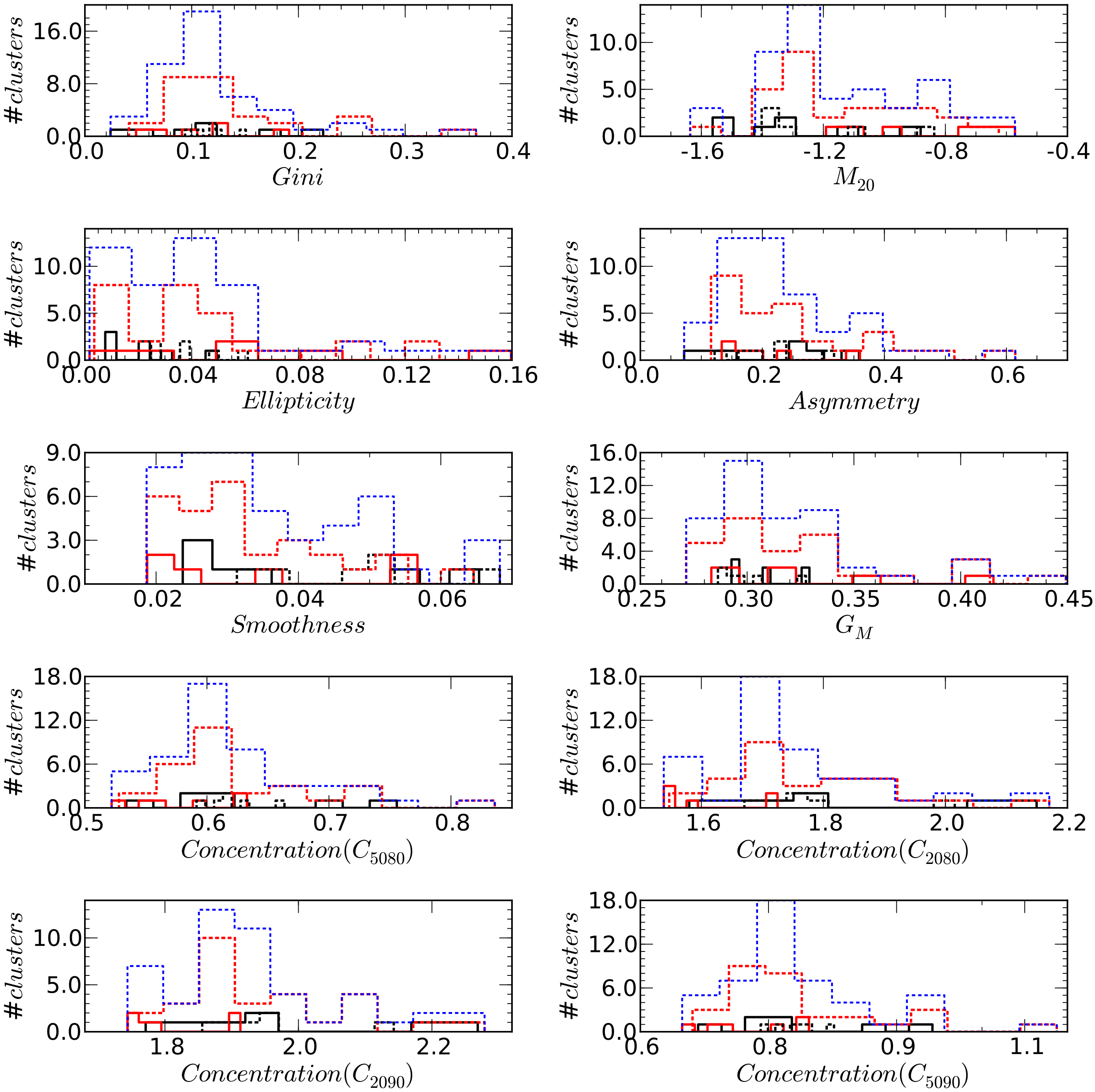

Figure 4.9: Distribution of seven morphology parameters based on the cluster temperature maps. Solid black line = strong relaxed (strong cool core) clusters; dotted black line = relaxed (cool core) clusters; dotted red line = non-relaxed (weak cool core) clusters; solid red line = strong non-relaxed (non-cool core) clusters; and dotted blue line = overall cluster morphology distribution for each parameter. All four definitions of the Concentration parameter were used. Cluster separation is based on the combination of Gini, M_{20} and Concentration parameters.

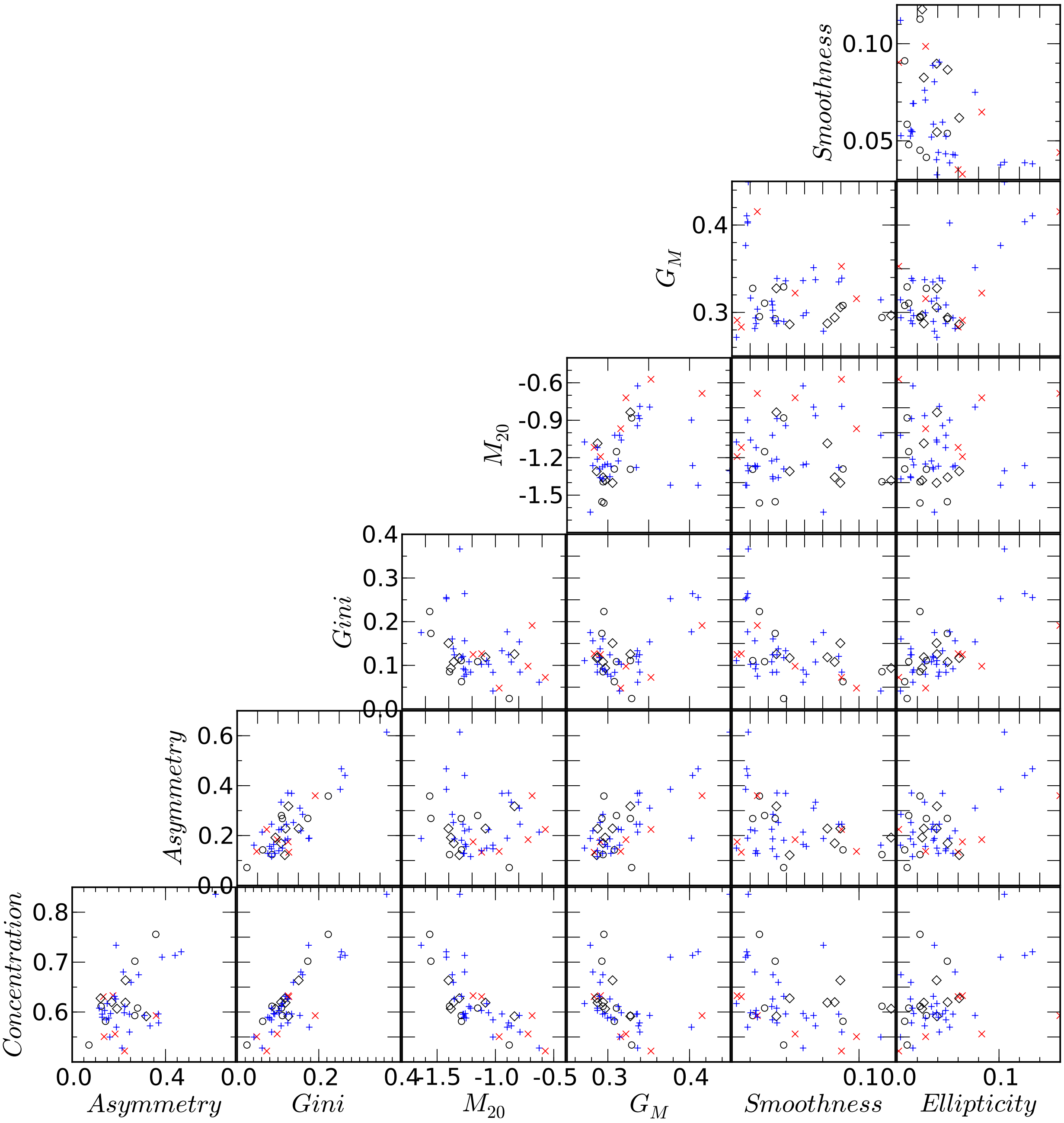

Figure 4.10: Seven morphology parameters plotted in the parameter-parameter planes (temperature maps). We plotted C_{5080} as the Concentration parameter. ○ = strong relaxed (strong cool core) clusters; ◊ = relaxed (cool core) clusters; + = non-relaxed (weak cool core) clusters; and × = strong non-relaxed (non-cool core) clusters.

implies minimum entropy emission in the core of strong relaxed clusters (strong cool core) and no entropy 'peaked' (anywhere) in the non-relaxed clusters. Further, we noticed peculiar objects such as A1795, A2204, A2029 and A478 in the Concentration vs M_{20} plot. These are strong relaxed clusters overlapped with intermediate clusters (relaxed and non-relaxed). This suggests that these clusters could have either AGN activity or small scale substructure at the cluster core (which could not be detected in their surface brightness maps), which might increase the entropy of the surrounding medium. Another possibility is that, in the cluster cores, radiative cooling process of these clusters removes low entropy gas from the hot ICM phase, which is substituted by higher entropy gas from large radii (Kravtsov & Borgani, 2012). § 4.10 describes further analysis of these strong relaxed clusters. Unlike our observation in the temperature plot, we did not detect any other peculiar objects of either non-relaxed or strong non-relaxed clusters.

We also observed a correlation between Gini and Concentration parameters with a few outliers, as given in the temperature plot analysis (A119, A3667, A85, A3562, and A3376 and A3395). We noted that strong relaxed clusters occupy the upper-right corner and strong non-relaxed clusters occupy the lower-left corner, while relaxed and non-relaxed (intermediate) clusters are spread between these two categories. This relationship suggests that a maximum of entropy (actually low entropy because we inverted these entropy maps) is distributed among only a few (bright) pixels in these strong relaxed clusters, and that these pixels are located at the cluster core (high Concentration).

Table 4.12 lists the mean, median, K-S and R-S tests values for the subsample of strong relaxed and strong non-relaxed clusters. The M_{20}, Concentration and G_M parameters have significant probabilities of the K-S and R-S tests compared with other parameters, and hence we can separate strong relaxed and strong non-relaxed clusters (defined by surface brightness maps) using these three parameters in the entropy maps.

Table 4.11: Value of morphology parameters for the low-z clusters (entropy maps). Values are listed with appropriate uncertainties of 1σ for each parameter.

Cluster name	Gini	M_{20}	Concentration	Asymmetry	Smoothness	G_M	Ellipticity
A3571	0.123 ± 0.001	-1.426 ± 0.087	1.867 ± 0.210	0.207 ± 0.028	0.033 ± 0.006	0.284 ± 0.003	0.036 ± 0.057
A2199	0.270 ± 0.001	-1.469 ± 0.055	2.348 ± 0.224	0.354 ± 0.029	0.024 ± 0.003	0.256 ± 0.008	0.043 ± 0.042
A0335	0.389 ± 0.003	-1.944 ± 0.088	3.263 ± 0.398	0.352 ± 0.035	0.025 ± 0.008	0.207 ± 0.007	0.070 ± 0.047
A496	0.332 ± 0.003	-1.770 ± 0.070	2.783 ± 0.400	0.327 ± 0.035	0.025 ± 0.007	0.217 ± 0.005	0.019 ± 0.061
A85	0.419 ± 0.002	-1.576 ± 0.064	2.749 ± 0.338	0.465 ± 0.016	0.018 ± 0.005	0.334 ± 0.004	0.092 ± 0.042
A478	0.245 ± 0.001	-1.715 ± 0.101	2.436 ± 0.414	0.099 ± 0.037	0.025 ± 0.003	0.229 ± 0.002	0.066 ± 0.067
A1795	0.333 ± 0.002	-1.862 ± 0.062	2.862 ± 0.405	0.262 ± 0.035	0.016 ± 0.003	0.215 ± 0.005	0.073 ± 0.038
A4038	0.247 ± 0.001	-1.565 ± 0.068	2.338 ± 0.174	0.166 ± 0.033	0.019 ± 0.003	0.241 ± 0.002	0.104 ± 0.063
A2052	0.272 ± 0.003	-1.740 ± 0.070	2.416 ± 0.366	0.359 ± 0.042	0.031 ± 0.005	0.278 ± 0.005	0.074 ± 0.048
Hydra-A	0.278 ± 0.004	-1.679 ± 0.073	2.459 ± 0.561	0.226 ± 0.047	0.040 ± 0.008	0.218 ± 0.006	0.043 ± 0.063
A2063	0.242 ± 0.001	-1.613 ± 0.110	2.381 ± 0.430	0.216 ± 0.029	0.031 ± 0.003	0.235 ± 0.003	0.055 ± 0.059
A3158	0.262 ± 0.000	-1.436 ± 0.047	2.282 ± 0.327	0.166 ± 0.024	0.013 ± 0.002	0.205 ± 0.001	0.089 ± 0.072
MKW3s	0.246 ± 0.003	-1.662 ± 0.058	2.349 ± 0.473	0.185 ± 0.064	0.030 ± 0.005	0.226 ± 0.003	0.076 ± 0.044
EXO0422	0.306 ± 0.003	-1.753 ± 0.049	2.709 ± 0.423	0.145 ± 0.044	0.031 ± 0.009	0.207 ± 0.001	0.081 ± 0.050
A4059	0.315 ± 0.004	-1.759 ± 0.149	2.924 ± 0.752	0.223 ± 0.046	0.047 ± 0.009	0.213 ± 0.007	0.058 ± 0.077
A2589	0.259 ± 0.002	-1.309 ± 0.084	2.190 ± 0.699	0.326 ± 0.040	0.038 ± 0.005	0.316 ± 0.005	0.132 ± 0.091
A3112	0.272 ± 0.005	-1.737 ± 0.129	2.521 ± 0.571	0.238 ± 0.085	0.059 ± 0.014	0.221 ± 0.005	0.064 ± 0.096
A1651	0.265 ± 0.001	-1.592 ± 0.085	2.481 ± 0.689	0.148 ± 0.021	0.026 ± 0.005	0.193 ± 0.002	0.039 ± 0.039
A576	0.182 ± 0.001	-1.349 ± 0.079	2.040 ± 0.407	0.363 ± 0.022	0.040 ± 0.005	0.300 ± 0.006	0.044 ± 0.035
A2657	0.206 ± 0.002	-1.527 ± 0.066	2.197 ± 0.436	0.214 ± 0.069	0.035 ± 0.005	0.236 ± 0.003	0.005 ± 0.079
A3391	0.240 ± 0.001	-1.436 ± 0.086	2.278 ± 0.339	0.212 ± 0.017	0.019 ± 0.004	0.237 ± 0.004	0.090 ± 0.073
A1650	0.283 ± 0.001	-1.576 ± 0.062	2.388 ± 0.515	0.355 ± 0.029	0.024 ± 0.003	0.265 ± 0.005	0.077 ± 0.055
S1101	0.313 ± 0.003	-1.764 ± 0.111	2.799 ± 0.514	0.204 ± 0.082	0.040 ± 0.006	0.215 ± 0.004	0.093 ± 0.058
zwcl1215	0.219 ± 0.001	-1.461 ± 0.067	2.226 ± 0.308	0.161 ± 0.027	0.025 ± 0.003	0.245 ± 0.003	0.089 ± 0.081
A2597	0.483 ± 0.003	-2.096 ± 0.157	3.907 ± 0.793	0.279 ± 0.082	0.021 ± 0.008	0.170 ± 0.015	0.040 ± 0.075
A133	0.310 ± 0.004	-1.891 ± 0.127	2.838 ± 0.538	0.274 ± 0.078	0.050 ± 0.011	0.242 ± 0.009	0.062 ± 0.098

Continued on next page

Table 4.11 – *Continued from previous page*

Cluster name	Gini	M_{20}	Concentration	Asymmetry	Smoothness	G_M	Ellipticity
A2244	0.321 ± 0.003	-1.728 ± 0.105	2.764 ± 0.571	0.252 ± 0.037	0.023 ± 0.003	0.199 ± 0.005	0.016 ± 0.043
RXJ1504	0.368 ± 0.005	-1.927 ± 0.151	3.166 ± 0.965	0.180 ± 0.090	0.053 ± 0.007	0.173 ± 0.007	0.060 ± 0.099
A2204	0.296 ± 0.004	-1.869 ± 0.160	2.760 ± 0.973	0.185 ± 0.066	0.048 ± 0.007	0.205 ± 0.003	0.016 ± 0.067
A2029	0.307 ± 0.002	-1.745 ± 0.072	2.718 ± 0.492	0.279 ± 0.027	0.019 ± 0.005	0.200 ± 0.007	0.025 ± 0.052
A2142	0.302 ± 0.001	-1.592 ± 0.084	2.548 ± 0.466	0.265 ± 0.039	0.022 ± 0.005	0.245 ± 0.003	0.079 ± 0.049
A3562	0.399 ± 0.001	-1.651 ± 0.047	2.697 ± 0.537	0.408 ± 0.029	0.019 ± 0.002	0.319 ± 0.003	0.101 ± 0.055
A401	0.238 ± 0.001	-1.556 ± 0.072	2.278 ± 0.296	0.147 ± 0.024	0.018 ± 0.004	0.222 ± 0.002	0.080 ± 0.059
A3558	0.162 ± 0.002	-1.309 ± 0.106	2.005 ± 0.437	0.323 ± 0.040	0.049 ± 0.005	0.310 ± 0.004	0.067 ± 0.064
A2147	0.155 ± 0.001	-0.960 ± 0.050	1.882 ± 0.524	0.200 ± 0.043	0.034 ± 0.003	0.294 ± 0.003	0.107 ± 0.079
A3266	0.113 ± 0.001	-1.165 ± 0.083	1.823 ± 0.363	0.164 ± 0.031	0.050 ± 0.009	0.285 ± 0.002	0.051 ± 0.051
A119	0.271 ± 0.001	-1.390 ± 0.077	2.065 ± 0.440	0.216 ± 0.018	0.019 ± 0.001	0.348 ± 0.001	0.086 ± 0.078
A1644	0.241 ± 0.004	-1.666 ± 0.060	2.299 ± 0.529	0.316 ± 0.043	0.048 ± 0.004	0.273 ± 0.001	0.011 ± 0.076
A1736	0.091 ± 0.001	-0.769 ± 0.095	1.668 ± 0.304	0.242 ± 0.011	0.051 ± 0.005	0.335 ± 0.004	0.009 ± 0.075
A3395	0.308 ± 0.001	-0.692 ± 0.040	1.759 ± 0.237	0.488 ± 0.018	0.027 ± 0.003	0.443 ± 0.001	0.234 ± 0.035
A2065	0.305 ± 0.002	-1.628 ± 0.099	2.623 ± 0.377	0.288 ± 0.026	0.021 ± 0.004	0.234 ± 0.005	0.111 ± 0.057
A3822	0.245 ± 0.001	-1.567 ± 0.058	2.351 ± 0.658	0.268 ± 0.022	0.026 ± 0.002	0.259 ± 0.003	0.081 ± 0.077
A3667	0.387 ± 0.001	-1.513 ± 0.094	2.804 ± 0.284	0.311 ± 0.007	0.015 ± 0.003	0.305 ± 0.002	0.116 ± 0.073
A754	0.238 ± 0.000	-1.161 ± 0.064	2.171 ± 0.333	0.219 ± 0.014	0.015 ± 0.003	0.240 ± 0.002	0.092 ± 0.054
A2256	0.248 ± 0.001	-1.188 ± 0.050	2.230 ± 0.311	0.161 ± 0.014	0.016 ± 0.002	0.235 ± 0.001	0.113 ± 0.052
A399	0.204 ± 0.001	-1.439 ± 0.083	2.195 ± 0.300	0.182 ± 0.028	0.019 ± 0.003	0.252 ± 0.002	0.080 ± 0.070
A2163	0.162 ± 0.002	-1.294 ± 0.164	2.045 ± 0.900	0.212 ± 0.030	0.051 ± 0.011	0.246 ± 0.002	0.031 ± 0.114
A3376	0.479 ± 0.002	-1.401 ± 0.076	2.763 ± 0.331	0.652 ± 0.019	0.021 ± 0.003	0.419 ± 0.003	0.087 ± 0.057

Table 4.12: Statistics for the subsample of strong relaxed (SR), and strong non-relaxed (SNR) clusters (entropy maps). K-S and R-S statistics were performed between strong relaxed and strong non-relaxed clusters to test whether they have the same distribution or not.

Parameters	mean	median	K-S prob.	R-S prob.
	SR SNR	SR SNR	SR SNR	SR SNR
Gini	0.35 0.19	0.33 0.20	4.78×10^{-02}	1.52×10^{-02}
M_{20}	-1.88 -0.99	-1.87 -1.06	7.95×10^{-04}	2.70×10^{-03}
Concentration	1.03 0.65	0.97 0.63	7.95×10^{-04}	2.70×10^{-03}
Asymmetry	0.23 0.25	0.26 0.21	5.43×10^{-01}	6.68×10^{-01}
Smoothness	0.05 0.06	0.04 0.05	7.77×10^{-01}	1.00
G_M	0.20 0.31	0.20 0.29	7.95×10^{-04}	2.70×10^{-03}
Ellipticity	0.05 0.10	0.06 0.10	6.16×10^{-02}	1.53×10^{-01}

4.9.4 Pressure map

Pressure maps are useful in the study of the hydrodynamic balance/unbalance between the dense cluster core and the outer gas. In regular, relaxed and cool core cluster, the cooling flow mechanism entails surrounding gas being pressurised towards the centre of the cluster, while maintaining its density. In the case of hydrostatic equilibrium, pressure of the external gas is in balance with central density. The gas in many clusters is close to hydrostatic equilibrium. But, in the case of non-relaxed and merger cluster, strong merger shocks could disturb this hydrodynamic balance. Strong AGN outbursts could also responsible to interrupt hydrodynamic balance.

We calculated morphology parameters for the pseudo pressure maps of the low-z clusters. Fig. 4.13 gives a histogram plot which shows the parameter distribution, while Fig. 4.14 illustrates the parameter vs parameter plot. Table 4.13 lists all parameter values calculated for pressure maps, together with 1σ uncertainty (see Chapter 2, § 2.2.5). In the histogram plot, the Gini, M_{20} and Concentration parameters separate strong relaxed and strong non-relaxed clusters. In the scatter plots (parameter vs parameter), Concentration vs M_{20} distinguishes strong relaxed and strong non-relaxed clusters. Two peculiar objects - A2597 and 2A-0335 - were, however, noticed on the M_{20} vs Concentration plot. These two clusters are strong relaxed clusters overlapped with intermediate clusters. This could suggest that they have disturbed (cluster core) pressure morphology caused by AGN or cold front activities (McNamara et al., 2001; Mazzotta et al., 2003). In the Gini vs Concentration or M_{20} plots, we see the same outliers as previously observed.

Table 4.14 lists mean, median, K-S and R-S tests values for the subsample of strong relaxed and strong non-relaxed clusters. M_{20} and Concentration parameters have significant probabilities of the K-S and R-S tests, and can separate strong relaxed clusters from strong non-relaxed clusters in the pressure maps.

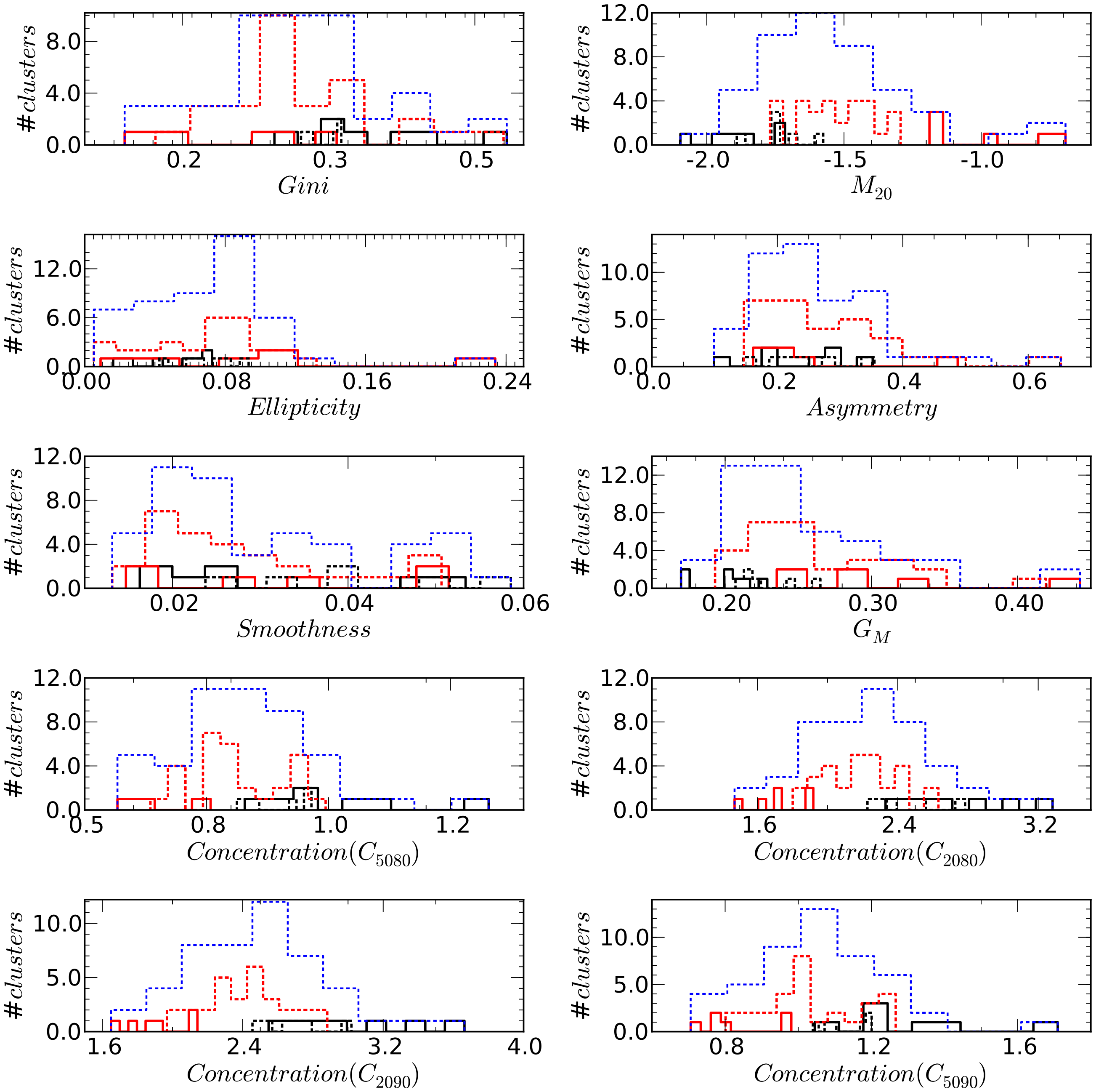

Figure 4.11: Distribution of seven morphology parameters based on the cluster entropy maps. Solid black line = strong relaxed (strong cool core) clusters; dotted black line = relaxed (cool core) clusters; dotted red line = non-relaxed (weak cool core) clusters; solid red line = strong non-relaxed (non-cool core) clusters; and dotted blue line = overall cluster morphology distribution for each parameter. All four definitions of the Concentration parameter were used. Cluster separation is based on the combination of Gini, M_{20} and Concentration parameters.

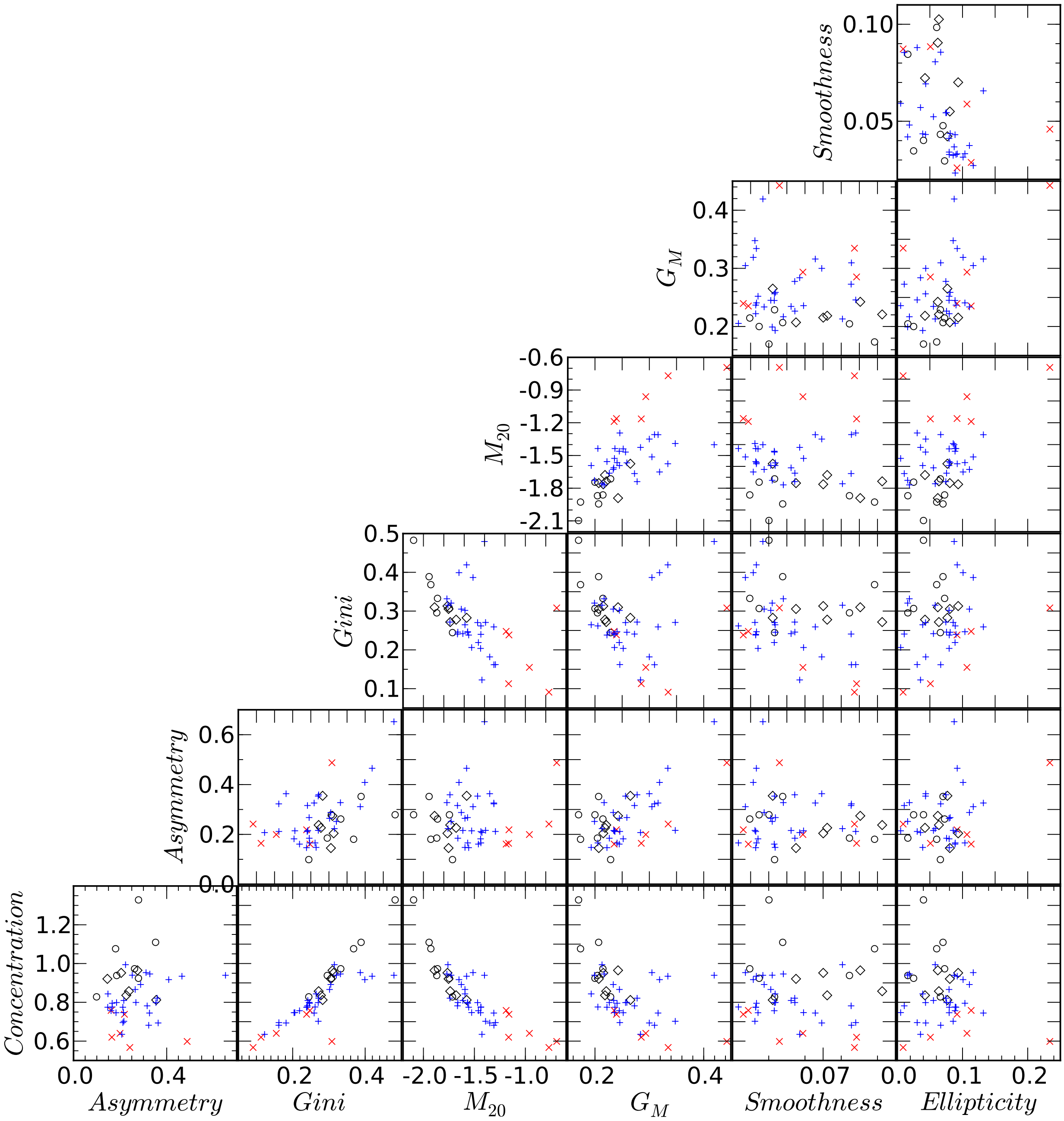

Figure 4.12: Seven morphology parameters plotted in the parameter-parameter planes (entropy maps). We plotted C_{5080} as the Concentration parameter. ○ = strong relaxed (strong cool core) clusters; ◇ = relaxed (cool core) clusters; + = non-relaxed (weak cool core) clusters; and × = strong non-relaxed (non-cool core) clusters.

Table 4.13: Value of morphology parameters for the low-z clusters (pressure maps). Values are listed with appropriate uncertainties of 1σ for each parameter.

Cluster name	Gini	M_{20}	Concentration	Asymmetry	Smoothness	G_M	Ellipticity
A3571	0.160 ± 0.002	-1.467 ± 0.023	1.991 ± 0.118	0.178 ± 0.024	0.029 ± 0.004	0.274 ± 0.004	0.072 ± 0.028
A2199	0.252 ± 0.001	-1.520 ± 0.045	2.205 ± 0.115	0.337 ± 0.026	0.022 ± 0.004	0.271 ± 0.005	0.062 ± 0.028
A0335	0.149 ± 0.001	-1.517 ± 0.034	1.948 ± 0.131	0.183 ± 0.020	0.027 ± 0.005	0.272 ± 0.005	0.034 ± 0.026
A496	0.138 ± 0.001	-1.376 ± 0.028	1.851 ± 0.124	0.232 ± 0.019	0.028 ± 0.005	0.292 ± 0.004	0.030 ± 0.021
A85	0.278 ± 0.001	-1.599 ± 0.031	2.266 ± 0.139	0.414 ± 0.018	0.020 ± 0.003	0.407 ± 0.003	0.087 ± 0.015
A478	0.324 ± 0.002	-1.761 ± 0.037	2.819 ± 0.109	0.093 ± 0.033	0.020 ± 0.010	0.184 ± 0.003	0.073 ± 0.018
A1795	0.284 ± 0.001	-1.682 ± 0.040	2.476 ± 0.101	0.220 ± 0.023	0.015 ± 0.006	0.215 ± 0.005	0.050 ± 0.024
A4038	0.161 ± 0.001	-1.581 ± 0.030	2.133 ± 0.172	0.117 ± 0.015	0.025 ± 0.005	0.279 ± 0.001	0.030 ± 0.027
A2052	0.182 ± 0.002	-1.572 ± 0.058	2.019 ± 0.307	0.299 ± 0.034	0.030 ± 0.003	0.294 ± 0.007	0.025 ± 0.046
Hydra-A	0.183 ± 0.003	-1.683 ± 0.086	2.104 ± 0.274	0.231 ± 0.050	0.051 ± 0.009	0.298 ± 0.006	0.031 ± 0.034
A2063	0.098 ± 0.002	-1.355 ± 0.039	1.799 ± 0.171	0.159 ± 0.024	0.040 ± 0.003	0.303 ± 0.001	0.003 ± 0.029
A3158	0.162 ± 0.001	-1.590 ± 0.018	2.069 ± 0.157	0.158 ± 0.022	0.019 ± 0.003	0.282 ± 0.002	0.041 ± 0.028
MKW3s	0.183 ± 0.002	-1.541 ± 0.057	2.140 ± 0.263	0.149 ± 0.029	0.035 ± 0.007	0.251 ± 0.002	0.051 ± 0.033
EXO0422	0.183 ± 0.001	-1.681 ± 0.050	2.249 ± 0.330	0.114 ± 0.025	0.039 ± 0.005	0.278 ± 0.001	0.032 ± 0.053
A4059	0.066 ± 0.002	-0.827 ± 0.023	1.602 ± 0.164	0.177 ± 0.045	0.049 ± 0.007	0.312 ± 0.003	0.032 ± 0.026
A2589	0.134 ± 0.002	-0.858 ± 0.026	1.742 ± 0.181	0.309 ± 0.039	0.042 ± 0.004	0.307 ± 0.006	0.021 ± 0.032
A3112	0.181 ± 0.004	-1.576 ± 0.048	2.155 ± 0.342	0.160 ± 0.056	0.065 ± 0.011	0.271 ± 0.005	0.068 ± 0.056
A1651	0.211 ± 0.003	-1.666 ± 0.037	2.319 ± 0.189	0.124 ± 0.023	0.031 ± 0.005	0.249 ± 0.003	0.028 ± 0.031
A576	0.137 ± 0.001	-1.243 ± 0.040	1.795 ± 0.263	0.270 ± 0.029	0.042 ± 0.006	0.308 ± 0.004	0.058 ± 0.039
A2657	0.124 ± 0.001	-1.395 ± 0.059	1.912 ± 0.215	0.152 ± 0.020	0.043 ± 0.006	0.290 ± 0.001	0.042 ± 0.034
A3391	0.184 ± 0.001	-1.463 ± 0.017	1.990 ± 0.187	0.215 ± 0.013	0.023 ± 0.003	0.292 ± 0.002	0.056 ± 0.028
A1650	0.239 ± 0.003	-1.643 ± 0.044	2.246 ± 0.191	0.216 ± 0.024	0.026 ± 0.005	0.243 ± 0.005	0.040 ± 0.022
S1101	0.218 ± 0.003	-1.665 ± 0.071	2.393 ± 0.404	0.161 ± 0.055	0.049 ± 0.007	0.253 ± 0.002	0.033 ± 0.071
zwcl1215	0.163 ± 0.001	-1.459 ± 0.029	2.053 ± 0.156	0.141 ± 0.019	0.030 ± 0.003	0.263 ± 0.003	0.023 ± 0.033
A2597	0.234 ± 0.002	-1.442 ± 0.031	2.104 ± 0.140	0.428 ± 0.024	0.026 ± 0.004	0.315 ± 0.004	0.012 ± 0.029
A133	0.107 ± 0.002	-1.259 ± 0.028	1.815 ± 0.225	0.218 ± 0.036	0.052 ± 0.005	0.304 ± 0.006	0.002 ± 0.033

Continued on next page

Table 4.13 – *Continued from previous page*

Cluster name	Gini	M_{20}	Concentration	Asymmetry	Smoothness	G_M	Ellipticity
A2244	0.186 ± 0.002	-1.651 ± 0.023	2.093 ± 0.229	0.201 ± 0.033	0.031 ± 0.006	0.279 ± 0.004	0.050 ± 0.027
RXJ1504	0.326 ± 0.007	-1.896 ± 0.081	2.971 ± 0.418	0.212 ± 0.067	0.061 ± 0.026	0.199 ± 0.004	0.035 ± 0.044
A2204	0.290 ± 0.005	-1.816 ± 0.079	2.798 ± 0.291	0.118 ± 0.050	0.046 ± 0.016	0.211 ± 0.001	0.030 ± 0.025
A2029	0.277 ± 0.002	-1.731 ± 0.031	2.538 ± 0.133	0.214 ± 0.032	0.019 ± 0.004	0.237 ± 0.004	0.044 ± 0.016
A2142	0.180 ± 0.002	-1.501 ± 0.025	2.103 ± 0.111	0.133 ± 0.021	0.027 ± 0.006	0.280 ± 0.002	0.038 ± 0.027
A3562	0.284 ± 0.002	-1.362 ± 0.019	2.089 ± 0.171	0.436 ± 0.020	0.023 ± 0.003	0.410 ± 0.002	0.078 ± 0.025
A401	0.147 ± 0.002	-1.514 ± 0.027	2.011 ± 0.149	0.148 ± 0.020	0.025 ± 0.005	0.284 ± 0.001	0.046 ± 0.029
A3558	0.119 ± 0.002	-1.346 ± 0.048	1.814 ± 0.188	0.209 ± 0.021	0.049 ± 0.006	0.302 ± 0.004	0.037 ± 0.026
A2147	0.119 ± 0.001	-1.261 ± 0.058	1.829 ± 0.303	0.186 ± 0.024	0.040 ± 0.006	0.307 ± 0.003	0.056 ± 0.036
A3266	0.077 ± 0.003	-1.349 ± 0.056	1.747 ± 0.202	0.143 ± 0.033	0.055 ± 0.009	0.302 ± 0.002	0.007 ± 0.038
A119	0.234 ± 0.001	-1.219 ± 0.036	1.873 ± 0.117	0.243 ± 0.013	0.021 ± 0.002	0.382 ± 0.002	0.059 ± 0.032
A1644	0.143 ± 0.003	-1.161 ± 0.049	1.808 ± 0.284	0.234 ± 0.033	0.048 ± 0.005	0.321 ± 0.007	0.030 ± 0.032
A1736	0.087 ± 0.001	-0.937 ± 0.060	1.708 ± 0.179	0.224 ± 0.028	0.048 ± 0.007	0.308 ± 0.002	0.012 ± 0.041
A3395	0.213 ± 0.001	-0.792 ± 0.022	1.723 ± 0.101	0.344 ± 0.013	0.028 ± 0.002	0.399 ± 0.001	0.146 ± 0.031
A2065	0.109 ± 0.001	-1.191 ± 0.025	1.779 ± 0.157	0.200 ± 0.016	0.028 ± 0.005	0.306 ± 0.002	0.037 ± 0.026
A3822	0.148 ± 0.001	-1.376 ± 0.024	1.946 ± 0.157	0.177 ± 0.016	0.029 ± 0.003	0.272 ± 0.002	0.045 ± 0.041
A3667	0.260 ± 0.002	-1.326 ± 0.030	2.075 ± 0.186	0.551 ± 0.022	0.019 ± 0.003	0.420 ± 0.003	0.136 ± 0.024
A754	0.113 ± 0.001	-1.112 ± 0.013	1.711 ± 0.106	0.215 ± 0.015	0.020 ± 0.003	0.305 ± 0.001	0.009 ± 0.009
A2256	0.111 ± 0.001	-1.282 ± 0.021	1.786 ± 0.051	0.151 ± 0.016	0.022 ± 0.003	0.306 ± 0.002	0.033 ± 0.015
A399	0.144 ± 0.001	-1.484 ± 0.021	1.992 ± 0.117	0.146 ± 0.026	0.023 ± 0.004	0.269 ± 0.002	0.037 ± 0.021
A2163	0.169 ± 0.005	-1.471 ± 0.054	2.100 ± 0.120	0.206 ± 0.063	0.051 ± 0.006	0.256 ± 0.005	0.039 ± 0.034
A3376	0.278 ± 0.002	-0.848 ± 0.022	1.930 ± 0.135	0.594 ± 0.027	0.023 ± 0.002	0.478 ± 0.001	0.135 ± 0.018

Table 4.14: Statistics for the subsample of strong relaxed (SR), and strong non-relaxed (SNR) clusters (pressure maps). K-S and R-S statistics were performed between strong relaxed and strong non-relaxed clusters to test whether they have the same distribution or not.

Parameters	mean	median	K-S prob.	R-S prob.
	SR SNR	SR SNR	SR SNR	SR SNR
Gini	0.27 0.12	0.28 0.11	6.35×10^{-03}	4.27×10^{-03}
M_{20}	-1.69 -1.12	-1.73 -1.19	7.95×10^{-04}	2.70×10^{-03}
Concentration	0.86 0.60	0.86 0.59	7.95×10^{-04}	2.70×10^{-03}
Asymmetry	0.21 0.21	0.21 0.20	9.07×10^{-01}	6.68×10^{-01}
Smoothness	0.05 0.06	0.05 0.06	6.21×10^{-01}	3.91×10^{-01}
G_M	0.23 0.32	0.21 0.31	6.35×10^{-03}	2.23×10^{-02}
Ellipticity	0.04 0.04	0.03 0.02	2.82×10^{-01}	3.91×10^{-01}

In general, morphology parameters are quite different in surface brightness, temperature, entropy and pressure maps. Different dynamical states of clusters, according to their surface brightness, occupy different positions in the parameters planes of temperature, entropy and pressure maps. The ‘peculiar’ objects we observed in various maps, actually revealed their thermodynamic footprint and associated gravitational or non-gravitational feedback mechanisms. Hence, cluster morphology of thermodynamic maps is a useful tool in understanding these complex processes. To understand the details of these processes, one needs to study each individual cluster using its thermodynamic maps. Cluster morphology of thermodynamic maps is, however, not useful in the study of cluster dynamics as surface brightness morphology.

4.9.5 Power-law slope vs Morphology parameters

From Tables 4.5 and 4.6 we observed that the pure power-law gives very good approximation regarding the polarity of slopes (positive slope value for temperature (T) and entropy (K); negative slope value for density (n_e) and pressure (P)). These slopes or gradients indicate whether the thermodynamic profile for each cluster is steep or flat. Furthermore, pure power-law model slopes are different for strong relaxed and strong non-relaxed clusters (according to the combination of surface brightness morphology parameters, as indicated earlier). For example, in the case of entropy, strong relaxed clusters have steep profiles, hence larger slope values, and smaller slope values for strong non-relaxed clusters due to their shallower profiles. Temperature slope values, on the other hand, do not separate different dynamical states of clusters, in the same way as temperature morphology is not useful in the separation of different dynamical states of clusters, as discussed in § 4.9.2. The contrast between the slope values in the thermodynamic maps (with the exception of the temperature map) encouraged us to compared them with corresponding surface brightness cluster morphology. What follows is a comparison between the value of pure power-law slopes derived for individual low-z clusters in their thermodynamic maps with the corresponding morphology parameters calculated for surface brightness maps. Tables 4.3 and 4.4 lists these slope values for each low-z cluster.

Figs. 4.15, 4.16, 4.17 and 4.18 compare the values of the best-fitting (pure) power-law slopes of temperature, entropy, density and pressure profiles, respectively, with morphology parameters calculated for surface brightness maps. We observe that, except for the best-fitting slope of the temperature profiles, three promising parameters, the Gini, M_{20} and Concentration, are

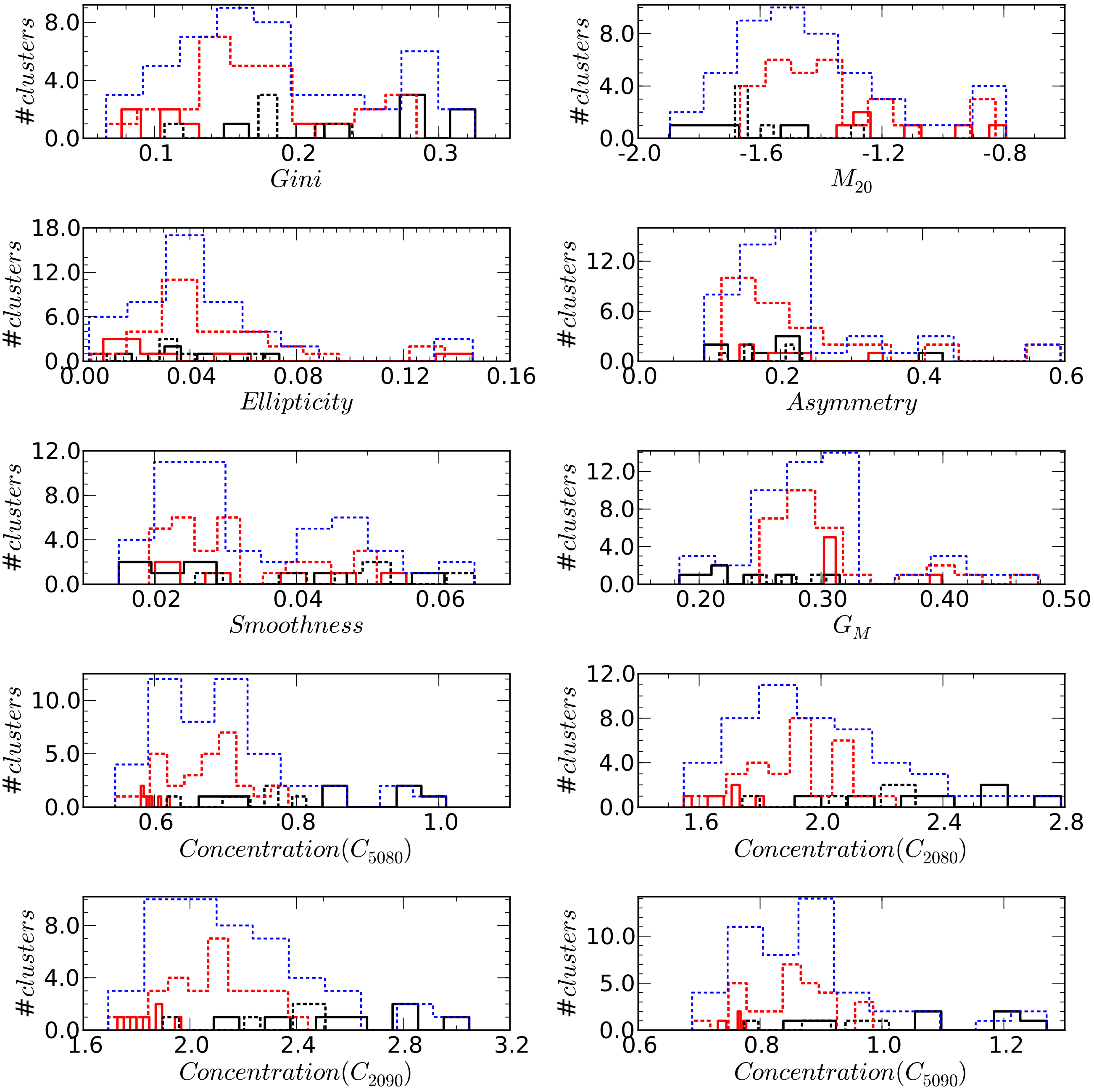

Figure 4.13: Distribution of seven morphology parameters based on the cluster pressure maps. Solid black line = strong relaxed (strong cool core) clusters; dotted black line = relaxed (cool core) clusters; dotted red line = non-relaxed (weak cool core) clusters; solid red line = strong non-relaxed (non-cool core) clusters; and dotted blue line = overall cluster morphology distribution for each parameter. All four definitions of the Concentration parameter were used. Cluster separation is based on the combination of Gini, M_{20} and Concentration parameters.

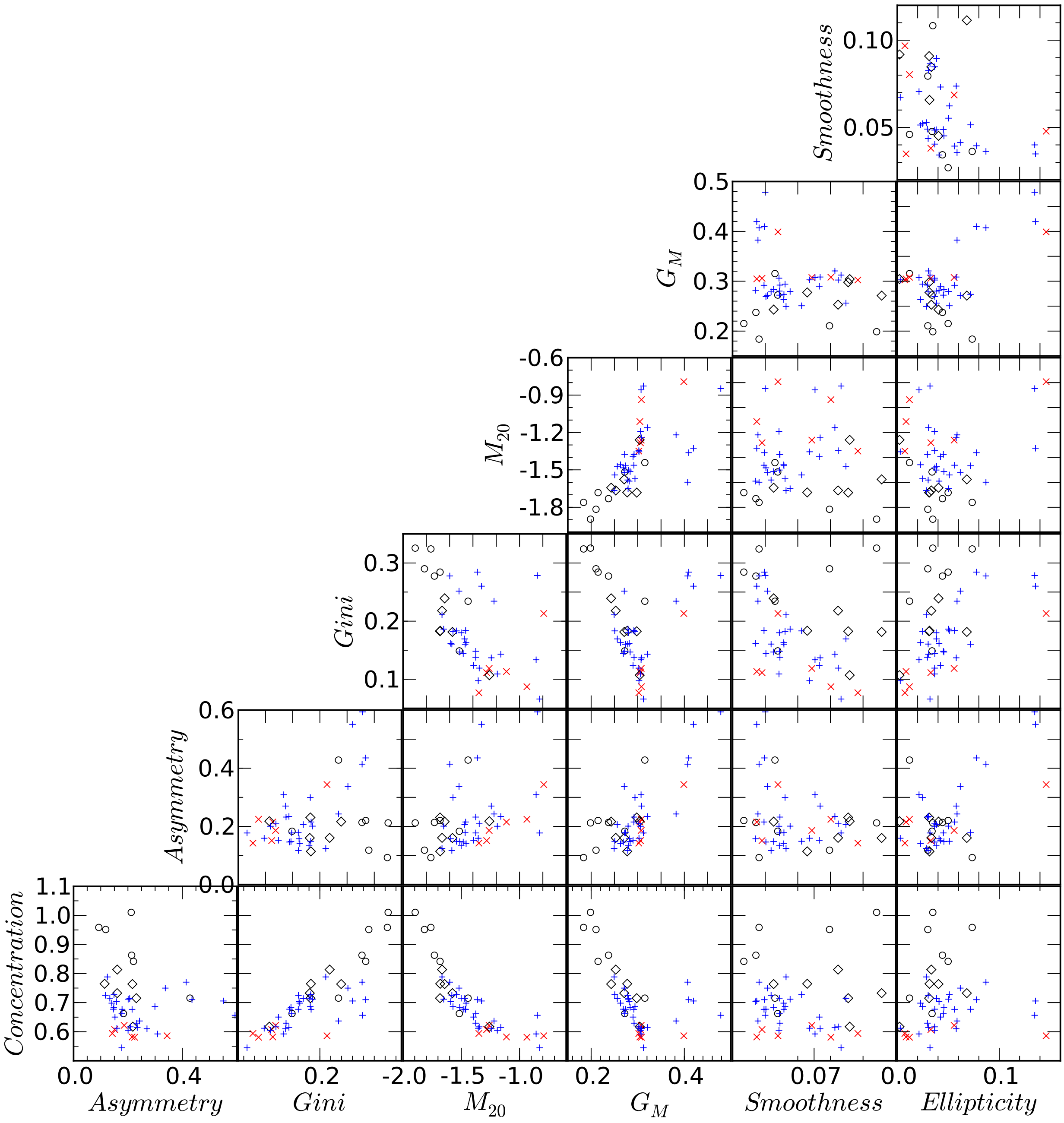

Figure 4.14: Seven morphology parameters plotted in the parameter-parameter planes (pressure maps). We plotted C_{5080} as the Concentration parameter. ○ = strong relaxed (strong cool core) clusters; ◊ = relaxed (cool core) clusters; + = non-relaxed (weak cool core) clusters; and × = strong non-relaxed (non-cool core) clusters.

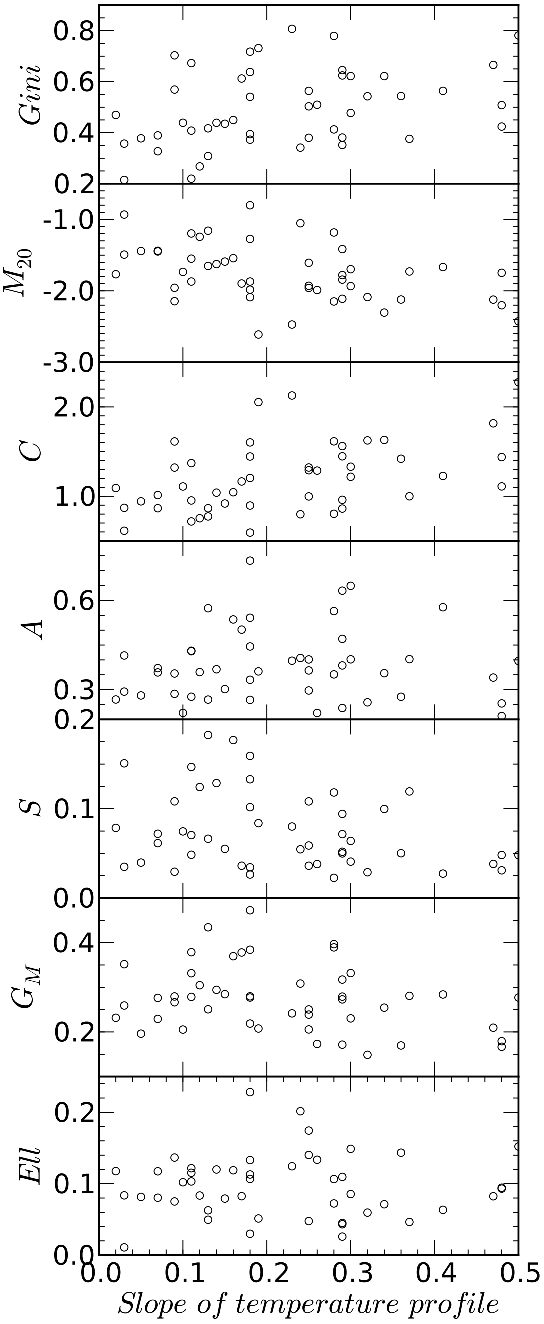

Figure 4.15: Surface brightness morphology parameters plotted against the best-fitting power-law slope (α) of the temperature profile.

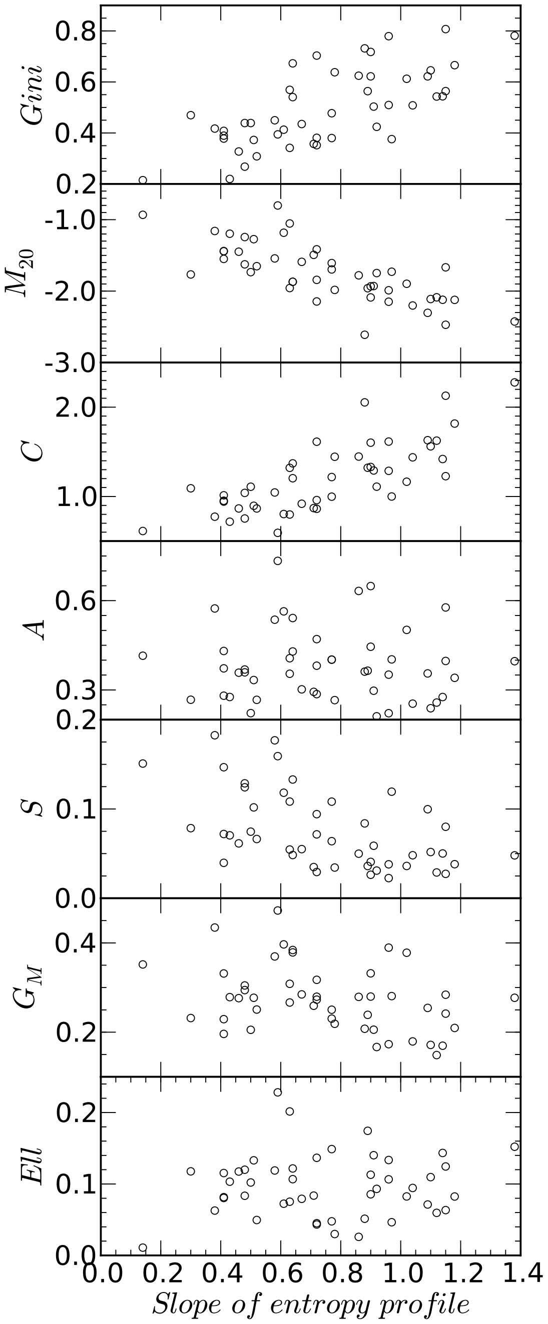

Figure 4.16: Surface brightness morphology parameters plotted against the best-fitting power-law slope (α) of the entropy profile.

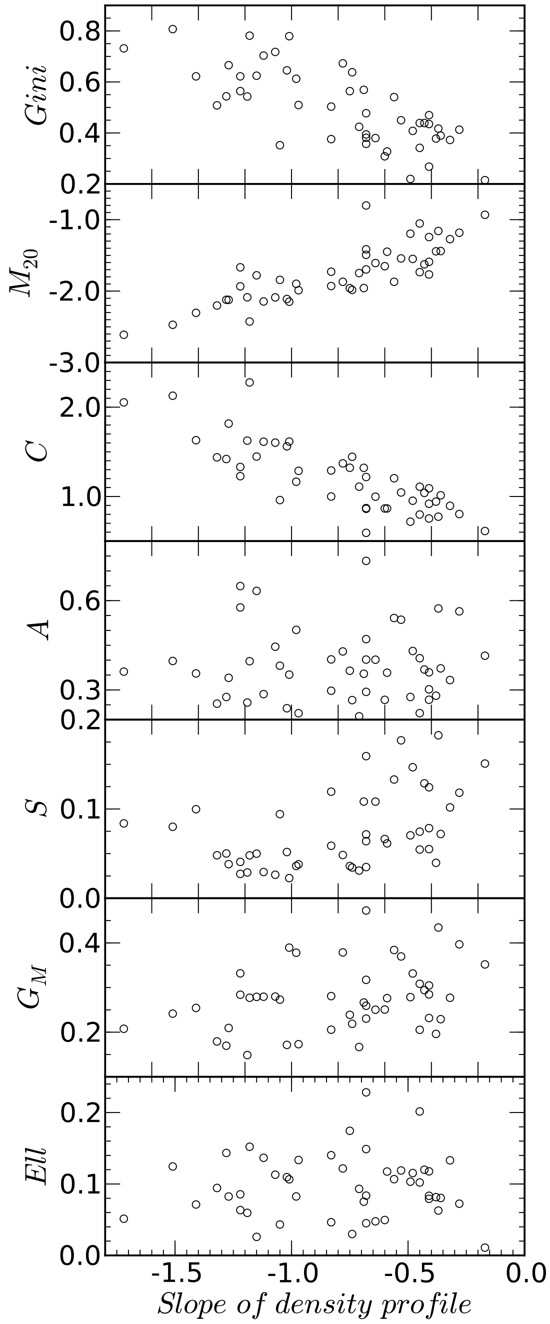

Figure 4.17: Surface brightness morphology parameters plotted against the best-fitting power-law slope (α) of the density profile.

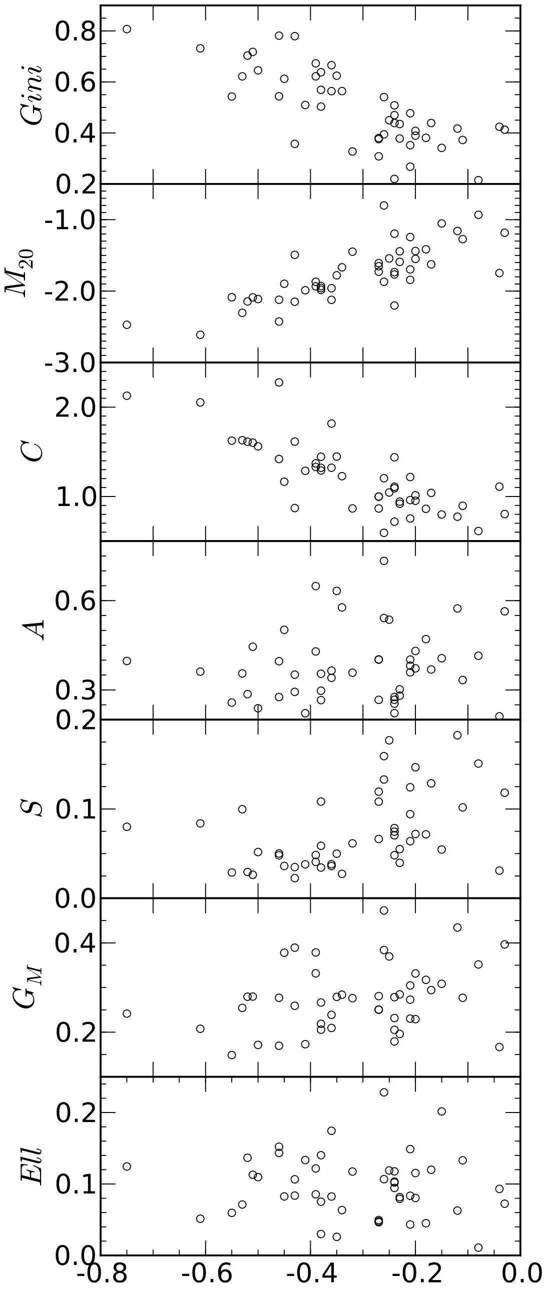

Figure 4.18: Surface brightness morphology parameters plotted against the best-fitting power-law slope (α) of the pressure profile.

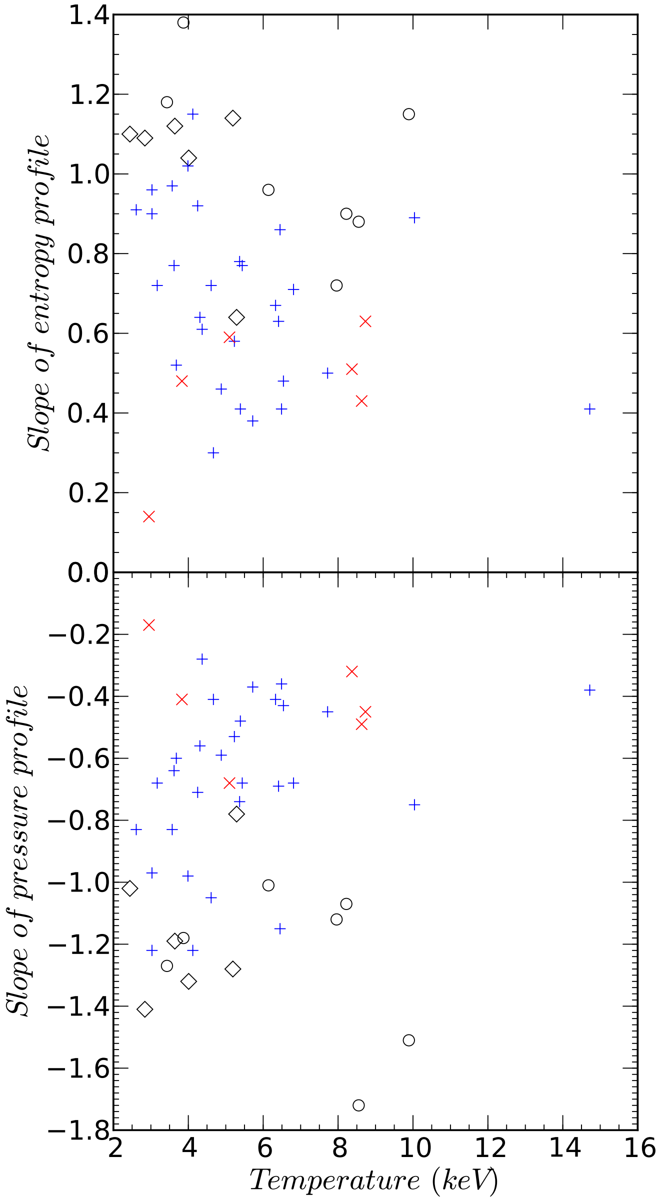

Figure 4.19: Best-fitting slope of the entropy and pressure profiles plotted against mean system temperature. ○ = strong relaxed (strong cool core) clusters; ◊ = relaxed (cool core) clusters; + = non-relaxed (weak cool core) clusters; and × = strong non-relaxed (non-cool core) clusters.

Table 4.15: Spearman coefficient, ρ, calculated for morphology parameters and power-law slope (α) of temperature, entropy, pressure and density profiles.

Morphology parameters	Temperature profile	Entropy profile	Pressure profile	Density profile
Gini	0.37	0.66	-0.73	-0.72
M_{20}	-0.46	-0.76	0.79	0.84
Concentration	0.47	0.75	-0.77	-0.81
Asymmetry	0.05	-0.11	0.17	0.07
Smoothness	-0.29	-0.56	0.49	0.50
G_M	-0.23	-0.35	0.28	0.33
Ellipticity	-0.03	0.05	-0.12	-0.02

Table 4.16: Spearman test probability, p, calculated for morphology parameters and power-law slope (α) of temperature, entropy, pressure and density profiles.

Morphology parameters	Temperature profile	Entropy profile	Pressure profile	Density profile
Gini	0.01	0.0	0.0	0.0
M_{20}	0.0	0.0	0.0	0.0
Concentration	0.0	0.0	0.0	0.0
Asymmetry	0.74	0.46	0.26	0.63
Smoothness	0.05	0.0	0.0	0.0
G_M	0.12	0.02	0.06	0.02
Ellipticity	0.85	0.74	0.40	0.90

correlated/anti-correlated with the best-fitting slopes of the entropy, density and pressure profiles. Table 4.15 and Table 4.16 list the Spearman coefficient values, ρ, and corresponding probability, p, respectively to test the correlation/anti-correlation between the morphology of clusters and corresponding best-fitting slope values.

We noted that the pure power-law does not have a good approximation of profiles compared with that of the power-law with constant base. In general, morphology parameters measure the degree of disturbance in a given cluster, while α (derived from the pure power-law) measures only the steepness or gradient of profiles, in other words, temperature or density distribution as a function of radius. In the case of the density profile, α is similar to the "cuspiness parameter" (Vikhlinin et al., 2007; Hudson et al., 2010; Maughan et al., 2012), and is used to differentiate cool core clusters from non-cool core clusters. Hence we expect a relationship between α (for the density profiles) and morphology parameters. Sanderson et al. (2009a) noted the correlation between the projected X-ray-BCG offset (also an indicator of merger) and the slope of the gas density profile. This correlation suggested that the strength of the cool core declines in more disturbed clusters, and that, subsequently, their cool cores are erased by cluster merger. Our findings are similar, and useful in evaluating the gradient of density or entropy simply from the cluster surface brightness morphology. High Concentration, high Gini and low M_{20} parameters indicate that relaxed clusters have dense and concentrated cores and steep profiles in the central region, so that relaxed clusters have higher slope values. By contrast, non-relaxed clusters have flatter profiles in the core, and lower slope values.

Fig. 4.19 suggests that there is no evidence of any systematic variation in the slope of the entropy and pressure profiles with the mean temperature (V09) of low-z clusters, which is similar to the findings of Sanderson et al. (2009b). In this plot, we observed that strong relaxed clusters have a high entropy slope and a low pressure slope. These observations could suggest that the entropy and pressure distributions are much more correlated with the electron density distribution than they are with temperature in the cluster core. Chapters 2 and 3 discussed usefulness of morphology parameters in the investigation of the dynamical states of high redshift clusters. Another interpretation of this correlation could be that we are able to evaluate the entropy or density gradient of high redshift clusters using morphology parameters where it is difficult to measure gradients using conventional techniques (such as the XMC, or by extracting spectrum, finding the density and temperature, and then plotting entropy or pressure as a function of radius). This could be due to the observation of fewer photons in high-z clusters.

4.10 Substructure diagnostics with thermodynamic radial profiles

There is another way to investigate substructure in the 2-D thermodynamic maps of a given (individual) galaxy cluster, namely by studying its radial profiles. In radial profiles of thermodynamic maps, we might see the high amplitude of fluctuations and/or discontinuities. These "disturbances" in radial profiles could suggest the presence of substructure or a cluster merging process. It is believed that larger fluctuations (in the radial profile) could be associated with non-relaxed clusters, in contrast with smooth profiles which are associated with relaxed and regular clusters. The important reason for studying these fluctuations in radial profiles is that they help in investigating the link between scatter of the scaling relations of clusters and the possible unnoticed underlying substructure in the X-ray observables of the ICM density and surface brightness maps. This encouraged us to study radial profiles of individual low-z clusters. As mentioned in Chapter 3, § 3.5, however, there are seven strong relaxed clusters (A2597, 2A-0335, A478, A1795, A2029, RXJ1504, and A2204), six strong non-relaxed clusters (A2147, A3266, A1736, A3395, A754, and A2256), and thirty five intermediate clusters. It is possible that we could miss merging activity in the surface brightness (and density) maps of these strong relaxed clusters. It is, therefore, essential to investigate the thermodynamic radial profiles of these strong relaxed clusters and compare these profiles with profiles of strong non-relaxed clusters to look for possible substructure in strong relaxed clusters (it being known that intermediate clusters have minor and major merging activities). This will also allow us to compare our morphological measurements of thermodynamic maps (§ 4.9) with its radial profiles.

We studied radial profiles of temperature, entropy, density and pressure directly from their maps. We measured standard deviation (std) in each radial bin, considering it a fluctuation. Overall fluctuations in each radial bin could describe the underlying substructure and dynamical state of the cluster. The error on the X-axis is measured by $0.5(r_2 - r_1)$ where r_2 is the outer radius and r_1 is the inner radius. We used (0.01, 0.02, 0.03, 0.04, 0.05, 0.06, 0.07, 0.08, 0.09, 0.1, 0.15, 0.2, 0.25, 0.3, 0.4, 0.5)R_{500} radial bins for RXJ1504 ($z = 0.2169$), A2204 ($z = 0.1511$) and A2163 ($z = 0.203$) because of their high redshift.

Comparison between seven strong relaxed and six strong non-relaxed clusters (as classified by combination of morphology parameters) in terms of fluctuations in their corresponding radial profiles, is given below.

4.10.1 A2597

A2597 is one of the most relaxed clusters in the V09 sample (on the morphology parameter planes, it has the highest Concentration and lowest M_{20} parameter values). McNamara et al. (2001); Clarke et al. (2005b) detected "ghost" cavities in A2597 which are associated with faint extended radio emission. They argued that these cavities are buoyantly rising relics of radio outbursts. In Fig. 4.20 we display density, temperature, entropy and pressure maps together with corresponding projected radial profiles.

On the log-log plane of A2597 radial profiles, we fitted the power-law models for the temperature, density, entropy and pressure profiles in the form of (1) $F(r) = F_0 + F(R_{500})^{\alpha}$ (solid red line) and (2) $F(r) = F(R_{500})^{\alpha}$ (dotted green line) (see § 4.8). Tables 4.3 and 4.4 list best-fit values for these power-law models. We fitted the power-law model with constant base to the temperature, density, entropy and pressure radial profile solely to illustrate fitting. The pure power-law model was derived to evaluate the gradient for the corresponding thermodynamic maps which were compared with cluster surface brightness morphology parameters in § 4.9.5.

In the thermodynamic maps, we observe that A2597 is a regular and relaxed cluster. In the projected radial profile plots, the y-axis error bar corresponds to the std in each radial bin. This std is plotted in the form of fluctuations together with the corresponding mean value of each radial bin. A2597, a strong relaxed cluster, shows relatively less fluctuation and no discontinuity compared with the radial profiles of other clusters. The temperature and entropy profiles look similar to the typical profiles for relaxed clusters, where temperature and entropy decline towards the cluster centre because of strong cooling flow. A2597 has a very steep gradient in its temperature and entropy profiles where the pure power-law model (dotted green line) is deviated at $\sim 0.05\ R_{500}$. The pure power-law model could not fit into the inner core region of A2597. In the density radial profile, the power-law with constant base as well as the pure power-law models did not fit at $\gtrsim 0.1\ R_{500}$. In § 4.9.4, where we plotted (morphology) parameter vs parameter for pressure maps, A2597 was identified as a peculiar object. Its pressure map indicated low Concentration and high M_{20} values. A2597 has a gradual pressure gradient in the core region (at $< 0.1\ R_{500}$), which indicates that the pressure morphology of A2597 is disturbed. According to smooth and continuous radial profiles of the A2597, however, it is a strong cool core and strong relaxed cluster.

4.10.2 2A-0335

2A-0335 is a strong relaxed cluster in the V09 sample. This cluster has a dense and cool core. It hosts a cold front, and the cool core of the cluster is moving relatively to the surrounding gas (Mazzotta et al., 2003). Fig. 4.21 shows density, temperature, entropy and pressure maps together with the corresponding projected radial profiles. On the log-log plane of 2A-0335 radial profiles, we fitted the power-law models as described above. Tables 4.3 and 4.4 list best-fit values. The X-ray surface brightness or density map appears symmetric and regular. The temperature radial profile shows small fluctuations in the centre ($\lesssim 0.05\ R_{500}$) which could be associated with the central complex morphology consisting of a number of X-ray bright knots which, in turn, emit soft X-rays (Mazzotta et al., 2003). In the density radial profile, the power-law models did not fit at $\gtrsim 0.1\ R_{500}$. In § 4.9.4, we described how 2A-0335 is identified as a peculiar object on the Concentration vs M_{20} plane for pressure maps. It has the lowest Concentration and highest M_{20} values of all strong relaxed clusters for its pressure map. Its pressure profile is flatter in the core region (at $< 0.1\ R_{500}$) which indicates that the pressure morphology of 2A-0335 is disturbed. There is no fluctuation or discontinuity among the radial profiles of 2A-0335, which suggests that 2A-0335 is a strong relaxed, regular cluster.

4.10.3 A478

A478 is a strong relaxed, cooling flow cluster which hosts the X-ray cavities in its central region together with two low-power, small radio lobes emerging from the central nucleus (Sun et al., 2003; de Plaa et al., 2004). Subsequently, Sanderson et al. (2005) suggested the possibility of

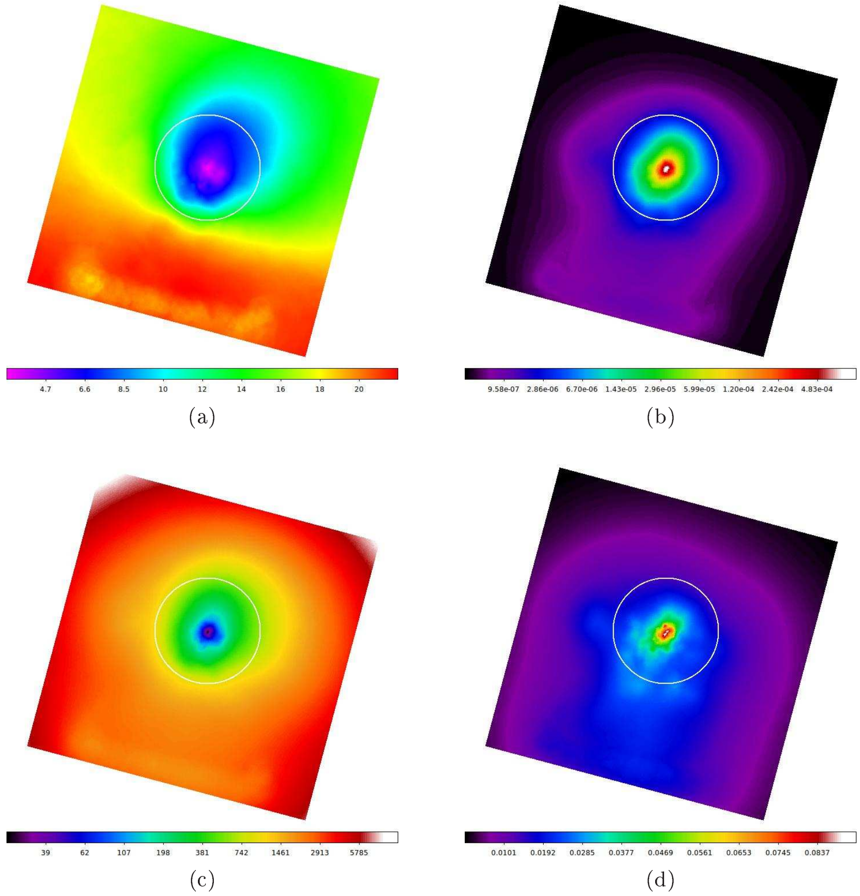

(a) (b)

(c) (d)

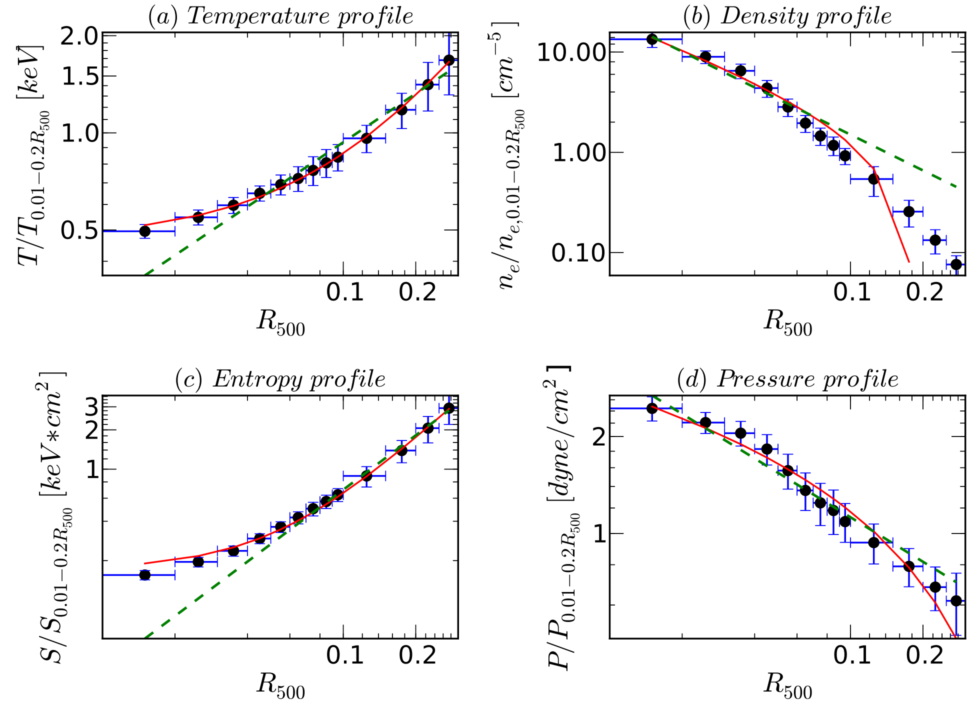

Figure 4.20: *Top* A2597 2-D thermodynamic maps. (a) is the A2597 temperature map, (b) is the A2597 density map, (c) is the A2597 pseudo-entropy map, and (d) is the A2597 pseudo-pressure map. The white circle shows the 0.3 R_{500} scaled radius centred on the cluster centroid. As can be seen, higher distance from the cluster centroid is not reliable and contains mainly noise due to fewer photons in the observation. *Bottom* Projected radial profiles of A2597 for (a) temperature, (b) density, (c) entropy and (d) pressure. The y error bar shows the standard deviation in each radial bin in the form of fluctuations. Solid red line shows the power-law model with constant base fitting, while dashed green line shows the pure power-law model fitting.

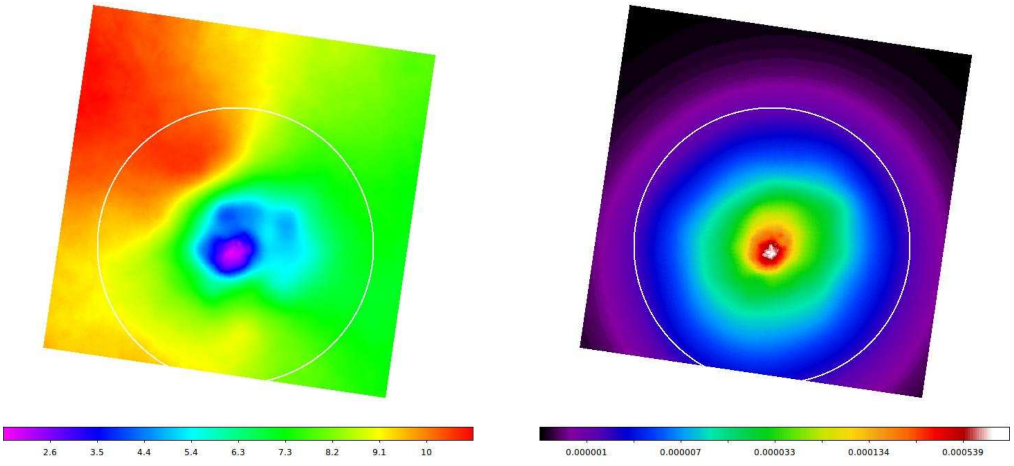

(a) (b)

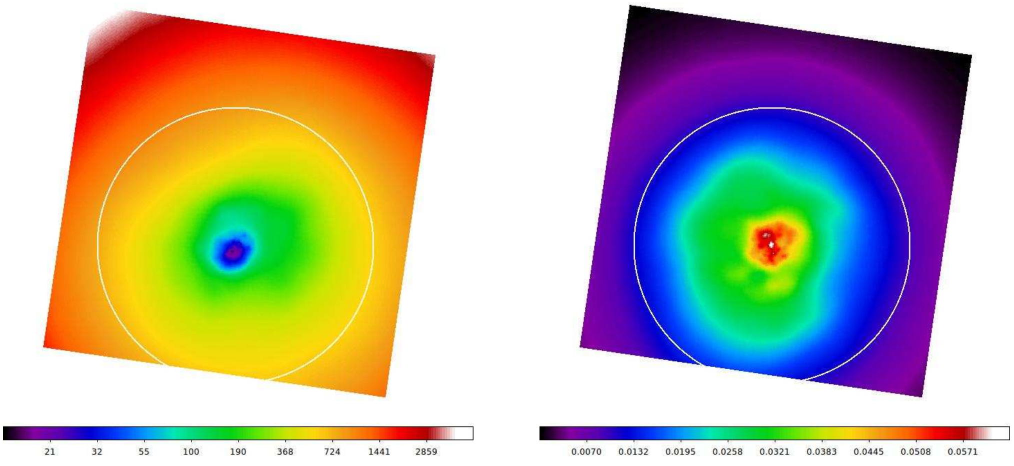

(c) (d)

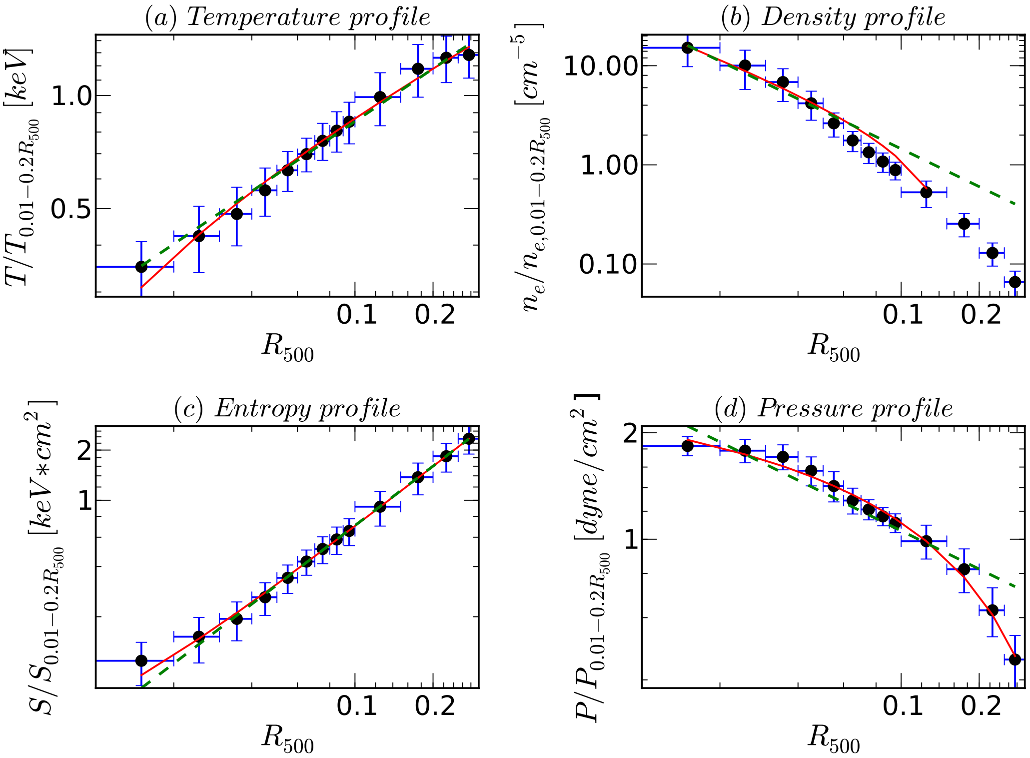

Figure 4.21: Same as Fig. 4.20, except for 2A-0335.

AGN heating the cool core of A478. They discovered four hot spots situated within the cool core of A478. These hot spots could be associated with strong-shock heating by the AGN jet. Fig. 4.22 illustrates our thermodynamic maps of A478 together with the corresponding radial profiles. Tables 4.3 and 4.4 list best-fit values derived from the power-law models. We observed fluctuation in the temperature profile, at $< 0.1\ R_{500}$, which could be due to the shock-affected central region of A478. In A478, the temperature of the cool core is approximately double that of the surrounding temperature (Sanderson et al., 2005). We noticed, in the morphology parameter vs parameter plane of Concentration vs M_{20} for temperature and entropy maps, that A478 falls on the non-relaxed side (see § 4.9.2 and 4.9.3). The entropy profile appears to be a typical relaxed cluster profile with no fluctuation and discontinuity. This could suggest that heating is spread somehow throughout the (dense) cluster core (Brüggen & Kaiser, 2002), possibly resulting in less fluctuation in the entropy profile. Density and pressure decline sharply when moving outwards from the cluster centre. In contrast to the two clusters described earlier, we were able to fit only the constant base power-law model to the density distribution at $> 0.1\ R_{500}$.

4.10.4 A1795

A1795 displays the relaxed and regular X-ray morphology in its surface brightness/density map. Markevitch et al. (2001) found a cold front in the core of A1795, which they attributed to sloshing gas. In addition to that, Fabian et al. (2001) noticed the cool gas filaments extending from the cD galaxy towards this cold front and the bulk of the central gas moving around the cD galaxy. Fig. 4.23 shows A1795 thermodynamic maps together with corresponding radial profiles. Tables 4.3 and 4.4 list best-fit values derived from the power-law models. In our observation, small fluctuations in the temperature profile in the inner core region ($\lessapprox 0.05\ R_{500}$) as well as outside of the radius 0.2 R_{500} were evident, but the temperature dropped in the core, and there was no discontinuity. There was also no corresponding fluctuation in the entropy profile, suggesting that the cool and dense cluster core of A1795 dissipates the (excess) temperature or heating into the core. In the parameter-parameter plane of temperature and entropy, we noticed that A1795 has low Concentration and high M_{20} values. This is consistent with the observed cold front activity in the core of A1795, which could be responsible for disturbing the core temperature and entropy morphology of A1795. In the density radial profile, power-law models did not fit at $\gtrsim 0.1\ R_{500}$. In general, there is no (high) fluctuation or discontinuity among the radial profiles of A1795, which indicates A1795 is a strong relaxed and regular cluster.

4.10.5 A2029

A2029 is a complex cooling core cluster which has asymmetric X-ray emission in the core. Clarke et al. (2004) analysed the *Chandra* data of A2029 and observed a number of X-ray filaments in the central region, filaments which could be connected with the presently active central radio galaxy. They also noticed spiral-sloshing motions in the cluster core possibly caused by a past merger activity. This disturbed morphology of A2029 is seen in the temperature and entropy maps, since we noticed in the parameter-parameter planes (for temperature and entropy maps) that A2029 has low Concentration and high M_{20} values. Fig. 4.24 shows thermodynamic maps of A2029 together with the corresponding radial profiles. We fitted the power-law models onto the log-log plane

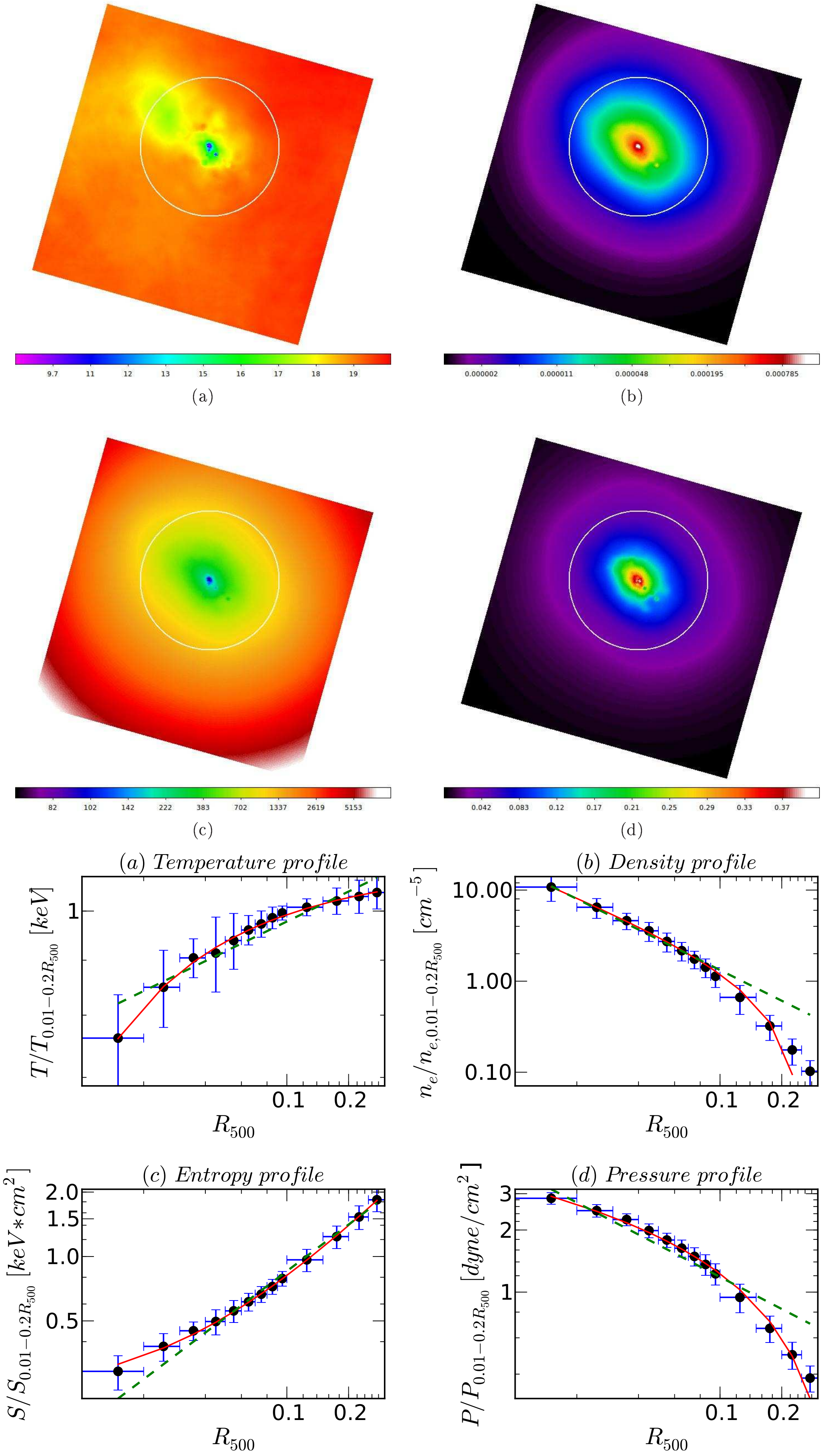

(a) (b) (c) (d)

Figure 4.22: Same as Fig. 4.20, except for A478.

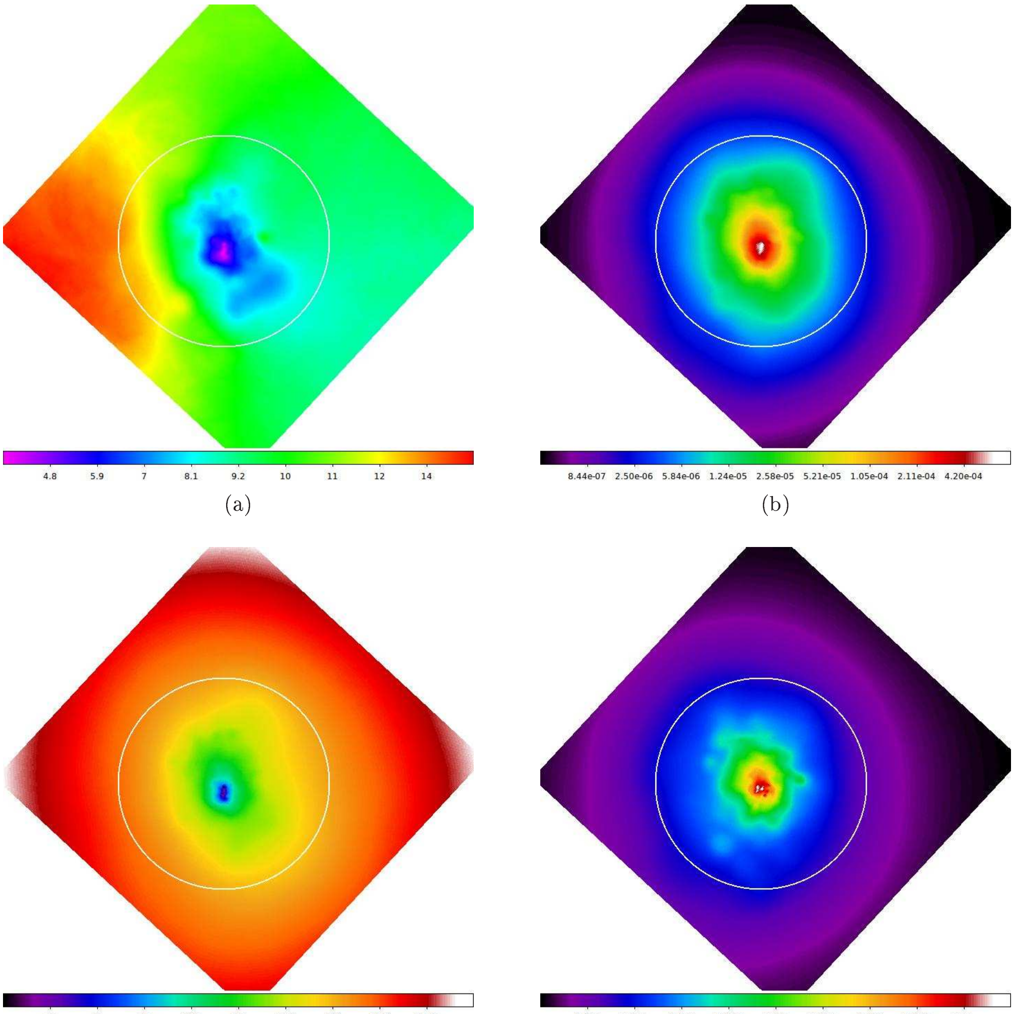

(a) (b)

(c) (d)

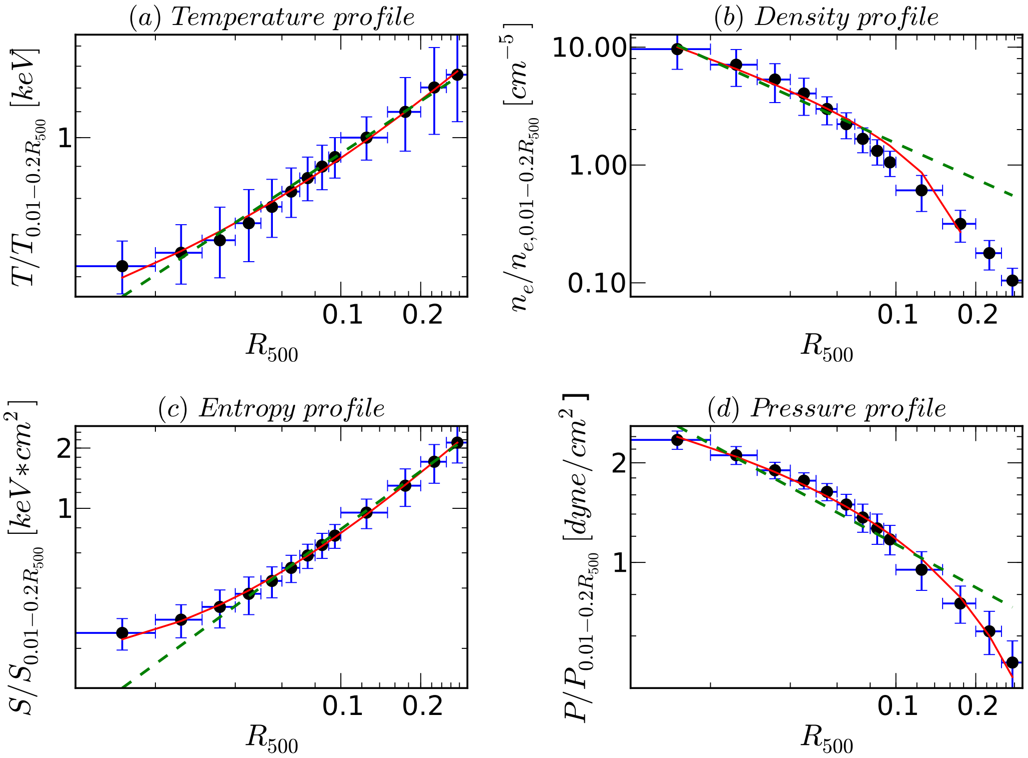

(a) *Temperature profile*

(b) *Density profile*

(c) *Entropy profile*

(d) *Pressure profile*

Figure 4.23: Same as Fig. 4.20, except for A1795.

of the A2029 radial profiles. Tables 4.3 and 4.4 list best-fit values derived from the power-law models. In the temperature map, we observed a hotter region in the North-West direction from the cluster centre. We suspect that this is an artifact resulting from the XMC modelling, visible in the temperature map only. In the temperature profile, we observed high fluctuation at 0.2 R_{500} corresponding to this artifact. The artifact may be the result of an insufficient number of photons in the observation of A2029. In the density radial profile, power-law models did not fit at $\gtrsim 0.1$ R_{500}. From the analysis of the inner region of A2029, however, this cluster appears relaxed. There is no fluctuation or discontinuity in radial profiles, which could indicate that there is presently no substructure located in A2029.

4.10.6 RXJ1504

RXJ1504 is the highest redshift ($z = 0.2169$) cluster in the low-z cluster sample. RXJ1504 is massive, luminous and extremely compact, and has a particularly dense central region. Its high X-ray luminosity belongs mainly to the central core (Böhringer et al., 2005). Surface brightness morphology parameters of RXJ1504 also suggest that it is a highly regular and strong relaxed cluster, similar to A2597. Fig. 4.25 shows RXJ1504 thermodynamic maps together with the corresponding radial profiles. We fitted the power-law models onto the log-log plane of the RXJ1504 radial profiles. Tables 4.3 and 4.4 list best-fit values derived from the power-law models. All the thermodynamic maps appeared regular, and there was no substructure visible. We also observed an unremoved point source (from the input event file) in the South-West direction from the main cluster, in all the thermodynamic maps. In the density radial profile, the power-law models did not fit at $\gtrsim 0.1$ R_{500}. A high central temperature could be the result of central AGN heating, as argued by Böhringer et al. (2005). This is in agreement with our finding that RXJ1504 has low Concentration and high M_{20} values for its temperature map. There is no fluctuation or discontinuity in any of the radial profiles of RXJ1504 which could indicate that it is a strong relaxed and regular galaxy cluster.

4.10.7 A2204

A2204 is at redshift $z = 0.1511$. Surface brightness morphology parameters suggested that A2204 is a strong cool core cluster (with highest Concentration and lowest M_{20} values for its density map). The central cooling time ($0.25\ h_{71}^{-1/2} Gyr$) of A2204 is the lowest of all relaxed clusters in the V09 sample, as well as having very high central electron density (Sanders et al., 2005; Hudson et al., 2010). The temperature map and discontinuity in the temperature radial profile (Fig. 4.26) together suggest that the core is disturbed and that there could be a substructure in the central region. In the temperature and density maps, the North emission corresponds to unremoved point source(s). The temperature map indicates high temperature and a tail-like structure extending Eastwards from the cluster core. This is consistent with the our previous finding that A2204 has low Concentration and high M_{20} values for its temperature map. The temperature radial profile shows a flattening or discontinuity at ~ 0.1 R_{500} before a further temperature decline in the core. The corresponding entropy profile of A2204 does not indicate any flattening or discontinuity. Sanders et al. (2005) noticed a similar morphology in the core of A2204. They argued that this structure is a result of cluster merger with unequal mass, the central subcluster having a much smaller mass then

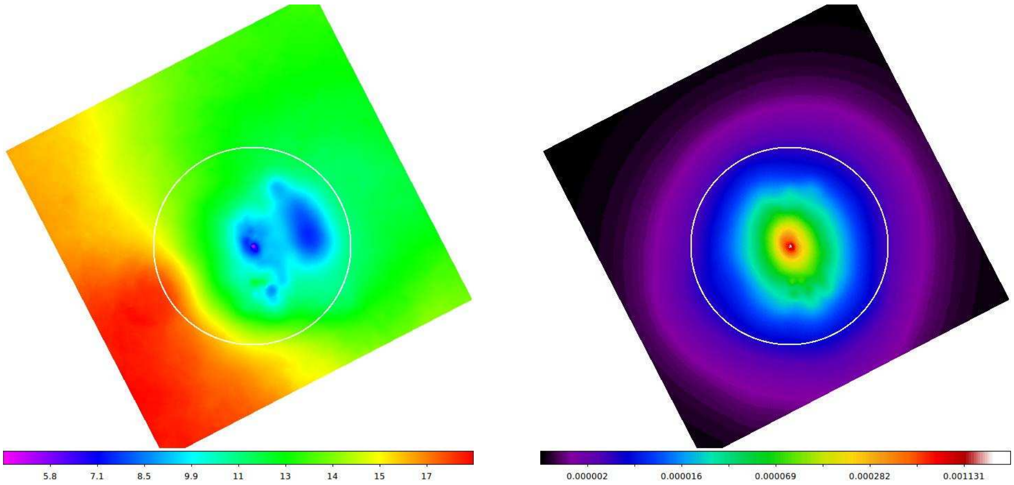

(a) (b)

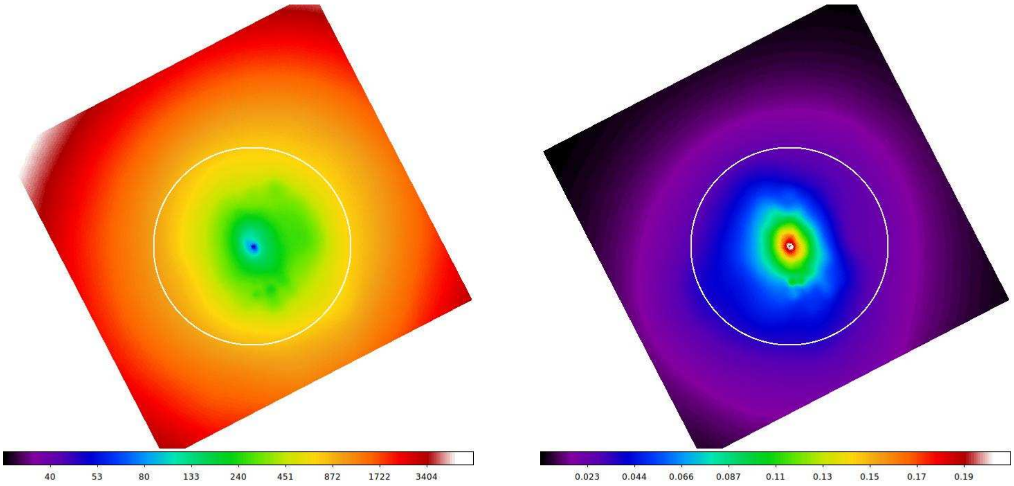

(c) (d)

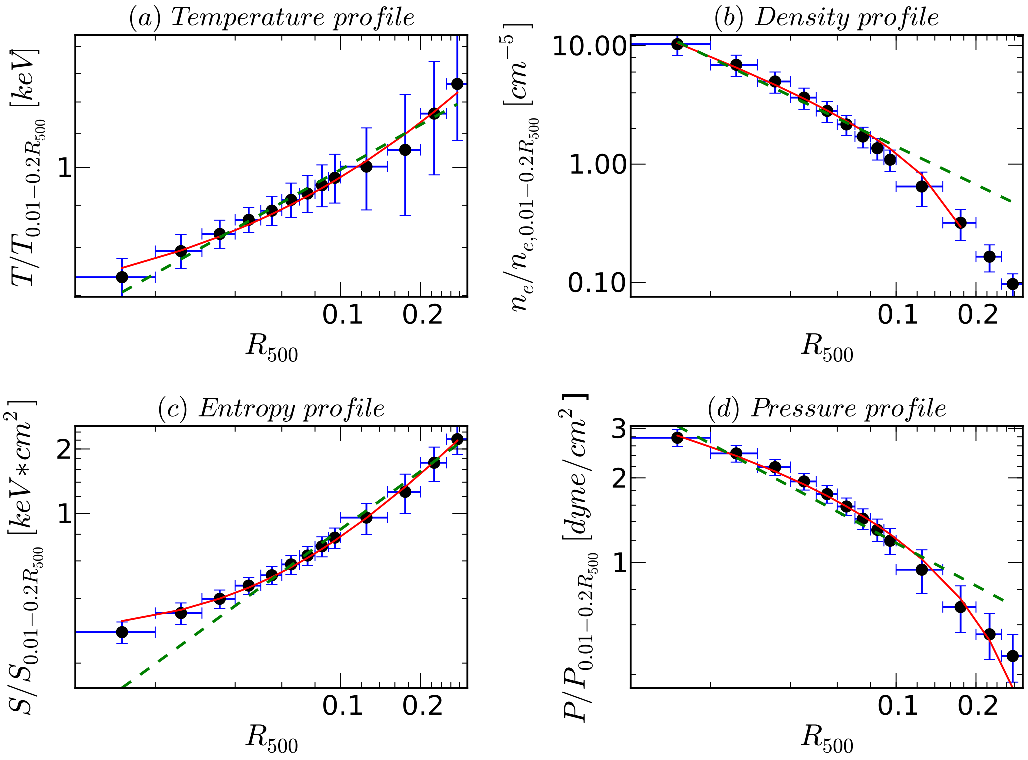

Figure 4.24: Same as Fig. 4.20, except for A2029.

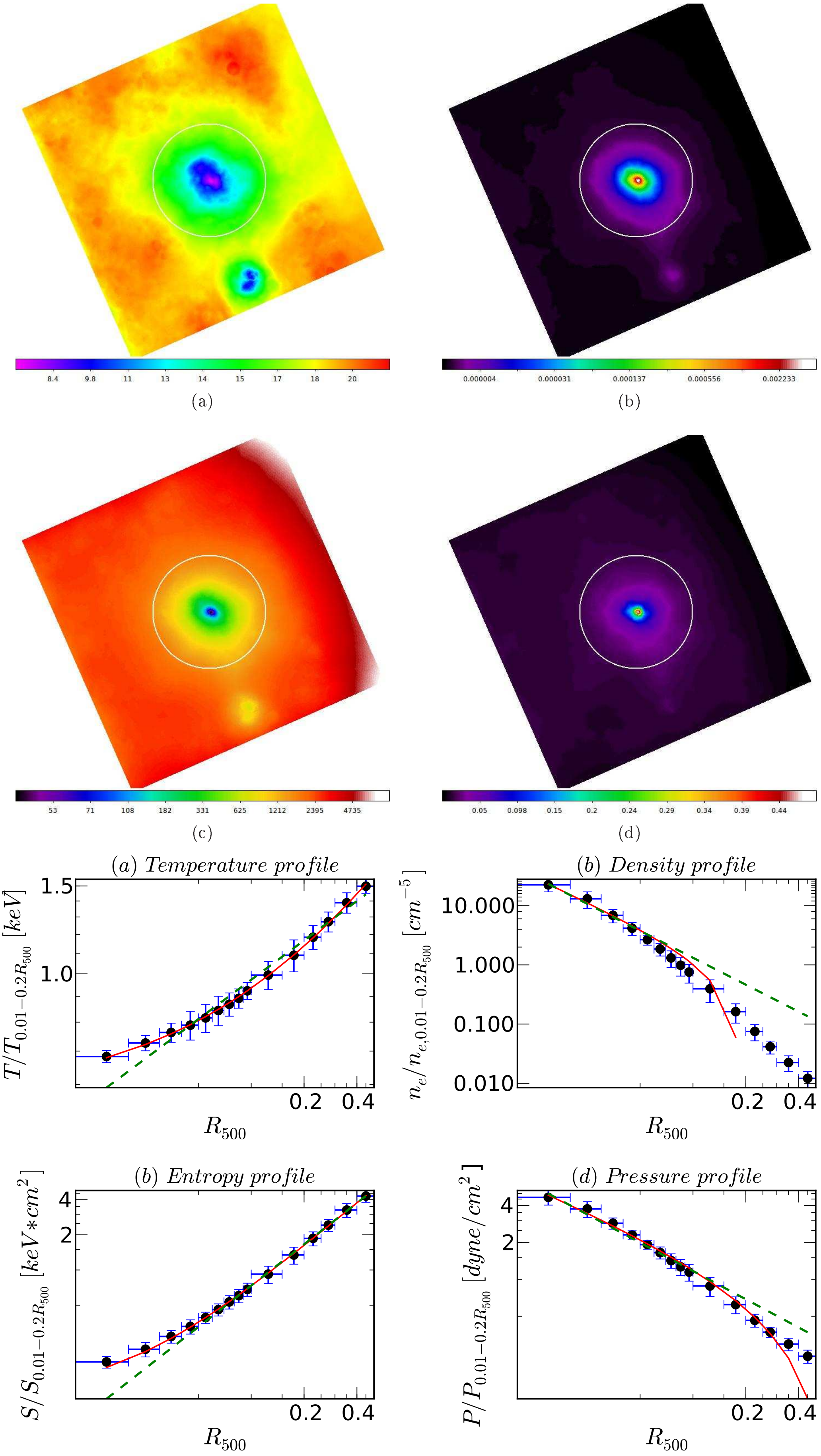

(a) (b)

(c) (d)

Figure 4.25: Same as Fig. 4.20, except for RXJ1504.

that of the main cluster. We did not observe any significant substructure in the density, pressure and entropy maps, nor fluctuation and/or discontinuity in their radial profiles. Consequently, overall this appears to be a relaxed and regular cluster except for small scale merging activity in the cluster core. A2204 is a good example of a cluster with small scale merging activity not detected in its surface brightness morphology parameters, and which would go unnoticed without a temperature map.

4.10.8 A2147

A2147 is a member of the Hercules supercluster. The irregular X-ray morphology of the A2147 cluster indicates merging activity. Fig. 4.27 illustrates our thermodynamic maps together with the corresponding radial profiles. We fitted the power-law models onto the log-log plane of the A2147 radial profiles. Tables 4.3 and 4.4 list best-fit values derived from the power-law models. All of its thermodynamic maps indicate that A2147 is a merging cluster. We observed that, in the density map, the X-ray emission extends Southwards from the cluster center. The temperature and entropy maps display multiple X-ray emission spots which could be associated with merging activity. Furthermore, the temperature and entropy maps show an extended region towards the South-East not clearly visible in the surface brightness or density maps. There is also less X-ray emission visible in the North-Westerly direction. The temperature and entropy profiles show discontinuity (profile becomes flat at $\lesssim 0.1\ R_{500}$), and fluctuation, which are typical indicators of merger. In particular, at a radius of $\gtrsim 0.1\ R_{500}$, both the temperature and entropy profiles show high fluctuation. This implies possible heating by merger shocks which increase the ICM entropy. In both of these profiles, pure power-law is not fitted well in either the core region ($\lesssim 0.1\ R_{500}$) or outside of it. It is possible that the pure power-law model is not sufficient in evaluating profiles of temperature and entropy for A2147. The density profile appears flat in the central region ($\lesssim 0.1\ R_{500}$), which is opposite to that of a relaxed cluster profile whose density declines sharply when moving outward from the cluster centre. Unlike the relaxed clusters, in the density profile of A2147, the power-law (with constant base) can be fitted up to 0.3 R_{500}. Overall, A2147 is a strong non-relaxed cluster because of the high fluctuation and discontinuity in its temperature and entropy radial profiles.

4.10.9 A3266

The surface brightness map of A3266 shows an elongated morphology and that it is a merging cluster (Finoguenov et al., 2006). Fig. 4.28 displays our thermodynamic maps together with the corresponding radial profiles. Tables 4.3 and 4.4 list best-fit values derived from the power-law models. A3266 is a very hot cluster. Finoguenov et al. (2006) found low entropy gas flowing in a North-Easterly (merger-axis) direction from the primary cluster core, corresponding to in-falling subcluster gas stripped from the foreground. Our temperature and entropy maps indicate two nuclei lying in the North-East, which concur with the findings of Finoguenov et al. (2006). We observed fluctuation and discontinuity in the radial profiles of temperature and entropy. The temperature and entropy profiles are flat in the cluster core region ($\lesssim 0.1\ R_{500}$), and the pure power-law model did not fit well. Unlike the relaxed clusters, in the density profile of A3266, the

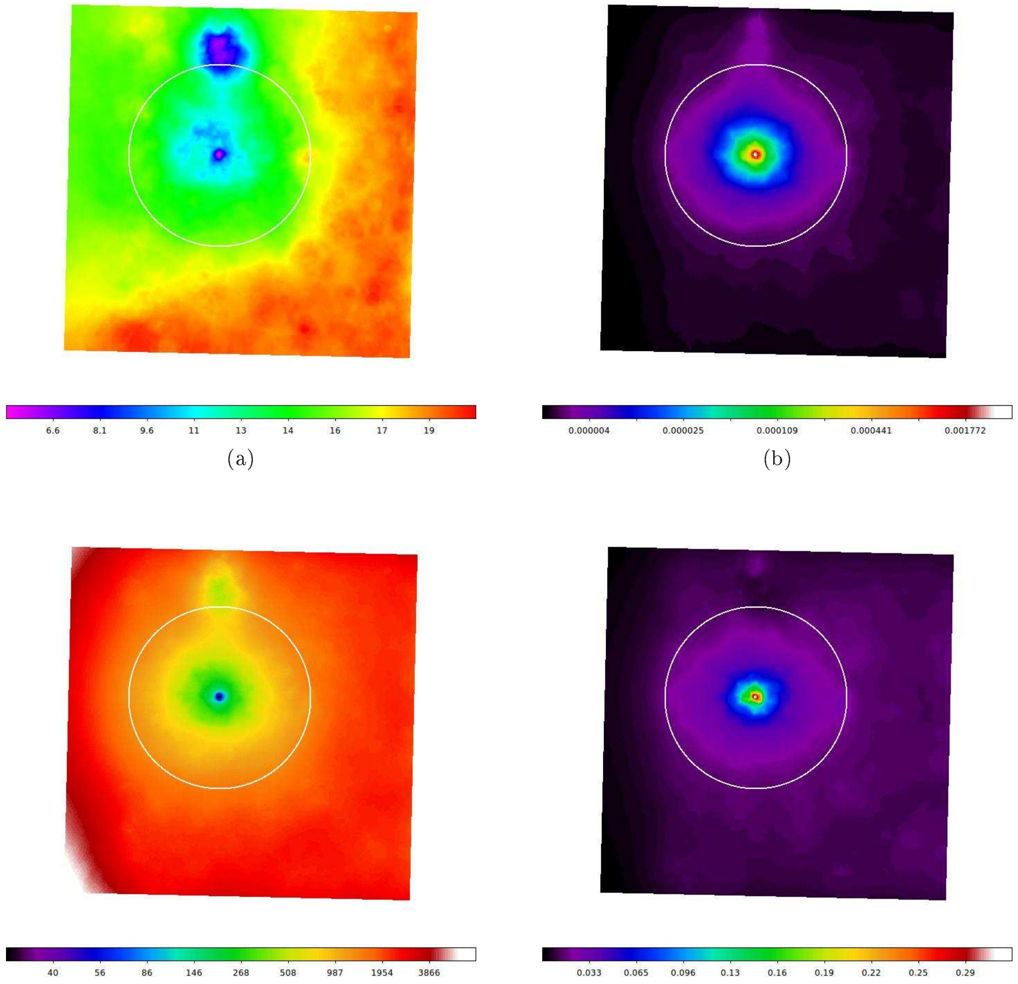

(a) (b)

(c) (d)

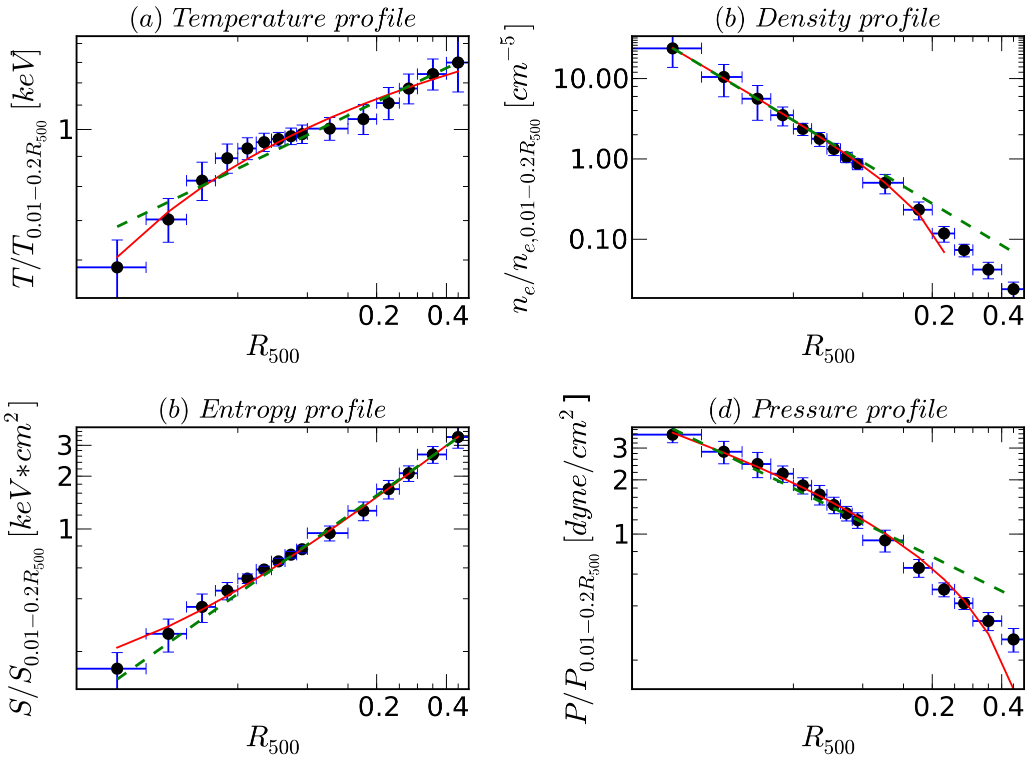

Figure 4.26: Same as Fig. 4.20, except for A2204.

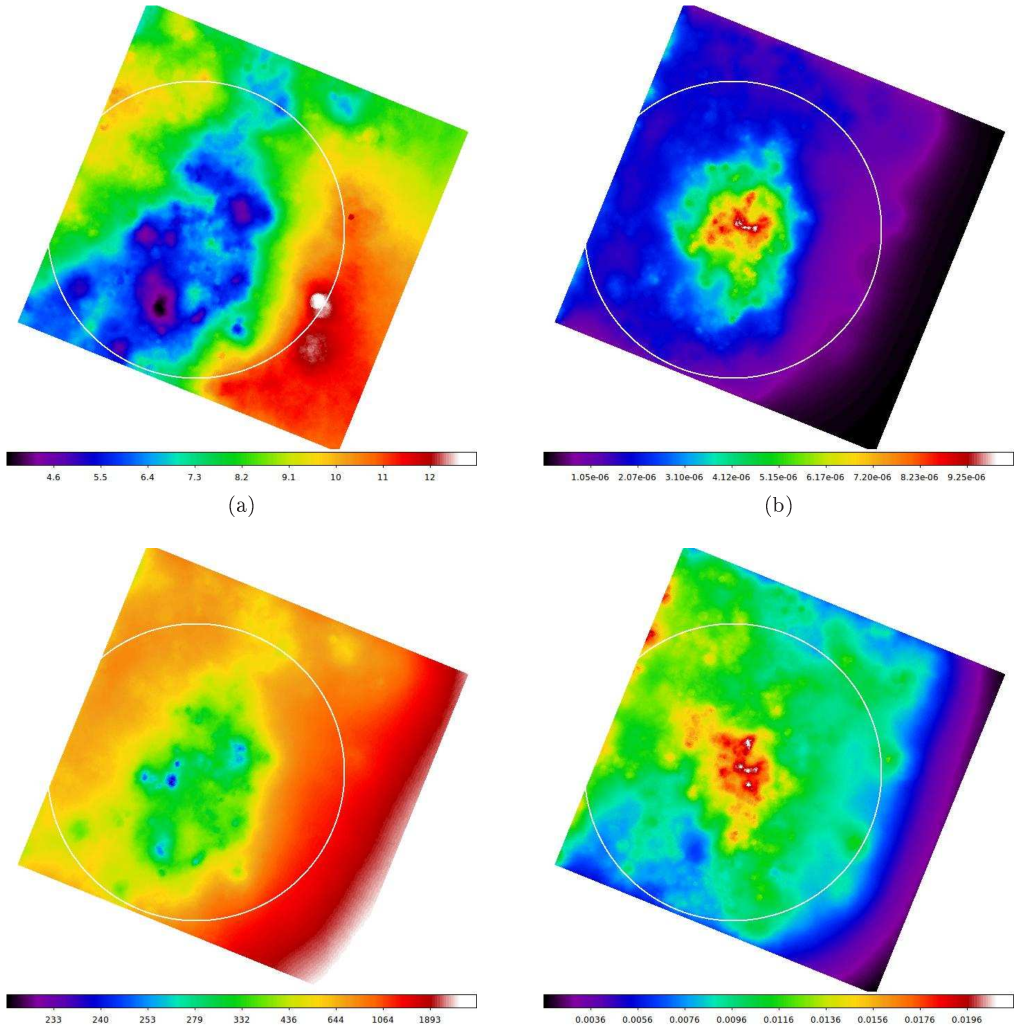

(a) (b)

(c) (d)

(a) *Temperature profile* (b) *Density profile*

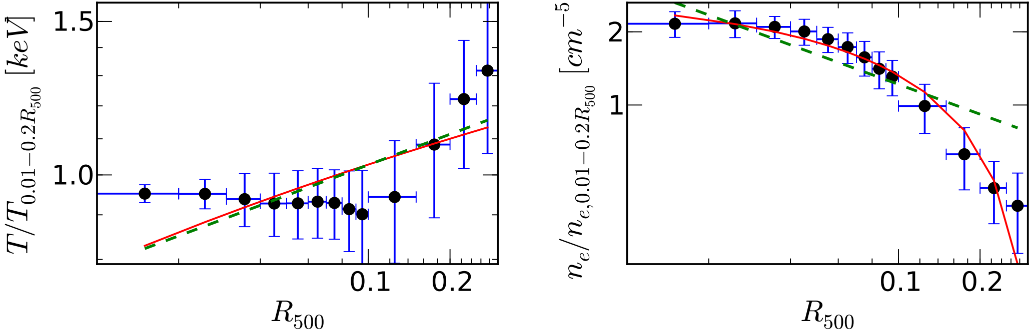

(c) *Entropy profile* (d) *Pressure profile*

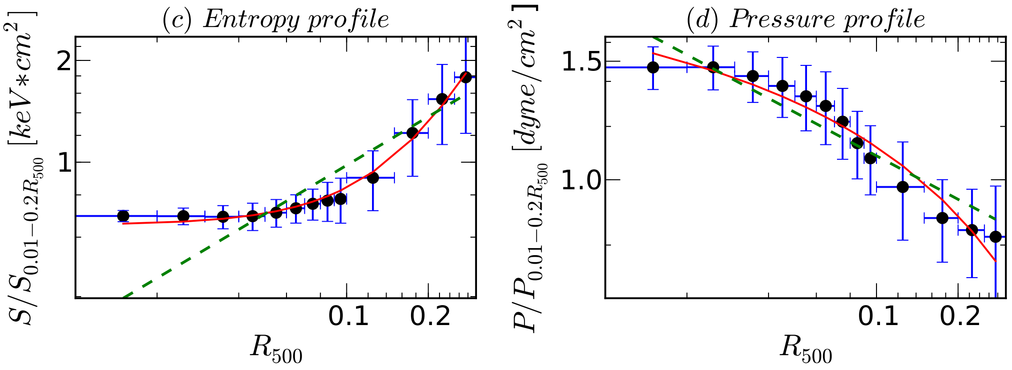

Figure 4.27: Same as Fig. 4.20, except for A2147.

power-law (with constant base) can be fitted up to 0.3 R_{500}. In brief, A3266 is a strong non-relaxed cluster because of high fluctuation and discontinuity in temperature and entropy radial profiles.

4.10.10 A1736

A1736 belongs to the Shapely Supercluster. X-ray morphology of this cluster shows a complex and irregular shape with no well defined core (Ettori et al., 1997). This is one of the most disturbed clusters in the (surface brightness) morphology parameter-parameter plane (i.e. it has the lowest Gini and Concentration values and highest M_{20} value). Fig. 4.29 shows our thermodynamic maps together with the corresponding radial profiles. Tables 4.3 and 4.4 list best-fit values derived from the power-law models. The temperature and entropy distribution of A1736 is very complex. In the density map, the centroid is located in the West. In the temperature and entropy maps, we observed peak emission from the East and West extending towards the South. The temperature radial profile appeared to be flat in both the central core and outer region. In the entropy profile, we noted discontinuity to be at $\lesssim 0.1\ R_{500}$. We saw high fluctuation in the temperature and entropy profiles. The density and pressure profiles also appeared flat in the cluster core. The pure power-law model did not fit well to any of the radial profiles of A1736. All of our thermodynamic maps and radial profiles suggest that A1736 is a strong non-relaxed cluster.

4.10.11 A3395

A3395 is a complex merger having multiple components - A3395 (North-East), A3395 (South-West), A3395 (North-West), A3395 (West), and filaments between the N-E and W components (Tittley & Henriksen, 2001; Lakhchaura et al., 2011). In our analysis, we excluded the N-E component. There is no shock front in A3395. Fig. 4.30 gives our thermodynamic maps together with the corresponding radial profiles. Tables 4.3 and 4.4 list best-fit values derived from the power-law models. All of the maps indicated that merging activity is on-going between A3395 (North-East) and A3395 (South-West). The hot ICM extends from the South-West to West, and high entropy gas flows from the filaments. The temperature profile indicated high fluctuation, but there was no sign of flattening in the core, nor was there any discontinuity visible in either the temperature or entropy profiles. A3395 is identified as a strong non-relaxed cluster in terms of the combination of (surface brightness) morphology parameters, but its radial profiles (with the exception of high fluctuation in temperature and pressure) do not suggest that it is a strong non-relaxed cluster as is A1736.

4.10.12 A754

The X-ray morphology of A754 shows irregularity and very complex behaviour, indicating that it is undergoing a violent merger (Kassim et al., 2001; Henry et al., 2004; Clarke et al., 2005a; Macario et al., 2011). Fig. 4.31 gives our thermodynamic maps together with the corresponding radial profiles. Tables 4.3 and 4.4 list best-fit values derived from the power-law models. In the thermodynamic maps, we observed that the X-ray emission extends from the East to the West. A large hot area in the South and South-West, together with cool gas situated at the tip of the bright tongue-like structure, were also observed by Govoni et al. (2004) in their temperature map. It is

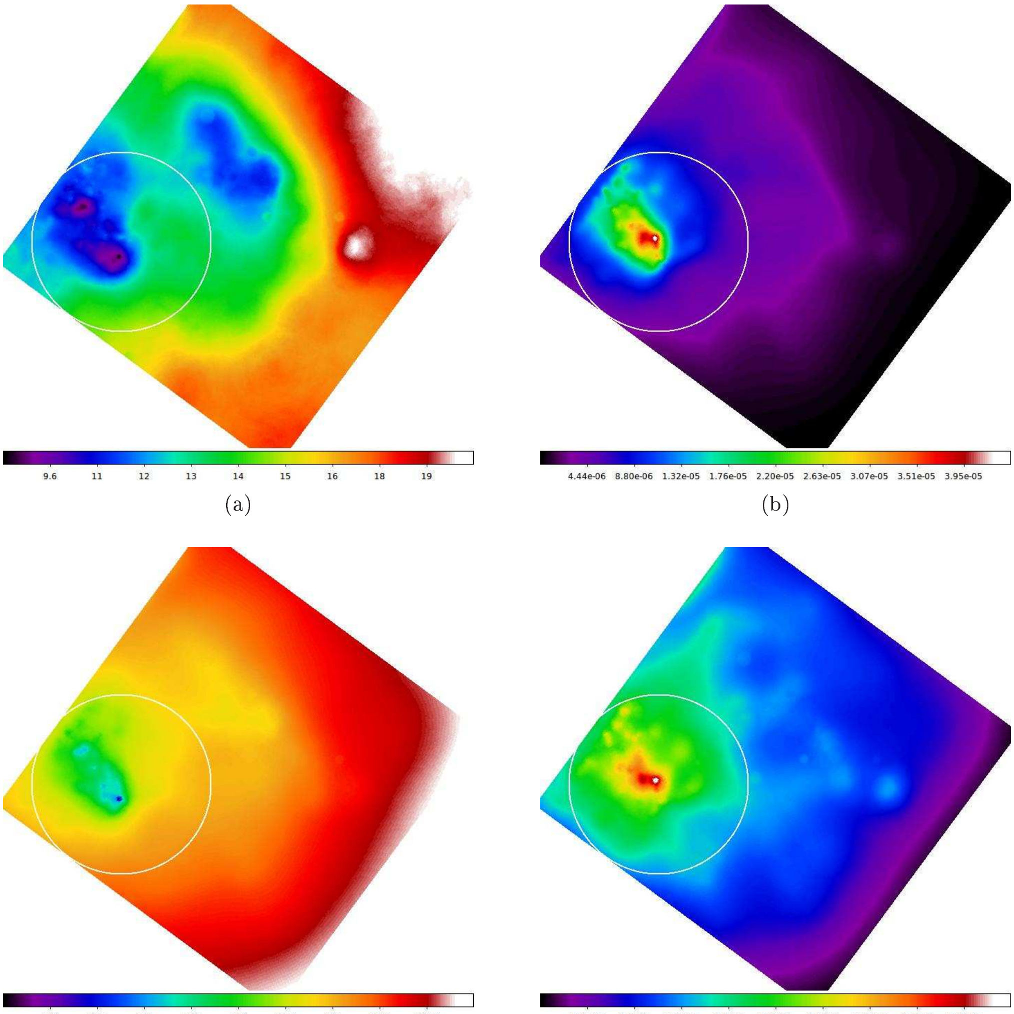

(a) (b)

(c) (d)

(a) *Temperature profile* (b) *Density profile*

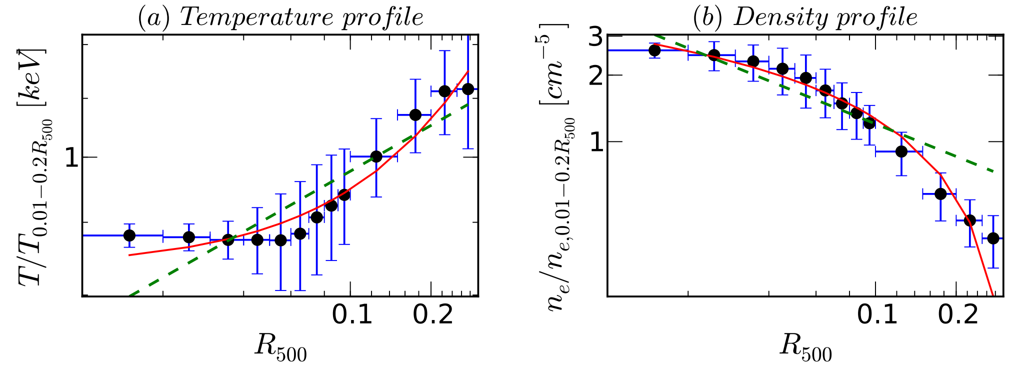

(c) *Entropy profile* (d) *Pressure profile*

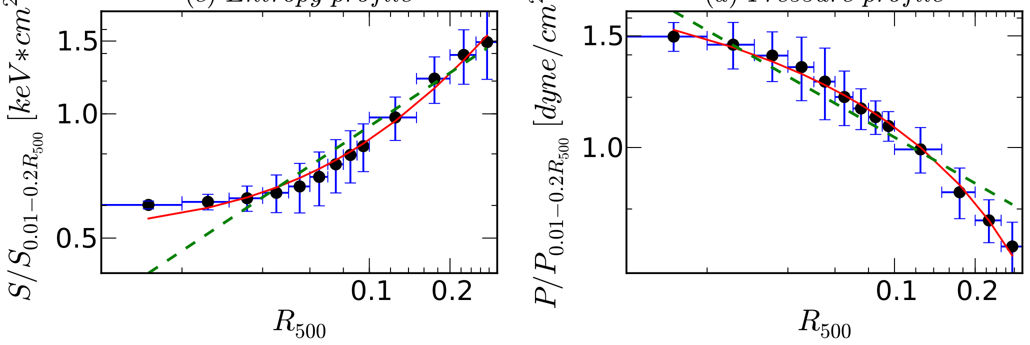

Figure 4.28: Same as Fig. 4.20, except for A3266.

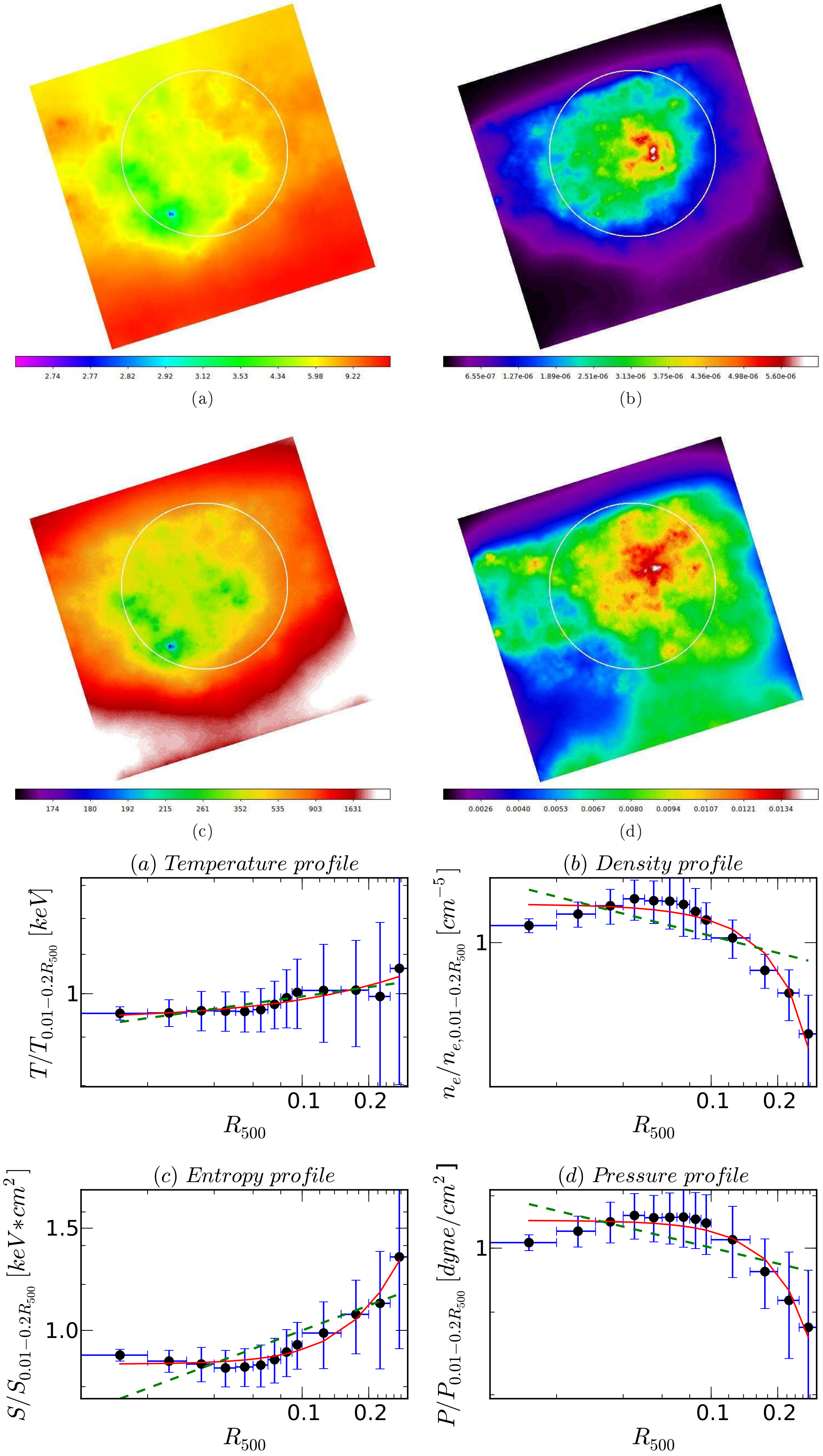

(a) (b)

(c) (d)

Figure 4.29: Same as Fig. 4.20, except for A1736.

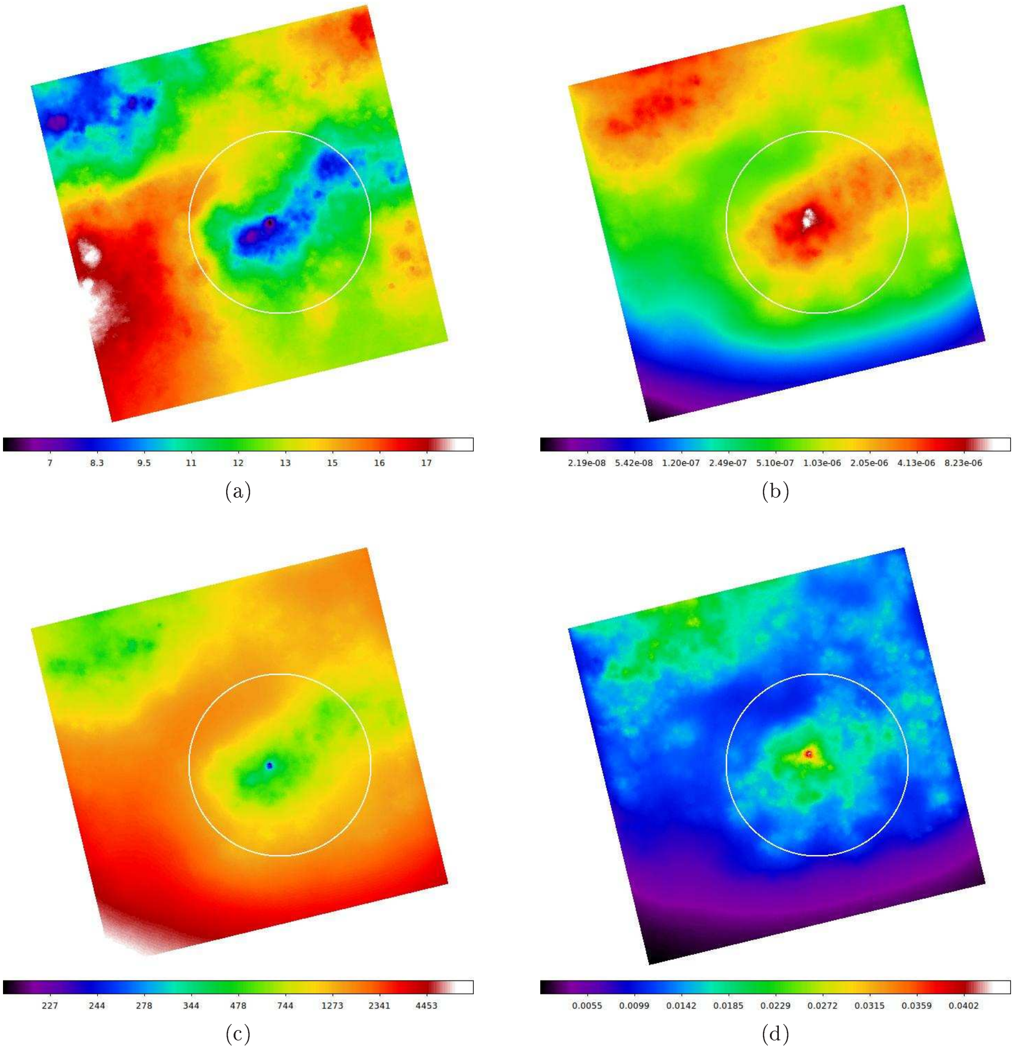

(a) (b) (c) (d)

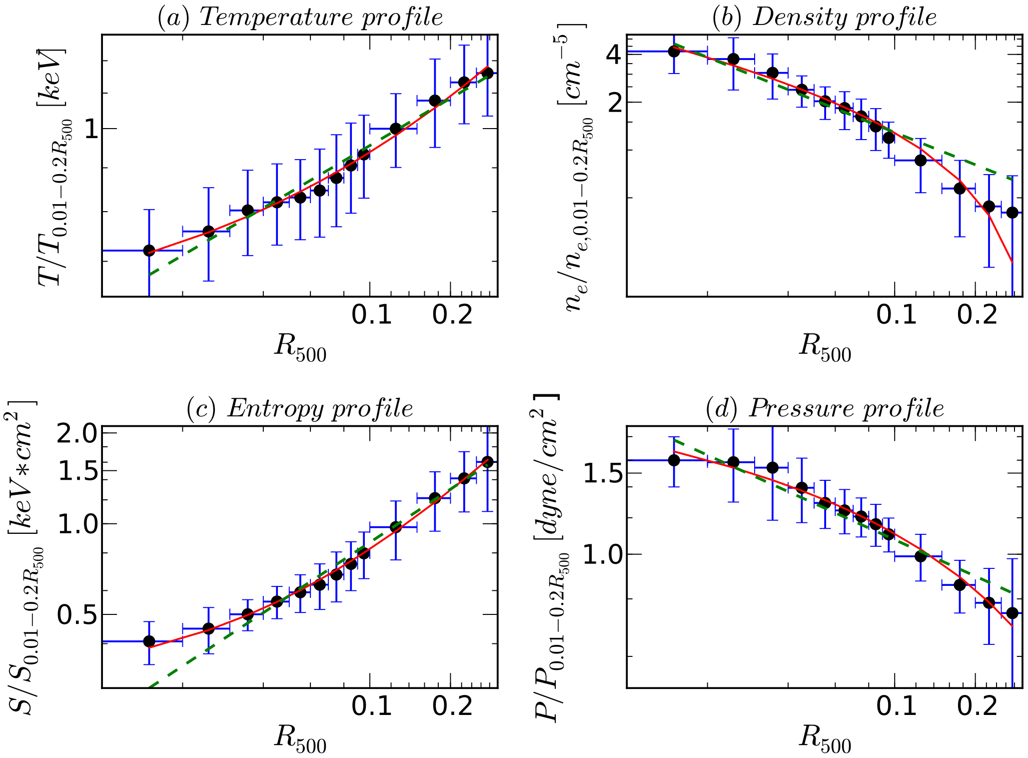

Figure 4.30: Same as Fig. 4.20, except for A3395.

possible that this structure could be a remnant of the core of one of the substructures currently moving in the North-Easterly direction. Henry et al. (2004) provided a detailed analysis of A754 using pseudo entropy and pressure maps. In the parameter-parameter plane for the temperature maps, we observed that A754 has a high Concentration and low M_{20} value compared with those of other strong non-relaxed clusters. It is possible that the core of A754 is not yet affected by merging activity. However, our radial profiles, particularly temperature and pressure, show high fluctuation; but, consistent with our temperature morphology parameter result, in the inner core region there is no temperature fluctuation ($\lesssim 0.05\ R_{500}$). The temperature and entropy profiles indicate discontinuity and that they are flat in the core ($\lesssim 0.1\ R_{500}$), and also that the pure power-law model is not adequate in evaluating the profiles of temperature and entropy. Hence, the radial profiles indicate that A754 is a violent merger.

4.10.13 A2256

A2256 is at an early stage of merger, and the main body of the cluster is not yet much disturbed by ongoing merging activities (Sun et al., 2002). This is in agreement with our previous finding that A2256 has high Concentration and low M_{20} values for its temperature map. Fig. 4.32 gives our thermodynamic maps together with the corresponding radial profiles. Tables 4.3 and 4.4 list best-fit values derived from the power-law models. The A2256 temperature map also shows that a subcluster in the West has a lower temperature (as well as low entropy) than that of the main cluster (Sun et al., 2002). We also noticed a distortion in the morphology of the subcluster, which could be the result of the infalling of groups or a cluster from the West. Both the temperature and entropy profiles are flat and discontinue at $\lesssim 0.1\ R_{500}$. The density and pressure profiles are also flat in the core region. There is high fluctuation visible in the temperature and pressure profiles. None of the profiles is fitted with the pure power-law model. The radial profiles of A2256 suggest that it is a strong merging cluster.

In summary the diagnostics of substructure and cluster merger using thermodynamic maps and corresponding radial profiles of galaxy clusters contribute significantly to the knowledge of the dynamical state of clusters. We observed more fluctuation and discontinuity in radial profiles of significantly disturbed clusters, compared with smooth and steady profiles of relaxed and regular clusters. Of all thermodynamic maps, the **temperature map** is the most sensitive indicator of merging activities. In relaxed clusters, a subcluster sometimes goes unnoticed in their density or surface brightness maps, but could be detected in the temperature maps of corresponding relaxed clusters, using either morphology parameters (Concentration and M_{20}) or a 1-D radial profile together with fluctuation and/or discontinuity. This study includes only (V09) low-z strong relaxed and strong non-relaxed clusters in the analysis of radial profiles. There is a possibility of mismatch in cluster dynamical states derived by (1) surface brightness morphology parameters and (2) thermodynamic maps. For example, A3376 is classified as a non-relaxed cluster (weak cool core) by a combination of surface brightness morphology parameters, while its thermodynamic radial profiles (Fig. 4.33) show more fluctuation and discontinuity (compared with other non-relaxed clusters), which makes this cluster a strong merger or disturbed cluster according to its thermodynamic maps.

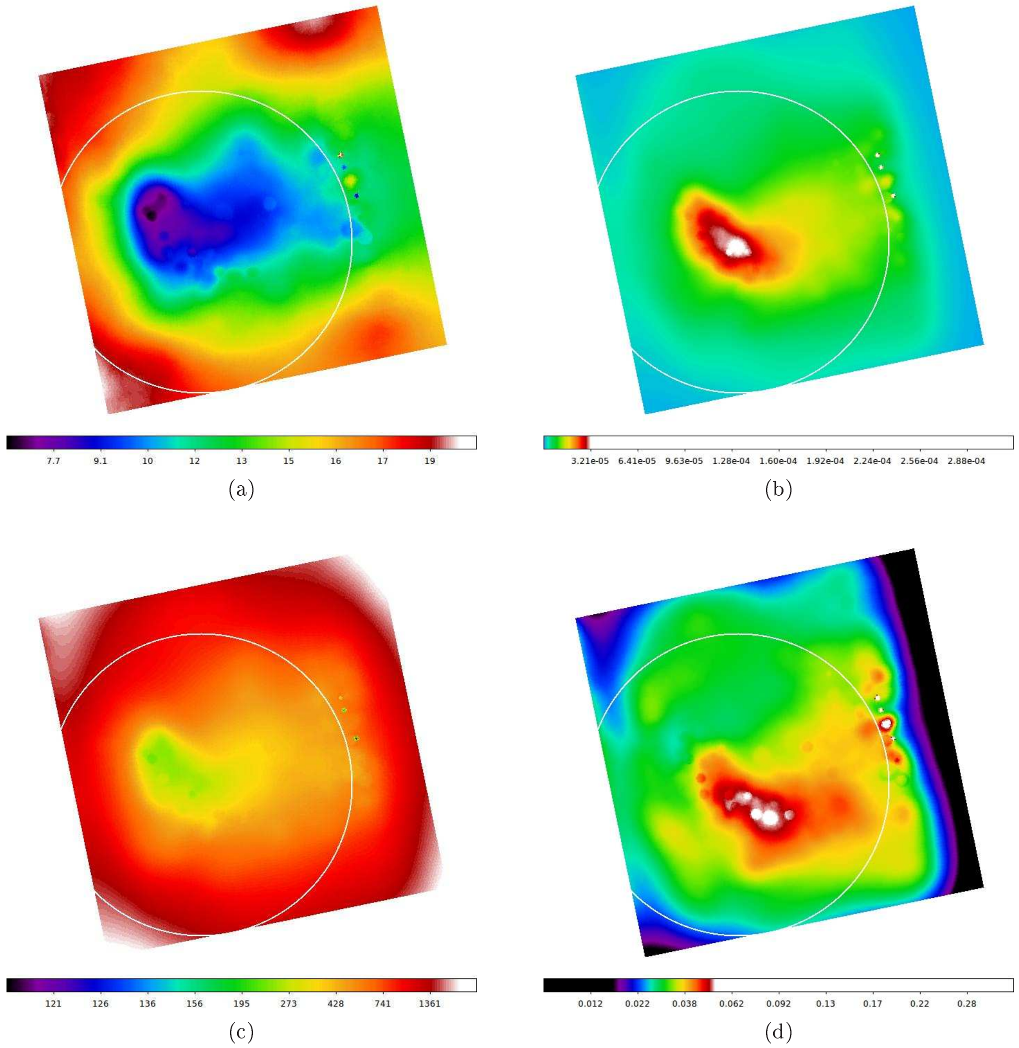

(a) (b)

(c) (d)

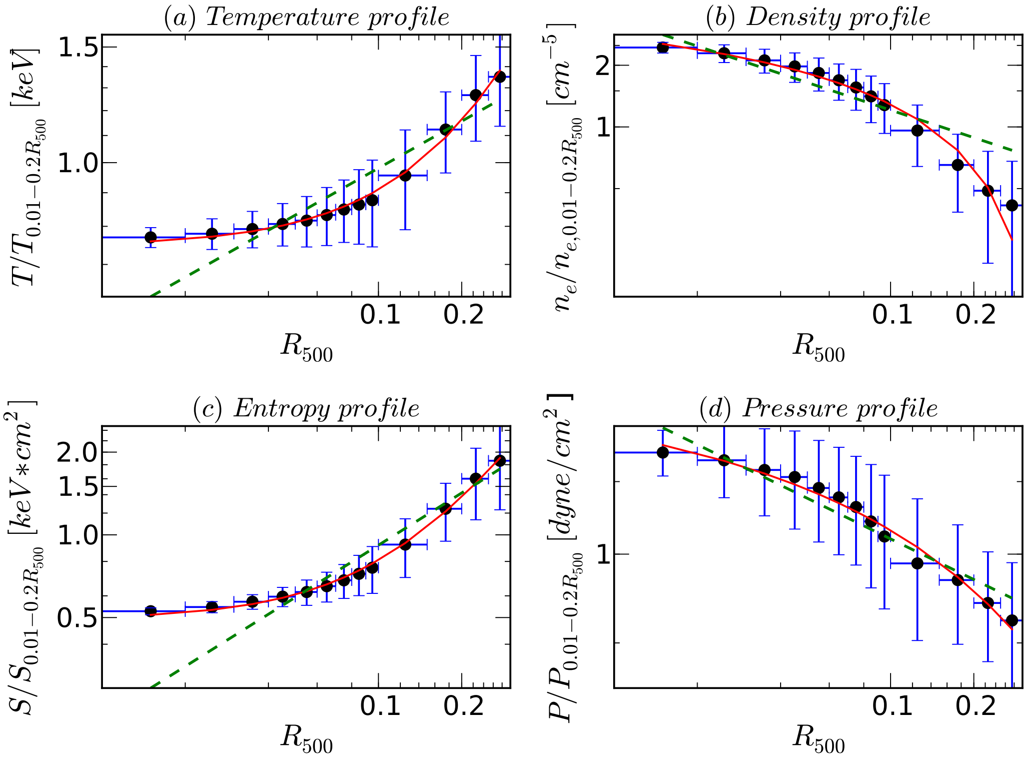

Figure 4.31: Same as Fig. 4.20, except for A754.

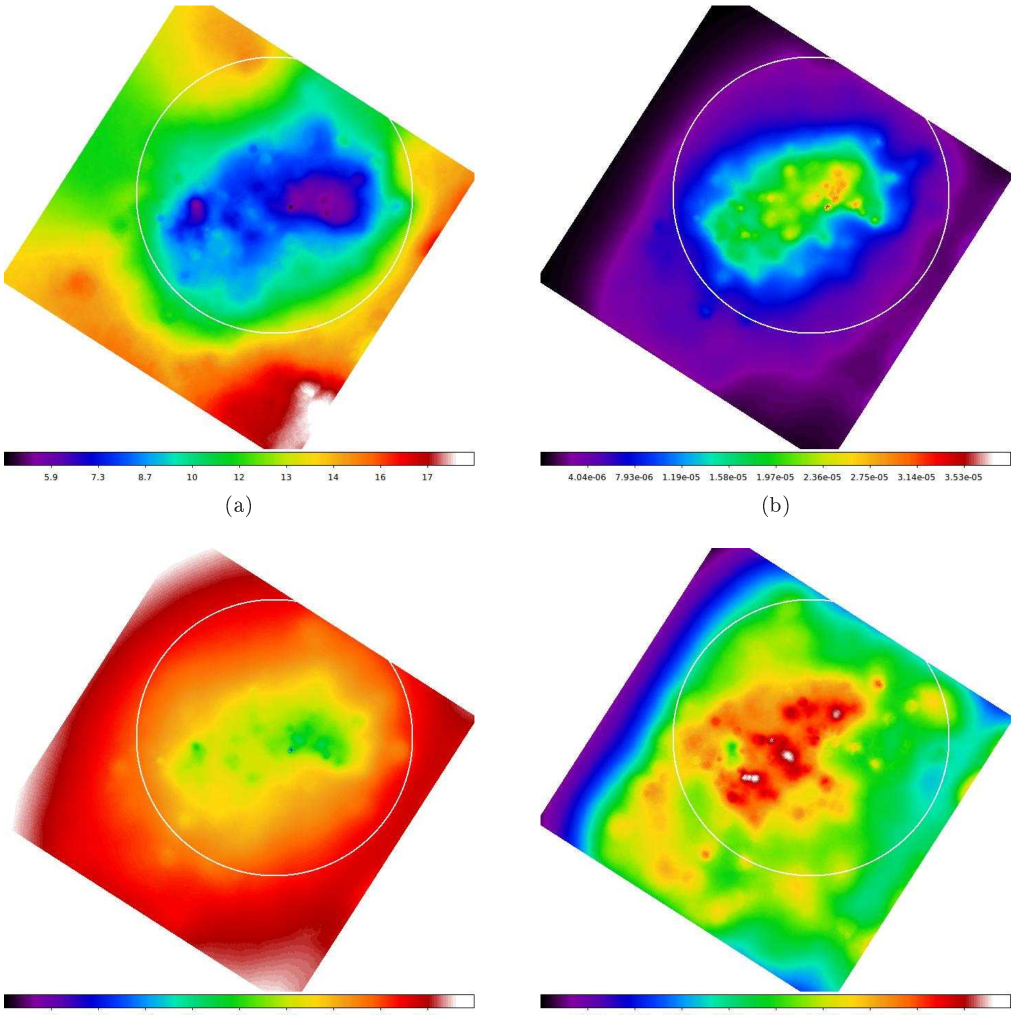

(a) (b)

(c) (d)

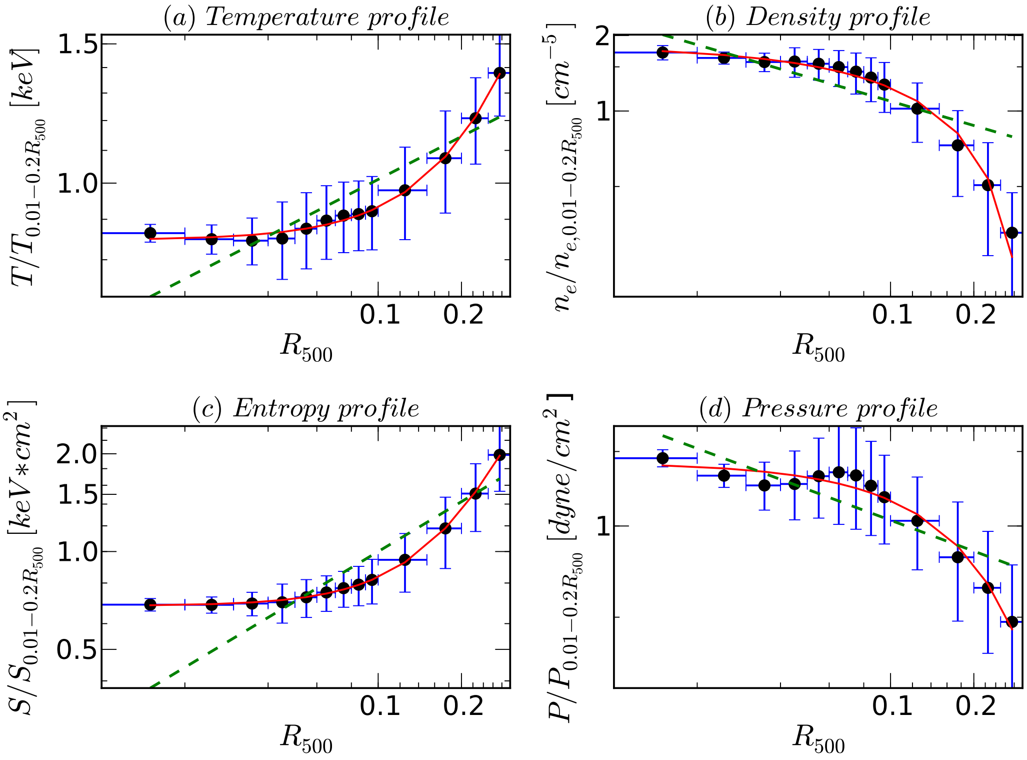

Figure 4.32: Same as Fig. 4.20, except for A2256.

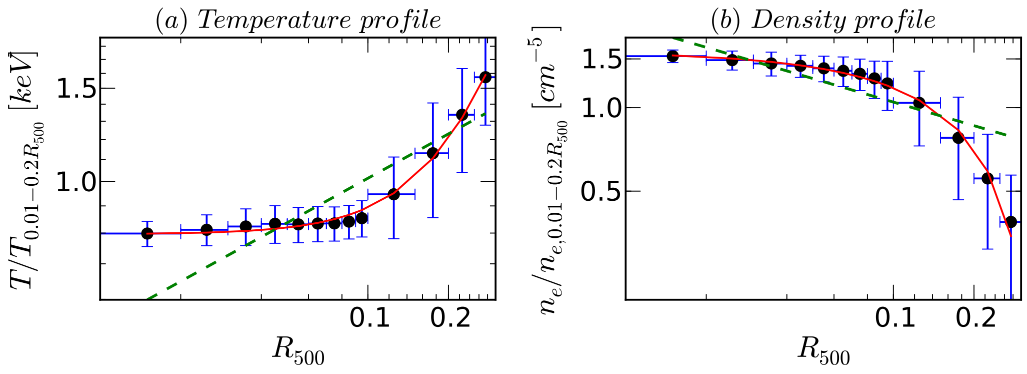
(a) *Temperature profile*

(b) *Density profile*

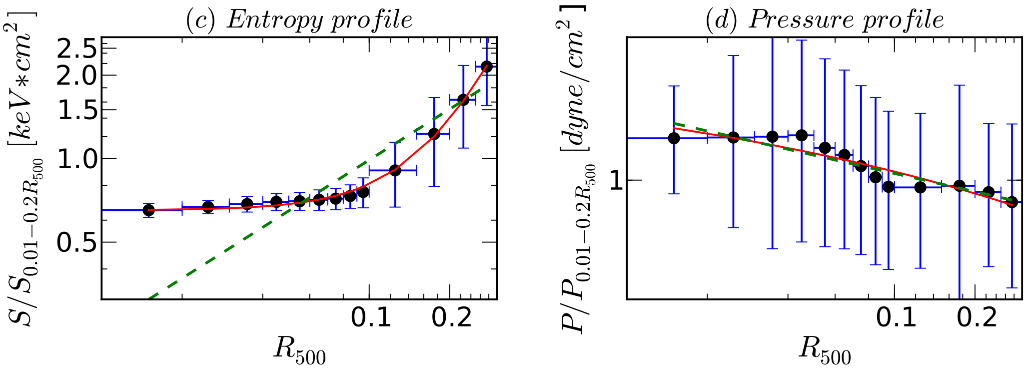
(c) *Entropy profile*

(d) *Pressure profile*

Figure 4.33: Radial profiles of A3376. This cluster is identify as non-relaxed or intermediate by morphology parameters in its surface brightness map, but shows more fluctuation and discontinuity in temperature and pressure profiles.

4.11 Sample of *XMM-Newton* observed clusters

The KA09 study used 101 X-ray galaxy clusters to quantify the scatter and evolution of the $L_X - T$ relationship, and to examine the evolution of substructure with redshift. They analysed this using luminosity/density and temperature 2-D maps derived by the XMC technique (was developed for the *XMM-Newton* telescope). They used the temperature and luminosity contrast method (KA09) to determine the presence of cooling cores (or dynamical activity) in a given cluster. At our request, they provided us with luminosity and temperature maps for comparison with our previous *Chandra* measurements. These luminosity/density maps are similar to their surface brightness maps. They are already exposure corrected and smoothed, so there is no need to apply additional treatment to these maps. In this study, our aim is to investigate the density and temperature morphology of KA09 clusters using morphology parameters. Our study provides additional benefits by way of checking the robustness of morphology parameters on *XMM-Newton* observed clusters, and by distinguishing relaxed and non-relaxed clusters in their density maps. The KA09 sample that we received contained 100 out of 101 clusters; RXJ1347-1145 was missing. Individual cluster analysis using the density and temperature radial profiles is beyond the scope of this work.

For this sample of clusters, we decided to use only three promising morphology parameters (Gini, M_{20} and Concentration). In calculating the morphology parameters, we followed the approach described in Chapters 2 and 3. All density and temperature maps in this sample have uniform pixel size of 10 kpc and 200 × 200 pixels. FOV of the *XMM-Newton* is sufficient to cover the 500 kpc region for each cluster. We determined the centroid of each cluster using the same technique as that described in Chapter 2, § 2.4. We calculated three morphology parameters (Gini, Concentration and M_{20}) for the 500 kpc region for both density and temperature maps. Fig. 4.34 shows parameter vs parameter planes for the density maps. In this work, we did not have clear information about the dynamical state of each cluster. We therefore plotted all clusters using the same symbol. For *Chandra* clusters, we found boundary values for Gini, Concentration and M_{20}, in order to separate relaxed and non-relaxed clusters (see Chapter 3). Using the same boundary values, we separated the KAO9 *XMM-Newton* observed clusters (Fig. 4.34). Furthermore, we separated the dynamical state of each cluster using a combination of Gini, M_{20} and Concentration parameters (Chapter 3, § 3.5), and recorded the dynamical state of each cluster (Table 4.1). As illustrated in Fig. 4.34, calculated morphology parameters for these density maps are in the same range as those calculated for density maps of *Chandra* data (§ 4.9.1). Because of the same range of (Gini, M_{20} and Concentration) morphology parameters in both the *Chandra* and it XMM-Newton sample clusters, we were able to apply the same boundary values to these parameters used in the calculation of the KA09 density maps, in order to study the dynamical state of each cluster. Of the 100 clusters available to us, we found 20 clusters to be strong relaxed (20%), 13 clusters relaxed (13%), 58 clusters non-relaxed (58%), and 9 clusters strong non-relaxed (9%). These statistics are similar those of the V09 cluster sample in which intermediate clusters are more dominant, and evolving continuously via merger. This analysis shows that these morphology parameters are equally applicable to *XMM-Newton* data and helpful in distinguishing relaxed clusters from non-relaxed clusters.

We subsequently calculated morphology parameters for the temperature maps of the KA09 cluster sample. In order to calculate this, we inverted each temperature map (see § 4.9). We applied the same area and centroid of each density map to that of its corresponding temperature map for every cluster. Fig. 4.35 shows the parameter calculations for the temperature maps of the KA09 cluster sample. From this, we observed the anti-correlation between the M_{20} and Concentration parameters. As previously indicated (§ 4.9.2), this plane is important in investigating the presence of any disturbed temperature morphology in relaxed clusters (according to their surface brightness maps). Relaxed clusters generally appear to be smooth and undisturbed in their surface brightness or density maps, but it is possible that they have (hidden) small scale substructure or strong AGN activity at the cluster core which could be responsible for disturbing the core, and this would be detected only in its temperature map. In this plane, we observed several peculiar clusters. Only one strong relaxed cluster (according to its surface brightness), RXCJ2319.6-7313 and two relaxed clusters (according to their surface brightness), RXCJ0211.4-4017 and RXCJ1236.7-3354 had high Concentration and low M_{20} values compared with other strong relaxed and relaxed clusters for their temperature maps. This suggests that only these (relaxed) clusters have undisturbed temperature morphology in their cores. The remaining strong relaxed and relaxed clusters (according to their surface brightness) were overlapped with non-relaxed and strong non-relaxed clusters indicating that their temperature morphology is disturbed in small scale to large. CLJ1226.9+3332 is a relaxed cluster (according to its surface brightness), but it has the lowest Concentration and highest M_{20} values for its temperature map compared with the all other clusters (Fig. 4.35). This indicates that, even though its surface brightness or density map appears relaxed, it has significant disturbed temperature morphology which may be caused by powerful AGN activity or small scale merger in the core of the cluster. We found that $\sim 90\%$ of clusters have low Gini value (< 0.05). This could indicate that, unlike surface brightness or density distribution, temperature distribution does not have compact bright pixels (or bright temperature spots) located at any one position in the given aperture. These temperature (bright) spots are distributed throughout the ICM in both the relaxed and non-relaxed clusters.

4.12 Discussion and Conclusion

In this work, we employed a novel technique known as the XMC to model X-ray galaxy clusters of the low-z (0.02-0.3) V09 sample. Our aim was to identify dynamically relaxed or cool core clusters from non-relaxed (disturbed) clusters, using their thermodynamic maps. We generated density, temperature, pseudo entropy and pseudo pressure maps using the XMC method. In current X-ray observation, modern X-ray data are very complex because radiating source and instrument response both vary spectrally and spatially. This makes it more difficult to analyse composite X-ray data. To facilitate this, Peterson et al. (2007) and Andersson et al. (2007) developed the XMC technique. The XMC is a highly flexible and advanced analysis system developed for analysing the *XMM-Newton* data and subsequently *Chandra* data. In this technique, X-ray clusters are modelled with a combination of the ICM plasma model, background model and instrument model of the telescope. These models have a number of local and global parameters which populate in a multi-dimensional space explored with a Markov Chain Monte Carlo sampler. Further, there are number of Gaussian "blobs" of different size, position, energy, temperature, etc., used to characterise the ICM. These blobs are propagated through the telescope and generate the X-ray events similar

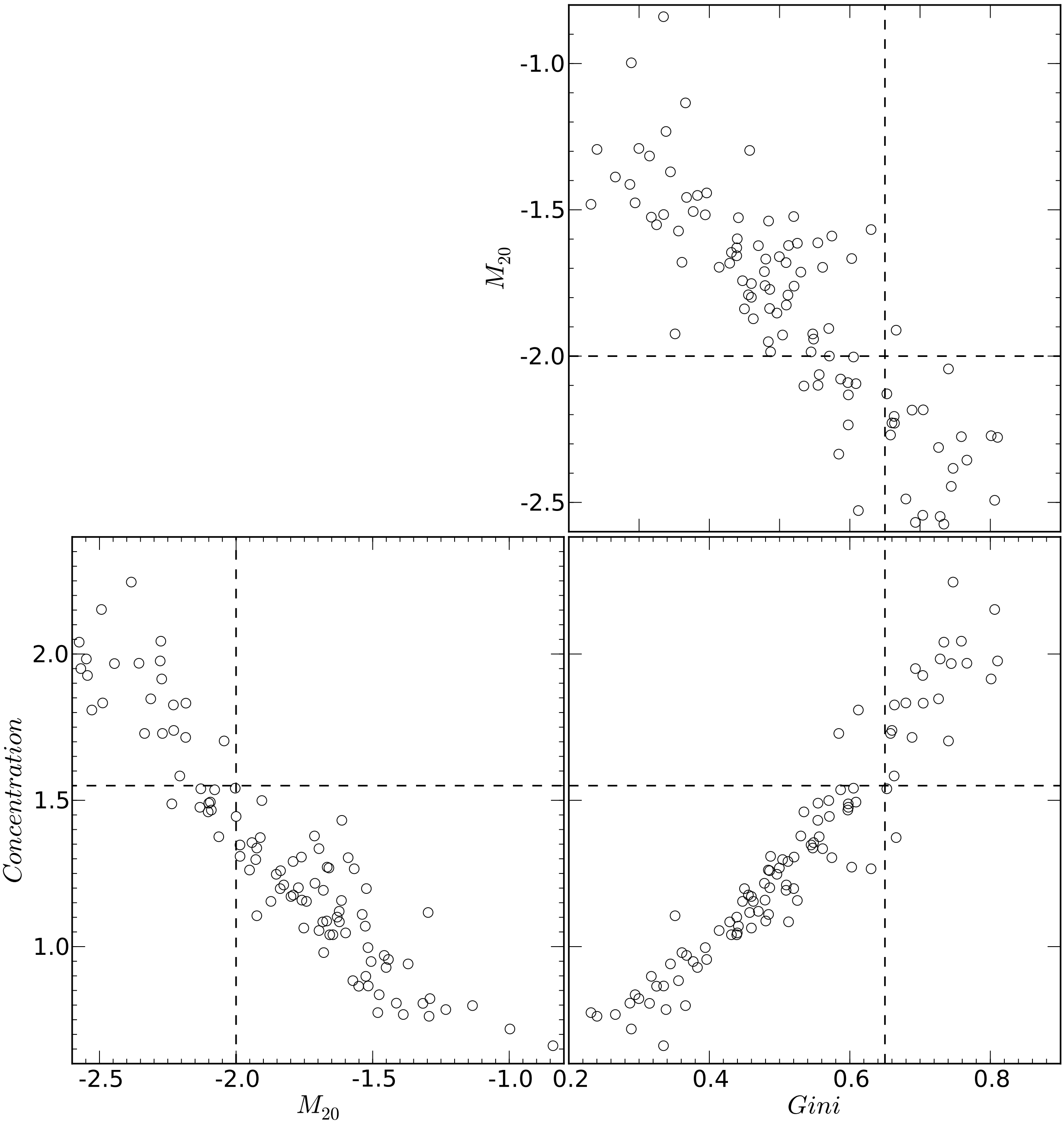

Figure 4.34: Three parameters plotted in the parameter-parameter planes to show separation between relaxed and non-relaxed clusters from the KA09 cluster sample (density maps). Here we plotted C_{5080} as the Concentration parameter. Dashed lines correspond to the boundaries between relaxed and non-relaxed clusters. Boundary values for Gini = 0.65, M_{20} = -2.0, and Concentration = 1.55. R = relaxed clusters; and N-R = non-relaxed clusters.

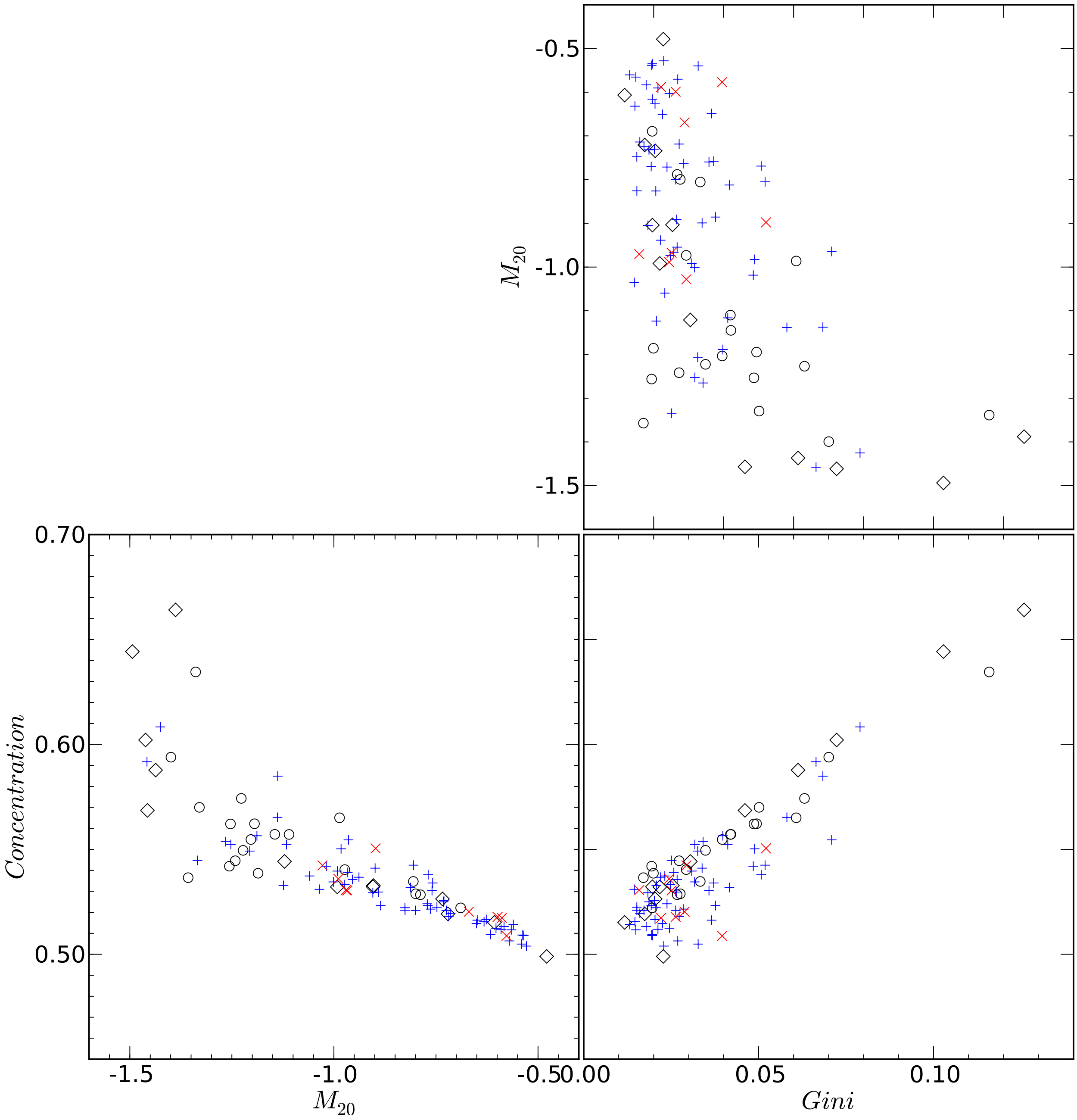

Figure 4.35: Three parameters plotted in the parameter-parameter planes of the KA09 temperature maps. Here we plotted C_{5080} as the Concentration parameter. Clusters classification is based on its density maps. ○ = strong relaxed (strong cool core) clusters; ◊ = relaxed (cool core) clusters; + = non-relaxed (weak cool core) clusters; and × = strong non-relaxed (non-cool core) clusters.

to the actual X-ray data. The XMC can simultaneously fit the spatial (position and size) and spectral (temperature, energy, flux, etc.) parameters of the X-ray emitting plasma, making it a powerful and sophisticated method to analyse complex X-ray data of modern X-ray telescope(s). With enough MCMC samples, or from the converged part of the chain, we generated 2-D median maps of density and temperature. These observable quantities were further useful in generating pseudo entropy and pseudo pressure maps of the clusters. We noted that our temperature maps are emission weighted and that they have an overlap of multi-temperature plasma. This situation is more realistic than it is when adapting in conventional method the assumption that, at any given point in the projected cluster image, it can be described as a single-temperature phase. Comparison with other analyses, however, requires the projection of a single value obtained from a distribution of either density or temperature. We used the median of that distribution (500 to 3000 iterations) in each $4'' \times 4''$ pixel in temperature (or density) maps together with its associated 1σ error. In future studies, it is possible that the XMC technique will be significant in calculating cluster mass in 3-D projection. A natural extension of the XMC, with several additional assumptions, would be to allow the determination of the 3-D distribution of density and temperature of clusters, thus determining the mass of both the ICM and dark matter substances (KA09). This is important for cosmological applications, but the present capability of the XMC is not sufficient for estimating cluster mass via 3-D modelling.

We combined the radial profiles of all low-z clusters to study the trend of thermodynamic profiles for strong relaxed, intermediate and strong non-relaxed clusters. We observed, from all thermodynamic radial profiles, a wide dispersion in the cluster core at $\sim 0.02\ R_{500}$. At radius $\sim 0.1\ R_{500}$, all profiles converged and again dispersed at $\sim 0.2\ R_{500}$, although the dispersion was not as large as that of the core. We observed two different trends of evolution between strong relaxed and strong non-relaxed clusters. Both of these profiles were overlapped with profiles of intermediate clusters (relaxed and non-relaxed). We observed shallower profiles for strong non-relaxed clusters and steeper profiles for strong relaxed clusters in both the entropy and temperature radial profiles. Sanderson et al. (2009b) noticed similar to that non-relaxed clusters have significantly higher entropy in the core for a sample of 20 galaxy clusters. They also observed the entropy profiles of relaxed clusters were tightly grouped as compared to those of non-relaxed clusters which indicates larger scatter. We found in the core a deviation in the temperature profiles $\sim$ 24%, and the entropy profiles $\sim$ 50%. There are two strong relaxed clusters, A478 and A2029, with flattened temperature profiles in the core. This could be the result of a central AGN outburst, increasing the surrounding temperature (Clarke et al., 2004; Sanderson et al., 2005). The energy input from an AGN is regularly invoked as a way of moderating cooling at the core of galaxy clusters and preventing condensation. Another two strong relaxed clusters, A2597 and A2204, show interaction between radio and X-ray plasma, and yet the entropy of all these strong relaxed clusters is low in the core. It is possible that, in these clusters, the heating is distributed via, e.g., weak shocks (Fabian et al., 2003), or kinetic energy from an outburst of AGN is $\lesssim 10^{45}$ erg/s, or that heat is dissipated uniformly in the high central electron density. In the case of non-relaxed and disturbed clusters, diverse heating processes affecting them. The observed high central entropy could be a result of a combination of heating and continuous ICM mixing due to merging may have kept these clusters on a higher adiabat. In the central region of both subsamples of strong relaxed and strong non-relaxed clusters, the dispersion in the density profiles proved to highest ($\sim$ 78%). It is apparent that the two subgroups have different electron density distribution and structure. Relaxed clusters have high electron density and pressure compared with those of non-relaxed clusters. Relaxed clusters have systematically denser, more concentrated and cuspy cores, where steady cooling flow increase the central density which is in balance with the surrounding gas pressure equilibrium, in contrast to non-relaxed clusters which are more diffuse, patchy and have non-cuspy cores with the absence of cooling flow in most cases.

In Chapters 2 and 3, we demonstrated that the morphology parameters (particular Gini, M_{20} and Concentration) are very promising for the study of the dynamical state of X-ray galaxy clusters for a large number of sample clusters. We applied these parameters to all thermodynamic maps of the low-z clusters to determine how useful thermodynamic maps are in distinguishing relaxed or cool core clusters from non-relaxed clusters. The reason for using thermodynamic maps is that, for e.g. in the case of the temperature map, we see hot regions caused by a currently-propagating or just-passed merger shock. In these shock-heated regions, gas expands rapidly adiabatically, obtaining pressure equilibrium with the surroundings environment after the passage of the shock. We also see patchy temperature structure, because of large-scale gas motions during the merger causing subsequent mixing of gases of different temperature. In order to study these thermodynamic structures and morphologies, we calculated morphology parameters for these maps.

In morphology parameter calculations for the thermodynamic maps, we found the following:

(1) Distribution of morphology parameters for the density maps is similar to distribution of parameters for the surface brightness maps. Parameters calculated for density maps had similar range and boundary values compared with those calculated for surface brightness maps. Only Gini, M_{20} and Concentration parameters are capable of separating strong relaxed clusters, intermediate (relaxed and non-relaxed) clusters, and strong non-relaxed clusters. This finding suggests the hierarchical evolution of clusters: strong non-relaxed clusters → non-relaxed or weak cool clusters → relaxed or cool core clusters → strong relaxed or evolved clusters.

(2) For calculating parameters of temperature maps, we inverted the maps to maintain the 'definition' of morphology parameters, since these parameters had originally been derived for surface brightness maps. Distribution of morphology parameters for temperature maps does not reveal the separation between strong relaxed and strong non-relaxed clusters. From the combination of M_{20} and Concentration parameters we identified several peculiar objects: A3376, A3562, A3667, A85, A4059, A754, A2256, A478, A2029, A2204, A1795 and RXJ1504. These peculiar objects could suggest that the dynamical states of these clusters differ for each of their temperature and surface brightness maps. A3376, A3562, A3667, A85, A4059, A754, and A2256 are identified as non-relaxed clusters by their surface brightness distribution, but they overlap with relaxed clusters (high Concentration and low M_{20} values) in the Concentration vs M_{20} plot for temperature maps. In all of these cases, the cluster cores seemed relatively unaffected by merger shocks. By contrast, the strong relaxed clusters, A478, A2029, A2204, A1795 and RXJ1504, have low Concentration and high M_{20} values in their temperature maps. This could indicate that there is AGN or a small scale (past) merger (not detected in their surface brightness maps) situated at the centre of the cluster, which might have disturbed the temperature morphology of the core. This is a possible cause of asymmetry in the temperature distribution, and therefore these relaxed clusters fall into the non-relaxed cluster category in the Concentration vs M_{20} plane for their temperature maps. The Gini parameter indicates that bright spots are distributed throughout the ICM in both the relaxed

and non-relaxed cluster temperature maps. None of the parameters has a significant probability of the K-S and R-S statistics to distinguish strong relaxed and strong non-relaxed clusters.

(3) 2-D entropy structure of clusters is important in investigating excess heat input/generation in the ICM from different locations of the cluster, from the edges to the core. As for temperature distribution, the cluster core has low entropy (or low pixel values), so we inverted a pseudo entropy map ($\frac{k_B T}{n_e^{0.33}}$) for each cluster to calculate morphology parameters. In our parameter distributions, the Gini, M_{20} and Concentration parameters separated the strong relaxed and strong non-relaxed clusters. This suggests that entropy morphology could be different for strong relaxed and strong non-relaxed clusters. This also means that cluster entropy morphology might indicate the dynamical state of the cluster. Furthermore, the Gini, M_{20} and Concentration parameters are useful in tracing the central entropy region of different dynamical states of a cluster. These parameters suggest that relaxed clusters have high Concentration and 'valley' entropy emission in the core of the cluster, while there in no entropy 'peak' (anywhere) in the non-relaxed cluster. This could indicate that non-relaxed clusters are heated equally by merger shock or a gravitational process. We observed four peculiar relaxed clusters - A1795, A2204, A2029 and A478 - on the M_{20} vs Concentration plot for the entropy maps. These are strong relaxed clusters (based on their surface brightness), which overlap with intermediate clusters (low concentration and high M_{20}) in entropy maps. This is a possible indication that these strong relaxed clusters have either AGN activity or small substructure at the cluster core which could increase the entropy of the surrounding medium. The M_{20}, Concentration and Gini of the second order moment parameters have significant probabilities of the K-S and R-S tests compared with other parameters, and hence we were able to separate strong relaxed from strong non-relaxed clusters (defined by surface brightness maps) using these two parameters in the entropy maps.

(4) In the case of pseudo pressure maps ($k_B T \times n_e^{0.5}$), Gini, M_{20} and Concentration parameters can separate strong relaxed and strong non-relaxed clusters (according to cluster surface brightness morphology). On the M_{20} vs Concentration plot of pressure maps, however, we found two peculiar clusters - A2597 and 2A-0335. These two are strong relaxed clusters (according to their surface brightness) which overlap with intermediate clusters. This could indicate that they have disturbed pressure morphology in the core caused by an active radio galaxy or by cold front activity (McNamara et al., 2001; Mazzotta et al., 2003). The M_{20} and Concentration have significant probabilities of the K-S and R-S tests compared with other parameters.

We compared derived best-fit power-law slope values of temperature, density, entropy and pressure radial profiles of low-z clusters with corresponding surface brightness morphology parameters. We observed that slope of density, entropy and pressure are related to (surface brightness) cluster morphology. We noted that the pure power-law model did not fit well to the mean radial profiles compared with the power-law with constant base. The pure power-law slope suggested only the gradient of the radial profiles. For relaxed clusters, the temperature and entropy profiles are steep in the core, and the density and pressure profiles are high, monotonically decreasing outside of the core. By contrast, for non-relaxed clusters, the temperature and entropy profiles are flatter in the core, while the density and pressure profiles are constant in the core, decreasing monotonically outside of the core. We observed that (surface brightness) cluster morphology and best-fit pure power-law slopes for density, entropy and pressure are related, indicating a possibility that the strength of the cool core diminishes in more disturbed clusters and that, subsequently, the cool core is erased by the cluster merger (Sanderson et al., 2009a). The high Concentration, high Gini and low M_{20} parameter values indicate that the dense cool core has high electron density and a steep profile in the central region, resulting in higher slope values for relaxed clusters (in contrast to non-relaxed clusters which have flatter profiles in the core and lower slope values). We found it easier to evaluate gradient of density or of entropy simply from cluster surface brightness morphology, making it possible to evaluate gradients for high redshift clusters in a large volume survey. Another conclusion is that entropy and pressure distributions are more closely related to the electron density distribution than they are to the temperature in the cluster core.

We conducted a further study to identify cluster merger or the presence of substructure in the 2-D thermodynamic maps of a galaxy cluster. We studied projected radial profiles of seven strong relaxed and six strong non-relaxed clusters. We provided a details of a 2-D diagnostics and complementary process (of the identifying substructure) - the radial studies of fluctuation and discontinuity in the 1-D radial profiles of density, temperature, entropy and pressure maps of clusters. We observed more fluctuation and discontinuity in the radial profiles of strong non-relaxed clusters, while the profiles for strong relaxed clusters were smoother and regular. We concluded that the radial profile, particularly of the temperature map, was highly sensitive in identifying the substructure. This was in accordance with the results of Zhang et al. (2009). It is possible that a (strong) relaxed cluster has minor scale merging activity, which would be unnoticed in the ICM density and surface brightness maps, but could be detected in the corresponding temperature map. In our analysis, A2204, for e.g., is identified as a strong relaxed cluster by the surface brightness morphology parameters, although its temperature profile shows discontinuity in the core region, possibly due to minimal substructure in the core, or that it had been heated by an unusually strong AGN outburst ($\sim 10^{46}$ erg/s) (Donahue et al., 2006a). We observed a mismatch, in a few cases, between cluster dynamical states according to (1) surface brightness morphology parameters and (2) thermodynamic radial profiles. Different merging events can result in substantial mixing of low and high entropy gas in the ICM, and hot locations visible in temperature maps could be the result of merger shocks, information about which is not obtained from cluster surface brightness maps. This re-distribution of entropy and temperature depends on the scale of the merger: whether the merger has disrupted the structure of the cool core, and time scale for re-establishment of the cool core has been disrupted. We noted that, although the morphological information about the cluster (based on surface brightness) suggested a weaker merger, their temperature and entropy profiles displayed stronger merging activity. This, however, would not rule out entropy or temperature modification due to an ancient merger, particularly if the relaxation time were shorter than the cooling time. In order to evaluate the radial profiles, we used the power-law models (pure power-law model and power-law model with constant base). We found that the pure power-law model was not applicable to radial profiles, particularly for non-relaxed clusters, and we used it only to study the gradient of radial profiles. The power-law model with constant base, on the other hand, fitted well for all the profiles, although, in the case of the density profiles of the strong relaxed clusters, it fitted well only in the core region ($< 0.1\ R_{500}$).

We studied the dynamical state of the *XMM-Newton* observed galaxy clusters of the KA09 sample. Unlike the case of the V09, we did not have prior information about the dynamical state of this sample of clusters. In Chapter 3, we estimated the boundary values of the Gini, M_{20} and Concentration parameters (between relaxed and non-relaxed clusters) for the V09 cluster sample.

Using these boundary values and the combination of these three parameters, we identified the dynamical state of the KA09 clusters. We found that, of the total of 100 clusters in the KA09 sample, 20 were strong relaxed (20%), 13 were relaxed (13%), 58 were non-relaxed (58%) and 9 were strong non-relaxed (9%). These statistics are similar those of the V09 cluster sample in which intermediate clusters are more dominant and could be evolving continuously via cluster merger. Another conclusion was that morphology parameters were eminently applicable to the *XMM-Newton* observed galaxy clusters in identifying their dynamical state. We also studied the morphology of temperature maps for this sample of clusters and, via these temperature maps, investigated disturbed clusters. We found that $\sim$ 95% and $\sim$ 85% of strong relaxed and relaxed clusters (according to their density/surface brightness maps), respectively, have (smaller or larger) disturbed temperature morphology in the cores. The possible causes are either past (minor) merging activity, small scale substructure, or AGN outbursts. The Concentration and M_{20} parameters were particularly useful in the study of these disturbed clusters (via their temperature maps), which would have remained unnoticed in their density/surface brightness maps.

5

Radio halo cluster morphology

5.1 Motivation

Giant *radio halos* and *relics* are large ($\sim$ Mpc size) diffuse synchrotron sources observed in a massive and merging galaxy clusters. *Radio halo* is a very complex subject and a rare phenomenon in the Universe. We have given brief introduction of these sources in Chapter 1. Previously it has been shown that X-ray data are crucial in the study of non-thermal radio emission from galaxy clusters. This emission is in the form of a cluster wide *radio halo* generally situated at the centre, and *radio relic(s)* found at the periphery (Feretti et al. 2012, and reference therein). Theoretical framework suggests that, *relic* sources are generally tracers of shock waves in merger events. The morphology of *relic* sources - elongated structure, almost perpendicular to the merger axis, and the observational evidences (Bagchi et al., 2002; Solovyeva et al., 2008; Barrena et al., 2009; Finoguenov et al., 2010) indicate the same that a shock is present in the cluster peripheral region, and it is very likely responsible for the electron re-acceleration and the magnetic field amplification that will give cause the cluster *relics*. Hence, formation of *relics* is not a difficult puzzle as formation of *radio halos* in the ICM of galaxy cluster. Furthermore, it is hard to compare X-ray and radio data of large *relics*, because most *radio relics* are situated at the cluster periphery, and sometime observed at outside, or at the edge, of available X-ray images. Therefore, in this analysis, we focused only on *radio halo* galaxy cluster and connection with its X-ray morphology.

A number of authors have shown the correlation between synchrotron monochromatic radio luminosity of a *radio halo* ($P_{1.4GHz}$) vs the host cluster X-ray luminosity (L_X), and mass vs temperature (Liang et al., 2000; Feretti, 2003; Cassano et al., 2006, 2007; Giovannini et al., 2009; Brunetti et al., 2009; Venturi, 2011; Cassano et al., 2011). These correlations suggest that the most powerful *radio halos* are found in the biggest and hottest clusters with the greatest X-ray luminosity. Furthermore, these correlations show a close link between non-thermal and thermal galaxy cluster physics. Govoni et al. (2001) showed the point-to-point correlation between X-ray and radio surface brightness for six *radio halo* clusters. This suggests a correlation between *radio halo* and X-ray emission in galaxy clusters. Buote (2001), Schuecker et al. (2001), Cassano et al. (2010b) showed a relationship between non-thermal radio sources and X-ray cluster morphology. This indicates a connection between the cluster dynamical state and the occurrence of a *radio halo*.

Buote (2001) first showed a correlation between the power-ratio (P_1/P_0) calculated for *ROSAT* observed ($\sim$ 14) X-ray clusters and $P_{1.4GHz}$ measured for radio data. The power-ratios measure both the multi-pole expansion of a 2-D structure and dynamical state of a cluster (Buote & Tsai, 1995a, 1996). Buote concluded that approximately $P_{1.4GHz} \propto P_1/P_0$, which means the clusters that host the most powerful *radio halos* are undergoing the greatest exodus from a virialized state. Recently, Cassano et al. (2010b) used three parameters, namely centroid shift (Mohr et al., 1993; Poole et al., 2006; Maughan et al., 2008; Böhringer et al., 2010), third order power ratio (P_3/P_0) (Weißmann et al., 2012) and Concentration (Santos et al., 2008) to demonstrate a relationship between cluster mergers and the presence of a *radio halo*. The analysis of Cassano et al. (2010b) supports the relationship between cluster dynamical activity (or dynamical state) and cluster-wide diffuse sources. This relationship, in turn, supports the secondary particle (re-)acceleration mechanism in the formation of *radio halos* in galaxy clusters. The current scenario indicates that diffuse radio features (*radio halos*) are seen only in merging clusters. There are a number of studies that point out the close relationship between X-ray observation of galaxy clusters and diffuse radio source properties. These have encouraged us to investigate the correlation between X-ray cluster morphology and corresponding *radio halo* properties. Since we show in this study that morphology parameters are useful to characterise the dynamical state of galaxy clusters, we now investigate any possible correlation between our set of morphology parameters and the presence of diffuse intracluster radio emission in galaxy clusters.

5.2 *Radio halo* cluster sample

Our study includes a total of 25 *radio halo* ($z < 0.4$) X-ray clusters (Table 5.1). Of these, we took *radio halo* clusters from Giovannini et al. (2009) (depending on availability of *Chandra* archival data), of which some are already present in the V09 cluster sample (A754, A2256, A401, A3562, A399, and A2163). We reduced the X-ray data of the sample of Giovannini et al. (2009) in a similar way to that described in Chapter 3. At the time this study commenced, Giovannini et al. (2009) had provided the latest information about *radio halos* and corresponding radio properties.

In our search for radio halo clusters, we took another sample, the KA09, which included 100 *XMM-Newton* observed clusters. All of these clusters were analysed with the XMC technique, from which a Luminosity map (closely related to electron density) of each cluster was generated (see Chapter 4 for further details).

5.3 *Radio halo* cluster dynamical states

To investigate the dynamical state of *radio halo* clusters, we applied morphology parameters to them. We already have shown that these parameters are quite useful to separate relaxed and non-relaxed clusters based on their surface brightness distribution, so we calculated parameter values for *radio halo* clusters and classified them according to their dynamical state. In Fig. 5.1 we plotted three morphology parameters (Gini, M_{20} and Concentration) and temperature. In this plot we compared the *radio halo* sample with only the relaxed and non-relaxed clusters (excluding *radio halo* clusters) of the V09 sample. Fig. 5.1 shows that Gini, M_{20} and Concentration parameters

Table 5.1: *Radio halo* sample clusters. (1) cluster name; (2) redshift; (3) conversion factor (angular size to linear size); (4) radio flux density (1.4 GHz); (5) error in estimated radio flux density; (6) total radio power (1.4 GHz); (7) radio largest linear size; (8) total X-ray luminosity (0.1–2.4 keV); (9) Temperature (keV); (9) Exposure time; (10) References.

Name	z	kpc/$''$	S (1.4) mJy	ΔS mJy	log P(1.4) W/Hz	LLS Mpc	Luminosity (10 ^{44} erg/s)	Temperature (keV)	Exposure time ks	Ref.
A1914	0.1712	2.88	64.0	3.0	24.71	1.04	10.42	10.50	19	1,2
A2218	0.1756	2.94	4.7	0.1	23.60	0.38	5.77	6.70	59	1,2
A665	0.1819	3.03	43.1	2.2	24.59	1.82	9.65	8.30	39	1,2
A520	0.1990	3.25	34.4	1.5	24.58	1.11	8.30	7.40	9	1,2
A773	0.2170	3.48	12.7	1.3	24.23	1.25	7.95	8.53	20	1,2
IE0657-56	0.2960	4.38	78.0	5.0	25.33	2.1	22.59	11.64	84	1,2
A2255	0.0806	1.50	56.0	3.0	23.94	0.90	2.64	6.42	39	1,2
A2319	0.0557	1.07	153.0	8.0	24.04	1.02	8.46	9.49	14	1,2
A754	0.0542	1.04	86.0	4.0	23.77	0.99	2.21	9.94	44	1,2
A2256	0.0581	1.11	103.4	1.1	23.91	0.81	3.75	6.90	12	1,2
A401	0.0737	1.38	17.0	1.0	23.34	0.52	6.52	8.07	18	1,2
A3562	0.0490	0.95	20.0	2.0	23.04	0.28	1.57	3.80	19	1,2
A399	0.0718	1.35	16.0	0	23.30	0.57	3.80	5.80	48	3,2
A2163	0.2030	3.31	155.0	2.0	25.26	2.28	22.73	12.12	71	1,2
A1300	0.3072	4.49	20.0	2.0	24.78	1.3	13.73	9.2	14	1,4
A1758	0.2790	4.20	16.7	0.8	24.60	1.51	7.09	7.95	7	1,2
A1995	0.3186	4.61	4.1	0.7	24.13	0.83	8.83	8.60	56	1,2
A2034	0.1130	2.03	13.6	1.0	23.64	0.61	3.81	7.15	195	1,2
A209	0.2060	3.34	16.9	1.0	24.31	1.40	6.17	8.28	20	1,2
A2219	0.2256	3.58	81.0	4.0	25.08	1.72	12.19	9.81	42	1,2
A2294	0.1780	2.98	5.8	0.5	23.71	0.54	3.90	7.10	10	1,2
A2744	0.3080	4.50	57.1	2.9	25.24	1.89	12.86	9.61	24	1,2
A521	0.2533	3.91	5.9	0.5	24.05	1.17	8.47	6.74	37	1,2
A697	0.2820	4.23	7.8	1.0	24.28	0.65	10.40	9.06	27	1,2
RXCJ2003.5-2323	0.3171	4.59	35.0	2.0	25.09	1.40	9.12	9.1	50	1,5

References: 1 = (Giovannini et al., 2009, and references therein); 2 = Cavagnolo et al. (2009); 3 = (Feretti et al., 2012, and references therein); 4 = Ziparo et al. (2012); 5 = Giacintucci et al. (2009).

are extremely useful for studying the dynamical state of *radio halo* clusters. In the bottom left and right plots, we see that the *radio halo* clusters are separated from the relaxed clusters, and overlap with non-relaxed clusters in M_{20} and Gini vs Concentration parameter planes, respectively. Similar results were observed by Buote (2001) and by Cassano et al. (2010b). In our plots, we roughly separated relaxed from non-relaxed clusters based on the M_{20} and Concentration parameters, where the region contained by M_{20} < -2.0 and Concentration > 1.55 gives relaxed clusters exclusively. Based on the Gini and Concentration plot, all non-relaxed clusters have Gini < 0.65 and Concentration < 1.55. The upper left and right plots in Fig. 5.1 show M_{20} vs temperature and Gini vs temperature, respectively. We subdivided the M_{20} vs temperature plot into three regions: (1) the M_{20} < -2.0 region which has all dynamically relaxed clusters, (2) the M_{20} > -2.0 and temperature < 6 keV region which has *radio quiet* merger clusters, and (3) the M_{20} > -2.0 and temperature > 6 keV region which has *radio loud* merger clusters. Similarly, the Gini vs temperature plot has three regions defined as (1) the Gini > 0.65 region which has dynamically relaxed clusters only, (2) the Gini < 0.65 and temperature < 6 keV region which has *radio quiet* merger clusters, and (3) the Gini < 0.65 and temperature > 6 keV region which has *radio loud* merger clusters (*radio halo* clusters). Based on this, our findings support current thinking that *radio halos* are found only in the hottest, most massive, and merging galaxy clusters. It is also possible that the limited sensitivity in current observations could be the cause of non-detection of these sources in low massive, but significantly disturbed clusters.

Similarly, we applied morphology parameters to the KA09 sample (in which, of the 100, 58 clusters are non-relaxed (58%) and 9 clusters are strong non-relaxed (9%)). In Fig. 5.2 we plotted three parameters (Gini, M_{20} and Concentration) and temperature for the KA09 cluster sample. Fig. 5.2 shows the separation of relaxed, non-relaxed and halo clusters of the KA09 sample with the same boundary as that given in Fig. 5.1 for Gini, M_{20}, Concentration and temperature. From this separation we found a total of 53 *radio halo* clusters which fall into region 3 of Fig. 5.2, considered to be a *radio halo* region, as stated above. We listed these halo clusters in Table 5.2 together with previous *radio halo* detection information.

There are many KA09 clusters in which *radio halos* have been detected. There are two *mini radio halos* - A2142 and A2390 - which fall into region 3. A2142 is a non-relaxed cluster and A2390 is a relaxed cluster (according to combination of morphology parameter), but both show complex structure around the cluster centre and their average temperature is high (8.15 and 8.68 keV, respectively). Based on the *ROSAT* observation of A2142, Henry & Briel (1996) showed that the A2142 is at a late stage of merger, beginning the process of relaxation. Subsequently, Markevitch et al. (2000) discovered a double cold front in the central region of the A2142, and showed that the central cooling flow had been disturbed but not destroyed by a (past) merger. In the case of the A2390, the diffuse *mini radio halo* is situated at the cluster centre, and is smaller than $2'$ in size (Bacchi et al., 2003). *Chandra* observation of the A2390 (Allen et al., 2001) shows the presence of a cooling flow in the core of the cluster, and exhibits some sub-structure on a large scale ($\gtrsim 2'$), which indicates that the cluster has not completely relaxed because of the most recent merger activity. Hence both clusters show significant sub-structure around the core, and it might be suggested that these two *mini radio halos* are associated with some minor merger activity (Feretti et al., 2012) in their parent clusters. We assume that the remaining clusters in Table 5.2 could also host *radio halos*. Some of these *radio halos* may have steep spectra and cut-off at frequency $\nu > \nu_c$, with ν_c determined by the efficiency of the acceleration process. This cut-off causes a bias in their detection, as these *radio halos* can be detected only in low frequency radio observations (Cassano et al., 2006; Brunetti et al., 2008) and hence may be missed by present radio surveys at $\sim$ GHz. These *radio halos* could be connected with less energetic cluster merging events, since many of them have a weak dynamical (non-relaxed) state identified by morphology parameters, and require high sensitive radio telescopes such as LOFAR (LOw Frequency ARray) and SKA (Square Kilometre Array).

Table 5.2: *Radio halo* (possible) candidate from the KA09 sample.

Radio halo clusters	Previously detected?	*Radio halo* clusters	Previously detected?
A399	Y	A267	N
A401	Y	A2390	Y (mini radio halo)
A2255	Y	RXCJ0307.0-2840	N
A1651	N	RXCJ2337.6+0016	N
A2142	Y (mini radio halo)	RXCJ0303.8-7752	N
A3827	N	A1758	Y
RXCJ0645.4-5413	N	RXCJ0232.2-4420	N
A1302	N	RXCJ0043.4-2037	N
RXCJ0020.7-2542	N	RXCJ0516.7-5430	N
RXCJ0145.0-5300	N	RXJ0658-55	N
A1413	N	RXCJ2308.3-0211	N
A3888	N	RXCJ1131.9-1955	Y
A2034	Y	RXCJ0014.3-3022	Y
RXCJ2234.5-3744	N	RXJ0256.5+0006	N
A2104	N	RXJ0318.2-0301	N
RXCJ0547.6-3152	N	RXJ0426.1+1655	N
A2218	Y	RXJ1241.5+3250	N
A1914	Y	A851	Y
A665	Y	RXCJ2228+2037	N
A1689	Y	CL0016+16	Y
A520	Y	MS0451.6-0305	N
A2163	Y	RXJ1120.1+4318	N
A209	Y	MS1137.5+6625	N
A963	N	MS1054.4-0321	N
A773	Y	WARPJ0152.7-1357	N
A1763	N	CLJ1226.9+3332	N
A2261	N		

5.4 Morphology parameters and *radio halo* properties

Giovannini et al. (2009) listed a number of *radio halo* properties that we compared with our measured X-ray surface brightness morphology parameters (Fig. 5.3), to search for any correlation between *radio halo* X-ray morphology and radio properties. As seen in Fig. 5.3, there is no strong correlation visible between parameters and radio properties such as radio output power, $P_{1.4GHz}$, and the largest linear size (LLS in Mpc) of the diffuse source of the cluster. We also listed the Spearman correlation rank, σ, and corresponding probability, p in Table 5.3 and Table 5.4, respectively. There is weak anti-correlation (Gini and Concentration) and correlation (M_{20}) visible

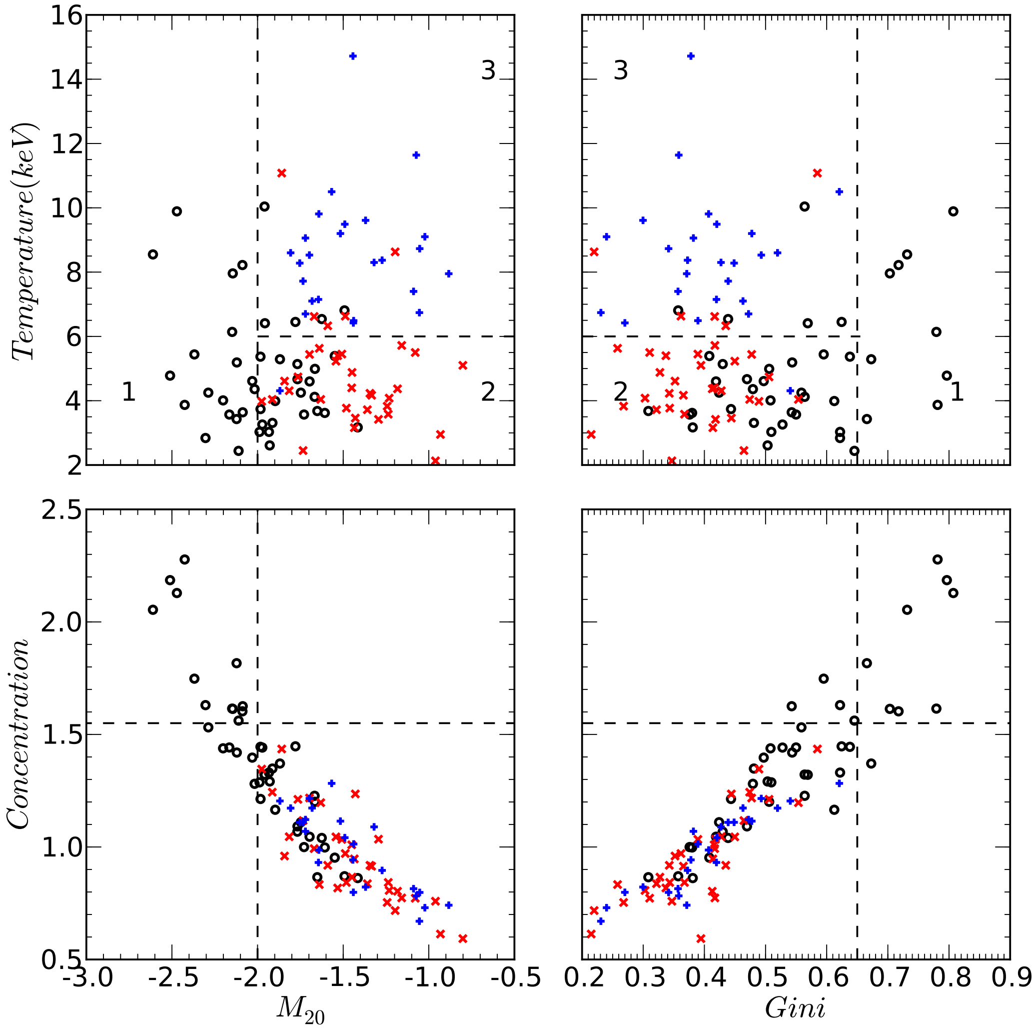

Figure 5.1: Bottom left and right plots show the M_{20} and Gini vs Concentration, respectively. Top left and right plots show the M_{20} and Gini vs temperature, respectively. ○ = **relaxed cluster; and** × = **non-relaxed cluster**. *Radio halo* clusters are identified with a "+" symbol. Galaxy cluster separation is based on the V09.

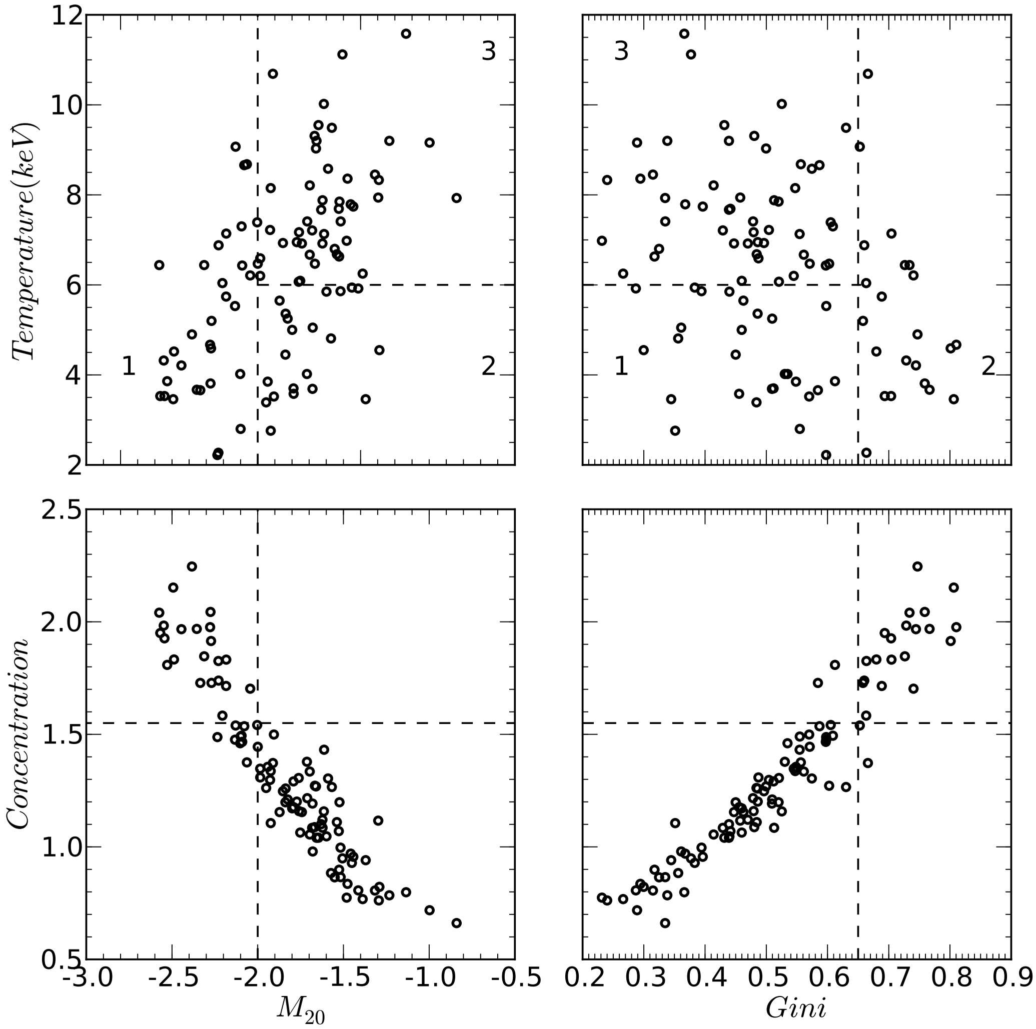

Figure 5.2: Plot showing possible candidates of *radio halos* in a cluster sample from the KA09. Clusters falling into region 3 may host *radio halos*; it is known that some, in fact, do. Bottom left and right plots show the M_{20} and Gini vs Concentration, respectively. Top left and right plots show the M_{20} and Gini vs temperature, respectively.

between parameters and LLS. This could suggests that low Gini or Concentration means a more disturbed X-ray cluster and hence the large linear size of the corresponding *radio halo*. Low surface brightness or faint observation of *radio halo* and less sensitive radio data make it more difficult to establish proper links between cluster morphology and radio properties.

As mentioned before, Buote (2001) found a correlation between the power-ratio and $P_{1.4GHz}$, but only for 14 clusters whereas we have a larger number of clusters in our sample. It is possible that some of the *radio halo* clusters in our sample, have less sensitive and shorter radio observations, resulting in poorer quality of image and which are not sufficient to measure $P_{1.4GHz}$ or LLS. This could be the reason for no correlation existing between morphology parameters and radio properties. This need to be investigate further with high quality radio images.

Table 5.3: Spearman rank correlation, ρ, between three parameters and *radio halo* properties.

Morphology parameters	Log $P_{1.4GHz}$(W/Hz)	LLS(Mpc)
Gini	-0.27	-0.36
Concentration	-0.38	-0.45
M_{20}	0.39	0.50

Table 5.4: Spearman test probability, p, between three parameters and *radio halo* properties.

Morphology parameters	Log $P_{1.4GHz}$(W/Hz)	LLS(Mpc)
Gini	0.19	0.08
Concentration	0.06	0.02
M_{20}	0.06	0.01

5.5 *Radio halo* thermodynamic maps

In Chapter 4, we showed that the complex ICM temperature (and thermodynamic) structure is a strong indication of cluster mergers. X-ray surface brightness distribution also shows substructure in the X-ray images that we can trace with morphology parameters, as mentioned in Chapters 2 and 3. All these dynamical properties of merger clusters are common to *radio halo* clusters. In contrast, thus far we have not detected extended *radio halos* in relaxed and regular clusters. Therefore, the available data indicate that *radio halos* are related to cluster mergers. Govoni et al. (2004) and Giacintucci et al. (2005) have shown the spatial relationship between *radio halos* and corresponding 2-D ICM temperature distribution. Thermodynamic maps of these clusters also suggest that the cluster is far from being in hydrostatic equilibrium, having experienced a massive merger event. Markevitch & Vikhlinin (2001); Markevitch et al. (2002, 2003c) have shown that hot regions in the cluster temperature maps could be associated with a recently propagating or just-passed merger shock. After the shock passage, there is a quick adiabatical expansion of shock-heated gas regions which develop pressure equilibrium with the surrounding gas. Magnetic field plays a major role in constraining the accelerated relativistic electrons from diffusing (as a result of merger shock) far from their origin at the centre of the cluster. It is believed that relativistic electrons follow the bulk motion of their host gas. Consequently, if merger shock is indeed responsible for the acceleration of relativistic electrons and a uniform magnetic field is taken into consideration, we can expect

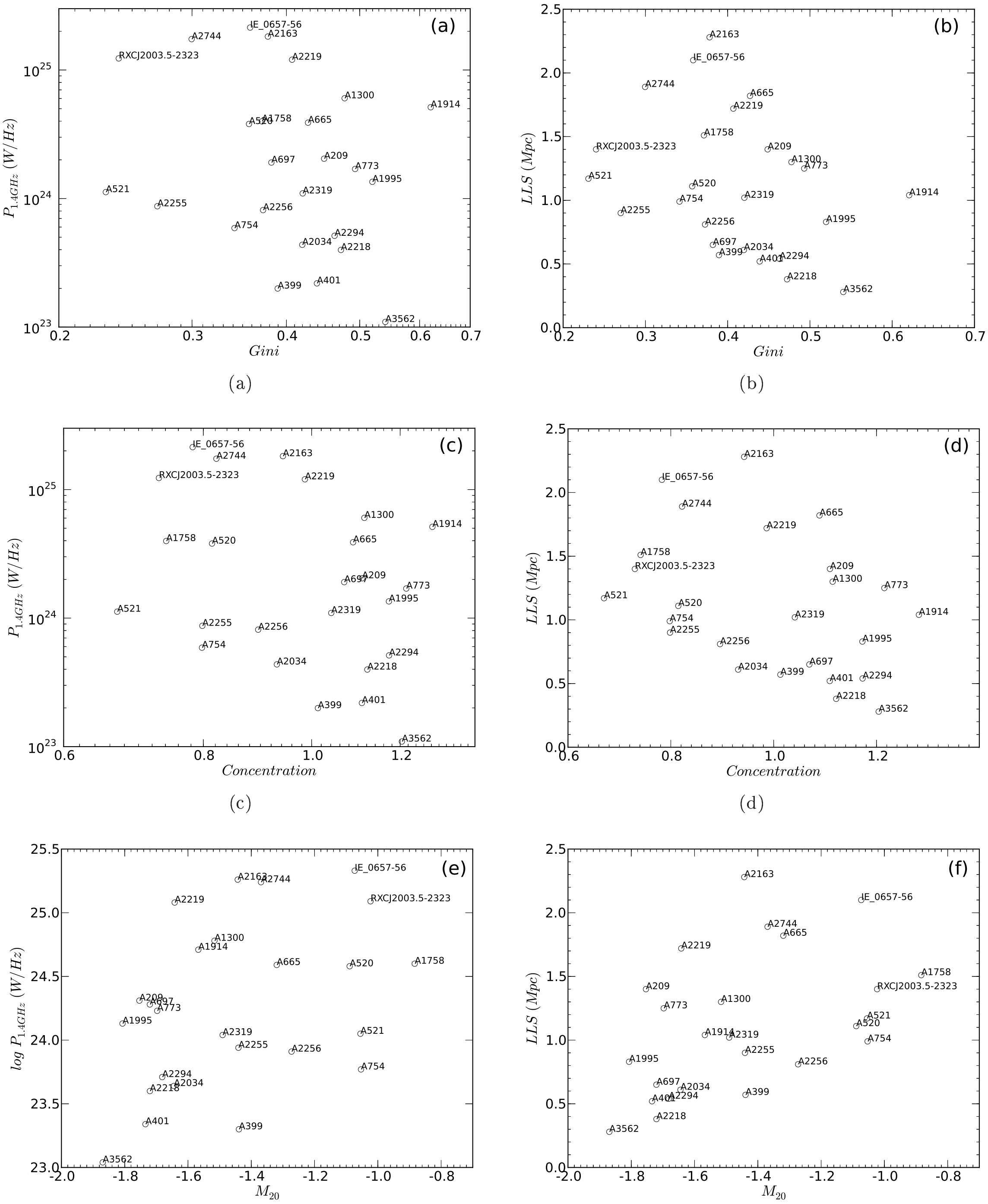

(a) (b)

(c) (d)

(e) (f)

Figure 5.3: Comparison of *radio halo* properties with X-ray cluster morphology parameters.

Table 5.5: Best-fitting values of the power-law model (constant base) derived for mean radial profiles of *radio halo* clusters. α = slope of profiles, T = temperature (keV), n_e = electron density (cm^{-5}), K = entropy (keV*cm^2), and P = pressure (dyne/cm^2). F = T, n_e, K and P for each mean profile of T, n_e, K and P, respectively. $F_0 = T_0$, n_{e0}, K_0 and P_0 for each mean profile of T, n_e, K and P, respectively.

Thermodynamic profiles	α	F	F_0
mean T	2.21 ± 0.09	6.21 ± 0.76	0.92 ± 0.00
mean n_e	0.77 ± 0.11	-5.49 ± 0.60	2.22 ± 0.13
mean K	2.08 ± 0.03	16.77 ± 0.63	0.71 ± 0.00
mean P	0.89 ± 0.09	-2.29 ± 0.21	1.40 ± 0.03

a strong spatial correlation between the distribution of the *radio halo* surface brightness and the hottest gas regions (Govoni et al., 2004).

In Chapter 4 we studied projected radial profiles of thermodynamic maps of the V09 low-z clusters. All thermodynamic maps are derived using the XMC technique (see Chapter 4). There are six non-relaxed clusters (A2256, A754, A3562, A399, A401 and A2163) in the low-z V09 sample, host *radio halo*. We plotted temperature, electron density, entropy and pressure radial profiles of *radio halo* clusters along with strong non-relaxed (A2147, A3266, A1736 and A3395) and strong relaxed clusters (A0335, A478, A1795, A2597, RXJ1504, A2204 and A2029) in Fig. 5.4 and the corresponding mean profiles in Fig. 5.5. In Fig. 5.4 we see all *radio halo* cluster profiles as a function of radius overlap with strong non-relaxed clusters for temperature, entropy, density and pressure. Mean radial profiles of *radio halo* clusters are flat in the core and lie close to the merger clusters. There is probably no difference in thermodynamic radial profiles of *radio halos* and non-relaxed clusters. This could suggests that thermodynamical properties of *radio halos* clusters are similar to those of merger clusters and *radio halos* are commonly associated with non-relaxed clusters. This means that merger shocks have heated the ICM and may increase the entropy, as well as possibly providing the energy to generate the non-thermal components in clusters through the acceleration of high-energy relativistic particles (Sarazin, 2002, 2009; Brunetti et al., 2009). As given in Chapter 4, we fitted two power-law models to all mean thermodynamic profiles. We used the power-law model with constant base simply to illustrate fitting. In Table 5.5 and Table 5.6, we list best-fit values of power-law models. As seen in Table 5.6, pure power-law model gives better indication about the gradient of profiles. Mean temperature profile of *radio halo* clusters is flat as compare to the mean entropy profile in the core of the clusters.

In Figs. 5.6 and 5.7 we showed unscaled thermodynamic radial profiles of all 25 *radio halo* clusters and corresponding mean profiles, respectively. For each *radio halo* cluster, temperature and entropy show shallower profiles in the core region, $\lesssim$ 100 kpc, where we expect most relativistic particle turbulence (due to passage of merger shock) and brightest radio luminosity. Density and pressure profiles are flat in the cluster core region, and there is no cusp visible as characteristic of relaxed clusters. There is a large scattering of thermodynamic profiles in the cluster core region which might indicate different levels of turbulence in different *radio halo* clusters. These profiles suggest that the characteristics of *radio halo* profiles are similar to those of cluster merger profiles. We list best-fit values of power-law models in Table 5.7 and Table 5.8.

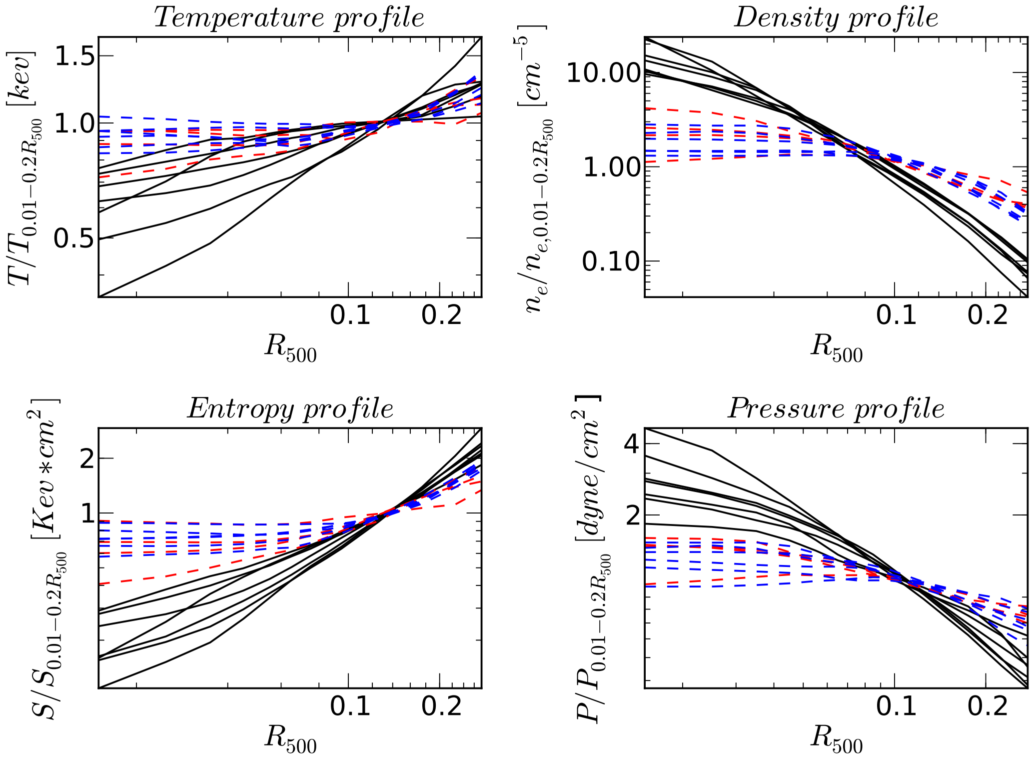

Figure 5.4: Thermodynamic profiles of *radio halo* clusters compared with strong relaxed and strong non-relaxed clusters of the V09 low-z clusters. The black solid line represents strong relaxed clusters; the red dashed line represents strong non-relaxed clusters; and the blue dashed line represents *radio halo* clusters.

5.6 Discussion and Conclusion

Current observations (Bagchi et al., 2006; van Weeren et al., 2009b,a; Giovannini et al., 2010; van Weeren et al., 2011) indicate that most massive and luminous galaxy clusters which show dynamical activity and merging processes can host diffuse radio sources in the form of *radio halos*. This demonstrates the presence of relativistic particles and magnetic fields in the ICM. Radio-X-ray correlation indicates that recent merger processes could provide energy for the relativistic electron re-acceleration and magnetic field amplification (Roettiger et al., 1999; Ricker & Sarazin, 2001; Dolag et al., 2005), allowing the production of faint but detectable synchrotron radio emission. Further, X-ray images of *radio halo* clusters show the presence of substructures and distortions in the brightness distribution, which suggests that a *radio halo* could be the result of subclump interactions (Schuecker et al., 2001; Buote, 2001). *Radio halo* clusters do not have the strong cooling flow typical of a relaxed cluster. It is believed that, where a strong merger process disrupts a cooling flow (Peres et al., 1998), this would indicate the connection between irregular and *radio halo* clusters. It is however, still debatable whether all merging clusters have cluster-wide *radio halos*, and what other phenomena could be behind the formation of *radio halos*.

In investigating the correlation between X-ray cluster dynamical states or morphology and cluster wide diffuse *radio halos*, we took 25 *radio halo* clusters, which are well-known non-relaxed clusters with host *radio halos*. Our morphology parameters are quite useful in the study of cluster

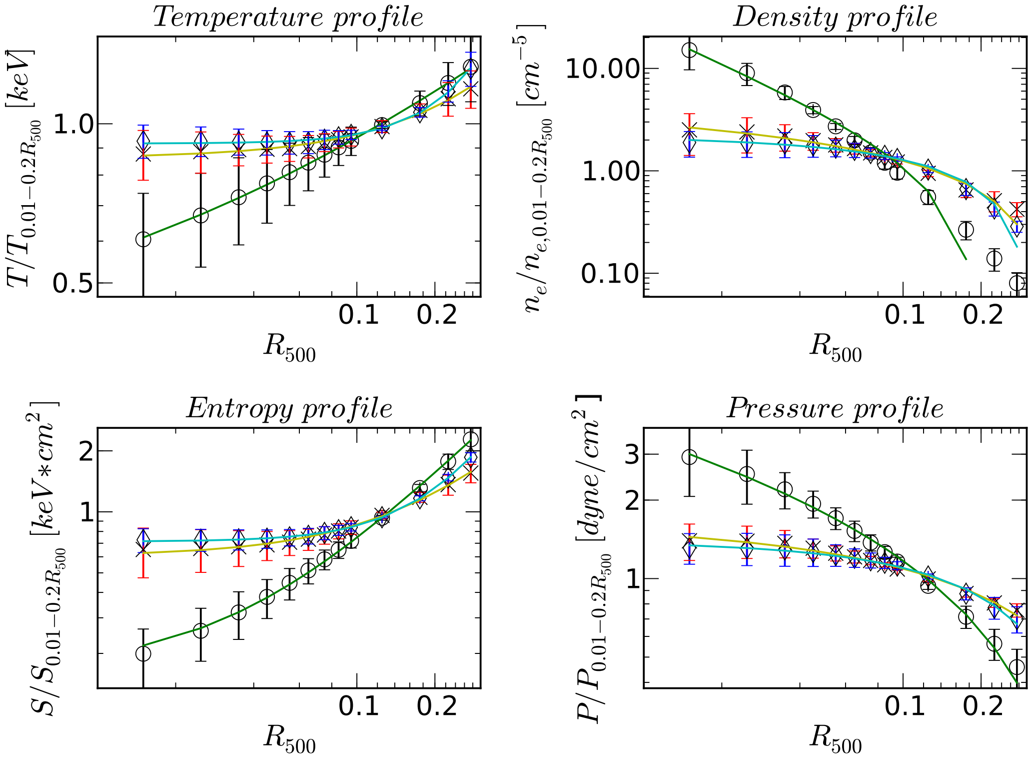

Figure 5.5: Thermodynamic mean profiles of *radio halo* clusters compared with strong relaxed and strong non-relaxed clusters. 'o' = strong relaxed, '◇' = *radio halo*, and 'x' = strong non-relaxed clusters. We fit the power-law models to each of the mean profiles of temperature, electron density, entropy and pressure simply to illustrate fitting lines. The solid green line shows the best-fit for strong relaxed clusters, the solid cyan line shows the best-fit for *radio halo* clusters, and the solid yellow line shows the best-fit for strong non-relaxed clusters. For simplicity, we show only the best-fitting line derived using the constant base power-law model.

dynamical activity, and distinguish between relaxed and non-relaxed clusters. Based on Gini, M_{20} and Concentration parameters (which have been demonstrated to be very useful in identifying a high degree of substructure), and in agreement with previous results (Cassano et al., 2010b), we found that only merging systems - although not all - host *radio halos*. We can do an approximate separation of *radio halo* clusters from relaxed clusters in parameter space for Concentration $<$ 1.55, M_{20} $>$ -2.0 and Gini $<$ 0.65. *Radio halo* clusters have temperature $>$ 6 keV. One interpretation of these trends in the parameter plots is that, in the high redshift Universe, younger clusters are most dynamically active, showing more sub-structure, distortion and merging phenomena. It is thought further that, at slightly later times, (some) merging clusters trigger a non-thermal synchrotron mechanism and, at a subsequent stage, become relaxed and radio quiet. It is yet unclear under what circumstances, and how, merging clusters activate synchrotron emission, because only a small fraction goes through this phase. Another possibility could be a bias in the sample. Modern radio telescopes do not have enough sensitivity to detect *radio halos* in low massive clusters and, because of that, we are unable to observe these objects in region 2 of the M_{20} and Gini vs temperature plot of Fig. 5.1.

We also studied the sample of the KA09 and, based on morphology parameters, we found a

Table 5.6: Best-fitting values of the power-law model (pure) derived for mean radial profiles of *radio halo* clusters. The meaning of α and F is same as in Table 5.5.

Thermodynamic profiles	α	F
mean T	0.11 $\pm$ 0.02	1.30 $\pm$ 0.08
mean n_e	-0.37 $\pm$ 0.07	0.49 $\pm$ 0.12
mean K	0.44 $\pm$ 0.07	2.78 $\pm$ 0.41
mean P	-0.18 $\pm$ 0.03	0.68 $\pm$ 0.06

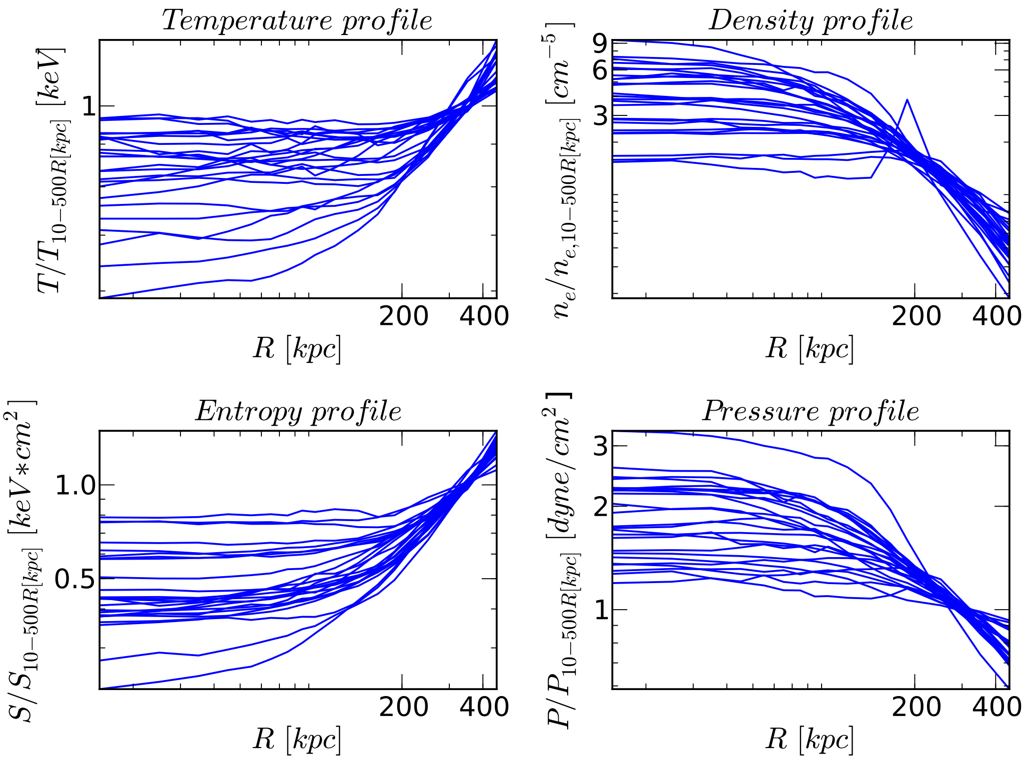

Figure 5.6: Unscaled thermodynamic profiles of *radio halo* clusters.

total of 53 disturbed and hottest clusters (M_{20} > -2 or Gini < 0.65 and temperature > 6 keV) in this sample. As we noted in previous paragraph, cluster with these criteria host *radio halo*. So based on this, we identified 53 possible *radio halo* clusters and already some of them (13 clusters) have detected with *radio halo*. It is possible that either the lack of sensitivity of current radio observations or the steep spectrum of these sources poses a challenge in the detection of these 'possible' *radio halos* in the KA09 sample. We also noticed two *mini radio halo* clusters - A2390 and A2142 - overlap with hottest and disturbed clusters. The origin of *mini radio halo* is still poorly known. Gitti et al. (2007) showed that sub-cluster or minor mergers could provide energy to electron re-acceleration in *mini radio halo* clusters to generate this faint and diffuse emission. This small scale merger that have not been able to destruct the cool core of the cluster and therefore, small scale of *mini radio halos* are detected in some cool core or relaxed clusters. ZuHone et al. (2011) presented simulations of core gas sloshing and particle re-acceleration in a galaxy cluster. They suggests that gas sloshing may generate turbulence in the core, which in turn may re-accelerate the relativistic electrons require to form a *mini radio halo*. In these both cases,

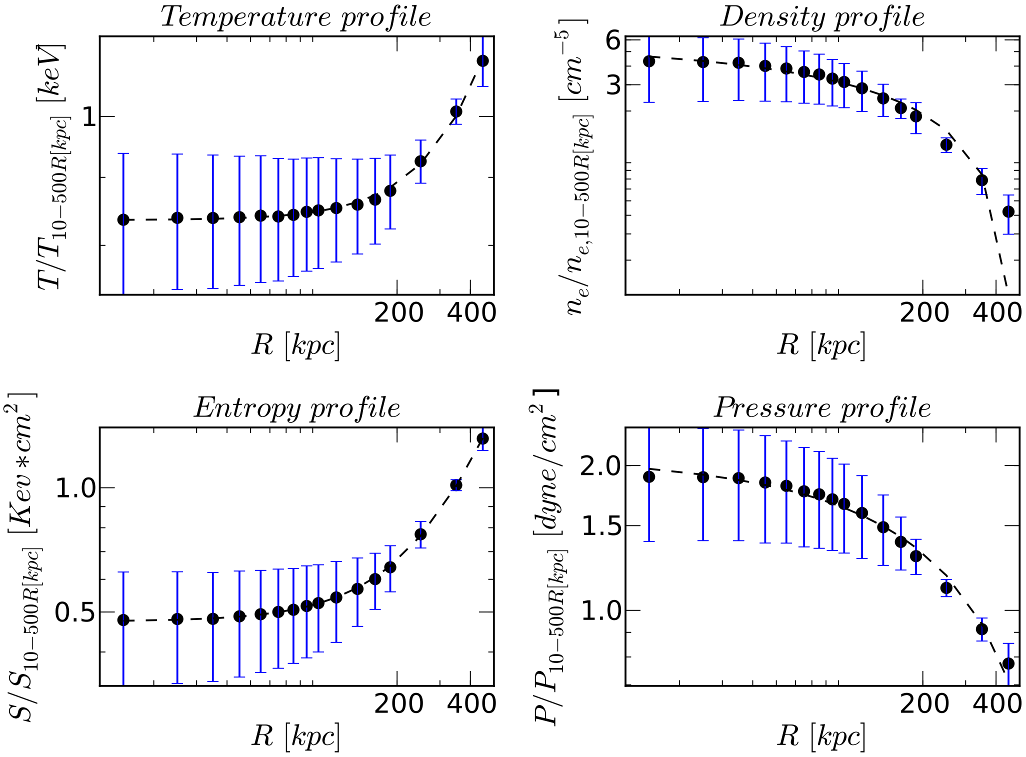

Figure 5.7: Unscaled thermodynamic mean profiles of *radio halo* clusters. The black dashed line shows the best-fit for the mean profile of *radio halo* clusters derived using the power-law (constant base) model.

Table 5.7: Best-fitting values of the power-law model (constant base) derived for unscaled mean radial profiles of *radio halo* clusters. The meaning of α, F and F_0 is same as in Table 5.5.

Thermodynamic profiles	α	F	F_0
mean T	1.95 ± 0.06	2.68e-06 ± 0.00	0.84 ± 0.00
mean n_e	0.47 ± 0.09	-0.32 ± 0.19	5.77 ± 0.54
mean K	1.82 ± 0.02	1.37e-05 ± 0.00	0.47 ± 0.00
mean P	0.71 ± 0.08	-0.02 ± 0.01	2.09 ± 0.06

X-ray image of relaxed cluster (e.g. A2390 and A2142) reveal complex morphology around the cluster centre, and thus this relaxed cluster overlap with non-relaxed clusters in parameter planes.

Future low frequency radio observation is crucial to shed new light on our current understanding of *radio halos*. Large numbers of *radio halos* are expected at fainter and more diffuse radio fluxes, by simply assuming the extrapolation of their 1.4 GHz number counts through the $P_{1.4GHz}$–X-ray luminosity correlation. Though faint and diffuse emission of *radio halos* is undetected using current radio telescopes at 1.4 GHz, since they have steep radio spectra, they should appear brighter at lower frequencies, enabling LOFAR and LWA to detect large numbers of these radio sources (Cassano, 2010; Feretti et al., 2012).

Deep (low frequency) radio surveys are necessary in the search for *radio halos*. Recent Monte Carlo calculations based on turbulent acceleration in galaxy clusters predict that the number of these (low radio power, faint and low frequency) *radio halos* could be detected at $\sim$ 120 MHz by

Table 5.8: Best-fitting values of the power-law model (pure) derived for unscaled mean radial profiles of *radio halo* clusters. The meaning of α and F is same as in Table 5.5.

Thermodynamic profiles	α	F
mean T	0.07 ± 0.02	0.63 ± 0.05
mean n_e	-0.37 ± 0.06	14.48 ± 3.41
mean K	0.40 ± 0.05	0.10 ± 0.03
mean P	-0.20 ± 0.03	3.80 ± 0.50

a high sensitive (0.1 mJy/beam) survey by the LOFAR over the northern hemisphere (Cassano et al., 2010a; Rottgering, 2010; Cassano et al., 2011). From this survey, we anticipate discovering $\sim$ 350 *radio halos* up to redshift of $\sim$ 0.6. This will increase the number of known *radio halos* almost ten fold. More than half of these halos will be 'ultra-steep spectrum' halos, with cut-off frequency $\nu_c < 600$ MHz. It will provide a clear test of the importance of turbulence in particle acceleration in merging clusters. Recently, Cassano et al. (2012) conducted a similar simulation, but for 1.4 GHz observations with the EMU + WODAN survey, both of which are designed to be carried out with ASKAP and Aperitif, respectively. The authored showed that these surveys have the potential to detect $\sim$ 200 new *radio halos* at 1.4 GHz, the clusters at redshift ≤ 0.6, and a below flux level of 10 mJy. It is of great interest to us to conduct similar studies with the ongoing South African radio continuum survey project known as 'The MeerKAT International Giga-Hertz Tiered Extragalactic Exploration' (MIGHTEE) with the MeerKAT path-finder telescope (Jonas, 2009; Norris et al., 2013). The primary goal of this project is to undertake a tiered extragalactic radio continuum survey to investigate AGN evolution, star-forming galaxies and galaxy clusters from the epoch of re-ionisation (EoR) through to the present day. The MIGHTEE survey aims to probe to much fainter flux densities (0.1–1 μJy/beam) over smaller sky areas ($\sim$ 35 deg^2) at higher angular resolution, at a 1.4 GHz observing frequency. The higher sensitivity will enable the search of more *radio halo* sources. Hence, according to our finding, these (KA09) clusters are the best candidates to observe with future radio telescopes, in order to increase the number of *radio halo* detections in galaxy clusters.

We compared morphology parameter calculations of 25 *radio halo* clusters with their radio properties of LLS and $P_{1.4GHZ}$. We did not see any strong relationship between X-ray morphology and radio properties. There could, however, be a weak relationship between the parameters and LLS. This could indicate that most disturbed clusters (low Gini and Concentration) host *radio halos* of large size. We do not rule out the possibility that poor sensitivity or low flux levels leads to ill-constrained radio quantities ($P_{1.4GHz}$ and LLS). This then makes it difficult to compare radio properties with X-ray morphology. In future, we will use these morphology parameters to study the morphology of *radio halos*, and compare it with X-ray cluster morphology. This will help in the understanding of how *radio halos* are generally distributed as the X-ray thermal gas, and how flux distribution of *radio halos* correlates with X-ray flux. For example, Feretti et al. (2010) compared the position of the *radio halo* with that of the X-ray gas distribution. In this study they found that *radio halos* can be very asymmetric with respect to X-ray gas distribution, and this becomes more pertinent when halos of smaller sized are considered, or have smaller LLS. Recently, Govoni et al. (2012) conducted similar studies for four newly detected *radio halo* clusters. They noticed that smaller sized *radio halos* show larger displacements between radio and X-ray peaks. Furthermore, these four *radio halos* are quite asymmetric with respect to the X-ray gas distribution. It is expected that smaller *radio halos* could have more distorted morphologies because they may be younger objects, which have a large scale of energy production due to the ongoing merging activity. This results in a non-uniform distribution of relativistic electrons and magnetic fields. Asymmetry in *radio halos* may arise by magnetic field fluctuations on a large scale $\sim$ 100 kpc (Vacca et al., 2010). These results may reveal the origin of *radio halos*, and link their morphological properties with those of the cluster dynamical state.

Finally, we studied temperature, electron density, entropy and pressure (scaled) radial profiles for strong non-relaxed clusters, strong relaxed clusters and *radio halo* clusters. These analyses indicate that the characteristics of thermodynamic profiles of *radio halo* clusters are similar to those of strong non-relaxed clusters. This phenomenon (diffuse radio emission) does not occur in strong relaxed clusters, but is linked with the cluster-cluster merging process. Further, merger shocks heat the ICM, and may increase the entropy as well as providing the energy to generate the non-thermal components in clusters through the acceleration of high-energy relativistic particles (Sarazin, 2002, 2009; Brunetti et al., 2009). When we plotted unscaled radial profiles for 25 *radio halo* clusters, we noticed a large scattering in the cluster core region ($\lesssim$ 100 kpc) in all thermodynamic profiles of *radio halo* clusters. This could indicate different levels of turbulence in different *radio halo* clusters. In future, we aim to study the point to point correlation between 2-D *radio halos* and thermodynamic images. With a large sample of *radio halo* clusters, this will help to understand how entropy and pressure are distributed across *radio halo* emission, and how merger shocks affect entropy and provide acceleration of relativistic particles throughout the cluster.

6

Summary and Future outlook

6.1 Summary

Structure formation in the Universe proceeds in a hierarchical manner with the most massive objects, clusters, forming last. Clusters continue to evolve by the infall of subclusters. The time between major mergers is typically $\sim$ 5 Gyr. Approximately 20% of clusters have had a recent merger or are undergoing merger. Merging events profoundly affect the properties of different components of a cluster, as understood from observations and numerical simulations. Multiple merger sequences could, for instance, be responsible for disturbing the dynamically relaxed cores of the X-ray emitting hot ICM, as well as its density, temperature and metallicity distribution. In addition, it is well known that a disturbed X-ray morphology is typical of dynamically perturbed galaxy clusters, and that it could be responsible for scattering in the scaling relations of X-ray clusters. It also affects the mass estimation of hot baryons. Investigating cluster dynamical states has important implications both in the use of clusters as tools for cosmology, as well as the study of the complex gravitational and non-gravitational processes acting during large-scale structure formation and evolution since, in both cases, we need to know if observed clusters are relaxed or not.

Another intrinsic feature connected to X-ray galaxy cluster observation is diffuse radio sources. Diffuse extended cluster-wide radio sources are currently grouped in three categories: *radio halos*, *relics* and *mini-halos* (Feretti et al., 2012, and references therein). *Radio halos* are found at the central cluster region, with typical extent $\sim$ 1 Mpc and steep spectra ($s \propto \upsilon^{-\alpha}$, α = 1-1.8). The relic sources are similar to the halos in their low surface brightness, large size and steep spectrum, but they are typically found in the peripheral regions of the cluster. Radio observations reveal the presence of diffuse and large-scale synchrotron radiation from the ICM. This suggests that magnetic fields, non-thermal components and relativistic particles are mixed with the hot ICM. The origin of these components is still not clear, and remains a subject of debate. In the case of *radio halos*, various research groups have proposed theories (primary and secondary relativistic particle models) about their formation, but none of them has had enough observational evidence.

It is believed that *radio halos* are linked with cluster dynamical activity. They are typically found in clusters with significant substructure and deviation from spherical symmetry in their X-ray morphology. This is confirmed by the high resolution X-ray data obtained via the *Chandra* and *XMM-Newton* X-ray telescopes. The available X-ray data suggest that *radio halos* are strongly related to the X-ray properties of the host clusters, as well as to the presence of cluster merger processes. They are not observed in relaxed and regular clusters. Observations show that the radio power of halos increases with X-ray luminosity and temperature, implying a direct connection between thermal and non-thermal cluster properties. The bi-model behaviour of *radio halos* suggests that only a fraction of massive, luminous and hot clusters host halos, while this phenomenon is completely absent in the majority of clusters. Simultaneous study of radio and X-ray data could provide significant information about *radio halo* formation.

Overall we attempted to investigate cluster dynamical states and their connection to the formation of *radio halos*. We studied X-ray cluster dynamical states using (1) seven morphology parameters which include the Gini, M_{20}, Concentration, Asymmetry, Smoothness, Ellipticity, and Gini of the second order moment (G_m), and (2) cluster thermodynamic maps. Morphology parameters are straightforward and, without any additional assumption or requirements of models, simple to calculate for a large number of clusters. On the other hand, for an in-depth analysis of a cluster, thermodynamic maps are essential in investigating its properties and accurate dynamical states. Generating these maps, however, is complex.

A brief description of the main outcomes of both of our analyses follows.

In order to study morphology parameters, we first simulated simple 2-D Beta model clusters with relaxed and non-relaxed morphologies. We tested our parameters for these 2-D Beta model images, as well as with added instrumental effects in those images. In both cases, six parameters, except for the Ellipticity, were capable of separating the different dynamical states of clusters.

Subsequently, we applied our various parameters to the V09 cluster sample, which included low- and high-z galaxy clusters. Of the seven morphology parameters, three - the Gini, M_{20} and Concentration - were promising in the investigation of the dynamical states of galaxy clusters. The Smoothness and Asymmetry were not applicable to our sample of clusters in that they did not have uniform exposure times for all clusters, as well as inadequate S/N. This was in agreement with our previous Beta model simulation results. In the case of distant clusters, the Concentration parameter could be replaced with the Gini in order to identify their dynamical states. The advantage of using the Gini is that it is independent of the central position of clusters. These three parameters were useful and robust in spite of the data having had low S/N and/or the cluster being at high-z.

Based on the combination of these three parameters, we investigated the evolution of galaxy clusters in terms of the trend of strong non-relaxed or non-cool core $\rightarrow$ mild merger or weak-cool core $\rightarrow$ relaxed or cool core $\rightarrow$ strong relaxed, strong cool core or evolved clusters. In this analysis, we found that a high fraction of clusters (in the V09 sample) is evolving or showing some substructure activity, while a low fraction is fully evolved.

These parameters are independent of cluster internal average properties such as luminosity, temperature and mass. In other words, cluster morphology is not related to its ICM properties. The Gini, Concentration and M_{20}, however, appear to be correlated with the cooling time of clusters. X-ray imaging and surface brightness maps are therefore helpful in the understanding of cooling times of relaxed clusters.

We showed that the XMC is a useful technique in analysing complex X-ray data. This ambitious new method models the ICM in clusters as a set of X-ray emitting smoothed particles of plasma. It is possible to simultaneously access the spatial and spectral information of X-ray clusters, and also to accommodate complex models of plasma in order to model X-ray clusters. This approach reproduces many of the features observed in the X-ray emission in a less assumption-dependent way than traditional analysis, and allows for a much more detailed characterisation of the density, temperature, entropy, pressure and metal abundance distribution of clusters. More work, however, is required to test the XMC for *Chandra* data. The only disadvantage is that it requires large computing power.

Using the XMC technique, we generated thermodynamic maps (temperature, density, pseudo entropy and pseudo pressure) of our low-z cluster sample (V09). First, we studied the distribution of thermodynamic quantities in relaxed and non-relaxed clusters. We plotted radial profiles of the combined clusters for each thermodynamic map. They indicated that the distribution is different for relaxed and non-relaxed clusters. Generally, in temperature and entropy maps, relaxed clusters have steep profiles, while non-relaxed clusters have shallow profiles; and in density and pressure maps, relaxed clusters have cups in their central regions (high density and pressure), while non-relaxed clusters have flatter profiles (low density and pressure) in the cluster cores.

It is conventional to use surface brightness images of X-ray clusters to study the morphology and detection of substructure. Furthermore, morphology parameters are useful in investigating the morphology of thermodynamic maps. Morphology of density maps is similar to that of surface brightness maps. Temperature and entropy maps reveal disturbance in the core, possible caused by a non-gravitational heating source such as AGN. We evaluated the slope of each thermodynamic radial profile using the power-law models. For density, entropy and pressure, we found different slope values for relaxed and non-relaxed clusters, but not for temperature. Furthermore, we found a relationship between surface brightness morphology and slope of density, entropy and pressure. This could suggest that cluster entropy and pressure depend largely on density. Using these morphology parameters only, it was evident that we would be able to evaluate the gradient of thermodynamic quantities for high-z clusters.

As stated previously in this section, in order to study a cluster in detail, it is necessary to investigate its thermodynamic radial profile. It is possible that (minor) substructure would not be noticed in the surface brightness map of a relaxed cluster, resulting in it not being possible to study accurately its dynamical state, and hence an incorrect estimation of its mass. To overcome this, and to compare our results with thermodynamic morphology parameters, we chose to study the radial profiles of clusters. We selected strong relaxed and strong non-relaxed clusters, as classified by their surface brightness morphology parameters. In the analysis we noticed, in the temperature map of A2244, small scale merging or disturbance which had been unnoticed in its surface brightness map. We found that temperature maps were more sensitive in identifying substructure in galaxy clusters. Fluctuation and discontinuity in radial profiles signify merging activity in galaxy clusters.

To illustrate the usefulness of morphology parameters, we used them to study the dynamical activity of *radio halo* clusters. We found that all *radio halo* clusters are dynamically disturbed, and are associated with the more massive and hotter clusters. This phenomenon is absent in relaxed and regular clusters. We also studied thermodynamic maps and radial profiles of *radio halo* clusters, and found that their thermodynamic properties were similar to those of cluster mergers. We noticed that their temperature and entropy profiles were both flat and discontinued in the cluster core. This supports the idea that diffuse radio emission is linked with cluster merger activity.

6.2 Future outlook

It is hoped that this work will be useful in conducting further study of X-ray and radio observations of galaxy clusters using future X-ray and radio telescopes. The morphology parameters derived should help in the selection of X-ray cluster candidates in the search for diffuse radio sources.

- Due to the advancement and interface of theoretical, computational, and observational knowledge, we have, in the past decade, greatly enhanced our view of cluster astrophysics. At present, it is preferable to give precedence to cluster surveys among other ambitious observational programs at a variety of facilities. Cluster surveys are useful in the understanding of large scale structure formation and its link with cosmology, as well as for approaching more serious questions such as: what causes high energy, non-thermal radio and hard X-ray emission in the ICM; what the origin of large scale magnetic fields is, and how they evolve in cluster volume; how shocks provide kinetic energy to relativistic particles, allowing them to accelerate in the ICM; what the characteristics of turbulence in the ICM are, and what their connection to the cluster structure is; and what the role of diffuse radio sources in cluster evolution is, and how they couple with ICM properties.

- Our goal is to conduct a continuum survey with the South African SKA precursor - KAT-7 and future MeerKAT radio telescope. In particular, we are interested in searching for diffuse radio emission sources in cluster surveys. This will enable us to compile a large and uniform set of cluster data, observed with one instrument and analysed consistently. Further, this will remove selection effects from a large cluster sample that may arise due to sensitivity, and allow us to test thoroughly various models of *radio halo* formations. We are also interested in developing an algorithm which will allow an automatic search of diffuse radio sources in radio images using different techniques such as Bayesian analysis, etc.

- Further plans include an analysis of a GMRT clusters sample. The GMRT conducted a 'Key Cluster Science Project' in the early days of its existence (around 2000). Due to technical reasons, the whole cluster data sets obtained from this project have not yet been analysed. There are data on $\sim$ 100 clusters available at 230 and 610 MHZ frequency bands. We found that, based on corresponding X-ray morphology analysis, some clusters are potential candidates in the search for diffuse radio emission. We plan to analyse these low frequency radio data and, based on any non-thermal detection, will observe the same cluster with the KAT-7 (at 1.4 GHz) to study the full spectral index map. Accordingly, we will also follow up the VLA observation.

- As observed in this study, X-ray properties as well as morphologies of galaxy clusters are crucial in the search for diffuse radio sources. Therefore, for the purpose of exploring a link between X-ray morphologies of *radio halo* clusters, morphology parameters have proved to be the best tool to characterise merging clusters and corresponding *radio halos*. Apart from

X-ray morphology, we plan to follow the multiwavelength morphology approach for *radio halo* clusters. It is of interest to us to study the morphology of *radio halos* in terms of their radio images, and compare their spatial distribution with corresponding X-ray gas using morphology parameters. In this study, we have generated thermodynamic maps of several *radio halo* clusters. It would be interesting to compare X-ray and thermodynamic morphologies with their radio counterparts, to understand the turbulent acceleration mechanism. Hitherto, it has been believed that radio emission is correlated spatially with its X-ray gas; but recently Govoni et al. (2012) found an offset between radio and X-ray emission for *radio halo* clusters. The desired morphology analysis would provide us with a better understanding of X-ray and radio spatial correlation. For *radio halo* clusters, it would also be important to study the (average) morphology of optical galaxies, to search for any connection between morphologies of *radio halos* and galaxies. This would enable us to investigate simultaneously the morphologies of *radio halos*, corresponding X-ray gas, and optical galaxies.

Bibliography

Abell, G. O. 1958, ApJS, 3, 211

Abraham, R. G., van den Bergh, S., & Nair, P. 2003, ApJ, 588, 218

Allen, S. W., Ettori, S., & Fabian, A. C. 2001, MNRAS, 324, 877

Allen, S. W., Evrard, A. E., & Mantz, A. B. 2011, ARA&A, 49, 409

Andersson, K., Peterson, J. R., & Madejski, G. 2007, ApJ, 670, 1010

Andersson, K., Peterson, J. R., Madejski, G., & Goobar, A. 2009, ApJ, 696, 1029 (KA09)

Andrade-Santos, F., Lima Neto, G. B., & Laganá, T. F. 2012, ApJ, 746, 139

Angus, G. W., Diaferio, A., Famaey, B., & van der Heyden, K. J. 2013, MNRAS, 436, 202

Arnaud, M. 2009, A&A, 500, 103

Arnaud, M., & Evrard, A. E. 1999, MNRAS, 305, 631

Bacchi, M., Feretti, L., Giovannini, G., & Govoni, F. 2003, A&A, 400, 465

Bagchi, J., Durret, F., Neto, G. B. L., & Paul, S. 2006, Science, 314, 791

Bagchi, J., Enßlin, T. A., Miniati, F., Stalin, C. S., Singh, M., Raychaudhury, S., & Humeshkar, N. B. 2002, New A, 7, 249

Bagchi, J. et al. 2011, ApJ, 736, L8

Bahcall, N. A. 1996, ArXiv e-prints:astro-ph/9611148

Balogh, M., McCarthy, I. G., Bower, R., & Voit, G. M. 2007, in Heating versus Cooling in Galaxies and Clusters of Galaxies, ed. H. Böhringer, G. W. Pratt, A. Finoguenov, & P. Schuecker, 268

Barrena, R., Girardi, M., Boschin, W., & Dasí, M. 2009, A&A, 503, 357

Bautz, L. P., & Morgan, W. W. 1970, ApJ, 162, L149

Bekki, K., Forbes, D. A., Beasley, M. A., & Couch, W. J. 2002, MNRAS, 335, 1176

Benson, B. A. et al. 2013, ApJ, 763, 147

Bershady, M. A., Jangren, A., & Conselice, C. J. 2000, AJ, 119, 2645

Blanchard, A., Vauclair, S. C., & Sadat, R. 2005, New A Rev., 49, 69

Blasi, P., & Colafrancesco, S. 1999, Astroparticle Physics, 12, 169

Boehringer, H., Voges, W., Fabian, A. C., Edge, A. C., & Neumann, D. M. 1993, MNRAS, 264, L25

Boehringer, H., & Werner, N. 2009, ArXiv e-prints:0907.4277

Böhringer, H., Burwitz, V., Zhang, Y.-Y., Schuecker, P., & Nowak, N. 2005, ApJ, 633, 148

Böhringer, H. et al. 2010, A&A, 514, A32

Bonafede, A., Giovannini, G., Feretti, L., Govoni, F., & Murgia, M. 2009, A&A, 494, 429

Borgani, S., Finoguenov, A., Kay, S. T., Ponman, T. J., Springel, V., Tozzi, P., & Voit, G. M. 2005, MNRAS, 361, 233

Borgani, S., Rosati, P., Tozzi, P., & Norman, C. 1999, ApJ, 517, 40

Bravo-Alfaro, H., Cayatte, V., van Gorkom, J. H., & Balkowski, C. 2000, AJ, 119, 580

Brüggen, M., & Kaiser, C. R. 2002, Nature, 418, 301

Brunetti, G., Cassano, R., Dolag, K., & Setti, G. 2009, A&A, 507, 661

Brunetti, G. et al. 2008, Nature, 455, 944

Brunetti, G., Setti, G., Feretti, L., & Giovannini, G. 2001, MNRAS, 320, 365

Buote, D. A. 2001, ApJ, 553, L15

Buote, D. A., & Tsai, J. C. 1995a, ApJ, 452, 522

——. 1995b, ApJ, 439, 29

——. 1996, ApJ, 458, 27

Burenin, R. A., Vikhlinin, A., Hornstrup, A., Ebeling, H., Quintana, H., & Mescheryakov, A. 2007, ApJS, 172, 561

Burns, J. O., Hallman, E. J., Gantner, B., Motl, P. M., & Norman, M. L. 2008, ApJ, 675, 1125

Cassano, R. 2010, A&A, 517, A10

Cassano, R., & Brunetti, G. 2005, MNRAS, 357, 1313

Cassano, R., Brunetti, G., Norris, R. P., Röttgering, H. J. A., Johnston-Hollitt, M., & Trasatti, M. 2012, A&A, 548, A100

Cassano, R., Brunetti, G., Röttgering, H. J. A., & Brüggen, M. 2010a, A&A, 509, A68

Cassano, R., Brunetti, G., & Setti, G. 2006, MNRAS, 369, 1577

Cassano, R., Brunetti, G., Setti, G., Govoni, F., & Dolag, K. 2007, MNRAS, 378, 1565

Cassano, R., Brunetti, G., & Venturi, T. 2011, Journal of Astrophysics and Astronomy, 32, 519

Cassano, R., Ettori, S., Giacintucci, S., Brunetti, G., Markevitch, M., Venturi, T., & Gitti, M. 2010b, ApJ, 721, L82

Cavagnolo, K. W., Donahue, M., Voit, G. M., & Sun, M. 2009, ApJS, 182, 12

Cavaliere, A., & Fusco-Femiano, R. 1976, A&A, 49, 137

Chatzikos, M., Sarazin, C. L., & Kempner, J. C. 2006, ApJ, 643, 751

Clarke, T. E., Blanton, E. L., & Sarazin, C. L. 2004, ApJ, 616, 178

Clarke, T. E., Kassim, N., Ensslin, T., & Neumann, D. 2005a, Highlights of Astronomy, 13, 330

Clarke, T. E., Sarazin, C. L., Blanton, E. L., Neumann, D. M., & Kassim, N. E. 2005b, ApJ, 625, 748

Clowe, D. et al. 2006, A&A, 451, 395

Colafrancesco, S., & Mele, B. 2001, ApJ, 562, 24

Conselice, C. J. 2003, ApJS, 147, 1

de Plaa, J., Kaastra, J. S., Tamura, T., Mendez, M., Peterson, J. R., Pointecouteau, E., & Arnaud, M. 2004, in The Riddle of Cooling Flows in Galaxies and Clusters of galaxies, ed. T. Reiprich, J. Kempner, & N. Soker, 23

Diaferio, A. 1999, MNRAS, 309, 610

Diaferio, A. 2000, in Astronomical Society of the Pacific Conference Series, Vol. 200, Clustering at High Redshift, ed. A. Mazure, O. Le Fèvre, & V. Le Brun, 182

Diaferio, A., Geller, M. J., & Rines, K. J. 2005, ApJ, 628, L97

Diaferio, A., & Ostorero, L. 2009, MNRAS, 393, 215

Diaferio, A., Schindler, S., & Dolag, K. 2008, Space Sci. Rev., 134, 7

Diehl, S., & Statler, T. S. 2006, MNRAS, 368, 497

Dolag, K., Vazza, F., Brunetti, G., & Tormen, G. 2005, MNRAS, 364, 753

Donahue, M., Horner, D. J., Cavagnolo, K. W., & Voit, G. M. 2006a, ApJ, 643, 730

Donahue, M., Sun, M., Cavagnolo, K., & Voit, G. 2006b, in Bulletin of the American Astronomical Society, Vol. 38, American Astronomical Society Meeting Abstracts, 998

Donnelly, R. H., Markevitch, M., Forman, W., Jones, C., Churazov, E., & Gilfanov, M. 1999, ApJ, 513, 690

Dressler, A. 1980, ApJ, 236, 351

Dupke, R. A., Mirabal, N., Bregman, J. N., & Evrard, A. E. 2007, ApJ, 668, 781

Ensslin, T. A., Biermann, P. L., Klein, U., & Kohle, S. 1998, A&A, 332, 395

Ettori, S., Fabian, A. C., Allen, S. W., & Johnstone, R. M. 2002, MNRAS, 331, 635

Ettori, S., Fabian, A. C., & White, D. A. 1997, MNRAS, 289, 787

Evrard, A. E., Mohr, J. J., Fabricant, D. G., & Geller, M. J. 1993, ApJ, 419, L9

Fabian, A. C. 1994, ARA&A, 32, 277

Fabian, A. C., Hu, E. M., Cowie, L. L., & Grindlay, J. 1981, ApJ, 248, 47

Fabian, A. C., Sanders, J. S., Allen, S. W., Crawford, C. S., Iwasawa, K., Johnstone, R. M., Schmidt, R. W., & Taylor, G. B. 2003, MNRAS, 344, L43

Fabian, A. C., Sanders, J. S., Ettori, S., Taylor, G. B., Allen, S. W., Crawford, C. S., Iwasawa, K., & Johnstone, R. M. 2001, MNRAS, 321, L33

Feretti, L. 2003, in Astronomical Society of the Pacific Conference Series, Vol. 301, Matter and Energy in Clusters of Galaxies, ed. S. Bowyer & C.-Y. Hwang, 143

Feretti, L., Bonafede, A., Giovannini, G., Govoni, F., & Murgia, M. 2010, Highlights of Astronomy, 15, 459

Feretti, L., Fusco-Femiano, R., Giovannini, G., & Govoni, F. 2001, A&A, 373, 106

Feretti, L., Giovannini, G., Govoni, F., & Murgia, M. 2012, A&A Rev., 20, 54

Ferrari, C., Arnaud, M., Ettori, S., Maurogordato, S., & Rho, J. 2006, A&A, 446, 417

Ferrari, C., Govoni, F., Schindler, S., Bykov, A. M., & Rephaeli, Y. 2008, Space Sci. Rev., 134, 93

Finoguenov, A., Böhringer, H., Osmond, J. P. F., Ponman, T. J., Sanderson, A. J. R., Zhang, Y.-Y., & Zimer, M. 2005a, Advances in Space Research, 36, 622

Finoguenov, A., Böhringer, H., & Zhang, Y.-Y. 2005b, A&A, 442, 827

Finoguenov, A., Henriksen, M. J., Miniati, F., Briel, U. G., & Jones, C. 2006, ApJ, 643, 790

Finoguenov, A., Sarazin, C. L., Nakazawa, K., Wik, D. R., & Clarke, T. E. 2010, ApJ, 715, 1143

Forman, W., & Jones, C. 1982, ARA&A, 20, 547

Forman, W., Jones, C., Markevitch, M., Vikhlinin, A., & Churazov, E. 2002, ArXiv e-prints:astro-ph/0207165

Frank, K. A., Peterson, J. R., Andersson, K., Fabian, A. C., & Sanders, J. S. 2013, ApJ, 764, 46

Fruscione, A. et al. 2006, in Society of Photo-Optical Instrumentation Engineers (SPIE) Conference Series, Vol. 6270, Society of Photo-Optical Instrumentation Engineers (SPIE) Conference Series

Gardini, A. 2002, in Astronomical Society of the Pacific Conference Series, Vol. 268, Tracing Cosmic Evolution with Galaxy Clusters, ed. S. Borgani, M. Mezzetti, & R. Valdarnini, 220

Giacintucci, S. et al. 2005, A&A, 440, 867

Giacintucci, S., Venturi, T., Brunetti, G., Dallacasa, D., Mazzotta, P., Cassano, R., Bardelli, S., & Zucca, E. 2009, A&A, 505, 45

Giovannini, G., Bonafede, A., Feretti, L., Govoni, F., & Murgia, M. 2010, A&A, 511, L5

Giovannini, G., Bonafede, A., Feretti, L., Govoni, F., Murgia, M., Ferrari, F., & Monti, G. 2009, A&A, 507, 1257

Giovannini, G., & Feretti, L. 2002, in Astrophysics and Space Science Library, Vol. 272, Merging Processes in Galaxy Clusters, ed. L. Feretti, I. M. Gioia, & G. Giovannini, 197–227

Giovannini, G., Tordi, M., & Feretti, L. 1999, New A, 4, 141

Gitti, M., Ferrari, C., Domainko, W., Feretti, L., & Schindler, S. 2007, A&A, 470, L25

Govoni, F., Feretti, L., Giovannini, G., Böhringer, H., Reiprich, T. H., & Murgia, M. 2001, A&A, 376, 803

Govoni, F., Ferrari, C., Feretti, L., Vacca, V., Murgia, M., Giovannini, G., Perley, R., & Benoist, C. 2012, A&A, 545, A74

Govoni, F., Markevitch, M., Vikhlinin, A., van Speybroeck, L., Feretti, L., & Giovannini, G. 2004, ApJ, 605, 695

Gu, L. et al. 2009, ApJ, 700, 1161

Hashimoto, Y., Böhringer, H., Henry, J. P., Hasinger, G., & Szokoly, G. 2007, A&A, 467, 485

Henry, J. P., & Briel, U. G. 1996, ApJ, 472, 137

Henry, J. P., Finoguenov, A., & Briel, U. G. 2004, ApJ, 615, 181

Hoeft, M., Brüggen, M., & Yepes, G. 2004, MNRAS, 347, 389

Holwerda, B. W., Pirzkal, N., Cox, T. J., de Blok, W. J. G., Weniger, J., Bouchard, A., Blyth, S.-L., & van der Heyden, K. J. 2011a, MNRAS, 416, 2426

Holwerda, B. W., Pirzkal, N., de Blok, W. J. G., Bouchard, A., Blyth, S.-L., & van der Heyden, K. J. 2011b, MNRAS, 416, 2437

Holwerda, B. W., Pirzkal, N., de Blok, W. J. G., Bouchard, A., Blyth, S.-L., van der Heyden, K. J., & Elson, E. C. 2011c, MNRAS, 416, 2401

——. 2011d, MNRAS, 416, 2415

Holwerda, B. W., Pirzkal, N., de Blok, W. J. G., & van Driel, W. 2011e, MNRAS, 416, 2447

Holwerda, B. W., Pirzkal, N., & Heiner, J. S. 2012, MNRAS, 427, 3159

Hudson, D. S., Mittal, R., Reiprich, T. H., Nulsen, P. E. J., Andernach, H., & Sarazin, C. L. 2010, A&A, 513, A37

Jee, M. J., & Tyson, J. A. 2009, ApJ, 691, 1337

Jeltema, T. E., Canizares, C. R., Bautz, M. W., & Buote, D. A. 2005, ApJ, 624, 606

Johnson, R. E., Markevitch, M., Wegner, G. A., Jones, C., & Forman, W. R. 2010, ApJ, 710, 1776

Jonas, J. L. 2009, IEEE Proceedings, 97, 1522

Jones, C., & Forman, W. 1991, in Bulletin of the American Astronomical Society, Vol. 23, Bulletin of the American Astronomical Society, 1338

Jones, C., & Forman, W. 1992, in NATO ASIC Proc. 366: Clusters and Superclusters of Galaxies, ed. A. C. Fabian, 49

Jones, C., & Forman, W. 1999, ApJ, 511, 65

Kaiser, N. 1986, MNRAS, 222, 323

Kapferer, W. et al. 2006, A&A, 447, 827

Kassim, N., Clarke, T. E., Ensslin, T. A., Cohen, A., & Neumann, D. 2001, in Clusters of Galaxies and the High Redshift Universe Observed in X-rays, ed. D. M. Neumann & J. T. V. Tran

Kempner, J. C., Blanton, E. L., Clarke, T. E., & Enßlin, T. A. 2004, in The Riddle of Cooling Flows in Galaxies and Clusters of galaxies, ed. T. Reiprich, J. Kempner, & N. Soker

Kempner, J. C., & Sarazin, C. L. 2001, ApJ, 548, 639

Kempner, J. C., Sarazin, C. L., & Ricker, P. M. 2002, ApJ, 579, 236

King, I. R. 1966, AJ, 71, 64

Kravtsov, A. V., & Borgani, S. 2012, ARA&A, 50, 353

Lakhchaura, K., Singh, K. P., Saikia, D. J., & Hunstead, R. W. 2011, ApJ, 743, 78

Liang, H., Hunstead, R. W., Birkinshaw, M., & Andreani, P. 2000, ApJ, 544, 686

Lorenz, M. O. 1905, Publications of the American Statistical Association, Volume 9, Number 70, p. 209-219, 9, 209

Lotz, J. M., Primack, J., & Madau, P. 2004, AJ, 128, 163

Macario, G., Markevitch, M., Giacintucci, S., Brunetti, G., Venturi, T., & Murray, S. S. 2011, ApJ, 728, 82

Markevitch, M. et al. 2003a, ApJ, 583, 70

Markevitch, M., Gonzalez, A. H., David, L., Vikhlinin, A., Murray, S., Forman, W., Jones, C., & Tucker, W. 2002, ApJ, 567, L27

Markevitch, M. et al. 2003b, ApJ, 586, L19

——. 2000, ApJ, 541, 542

Markevitch, M., & Vikhlinin, A. 2001, ApJ, 563, 95

——. 2007, Phys. Rep., 443, 1

Markevitch, M., Vikhlinin, A., & Forman, W. R. 2003c, in Astronomical Society of the Pacific Conference Series, Vol. 301, Matter and Energy in Clusters of Galaxies, ed. S. Bowyer & C.-Y. Hwang, 37

Markevitch, M., Vikhlinin, A., & Mazzotta, P. 2001, ApJ, 562, L153

Massey, R., Rhodes, J., Leauthaud, A., Ellis, R., Scoville, N., & Finoguenov, A. 2006, in Bulletin of the American Astronomical Society, Vol. 38, American Astronomical Society Meeting Abstracts, 966

Maughan, B. J. 2007, ApJ, 668, 772

Maughan, B. J., Giles, P. A., Randall, S. W., Jones, C., & Forman, W. R. 2012, MNRAS, 421, 1583

Maughan, B. J., Jones, C., Forman, W., & Van Speybroeck, L. 2008, ApJS, 174, 117

Maurogordato, S., Sauvageot, J. L., Bourdin, H., Cappi, A., Benoist, C., Ferrari, C., Mars, G., & Houairi, K. 2011, A&A, 525, A79

Mazzotta, P., Edge, A. C., & Markevitch, M. 2003, ApJ, 596, 190

McNamara, B. R., & Nulsen, P. E. J. 2007, ARA&A, 45, 117

McNamara, B. R. et al. 2001, ApJ, 562, L149

Miniati, F., Jones, T. W., Kang, H., & Ryu, D. 2001, ApJ, 562, 233

Mittal, R., Hicks, A., Reiprich, T. H., & Jaritz, V. 2011, A&A, 532, A133

Mohr, J. J., Evrard, A. E., Fabricant, D. G., & Geller, M. J. 1995, ApJ, 447, 8

Mohr, J. J., Fabricant, D. G., & Geller, M. J. 1993, ApJ, 413, 492

Moore, B., Lake, G., & Katz, N. 1998, ApJ, 495, 139

Muchovej, S. et al. 2007, ApJ, 663, 708

Murgia, M., Govoni, F., Feretti, L., & Giovannini, G. 2010, A&A, 509, A86

Neumann, D. M., & Arnaud, M. 1999, A&A, 348, 711

Neumann, D. M., Lumb, D. H., Pratt, G. W., & Briel, U. G. 2003, A&A, 400, 811

Norris, R. P. et al. 2013, PASA, 30, 20

Okabe, N., Zhang, Y.-Y., Finoguenov, A., Takada, M., Smith, G. P., Umetsu, K., & Futamase, T. 2010, ApJ, 721, 875

Peres, C. B., Fabian, A. C., Edge, A. C., Allen, S. W., Johnstone, R. M., & White, D. A. 1998, MNRAS, 298, 416

Peterson, J. R., & Fabian, A. C. 2006, Phys. Rep., 427, 1

Peterson, J. R., Marshall, P. J., & Andersson, K. 2007, ApJ, 655, 109

Petrosian, V. 2001, ApJ, 557, 560

Ponman, T. J., Sanderson, A. J. R., & Finoguenov, A. 2003, MNRAS, 343, 331

Poole, G. B., Fardal, M. A., Babul, A., McCarthy, I. G., Quinn, T., & Wadsley, J. 2006, MNRAS, 373, 881

Pratt, G. W., & Arnaud, M. 2003, A&A, 408, 1

Pratt, G. W. et al. 2010, A&A, 511, A85

Pratt, G. W., Croston, J. H., Arnaud, M., & Böhringer, H. 2009, A&A, 498, 361

Rasia, E., Meneghetti, M., & Ettori, S. 2012, ArXiv e-prints:1211.7040

Refregier, A. 2003, ARA&A, 41, 645, astro-ph/0307212

Reiprich, T. H., & Böhringer, H. 2002, ApJ, 567, 716

Reiprich, T. H., Sarazin, C. L., Kempner, J. C., & Tittley, E. 2004, ApJ, 608, 179

Richstone, D., Loeb, A., & Turner, E. L. 1992, ApJ, 393, 477

Ricker, P. M., & Sarazin, C. L. 2001, ApJ, 561, 621

Ritchie, B. W., & Thomas, P. A. 2002, MNRAS, 329, 675

Roettiger, K., Stone, J. M., & Burns, J. O. 1999, ApJ, 518, 594

Rood, H. J., & Sastry, G. N. 1971, PASP, 83, 313

Rosati, P. 2004, Clusters of Galaxies: Probes of Cosmological Structure and Galaxy Evolution, 72

Rosati, P., Borgani, S., & Norman, C. 2002, ARA&A, 40, 539

Rossetti, M., Ghizzardi, S., Molendi, S., & Finoguenov, A. 2007, A&A, 463, 839

Rottgering, H. J. A. 2010, in ISKAF2010 Science Meeting

Sanders, J. S., & Fabian, A. C. 2001, MNRAS, 325, 178

Sanders, J. S., Fabian, A. C., Allen, S. W., & Schmidt, R. W. 2004, MNRAS, 349, 952

Sanders, J. S., Fabian, A. C., & Taylor, G. B. 2005, MNRAS, 356, 1022

Sanderson, A. J. R., Edge, A. C., & Smith, G. P. 2009a, MNRAS, 398, 1698

Sanderson, A. J. R., Finoguenov, A., & Mohr, J. J. 2005, ApJ, 630, 191

Sanderson, A. J. R., O'Sullivan, E., & Ponman, T. J. 2009b, MNRAS, 395, 764

Santos, J. S., Rosati, P., Tozzi, P., Böhringer, H., Ettori, S., & Bignamini, A. 2008, A&A, 483, 35

Sarazin, C. L. 1988, X-ray emission from clusters of galaxies

Sarazin, C. L. 2002, in Astrophysics and Space Science Library, Vol. 272, Merging Processes in Galaxy Clusters, ed. L. Feretti, I. M. Gioia, & G. Giovannini, 1–38

——. 2003, Physics of Plasmas, 10, 1992

——. 2009, X-Ray Emission from Clusters of Galaxies

Scarlata, C. et al. 2007, ApJS, 172, 406

Schneider, P. 2006, Extragalactic Astronomy and Cosmology, pp. 223–275

Schuecker, P. 2005, in Reviews in Modern Astronomy, Vol. 18, Reviews in Modern Astronomy, ed. S. Röser, 76–105

Schuecker, P., Böhringer, H., Reiprich, T. H., & Feretti, L. 2001, A&A, 378, 408

Semler, D. R. et al. 2012, ApJ, 761, 183

Shapiro, P. R., & Iliev, I. T. 2000, ApJ, 542, L1

Smith, G. P., & Taylor, J. E. 2008, ApJ, 682, L73

Solovyeva, L., Anokhin, S., Feretti, L., Sauvageot, J. L., Teyssier, R., Giovannini, G., Govoni, F., & Neumann, D. 2008, A&A, 484, 621

Sun, M., Jones, C., Murray, S. S., Allen, S. W., Fabian, A. C., & Edge, A. C. 2003, ApJ, 587, 619

Sun, M., Murray, S. S., Markevitch, M., & Vikhlinin, A. 2002, ApJ, 565, 867

Tittley, E. R., & Henriksen, M. 2001, ApJ, 563, 673

Tozzi, P. 2007, Mem. Soc. Astron. Italiana, 78, 729

Tozzi, P., & Norman, C. 2001, ApJ, 546, 63

Vacca, V., Murgia, M., Govoni, F., Feretti, L., Giovannini, G., Orrã, E., & Bonafede, A. 2010, A&A, 514, A71

van Weeren, R. J., Hoeft, M., Röttgering, H. J. A., Brüggen, M., Intema, H. T., & van Velzen, S. 2011, A&A, 528, A38

van Weeren, R. J. et al. 2009a, A&A, 506, 1083 van Weeren, R. J., Röttgering, H. J. A., Brüggen, M., & Cohen, A. 2009b, A&A, 505, 991

Venturi, T. 2011, Mem. Soc. Astron. Italiana, 82, 499

Venturi, T., Bardelli, S., Dallacasa, D., Brunetti, G., Giacintucci, S., Hunstead, R. W., & Morganti, R. 2003, A&A, 402, 913

Venturi, T., Giacintucci, S., Brunetti, G., Cassano, R., Bardelli, S., Dallacasa, D., & Setti, G. 2007, A&A, 463, 937

Venturi, T., Giacintucci, S., Dallacasa, D., Cassano, R., Brunetti, G., Bardelli, S., & Setti, G. 2008, A&A, 484, 327

Vikhlinin, A., Burenin, R., Forman, W. R., Jones, C., Hornstrup, A., Murray, S. S., & Quintana, H. 2007, in Heating versus Cooling in Galaxies and Clusters of Galaxies, ed. H. Böhringer, G. W. Pratt, A. Finoguenov, & P. Schuecker, 48

Vikhlinin, A. et al. 2009a, ApJ, 692, 1033 (V09)

Vikhlinin, A., Kravtsov, A., Forman, W., Jones, C., Markevitch, M., Murray, S. S., & Van Speybroeck, L. 2006, ApJ, 640, 691

Vikhlinin, A. et al. 2009b, ApJ, 692, 1060

Vikhlinin, A., McNamara, B. R., Forman, W., Jones, C., Quintana, H., & Hornstrup, A. 1998, ApJ, 502, 558

Vikhlinin, A. A., & Markevitch, M. L. 2002, Astronomy Letters, 28, 495

Voit, G. M. 2005, Reviews of Modern Physics, 77, 207

Voit, G. M., Bryan, G. L., Balogh, M. L., & Bower, R. G. 2002, ApJ, 576, 601

Voit, G. M., Kay, S. T., & Bryan, G. L. 2005, MNRAS, 364, 909

Wang, T. et al. 2012, ApJ, 752, 134

Weißmann, A., Böhringer, H., Suhada, R., & Ameglio, S. 2012, ArXiv e-prints:1210.6445

Wise, M. W., Huenemoerder, D. P., & Davis, J. E. 1997, in Astronomical Society of the Pacific Conference Series, Vol. 125, Astronomical Data Analysis Software and Systems VI, ed. G. Hunt & H. Payne, 477

Wu, X.-P. 2000, MNRAS, 316, 299

Yitzhaki, S. 1991, JBES, 9, 235

Zamojski, M. A. et al. 2007, ApJS, 172, 468

Zhang, Y.-Y. et al. 2010, ApJ, 711, 1033

Zhang, Y.-Y., Reiprich, T. H., Finoguenov, A., Hudson, D. S., & Sarazin, C. L. 2009, ApJ, 699, 1178

Ziparo, F., Braglia, F. G., Pierini, D., Finoguenov, A., Böhringer, H., & Bongiorno, A. 2012, MNRAS, 420, 2480

ZuHone, J., Markevitch, M., & Brunetti, G. 2011, Mem. Soc. Astron. Italiana, 82, 632

Zwicky, F., Herzog, E., & Wild, P. 1968, Catalogue of galaxies and of clusters of galaxies

Zwicky, F., Herzog, E., Wild, P., Karpowicz, M., & Kowal, C. T. 1961, Catalogue of galaxies and of clusters of galaxies, Vol. I

Appendix

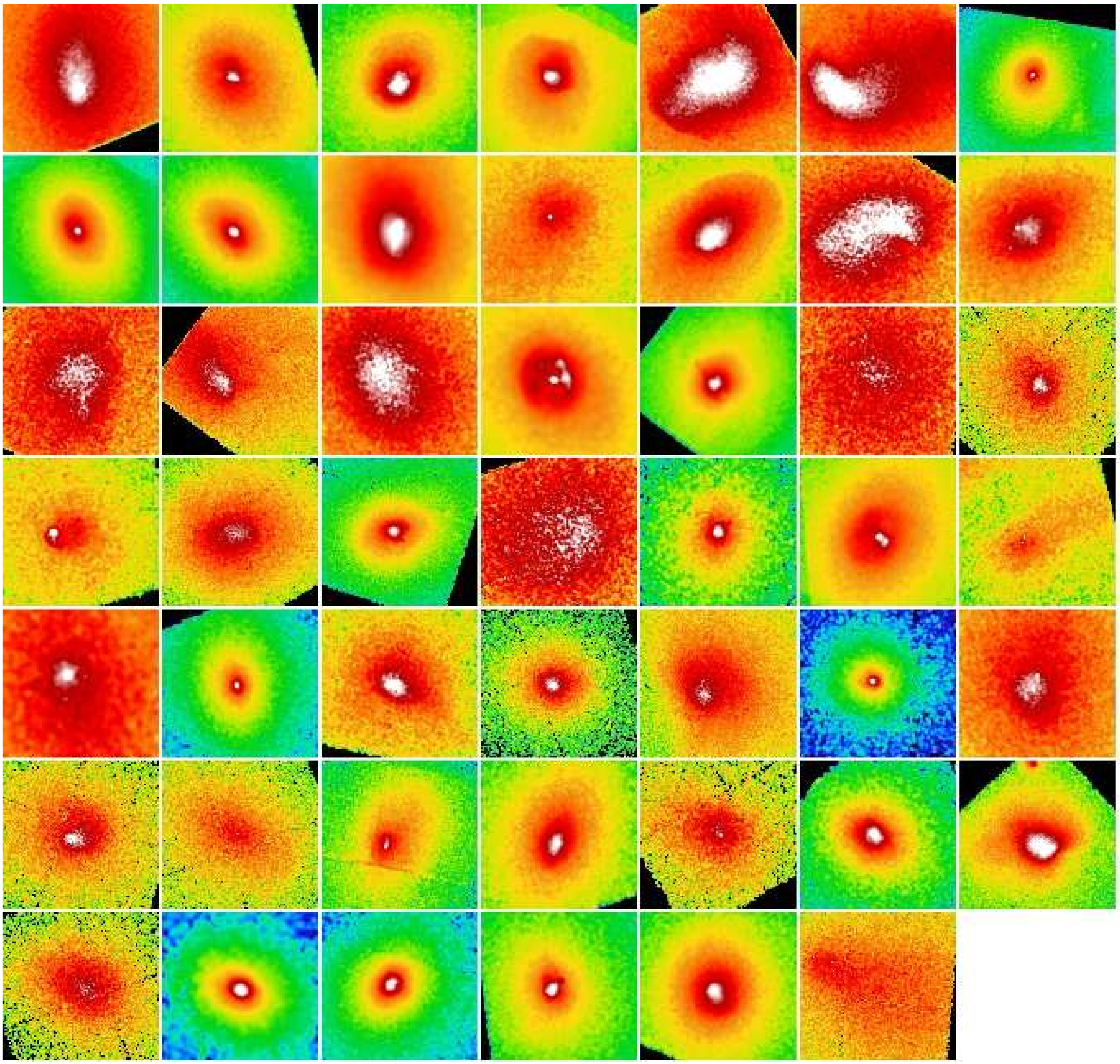

Figure 6.1: Low-z clusters of the V09. Cluster names of panels from top left to bottom right are listed as in Table 3.1.

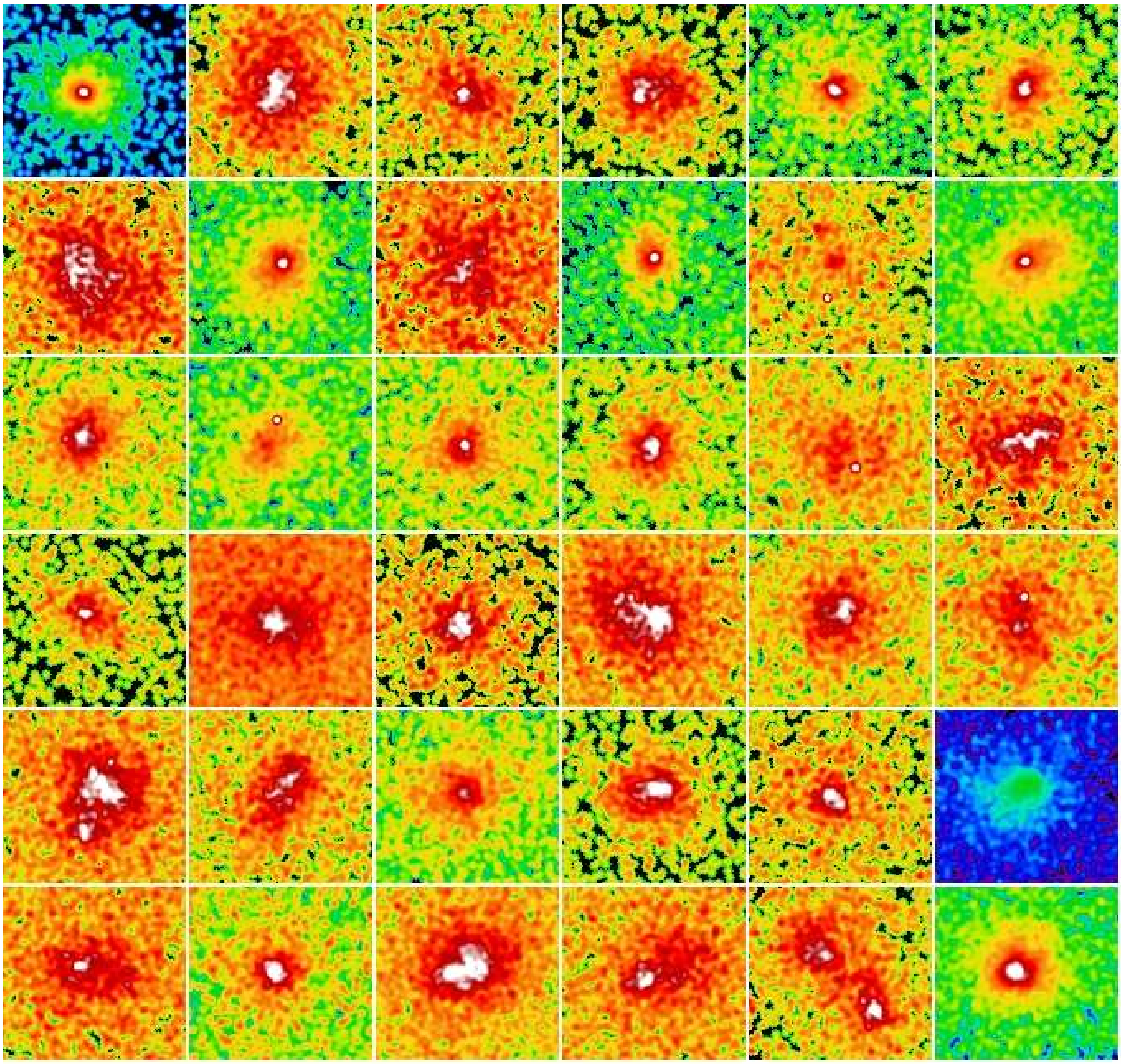

Figure 6.2: High-z clusters of the V09. Cluster names of panels from top left to bottom right are listed as in Table 3.2.

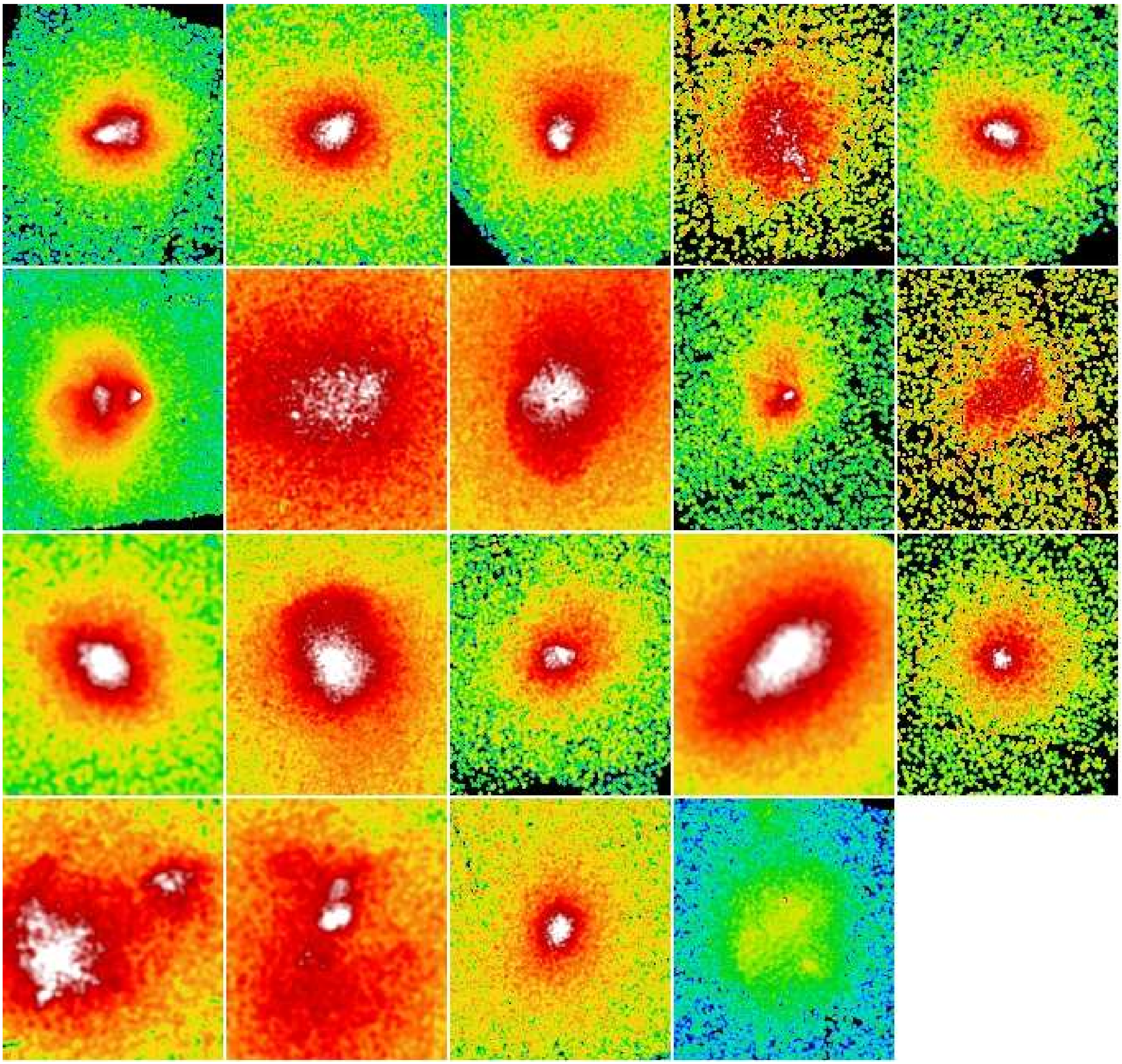

Figure 6.3: *Radio halo* clusters (Giovannini et al., 2009). Cluster names of panels from top left to bottom right are listed as in Table 5.1, except for the V09 *radio halo* clusters (A754, A2256, A401, A3562, A399, and A2163).